FACULTY OF SCIENCES

Investigation of the doping effect in bimetallic metal-organic frameworks to tune their structural flexibility

HANNES DEPAUW

Promotor : Prof. Dr. Pascal Van Der Voort
Co-Promotor : Prof. Dr. Ir. Henk Vrielinck

Thesis submitted in fulfillment of the requirements
for the degree of Doctor (Ph. D.) of Science: Chemistry

Department of Chemistry

Faculty of Sciences, Ghent University

2018

GHENT UNIVERSITY

Center for Ordered Materials, Organometallics & Catalysis

Research Foundation Flanders
Opening new horizons

Solid State Sciences

“When we all think alike,

then no one is thinking”

Benjamin Franklin

Table of contents

Dankwoord

Dit doctoraat startte in de zomer van 2013 bijna 5 jaar later is hier het resultaat!

Een krachtige golf is een geschikte metafoor om dit doctoraat te beschrijven. Aan de horizon kwam ze aangestormd, mijn surfplank draaide ik in de aanlooprichting, warmgehouden door een wetsuit vol enthousiasme. Ik zag de uitdaging, onwetend, onzeker waar ik finaal zou stranden. Of ik ooit deze golf zou kunnen bedwingen. Ik spande mijn spieren op en startte met peddelen. Vele collega's hielpen me met deze uitdaging, ze stuurden mij in de juiste richting. Ik kreeg voeling met het onderzoek en de jaren vlogen voorbij. Ondertussen sta ik recht op mijn surfplank, nu is het moment aangebroken om te genieten, het werk is af, ik *carve* naar het einde van deze mooie periode, op het strand wacht een nieuwe uitdaging!

Eerst en vooral wil ik mijn surfcoachen Prof. Pascal Van Der Voort en Prof. Henk Vrielinck bedanken voor hun onuitputtelijke aanmoediging, wetenschappelijke inzichten en om mij de opportuniteit te geven een doctoraat te kunnen starten. Prof. Pascal Van Der Voort, jij introduceerde mij in de wondere wereld van MOF's, het was een leerrijke ervaring van start tot finish. Bedankt voor de vele kansen, ik kon door jouw steun mijn onderzoek in zowel het COMOC labo als tijdens de korte buitenlandse onderzoeksopdrachten vlot uitvoeren.

Mijn tweede promoter Henk, jij hielp me met raad en daad en vol enthousiasme bij het bedwingen van de vele hindernissen die ik op dit traject tegenkwam. Bedankt voor de vele positieve feedback, ja MIL-53(Al/V) het is een apart materiaal, de grammen of kilogrammen die ik voor je gemaakt heb, daarop is heel robuust en gedetailleerd onderzoek uitgevoerd.

Ik dank ook van harte de leden van de lees- en examencommissie voor het grondig nalezen van dit werk en voor het zetelen in mijn jury.

In het bijzonder wil ik bedanken:

Prof. Freddy Callens voor zijn kritische blik tijdens onze maandelijkse vergadering en de hulp bij het optimaliseren van mijn papers en dit proefschrift.

Prof. Klaartje De Buysser, je hebt mijn laatste paper opnieuw leven in geblazen. Vooral de laatste maanden van mijn thesis waren cruciaal. Jouw rietveldberekeningen legden de laatste hand aan mijn finale paper. Bedankt voor je creatieve input.

Thomas, onze modelling expert. Bij jou kon iedereen altijd ten rade gaan voor informatie, de encylopedie van COMOC, met je nuchtere blik, je logische denkwijze, je loste in een mum van tijd elk vraagstuk op. Je bezorgde me een aantal interessante software tools, vele foto's in mijn artikels kwamen er door jouw input!

Els, jij zorgde voor mijn wetenschappelijke wederopstanding. De moeilijke momenten in mijn laatste jaartje, de druk om mijn artikels eindelijk eens te finaliseren. Dat laatste duwtje dat kwam van jou. Als ik al eens viel, hielp jij me opnieuw recht, zondermeer heb je een groot aandeel in dit eindresultaat. Ik herinner nog de toffe babbels, de uitstapjes die we samen organiseerden voor de groep.

Eén voor allen allen voor één, zoals we de laatste dagen afscheid namen van de onderzoeksgroep COMOC, zo spontaan verliep ook onze eerste ontmoeting. Sander, of beter Dr. Clerick, ik heb altijd met veel plezier geluisterd naar jouw ontdekkingen in de HPLC, schuun bollekes :D. Je goeie muzieksmaak kon ik ook wel appreciëren. En natuurlijk wat is een minivoetbalteam zonder goeie keeper.

Dr. Hendrickx, je hielp met het oplossen van mijn wetenschappelijke raadsels, rare diffracties in XRPD spectra. Ik genoot van je Continuo concerten en natuurlijk onze skireisjes… Ja 2019 dat wordt het jaar, het staat officieel op papier.

De collega's van de koffie en middagpauzes, zij geven aan S3 die persoonlijke sfeer, altijd ambiance: Pierre, Kathleen, Tom, Bart, Pat, Matthias, Jonathan, Niels, Els, Jonas B., Fady, Hannes R. Pieter, Hannes, Kim, Ward.

Katrien, jij maakte mooie foto's van mijn bimetallische materialen, de uren samen aan de TEM vlogen voorbij. De foto's waren enorm belangrijk voor deze thesis waarvoor dank.

Technisch team: Funda en Tom, de stilste werkers verrichten het meeste werk. Ook Ilse wil ik bedanken voor de toegewijde assistentie tijdens de practica en natuurlijk ook voor de lekkere koekjes en toffe babbels tijdens de practica.

Jeroen, MIL-101 boy, ik wil je bedanken voor de aangename tijd als collega en partner in crime voor het doceren van heterogene katalyse, bedankt voor alle hulp. De laatste maanden brachten we samen door op de bureau, een frietje stekken op een druilerige dinsdag, samen naar de fitness, onvergetelijke herinneringen.

Mijn masterstudenten Jonatan en Alexander, jullie wil ik bedanken voor de inzet, enthousiasme en leergierigheid. Het was een plezier om met jullie samen onderzoek uit te voeren.

Irena, my partner in crime, it was a marvelous time working together with you. The EPR specialist, yes that is what you are :D. Combining work and leisure was the best way to stay focused, UK, France, USA we worked, puzzled on our own scientific adventure in many places. I always enjoyed our talks, I wish you the best for the future.

Guangbo, we discovered that COMOC-2(V) is not always well behaving, it's a difficult stubborn person a bit a chameleon, one day green the other yellow. Together we try to unravel all the mysteries of this material. It was nice to work together with you, always motivated, you are a well talented chemist. I will never forget the late evening trip to Chinatown in London, taste with you the extraordinary Chinese food, awesome!

I want to thank everyone from the COMOC team: big smile for Judith, Flore, Chidharth, Norini, Himanshu, Shu Na, Mei, Xiao, Parviz, Sarah, Mieke, Koen and also ex colleagues Isabelle, Yesid, Ximena, Daniel, Asamanjoy, Ximena, Dolores, Ying-Ya, Shyam, Oriol, Matthias.

Ook Arne, Yannick en Guillaume jullie verdienen een vermelding, als ontspanning eens een pintje gaan drinken of een paar uurtjes fitnessen, dit zorgde voor de broodnodige afleiding tijdens het schrijven van dit manuscript.

Marie, jij steunde mij tijdens de laatste maandjes van dit werk. Je kon me begeleiden naar de finish met reeds champagne in de handen. Bedankt voor de goeie babbels, om altijd klaar te staan voor mij. Wuk is de keure dat we binnenkort samen in 't vliegtuig zitten? 1 :D.

Verder wil ik iedereen die ik niet expliciet bij naam vernoem bedanken, velen hadden een positieve invloed op mij, hoe ik denk als wetenschapper en als persoon. Enorm bedankt daarvoor.

Als laatste wil ik mijn ijzersterk, liefdevol thuisfront bedanken, mijn hevigste supporters mamsie, papsie en zusie, jullie haalden me door de moeilijkste periodes en steunden me onvoorwaardelijk! Dikke merci! ☺

Scientific publications

A1 publications

2015

- Multi-frequency (S, X, Q and W-band) EPR and ENDOR study of Vanadium (IV) incorporation in the aluminium metal-organic framework MIL-53.
  I. Nevjestić, H. Depauw, K. Leus, V. Kalendra, I. Caretti, G. Jescke, S. Van Doorslaer, F. Callens, P. Van Der Voort and H. Vrielinck, *ChemPhysChem.*, 2015, **16**, 2968-2973.

2016

- *In-situ* electron paramagnetic resonance and X-Ray diffraction monitoring of temperature-induced breathing and related structural transformations in activated V-doped MIL-53(Al).
  I. Nevjestić, H. Depauw, K. Leus, G. Rampelberg, C. Murray, C. Detavernier, P. Van Der Voort, F. Callens and H. Vrielinck, *Journal of Physical Chemistry C*, 2016, **120**, 17400-17407.

- Systematic study of the chemical and hydrothermal stability of selected 'stable' metal-organic frameworks.
  K. Leus, T. Bogaerts, J. De Decker, H. Depauw, K. Hendrickx, H. Vrielinck, V. Van Speybroeck and P. Van Der Voort, *Microporous and Mesoporous Materials*, 2016, **226**, 110-116.

- Enhanced gas sorption and breathing properties of the new sulfone functionalized COMOC-2 metal-organic framework.
  G.B. Wang, K. Leus, S. Couck, P. Tack, H. Depauw, Y.Y. Liu, L. Vincze, J.F.M. Denayer and P. Van Der Voort, *Dalton Transactions*, 2016, **45**, 9485-9491.

2017

- Synthesis, characterization and catalytic performance of Mo based metal-organic frameworks in the epoxidation of propylene by cumene hydroperoxide.
  X.L. Ni, J. Liu, Y.Y. Liu, K. Leus, H. Depauw, A.J. Wang, P. Van Der Voort, J. Zhang and Y.K. Hu, *Chinese Chemical Letters*, 2017, **28**, 1057-1061.

- Microwave induced “egg yolk” structure in Cr/V-MIL-53.
  H. Depauw, I. Nevjestić, J. De Winne, G.B. Wang, K. Haustraete, K. Leus, A. Verberckmoes, C. Detavernier, F. Callens, E. De Canck, H. Vrielinck and P. Der Voort, *Chemical Communications*, 2017, **53,** 8478-8481.

- Sensing the framework state and guest molecules in MIL-53(Al) *via* the electron paramagnetic resonance spectrum of V^{IV} dopant ions.
  I. Nevjestić, H. Depauw, P. Gast, P. Tack, D. Deduytsche, K. Leus, M. Van Landeghem, E. Goovaerts, L. Vincze, C. Detavernier, P. Van Der Voort, F. Callens and H. Vrielinck, *Physical Chemistry Chemical Physics*, 2017, **19**, 24545-24554.

- A series of sulfonic acid functionalized mixed-linker DUT-4 analogues: synthesis, gas sorption properties and catalytic performance.
  G.B. Wang, K. Leus, K. Hendrickx, J. Wiemme, H. Depauw, Y.Y. Liu, V. Van Specybroeck and P. Van Der Voort, *Dalton Transactions*, 2017,**46**, 14356-14364.

- Discovery of a novel, large pore phase in a bimetallic Al/V metal-organic framework.
  H. Depauw, I. Nevjestić, G.B. Wang, K. Leus, F. Callens, E. De Canck, K. De Buysser, H. Vrielinck and P. Van Der Voort, Journal of Materials Chemistry A, 2017,**5**, 24580-24584.

2018

- Elucidating the vibrational fingerprint of the flexible metal-organic framework MIL-53(Al) using a combined experimental/computational approach.
  A.E.J. Hoffman, L. Vanduyfhuys, I. Nevjestić, S.M.J. Rogge, J. Wieme, H. Depauw, P. Van Der Voort, H. Vrielinck and V. Van Speybroeck, Journal of physical chemistry C, 2018, **122**, 2734-2746.

- A fluorine-containing hydrophobic covalent triazine framework with excellent selective CO_2 capture performance.
  G.B. Wang, K. Leus, H. Sekhar Jena, C. Krishnaraj, S.N. Zhao, H. Depauw, N. Tahir, Y.Y. Liu and P. Van Der Voort, journal of Materials Chemistry A, 2018.

National and international poster presentations

2014

- Post-modification of a gallium based metal-organic framework, COMOC-4 as a catalyst for the epoxidation of cyclic olefins.
  H. Depauw, K. Leus and P. Van Der Voort, 15th Netherlands 'Catalysis and Chemistry Conference' (NCCC XV), 10-12 March 2014 Noordwijkerhout, The Netherlands

- Synthesis, characterization and catalytic performance of a Mo(VI) grafted metal-organic framework.
  H. Depauw, Y.Y. Liu, K. Leus, A. Wang and P. Van Der Voort, Dutch Zeolite Association (DZA), 07-October 2014, Ghent, Belgium

- Characterizing vanadium dopant sites in an Al-metal-organic framework by electron magnetic resonance spectroscopy.
  I. Nevjestić, H. Depauw, K. Leus, F. Callens, P. Van Der Voort and H. Vrielinck, 8th Belgian Crystallography symposium (BCS-8), 15-October 2014, Brussels, Belgium

- Confirming vanadium dopant incorporation in an Al-metal-organic framework by EPR and ENDOR spectroscopy.
  I. Nevjestić, H. Depauw, K. Leus, V. Kalendra, I. Caretti, G. Jescke, S. Van Doorslaer, F. Callens, P. Van Der Voort and H. Vrielinck, 13th Young Belgian Magnetic Resonance Scientist (YBMRS) symposium, 24-25 October 2014 Spa, Belgium

- Resolving the relative tilting of hyperfine and g tensors for vanadyl complexes in the Al-metal-organic framework MIL-53 by a multrifrequency (S, X, Q, and W-band) EPR approach.
  I. Nevjestić, H. Depauw, K. Leus, V. Kalendra, I. Caretti, G. Jescke, S. Van Doorslaer, F. Callens, P. Van Der Voort and H. Vrielinck, 22nd Meeting of the Benelux EPR Society, 22-May 2014, Maastricht, The Netherlands

- Studying the effectiveness of V-incorporation in Al-metal-organic framework MIL-53 with electron-nuclear double resonance spectroscopy.
  I. Nevjestić, H. Depauw, K. Leus, V. Kalendra, I. Caretti, G. Jescke, S. Van Doorslaer, F. Callens, P. Van Der Voort and H. Vrielinck, Defects in Insulating Materials, 12th Europhysical conference, 13-19 July 2014, Canterbury, United Kingdom

2015

- Breathing effect in activated V-doped Al-MOF studied with EPR.
  I. Nevjestić, H. Depauw, K. Leus, F. Callens, P. Van Der Voort and H. Vrielinck, 7th Summer school of the European Federation of EPR groups on Advanced EPR, 24-31 August, 2015, Berlin, Germany

- EPR and ENDOR study of a V-doped Al-metal-organic framework.
  I. Nevjestić, H.Depauw, K. Leus, V. Kalendra, I. Caretti, G. Jescke, S. Van Doorslaer, F. Callens, P. Van Der Voort and H. Vrielinck, 23rd Meeting of Benelux EPR Society, 22-May 2015, Ghent, Belgium

2016

- Breathing effect in V-doped metal-organic framework MIL-53(Al) studied by electron paramagnetic resonance (EPR).
  I. Nevjestić, H. Depauw, K. Leus, P. Van Der Voort, F. Callens and H. Vrielinck, General Scientific meeting 2016 of Belgian Physical Society (BPS), 18-May 2016, Ghent, Belgium

- Breathing effect in the V-doped metal-organic framework MIL-53(Al) monitored in-situ by electron paramagnetic resonance and X-Ray diffraction (XRD).
  I. Nevjestić, H. Depauw, K. Leus, P. Van Der Voort, F. Callens and H. Vrielinck, 24th Meeting of the Benelux EPR Society, 20 May, 2016, Liège, Belgium

- V^{IV} ions as paramagnetic probe for monitoring the structural flexibility of V-doped MIL-53(Al).
  I. Nevjestić, H. Depauw, K. Leus, P. Van Der Voort, F. Callens and H. Vrielinck, 10th Conference of the European Federation of EPR groups (EFEPR), 04-09 September, Torino, Italy

- A series of sulphonic acid functionalized mixed-linker DUT-4 analogues: synthesis, gas sorption properties and catalytic activity.
  G.B. Wang, K. Leus, H. Depauw, Y.Y. Liu, P. Van Der Voort, 5th International conference on Metal-Organic Frameworks & Open Framework Compounds (MOF 2016), 11-15 September 2016, Long Beach, California, United States of America

2017

- Sensing the environment of V^{4+} dopant ions in a metal-organic framework with EPR spectroscopy and X-Ray diffraction.
  I. Nevjestić, H. Depauw, K. Leus, P. Van Der Voort, F. Callens and H. Vrielinck, The 50th Annual International Meeting of ESR Spectroscopy Group of the Royal Society of Chemistry, 02-06 April 2017, Oxford, United Kingdom

National and international oral presentations

2016

- Breathing of V-doped MIL-53(Al) monitored in-situ by electron paramagnetic resonance and X-ray diffraction.
  H. Depauw and I. Nevjestić, 17 March 2016, Ghent, Belgium

- Tailoring the breathing effect of a flexible MOF, COMOC-2 by a mixed-metal approach.
  H. Depauw, I. Nevjestić, K. Leus, G.B. Wang, F. Callens, H. Vrielinck and P. Van Der Voort, 5th International conference on Metal-Organic Frameworks & Open Framework Compounds (MOF 2016), 11-15 September 2016, Long Beach, California, United States of America

- Temperature-induced breathing effect of V-doped MIL-53(Al) monitored *in-situ* by electron paramagnetic resonance and X-ray diffraction
  I. Nevjestić, H. Depauw, K. Leus, P. Van Der Voort, F. Callens and H. Vrielinck, 5th International conference on Metal-Organic Frameworks & Open Framework Compounds (MOF 2016), 11-15 September 2016, Long Beach, California, United States of America

- Regulating the breathing effect of a flexible biphenyl MOF, by a mixed-metal approach.
  H. Depauw, I. Nevjestić, K. Leus, F. Callens, H. Vrielinck and P. Van Der Voort, Chemical Research in Flanders (CRF 2016), 24-26 October 2016, Blankenberge, Belgium

List of acronyms and symbols

A

ANG	adsorbed natural gas
ARPA-E	Advanced Research Projects Agency-Energy

B

BASF	Badische Anilin- and Soda- Fabrik
BDC	benzene-1,4-dicarboxylate
BET	Brunauer-Emmett-Teller
BF	bright-field
BPD	benzene-1,4-dipyrazolate
BPDC	biphenyl-4,4'-dicarboxylate
BTB	benzene-1,3,5-triyltribenzoate
BTC	benzene-1,3,5-tricarboxylate

C

C	coulomb
CE	conventional electric
CNG	compressed natural gas
COF	covalent organic framework
COMOC	Center for Ordered Materials, Organosillica and Catalysis
cp	closed pore
CPM	crystalline porous material
CPO	coordination polymer of Oslo
CUS	coordinated unsaturated sites

D

DEF	N,N'-diethylformamide
DMF	N,N'-dimethylformamide
DMSO	dimethyl sulfoxide
DOBDC	2,5-dioxidobenzene-1,4-dicarboxylate
DOE	Department of Energy
DPPH	diphenylpicrylhydrazyl
DRIFTS	diffuse reflectance infrared Fourier transform spectroscopy
DSC	differential scanning calorimetry
DUT	Dresden University of Technology

E

EC	electrochemistry
EDX	electron dispersive X-ray spectroscopy
EtOH	ethanol
EPR	electron paramagnetic resonance
ENDOR	electron nuclear double resonance

F

FCTO	Fuel Cell Technologies Office
F(T)	vibrational and translational energies of the adsorbate molecule

G

g	gram

H

HT	high temperature
HKUST	Hong Kong University of Science and Technology
Hz	hertz

I

ICP	inductively coupled plasma
IM	imidiazolate
int	intermediate
IPCC	Intergovernmental Panel on Climate Change
IRMOF	isoreticular metal-organic framework
ITHD	ITHD net topology
IUPAC	International Union of Pure and Applied Chemistry
IVU	in-vacuum undulator

J

J	joule

L

lp	large pore
LT	low temperature

M

m	metre
MAC	multi-analyzer crystal
MAF	metal azolate framework
MC	mechanochemistry
MCT	mercury-cadmium-telluride
MeOH	methanol
MFM	Manchester framework material
MIL	Materials Institute Lavoisier
mim	2-methylimidiazolate
MOF	metal-organic framework
MS	mass spectroscopy
MW	microwave

N

NDC	naphthalene-2,6-dicarboxylate
NLE	negative linear expansion
NOAA	National Oceanic and Atmospheric Administration
np	narrow pore
np-d	narrow pore dehydrated
np-h	narrow pore hydrated
NU	Northwestern University

O

OES	optical emission spectroscopy

P

P	pressure
Pa	Pascal
PCN	porous coordination network
PIM	polymer of intrinsic microporosity
PLE	positive linear expansion
Post	Pohang university of science and technology
ppm	parts per million
PSA	pressure swing adsorption
PSD	position sensitive detector
PSM	post-synthetic modification

Q

Q	Quadrupole interactions

R

R	ideal gas constant
RT	room temperature

S

SBU	secondary building unit
SNU	Seoul National University
soc	square-octahedral hosting counter-ions
SOL	solvothermal
STEM	scanning transmission electron microscopy
STP	standard temperature and pressure
SURMOF	Surface anchored metal-organic framework

T

T	temperature
T-XRPD	temperature induced X-ray powder diffraction
TDPAH	2,5,8-tris(3,5-dicarboxylphenylamino)-s-heptazine
TEM	transmission electron microscopy
TGA	thermogravimetric analysis
THF	tetrahydrofurane
TPD	temperature programmed desorption
TSA	temperature swing adsorption

U

UiO	Universitet i Oslo
US	ultrasound
UTSA	University of Texas at San Antonio

V

V	volume
vnp	very narrow pore

W

W	work

X

XANES	X-ray absorption near edge structure
XRPD	X-ray powder diffraction

Z

ZIF	zeolitic imidazolate framework

Others

Å	Ångström
°C	Celcius
K	kelvin
ΔG	gibbs free energy
ΔH	isosteric heat of adsorption
ΔV	volume change
ʎ	wavelength
Ø	interaction potential
$Ø_D$	dispersion interaction
$Ø_R$	repulsion interaction
$Ø_{ind}$	induction energy
$Ø_{F\mu}$	interaction between electric field and permanent dipole
$Ø_{\nabla FQ}$	interaction between the field gradient and contribution of charges that create electrical field on solid surface
α	polarization
μ	permanent dipole
δ	bending vibration
ν	stretch vibration
ω	wagging
∇F	field gradient
$\Delta \bar{H}_l$	differential heat of adsorption
$\bar{H}_l$	molar enthalpy of gaseous adsorbate
$\tilde{H}_g$	partial molar enthalpy of gaseous adsorbate
q_{iso}	isosteric heat of adsorption
I_{G-G}	guest-guest interaction
I_{H-G}	host-guest interaction

1 *Introduction*

1.1 Preface

Human civilization has always been strongly influenced by material technology. The current age, featuring advanced plastics and fibre composites, provides the basic ingredients for a new era, the age of **smart materials**. [1] Tiwari *et al.* have defined these materials as *"Designed materials that have one or more properties that can be significantly changed in a controlled fashion by external stimuli (stress, temperature, moisture, pH, electric or magnetic fields, pressure, etc.)."* [2]

This dissertation focuses on an interesting area within molecular materials chemistry that has recently experienced extraordinary rapid progress: **metal-organic frameworks** or MOFs (Chapter 1), sometimes considered as a type of smart materials. These porous crystalline structures form a 3D framework with metal centres and organic linkers. The application fields (e.g., adsorption, catalysis, separation,…) that are currently being explored are very diverse. The primary goal of this project is to gather insights in the flexibility of these structures. Moreover, this research will contribute to a more efficient MOF design and will further explore the opportunities for MOFs to contribute to a sustainable future.

Adsorption (Chapter 2, section 2.1) is one of the foremost investigated applications of MOFs and is defined as the adhesion of a layer of molecules (gas, solutes, or liquids) to a surface of a solid body or liquid with which they make contact. [3]. The process of separation *via* adsorption is a widespread industrial technique mainly used in petroleum refining and petrochemical industries. The technique is applicable to capture pollutes or to store energy. The smart material MOF can be applied as a solid body to selectively adsorb different molecules, thereby separating one type of molecule from another. This work primarily focuses on the adsorption of one particular compound, i.e., CO_2. In literature, attempts have been made to exploit different MOF materials for adsorption processes with gases such as CO_2 and CH_4. From an environmental point of

view, these gases are polluting exhaust streams emitted by industrial processes. MOFs could capture and store these exhaust products. Vital for a successful outcome will not only be to enhance the adsorption capacity but also to understand the influence of different material characteristics such as history, flexibility and temperature on the final separation capacity and adsorption uptake.

Multiple MOFs behave as smart materials and undergo structural transformations driven by external stimuli such as gases, temperature, moisture and pressure. Such transformations entail a dramatic change of the material's pore size and shape. Literature describes these extraordinary changes in lattice parameters as "breathing". **Breathing** (Chapter 2, section 2.2) indicates that the crystalline material is flexible and can (reversibly) open and close similar to human lungs. Although a rationale for this activity is still hard to be found, such flexible behaviour has been reported for a variety of different frameworks. Extensive work has been done on monometallic frameworks, both from experimental and theoretical approaches. However, bimetallic frameworks have only been scarcely used in structural studies on MOFs yet are expected to play very promising role as breathing materials. By collecting experimental parameters, comparing new data and gathering innovative insights during this work, we hope the assembled information can help to unravel the missing links to complete the explanation and even predict breathing.

Vast experimental research has been performed on monometallic frameworks. **Bimetallic frameworks** (Chapter 3) add an extra degree of freedom for framework design, an innovative subset of new networks can be created. Studying gas adsorption processes in such MOFs provides detailed insight in the relation between structure and behaviour. This may even result in frameworks with different types of breathing behaviour, not yet observed with the monometallic structures. Moreover, tailoring the effect of breathing by metal doping is yet unexplored. A non-exhaustive overview of MOFs discussed and investigated in this work is presented in Table 1.1, together with the most reported frameworks according to Web of Knowledge. In this table, the frameworks are catalogued according to the organic linker used. The chosen MOFs in italic and bolt, presented in Table 1.1 are used in this dissertation and are particularly well-suited for studying the conditions of breathing, as two out of four monometallic

MOFs are flexible, while the other two remain rigid. For each set of investigated structures, one is flexible (MIL-53(Cr)/COMOC-2(V)) while the other (MIL-47(V)/DUT-5(Al)) is rigid. Because both structures are isostructural variants, the metal ion is assumed to be the only difference. Through this approach we assume by gradual doping with a second metal ion, one can follow the evolution of flexibility upon metal exchange.

In this dissertation, we describe two new bimetallic MOF series and elaborately analyse the material characteristics. This work thus contributes both to the field of **flexible** and **bimetallic metal** MOFs. We evaluate the transition in flexibility and gas uptake of the two completely novel bimetallic series. Furthermore, the influence of temperature on the flexibility is investigated.

The new insights obtained can inspire chemists to rationally design and develop new bi- and even multimetallic MOFs for advanced applications. However, a critical perspective in literature on this research field is still lacking. By the incorporation of multiple metals, a broad variety of new intrinsic properties could be envisaged in a bimetallic framework. Enormous potential and new degrees of freedom can be achieved by taking advantage of the properties of the cations. Moreover, a strengthening effect by a synergistic behaviour of the metals could create new materials with yet undiscovered capacity that will dominate their field of application. The incorporation of two metals into one framework could offer a unique method to tailor the structure for better adsorption uptake and/or separation capacity.

Table 1.1 Overview of MOFs discussed and investigated in this work. Framework name in bolt and italic are used in the experimental part of this work.

organic Linker	name	metal (M)	solvent	schematic representation	ref.
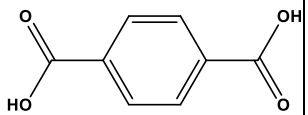 BDC	***MIL-47***	V	H_2O	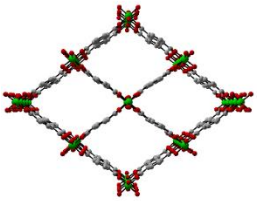	[4]
	MIL-53	Al, Cr, Ga, V, Sc, Fe, In, Cu	H_2O or DMF[a]	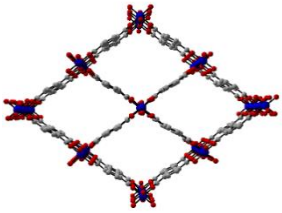	[5-10]
	MIL-101	Cr	H_2O	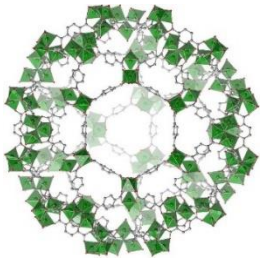	[11]
	UiO-66	Zr	DMF	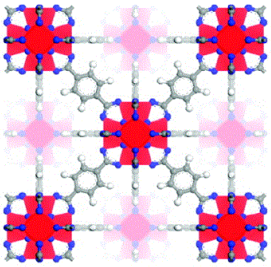	[12]
	MOF-5	Zr	DMF	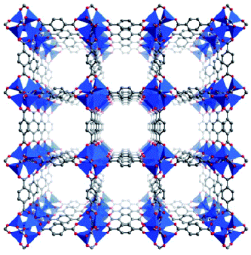	[13]

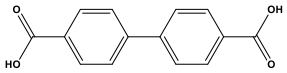 BPDC	***DUT-5***	Al	DMF	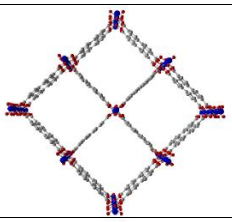	[14]
	COMOC-2	V	DMF	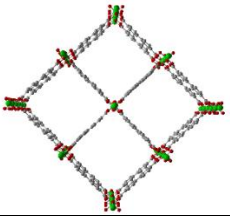	[15]
	UiO-67	Zr	DMF	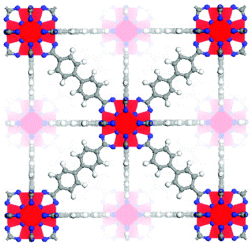	[12]
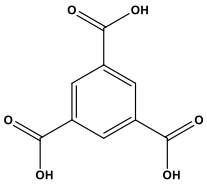 BTC	HKUST-1	Cu	H_2O or EtOH	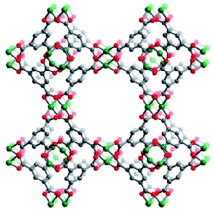	[16]
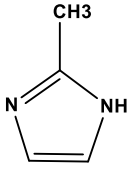 mim	ZIF-8	Zn	DMF	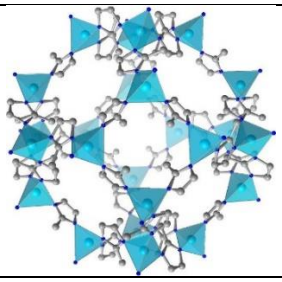	[17]
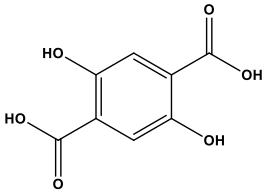 DOBDC	MOF-74	Mg, Zn, Co, Ni	DMF, 2-propanol, H_2O, EtOH or THF	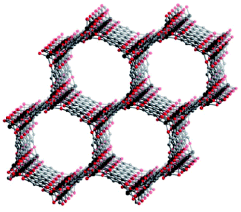	[18]

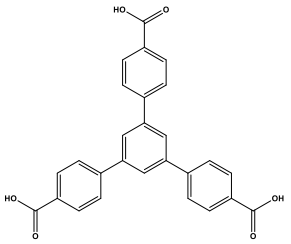 BTB	MOF-177	Zn	DEF	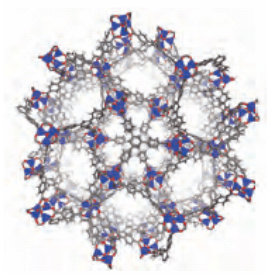	[19]

[a]MIL-53(Fe) is synthesized in DMF = N,N'-dimethylformamide, EtOH = ethanol, THF = tetrahydrofurane, DEF = N,N'-diethylformamide, BDC = benzene-1,4-dicarboxylate, BPDC = biphenyl-4,4'-dicarboxylate, BTC = benzene-1,3,5-tricarboxylate, mim = 2-methylimidiazolate , DOBDC = 2,5-dioxobenzene-1,4-dicarboxylate, BTB = benzene-1,3,5-triyltribenzoate.

1.2 Outline

This work consists of 7 Chapters where Chapter 1, 2 and 3 provide *a state-of-the-art* overview concerning the synthesis and applications of MOF materials. Chapters 4 and 5 combine the experimental work and describe the development of two novel series of bimetallic frameworks. Material characterization and framework induced flexibility are discussed in-depth. Finally, Chapter 6 offers a brief summary and the overall conclusion of this research. Chapter 7 entails a Dutch summary.

In **Chapter 1** a class of hybrid materials, named MOFs are introduced. The predominantly investigated structures are listed and general synthesis procedures of these nanomaterials are described. Emphasis is placed on the CO_2 adsorption of MOFs, this dissertation's main application. Furthermore, several other interesting applications and *state-of-the-art* adsorption by MOFs is discussed briefly.

Chapter 2 presents details concerning the concept of flexible MOFs. Fundamental notions and types of flexibility are discussed. The flexible behaviour of MIL-53 frameworks is highlighted as an example. The discussion is divided in three main parts, each presenting an important parameter: influence of the "guest", "host" and "ligand".

Chapter 3 elaborates on the topic of bimetallic frameworks. In this chapter, the different synthesis methods of bimetallic frameworks are addressed. Advantages and disadvantages of the direct and the post-synthetic metal exchange procedures are introduced. A final section summarizes *the state-of-the-art* concerning carbon dioxide and temperature induced flexibility in bimetallic MOFs.

Chapter 4 describes the synthesis of a new bimetallic series of COMOC-2(V)/DUT-5(Al) frameworks. First, the direct synthesis is probed and the resulting materials are elaborately characterized. Metal dispersion is investigated with EPR and BF-STEM-EDX. Afterwards, the influence of metal-doping on CO_2 uptake and material flexibility is examined. High pressure X-ray powder diffraction and high pressure adsorption reveal the co-existence of two different large and one narrow pore phase.

Chapter 5 focuses on the development of a second novel bimetallic series MIL-53(Cr)/MIL-47(V). Depending on the synthesis procedure used, homogeneous or inhomogeneous (egg-yolk) MOFs are obtained. The Cr/V dispersion is probed *via* BF-STEM EDX mapping. Finally, temperature influence on the flexibility and carbon dioxide adsorption is examined to evaluate the adsorbent.

Chapter 6 gives a short summary and general conclusions of this work and provides future perspectives.

Chapter 7 is the Dutch summary of this dissertation.

1.3 Introduction to the world of MOFs

This chapter covers an introduction to this dissertation's study subject: MOFs. Starting with a brief history of MOFs, the different synthesis pathways are explained. The final part discusses the major applications by zooming in on one specific aspect: CO_2 adsorption.

The Letter to Nature by Yaghi published in 1999 titled "*Design and synthesis of an exceptionally stable and highly porous MOF*" [13, 20] popularized this particular domain of hybrid porous solids. This work reported one of the first MOFs, labelled as MOF-5 and also known as IRMOF-1 ($Zn_4O(BDC)_3$, Table 1.1, and Figure 1.1, left), which remains crystalline after full desolvation and thermal activation.

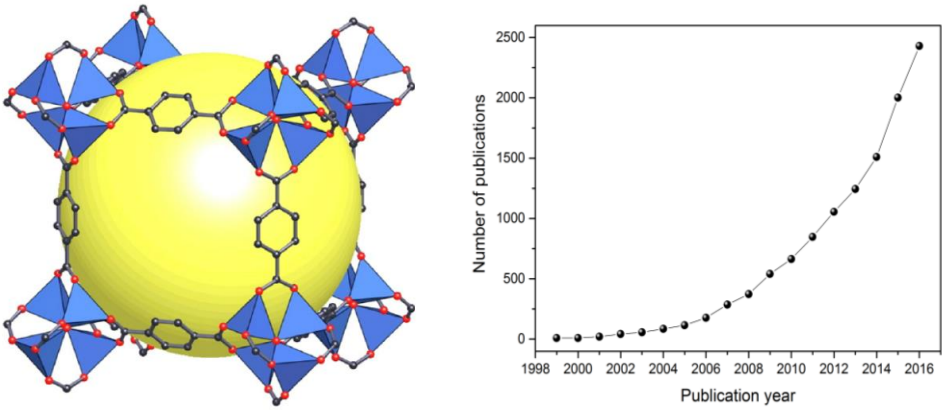

Figure 1.1 (left) MOF-5 structure with Zn_4O tetrahedra (blue), organic BDC linkers (black) and Van der Waals voids (yellow). (Reproduced from [21]); (right) Number of publications on the topic "MOFs" according to Web of Knowledge.

Since this ground breaking discovery, researchers all over the world have started to fully explore this new research domain. The number of publications dealing with MOFs increases exponentially, almost doubling every 2 years (Figure 1.1, right). According to Web of Knowledge, since 1999, more than 12000 publications on this family of hybrid porous materials have been reported. The synthesis and applications of MOFs have been summarized in different themed journals, reviews [22-24] and books. [25-27]

A MOF is a crystalline structure made up out of a metal ion or cluster connected *via* an organic linker, and is created by self-assembly generally from solution. The variety of metals and linkers yields an almost endless number of combinations, thus giving the possibility to tune the structure for well-desired applications. The resulting hybrid is a porous material, characterized by an exceptionally high surface area (reported up to 7100 $m^2 g^{-1}$ and with a theoretical limit of 14600 $m^2 g^{-1}$) [28] and ultra-high porosity. [26]

According to IUPAC (International Union of Pure and Applied Chemistry) porous materials are divided into 3 categories depending on their pore diameter [26]:

- Micropores: smaller than 2 nm.
- Mesopores: between 2 nm and 50 nm.
- Macropores: larger than 50 nm.

MOFs are mostly considered as microporous materials, although mesoporous variants have also been reported in literature. [29] The discovery of various "cornerstone" materials over the past decades has greatly expanded the domain of porous materials. These materials include zeolites, zeotypes, pillared interlayered clays, carbon nanotubes, mesoporous silica and of course MOFs and covalent organic frameworks (COFs). [30] In today's world, their prevalence and significance are undeniable as a research material and in the future as an industrial interesting adsorbents or catalyst. [25, 31]

1.4 From reagent to framework, crystal engineering

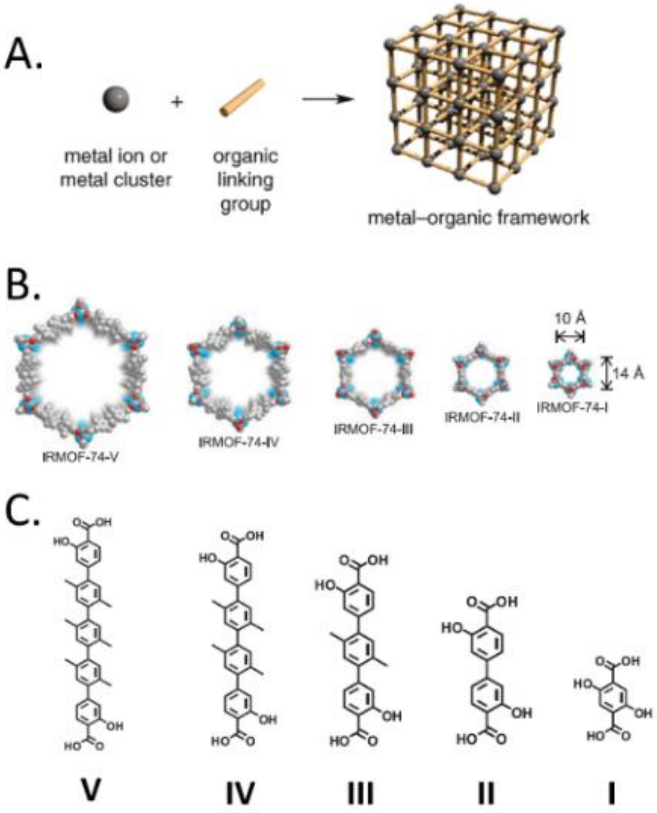

Figure 1.2 (A) Formation of a crystalline and porous MOFs from a combination of a metal ion or cluster and an organic linker. (B) Crystal structure of a IRMOF-74 series. (C) Chemical structures of organic units used in the synthesis of five isoreticular IRMOFs. (Reproduced from references [20, 32])

Networks or nets are not solely used by chemists in the field of material science, but are omnipresent in daily life: railways, electronic circuits, wireless local area, social networks and so on. Assembling the appropriate building blocks with the correct connectivity can design any type of coordination network, in particular a MOF. This methodology is known as reticular chemistry. [27] In essence, by linking inorganic metal nodes or secondary building units (SBUs), with organic building blocks, a 3D framework can be constructed, as shown in Figure 1.2 (A) The freedom to choose the initial building blocks gives the autonomy to tune the material for a desired application. [32] For a detailed explanation of the network topology, we refer the reader to two

interesting books. [25, 27]. By extending the linker, meanwhile maintaining the metal centre, isoreticular MOFs with increasing pore size are created. In Figure 1.2 (B) and (C) the example of IRMOF-74 (I to V) is presented. The expansion of a well-known MOF-74 (M_2(DOBDC), Table 1.1) with one phenylene ring, or with two(II), three(III), four (IV) and five (V) Figure 1.2 (C), gives structures with variable pore range. [20]

1.5 The family tree

Different topologies, metal ions and linkers give rise to own specific identities and consequently very characteristic physical and chemical properties for every framework. Thousands of well-defined structures, with a broad range of topologies, pore sizes and chemical functionalities, have fuelled the search for specific high-end applications. Out of this array of diverse compounds, some frameworks have been elaborately studied, generally because they have a track record in a particular desired application, due to certain specific characteristics, e.g., flexibility or due to their high chemical, thermal and mechanical stability. [5] A well-organized nomenclature for MOFs does not exist. Generally, a MOF is labelled in two parts, the first part is most often an acronym of the institute or group that first reported the compound. A couple of examples are MIL (Materials Institute Lavoisier), COMOC (Center for Ordered Materials, Organometallics and Catalysis) and DUT (Dresden University of Technology), HKUST (Hong Kong University of Science and Technology), UiO (Universitet i Oslo). The second part consist of a number, referring mostly to how many MOFs have previously been reported by that group, sometimes accompanied by the metal used.

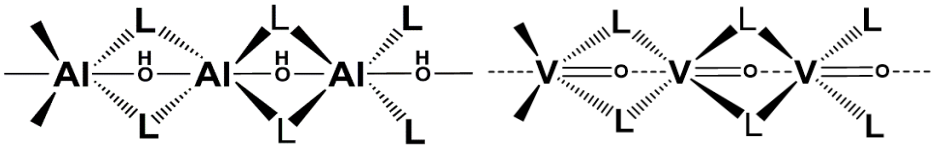

Figure 1.3 Schematic representation of the different bonds in (left) MIL-53(Al) and DUT-5(Al); (right) MIL-47(V) and COMOC-2(V). (Reproduced from ref [33])

Well-known and often used examples are MIL-47(V) [4] (V(O)BDC), MIL-53(M) [6] (M(OH)BDC, with M = Al, Cr, Ga, V, Fe, Sc), COMOC-2(V) [15] (V(O)BPDC) and DUT-5(Al) [14] (Al(OH)BPDC), see for an overview Table 1.1. The framework MIL-53(M) is constructed by trans chains of corner-sharing (*via* OH group) $M^{III}O_4(OH)_2$ octahedra (Figure 1.3, left) by BDC ligands represented by L in Figure 1.3. [34] The vanadium (V^{IV}) containing analogue of MIL-53(M) is the rigid structure MIL-47(V) made up of VO_6 octahedra (Figure 1.3, right). A second isotopologic "aluminium-vanadium" combination is COMOC-2(V) and DUT-5(Al). COMOC-2(V) (Figure 1.3, right) which is an

isoreticular variant of MIL-47(V). [4, 35] In contrary, DUT-5(Al) (Figure 1.3, left) is a rigid isoreticular variant of MIL-53(Al). [34]

The microporous tetravalent terephthalate MOFs MIL-47(V), UiO-66(Zr) [12] ($Zr_6O_4(OH)_4$), trivalent microporous MIL-53(Al), (Cr) and micro- and mesoporous MIL-101(Cr) [11] ($Cr_3(O)(OH)(BDC)_3$) are among the most important and most investigated MOFs in terms of thermal and chemical stability. [5, 36] For example, MIL-101(Cr) is highly stable for up to two months in both acidic (pH = 0) and basic (pH = 12) conditions, [36] whereas MIL-53(Al) is thermally stable up to temperatures of 773 K in air. [34]

MOF-177(Zn) [19] ($Zn_4O(BTB)_2$ combines an exceptionally high Langmuir surface area of 5250 $m^2\ g^{-1}$ or a S_{BET} (BET = Brunauer-Emmett-Teller) of 4500 $m^2\ g^{-1}$, and an extreme porosity represented by a low density (0.477 g cm^{-3}) with a high H_2 storage capacity at 70 bar and 77 K. [19, 37, 38]

MOF-74(Mg) [18] (Mg_2(DOBDC)) contains coordinated unsaturated metal sites, generated in the pores by solvent removal. These open metal sites show great affinity towards CO_2 molecules, increasing capture ability at low pressure. MOF-74(Mg) possesses one of the highest CO_2 uptakes among all MOFs at 1 bar and 298 K (up to 8 mmol g^{-1}). [3] Great interests in this research area has resulted in dedicated investigation, including modification of this framework.

Zeolite imidazole frameworks (ZIFs) are MOF structures maintaining a zeolite topology in which the tetrahedral atoms are transition metals, bridged by imidazolate (IM = $C_3N_2H_3^-$) units. [39] The crystals are formed by copolymerization of a metal and an imidazolate type linker. One chemically and thermally stable (up to 823 K) framework is ZIF-8(Zn) [17] ($Zn(mim)_2$, mim = 2-methylimidazolate).

HKUST-1(Cu) [16] ($Cu_3(BTC)_2$) also reported as CuBTC, shows upon hydration coordination of H_2O to the copper metal sites, creating intense deep blue crystals. Dehydration creates coordinative unsaturation of the Cu(II) sites which then become available for interaction with other probe molecules.

1.6 Synthesis of a MOF

A remarkably broad variety of methods is known for MOF synthesis. Different techniques can, starting from the same reaction mixture, lead to different structures. For every method, there is a variation in reaction time, particle size, morphology, yield as well as scale-up abilities. Figure 1.4 summarizes the different preparation methods of MOFs. In addition to room temperature (RT) crystallization such as solvent evaporation, layering solutions or slow diffusion, the general methods to create MOFs are: conventional electric (CE) heating (or briefly conventional synthesis), microwave (MW) heating, mechanochemistry (MC), electrochemistry (EC) and ultrasound (US). The next paragraphs will briefly discuss these methods. For further information regarding these synthesis procedures, we refer the reader to the topical review of Biswas *et al*. [23] After the synthesis, residual organic components are still left in the pores. To optimize the surface area, these leftovers are removed by a thermal, solvent, acidic or alkaline treatment. [40]

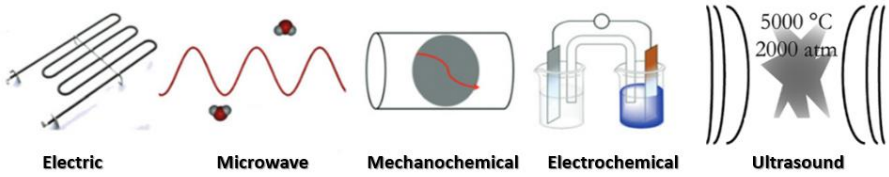

Figure 1.4 Overview of the different synthesis methods. (Reproduced from reference [23])

1.6.1 Conventional synthesis

Conventional synthesis covers all the reactions executed by conventional electric heating. One speaks of a solvothermal (SOL) and non-solvothermal procedure depending on the temperature range used. [23] The term solvo- or hydrothermal covers all heterogeneous reactions in the presence of (aqueous) solvents under high pressure and temperature ($T > T_b$ = boiling temperature) to dissolve and recrystallize the compounds that are rather insoluble under ordinary conditions. For this reason, special equipment such as stainless steel autoclaves equipped with Teflon liners are used. The term solvothermal is, however, also regularly used in MOF reports to describe synthesis conditions below T_b. [41] Due to the drastic changes of its solvothermal properties (e.g., dielectric, rheological, transport and chemical), high-temperature aqueous solutions

are involved in diverse technological processes. [42] Controlling the parameters of nucleation and crystal growth (i.e. time, temperature, pressure, concentration of the reagents) is an art in itself. However, they are a major importance to govern the resulting size, morphology and defect concentration of the MOF crystals. [43] For instance, extreme temperatures or prolonged reaction times can even lead to degradation of the MOF. [44]

1.6.2 Microwave synthesis

Diverse molecules have a dipole moment, water in particular, and rotate to align themselves with the alternating electrical field of the **microwaves**. The moving molecules collide, increasing the kinetic energy, generating heat. The energy is directly generated through the complete bulk of the material, which is a major difference compared to conventional conductional heating. In the latter, heat transfer starts from the external edges, shown in the heat profile in Figure 1.5. Microwaves are generated from a magnetron that is equipped with an oscillator that converts high voltage current into high frequency radiation. These microwaves transport energy from the magnetron to the sample chamber. Microwave heating is energy efficient, specific and almost instantaneous without temperature increase of the surrounding air or container. [43, 45] Characteristics of the microwave method are:

i) Microwave irradiation leads to "higher growth rate" of the MOF crystals, e.g., 3 h for MIL-47(V)/MIL-53(Al)/MIL-53(Cr) while the solvothermal method normally requires 96 h.

ii) Generally, it leads to "smaller crystals", due to faster nucleation.

iii) The surface area and gas adsorption capacity, e.g., for CO_2 are hardly affected when compared to the conventional approach.

iv) Variation in the composition of the reaction mixture (e.g., amount of solvent) can modify the size and quality of the crystals.

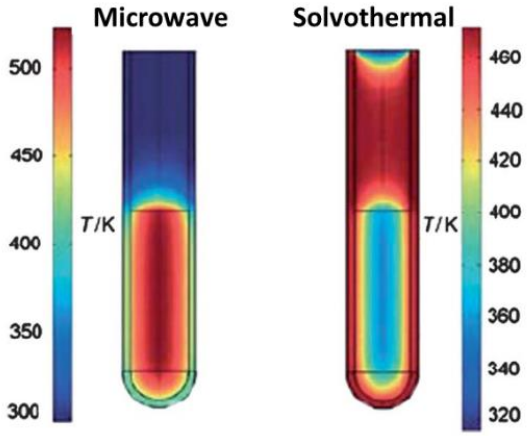

Figure 1.5 Temperature profile of microwave versus solvothermal. (Reproduced from [46])

1.6.3 Electro-, mechano- and sonochemical synthesis

The **electrochemical synthesis** of MOFs, mainly used for large-scale production, was developed by researchers of the chemical company BASF. [47, 48] The advantage of the electrochemical route is the possibility to run a continuous process instead of a batch setup. The metal ions are continuously introduced *via* an anionic dissolution that further contains dissolved carboxylates in a conduction salt. This reaction setup avoids safety issues due to high concentrations of anionic nitrate, perchlorate or chloride. [43, 48] BASF commercialized the following frameworks under the name Basolite®: Z1200: ZIF-8(Zn), A100: MIL-53(Al), C300: HKUST-1(Cu), and Z377: MOF-177(Zn).

Both physical and chemical reactions can be driven by a mechanical force. **Mechanochemistry** has a long history in synthetic chemistry in which the term is used for reactions caused by mechanical energy and was first reported for MOFs in 2006 [49]. In mechanochemical synthesis, intramolecular bonds are broken, continued by a chemical transformation. Mechanical energy is induced by (ball) milling or grinding of solid reagents. [43, 50]

Sonochemistry uses high-energy ultrasound to create acoustic cavitation in liquids. These sound waves have frequencies ranging from 20 kHz to 10 MHz, exceeding the upper limit of the human hearing range. This wavelength is significantly larger than the

molecular dimension, hereby there is no direct interaction between the ultrasound and molecule. Ultrasound interacts with liquids creating continuous cycles of rarefaction (low pressure) and compression (high pressure). In the rarefaction stage, the liquid pressure drops below the vapour pressure, creating cavities. Under the alternating pressure, these bubbles grow in volume through diffusion of solute vapour. The constant growth (up to a ring of 200 nm) is followed by a collapse, accompanied with rapid energy release with heating and cooling rates $>10^{10}$ K s^{-1}. In homogeneous liquids, chemical reactions can occur within, at the interface of the cavity or in the bulk media, where intense shear forces are observed. Ultrasound results in faster nucleation and growth rates in comparison with the MW method. [43]

1.7 Applications

Since the first MOF design over 20 years ago, the research field has stepwise explored different applications, discovering fields in which MOFs show an outstanding performance. The applications are numerous, going from water harvesters [51], eco-friendly adsorption chillers [52], over gas storage to medical applications, all merely a few out of many other applications. An overview is shown in Figure 1.6.

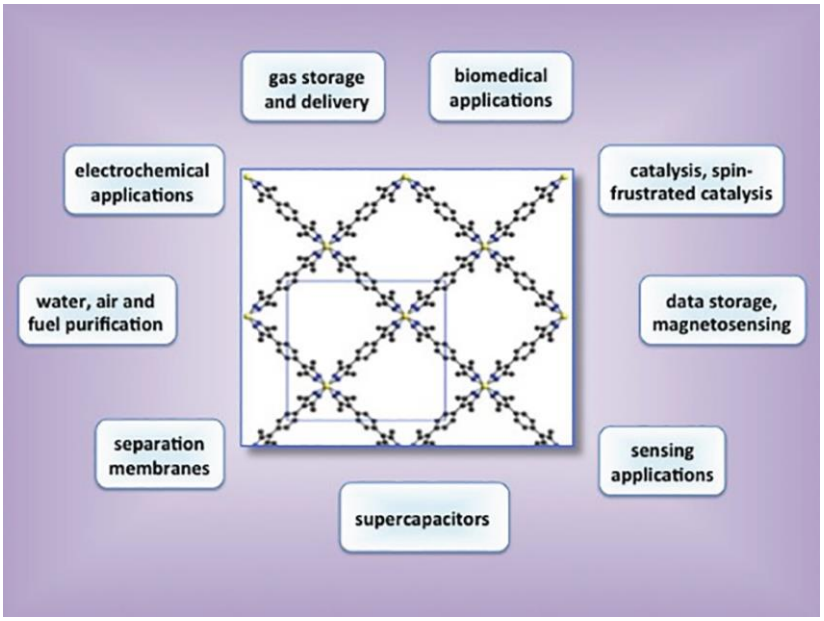

Figure 1.6 Applications of MOFs. (Reproduced from reference [53])

One particularly important field examines their use as a heterogeneous catalyst or catalytic support, essential to speed up chemical reactions. Besides the catalytic activity of the central metal nodes themselves, the MOF can furthermore be used as a host to encapsulate or anchor an active component on the pore walls. This method transforms a well-performing homogeneous catalyst into a greener heterogeneous version.

Two major applications are gas separation and adsorption for clean (mobile) energy storage. MOFs are particularly interesting because of their unique properties: high surface area, extreme tunability and diversity of the structure. The three most investigated gas molecules by academia and industry are hydrogen, methane and

carbon dioxide gas. In daily use on an industrial scale, it is not the storage capacity that matters but the performance of the adsorbent, defined by the working capacity as can be seen in Figure 1.7 for pressure (PSA) and temperature (TSA) swing adsorption-desorption. The idea behind these processes relies on the preferential adsorption of one gas component from a mixed feed stream at a certain operating pressure (P_{ads}) or temperature (T_{ads}). The adsorption is followed by desorption of the adsorbed components at reduced pressure (P_{des}) or increased temperature(T_{des}). The differential working capacity of the sorbent between P_{ads} and P_{des} or T_{ads} and T_{des} is called the working capacity expressed in mol/mol or mol/kg sorbent. [54]

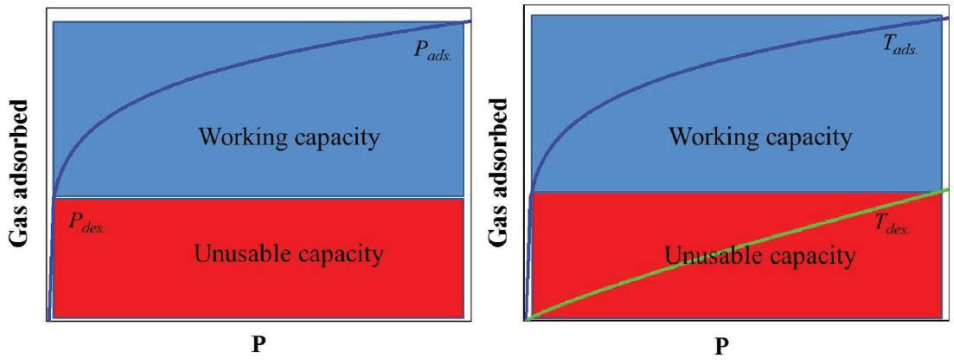

Figure 1.7 Working capacity in (left) pressure swing adsorption (PSA) and (right) temperature swing adsorption (TSA). (Reproduced from reference [3])

The final working capacity range depends on multiple factors of which the two most important are: use of the compressor (single/multi stage) to limit the pressure range and diffusion speed of the gas in/out the porous material. [3]

Hydrogen is definitely a very clean alternative for the fossil fuels used today, due to the high energy output with low environmental impact and water as only combustion exhaust product. The main problem arises when H_2 has to be produced, stored or transported because of its explosive and high diffusive nature risking H_2 embrittlement and in turn leading to cracks and leaks. [55] Storage at RT is energetically the most interesting. However, because researchers observed low reproducibility results for MOFs, the focus has shifted towards cryogenic storage. [56]

Table 1.2 Current benchmark MOFs for cryogenic (77 K) H_2 storage at high pressures. (Adapted from reference [57])

Material	Formula	S_{BET} area ($m^2\ g^{-1}$)	Capacity (wt%)	Pressure (bar)
MOF-210(Zn)	$(Zn_4O)_3(BTE)_4(BPDC)_3$	6240	15.0	80
DUT-32(Zn)	$(Zn_4O)_3(BTCTB)_4(BPDC)_3$	6411	14.2	80
NU-100(Cu)	$Cu_3(L^1)$	6143	14.1	70
MOF-200(Zn)	$Zn_4O(BBC)_2$	4530	14.0	80
NU-111(Cu)	$Cu_3(L^2)$	5000	11.9	110
MOF-205(Zn)	$(Zn_4O)_3(BTB)_4(NDC)_3$	4460	10.7	80
MOF-177(Zn)	$Zn_4O(BTB)_2$	4500	9.9	70
SNU-77H(Zn)	$Zn_4O(TCBPA)_2$	3670	9.9	90

H_3BTE, 4,4',4''-(benzene-1,3,5-triyl-tris(ethyne-2,1-diyl))tribenzoic acid; H_2BPDC, biphenyl-4,4'-dicarboxylic acid; H_3BTCTB, 4,4',4''-(benzene-1,3,5-triyltris(carbonylimino))tris-benzoic acid; H_6L^1, 5,5',5''- (((benzene-1,3,5-triyltris(ethyne-2,1-diyl))tris(benzene-4,1-diyl))tris(ethyne-2,1-diyl))triisophthalic acid; H_3BBC, 4,4',4''-(benzene-1,3,5-triyl-tris(benzene-4,1-diyl))tribenzoic acid; H_6L^2, 5,5',5''-(benzene-1,3,5-triyltris(buta-1,3-diyne-4,1-diyl))triisophthalic acid; H_3BTB, 4,4',4''-benzene-1,3,5-triyl-tribenzoic acid; H_2NDC, naphthalene-2,6-dicarboxylic acid; H_3TCBPA, tris(4'-carboxybiphenyl)amine; SNU, Seoul National University; DUT, Dresden University of Technology; NU, Northwestern University.

An overview of the current benchmark frameworks for H_2 adsorption in MOFs is given in Table 1.2. The track record at cryogenic conditions is set by MOF-210(Zn) with 15 wt% of H_2.

Nevertheless, the Fuel Cell Technologies Office (FCTO) of the U.S. Department of Energy (DOE) has set a target to develop an on-board automotive H_2 storage system that allows driving for more than 300 miles, divided-up into the DOE 2020 and DOE Ultimate System Target to pursuit, with a targeted working range from 253 K to 373 K. Using MOFs as gas storage systems poses both great challenges and opportunities for the creation or optimization of materials beyond their current gas storage and thermal stability level. [58] However the limited uptake due to the weak interaction of H_2 with the framework at RT, make MOFs rather incapable to store high quantities of H_2.

Out of the lower emission of greenhouse gases and other pollutants, natural gas that mainly contains **methane** presents itself as a reliable alternative for petroleum as transportation fuel. Its low price and enormous amounts of world reserves are the primary driving forces behind the increasing interest in CH_4. However, its low volumetric energy density compared to gasoline is problematic. Nevertheless, on mass

basis, its combustion heat even beats that of gasoline. In response to the economic competition concerning compressed natural gas (CNG) - which involves compression of natural gas to 200-300 bar at ambient temperature, and requires costly, multi-stage compressors at refilling stations - the Advanced Research Projects Agency-Energy (ARPA-E) [59] of the U.S. DOE has set the following target: one volume of adsorbent material should ideally deliver 263 volumes of CH_4 at standard temperature and pressure (STP) conditions. Translated to the working capacity with a 25% loss in capacity results in an absolute uptake of 350 $cm^3\ cm^{-3}$ as target. Adsorbents, in particular MOFs in an adsorbed natural gas (ANG) tank, offer the advantage of a low-cost single-stage compressor at a working pressure between 5 and 65 bar.

Table 1.3 Current benchmark MOFs for CH_4 adsorption at RT. (Adapted from reference [60])

Material	S_{BET}($m^2\ g^{-1}$)	Pore Volume ($cm^3\ g^{-1}$)	Absolute uptake[a]		Working capacity[b]	
			$g\ g^{-1}$	$cm^3\ cm^{-3}$	$g\ g^{-1}$	$cm^3\ cm^{-3}$
DOE target	-	-	0.5	350	-	263
MOF-74(Ni)	1350	0.51	0.148 (0.135)	251 (228)	0.077 (0.063)	129 (106)
MAF-38(Zn)	1850	0.81	0.247 (0.213)	263 (226)	0.176 (0.141)	187 (150)
HKUST-1(Cu)	2022	0.78	0.216 (0.184)	267 (227)	0.154 (0.122)	190 (150)
UTSA-76(Cu)	2820	1.09	0.263 (0.216)	257 (211)	0.201 (0.154)	197 (150)
Co(BPD)	2911	1.02	-	203 (161)	-	197 (155)[c]
Al-soc-MOF-1	5585	2.30	0.414 (0.259)	197 (123)	0.370 (0.218)	176 (104)
MOF-210(Zn)	6240	3.60	0.410 (0.238)	143 (83)	0.376 (0.204)	131 (71)

MAF = metal azolate framework; UTSA = University of Texas at San Antonio;
BPD = 1,4-benzenedipyrazolate; soc = square-octahedral hosting counter-ions
[a] At RT and 65 (35) bar.
[b] Defined as the difference in methane uptake between 65 (35) and 5 bar.
[c] Between 65 (35) and 5.8 bar.

Frameworks with coordinated unsaturated sites (e.g., HKUST-1(Cu), MOF-74(Ni)) [61] as shown in Table 1.3, are by far the most promising materials. Hydrophobic groups, large pores and low framework density are critical parameters for a maximum CH_4 adsorption capacity. Although considerable progress has been made, high throughput

screening of the materials raises severe doubts about the feasibility of the ARPA-E target. Calculations performed by the group of Simon *et al*. [62] indicated that none of the materials currently being investigated are able to reach these targets.

Fossil fuel combustion and industrial processes are the main sources of **carbon dioxide** emission. One of the most urgent climate issues of the current age is the anthropogenic greenhouse gas molecule CO_2, released in the atmosphere by burning fossil fuels, industrial processes and land use activities. About 76 % of all emitted greenhouse gases is CO_2, followed by CH_4, N_2O and F-gases as presented in Figure 1.8, (left) and published by the Intergovernmental Panel on Climate Change (IPCC). Estimated reserves of oil and gas cover approximately 300 Gton of carbon containing gases. Immediate release in the atmosphere would roughly double the present CO_2 concentration of 410 ppm, which has already increased with 30 to 40 % above the pre-industrial average and rose with 90 ppm from 1960 onwards (Figure 1.8, right) measured at Mauna Loa Observatory (Hawaii).

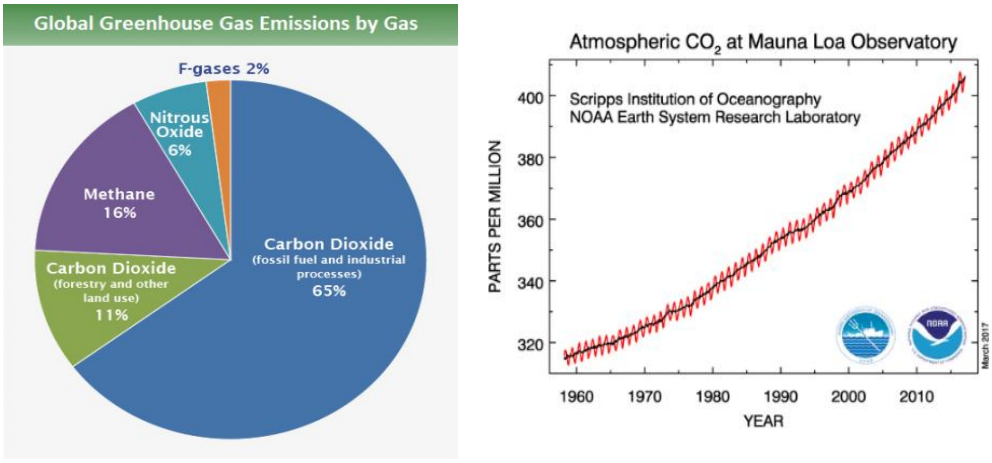

Figure 1.8 (left) Global greenhouse gas emission based on global emissions of 2010 by IPCC (2014). (Reproduced from reference [63]); (right) Trend in earth's atmospheric CO_2 concentration (March 1958-August 2017) by the National Oceanic and Atmospheric Administration (NOAA) Earth System Research Laboratory. (Reproduced from reference [64])

MOFs can be a vital component in several applications. They can act as a sorbent to sweeten a gas stream and filter out the air pollutants as well as, a storage medium or play a key role in reducing the rising concentration of CO_2 in the atmosphere. In contrast to CH_4 and H_2, no specific targets have yet been proposed for CO_2 applications. To improve the adsorption capacity of a MOF, the framework interaction with the CO_2, which is considered one of the most critical parameters, must be significantly enhanced. This can be achieved through multiple strategies: the use of CUS, metal doping of the structure, including amine groups and by control of the pore and window size of the structure. [3] These factors are important to maximize affinity towards the CO_2 molecule; in contrast, high surface area and pore volume are not mandatory for CO_2 capture at low pressure.

One MOF with great potential for use as a capture medium, is the open metal site MOF-74(Mg) [65] as shown in Table 1.4, where the benchmark MOFs for CO_2 adsorption are presented. More information about CO_2 sorption and interactions can be found in Chapter 2.

Table 1.4 Current benchmark MOFs for CO_2 adsorption. (Adapted from reference [3])

Material	S_{BET} ($m^2\ g^{-1}$)	$S_{langmuir}$ ($m^2\ g^{-1}$)	Pore volume ($cm^3\ g^{-1}$)	CO_2 adsorption capacity (mmol g^{-1})		Q_{st}^0 (kJ mol^{-1})
				1 bar	T	
MOF-74(Mg)	1495	1905	-	8.0	296 K	-47
MOF-74(Co)	1080	-	-	7.0	296 K	-37
MOF-74(Zn)	816	-	-	5.1	296 K	-
MOF-74(Ni)	1070	-	-	5.8	296 K	-41
HKUST-1(Cu)	-	1492	-	4.7	298 K	-
PCN-61(Cu)	3000	3500	1.36	2.8	298 K	-21
PCN-66(Cu)	4000	4600	1.63	1.8	298 K	-26.2
PCN-68(Cu)	5109	6033	2.13	1.4	298 K	-21.2
Cu_3(TDPAH)	2171	2540	0.91	5.2	298 K	-33.8
CPM-200-(Fe/Mg)	1459	2024	-	5.68	298 K	-

PCN = porous coordination network; CPM = crystalline porous material;
TDPAH = 2,5,8-tris(3,5-dicarboxylphenylamino)-*s*-heptazine

The aim of this work is not to create or optimize a sorbent for CO_2 adsorption, but rather to focus on thoroughly understanding the flexibility of MOFs. In this context, we particularly focus on bimetallic MOFs and how certain parameters influence this framework flexibility using CO_2 adsorption as characterization tool. [66]

With a sustainable evolution of our society as ultimate objective, researchers and engineers stimulated by governmental institutions have increasingly prioritized topics such as environmentally friendly and economically interesting storage, capture and separation of small gas molecules as CO_2, CH_4, H_2, etc. [67, 68] Capturing pollutants, starting from the point of emission and primarily executed *via* PSA, is key to a successful outcome. For the capture of CO_2, adsorbents such as zeolites are plausible candidates yet are difficult to regenerate without significant heating, entailing low productivity and high operation costs. With this in mind, tunable nanoporous materials as MOFs are promising alternative solids for these applications. [69]

1.8 Conclusion

The demand for "smart materials" specifically designed at molecular, micron or millimetre level is unquenchable. Owing to their hybrid structure, MOFs bridge the gap between pure organic and inorganic materials. With 12000 publications over a period of 20 years, MOFs have become a major research field in chemistry. Tremendous progress has been made, major hurdles such as poor hydrothermal stability of early MOFs have been overcome, with nowadays about 20000 known unique MOF structures.

These porous crystalline compounds can be created *via* multiple synthesis pathways: solvothermal routes where the heat is supplied either electrically (resistive heating), *via* microwaves or sonochemicallly (both heating of the solvent). A few of these solids have recently become commercially available under the name of Basolite® by BASF and also smaller companies are catching up.

Applications of MOFs can already be seen in a range of different research fields: catalysis, biomedical applications, purification, sensing and of course separation and storage. The large tunability of pore size and material properties lead to unprecedented properties and applications. These MOF materials could lead to a breakthrough in tackling the current issue of CO_2 pollution where they can act as adsorbents based on their ability to separate, capture and store CO_2. Targets are set, and researchers continuously aim to develop MOFs with the well-desired characteristics *via* the combination of computational and experimental design.

1.9 References

1. M.V. Gandhi and B. Thompson, *Smart materials and structures*, Chapman & Hall, 1992.
2. A. Tiwari and H. Kobayashi, *Responsive Materials and Methods: State-of-the-art Stimuli-responsive Materials and Their Applications*, John Wiley & Sons, 2013.
3. Y. Lin, C. Kong, Q. Zhang and L. Chen, *Advanced Energy Materials*, 2017, **7**, 1-29.
4. K. Barthelet, J. Marrot, D. Riou and G. Férey, *Angewandte Chemie*, 2002, **114**, 291-294.
5. A.J. Howarth, Y. Liu, P. Li, Z. Li, T.C. Wang, J.T. Hupp and O.K. Farha, *Nature Reviews Materials*, 2016, **1**, 1-16.
6. F. Millange, C. Serre and G. Ferey, *Chemical Communications*, 2002, **0**, 822-823.
7. M. Vougo-Zanda, J. Huang, E. Anokhina, X. Wang and A.J. Jacobson, *Inorganic Chemistry*, 2008, **47**, 11535-11542.
8. J.P.S. Mowat, S.R. Miller, A.M.Z. Slawin, V.R. Seymour, S.E. Ashbrook and P.A. Wright, *Microporous and Mesoporous Materials*, 2011, **142**, 322-333.
9. M. Anbia and S. Sheykhi, *Journal of Natural Gas Chemistry*, 2012, **21**, 680-684.
10. E.V. Anokhina, M. Vougo-Zanda, X. Wang and A.J. Jacobson, *Journal of the American Chemical Society*, 2005, **127**, 15000-15001.
11. G. Férey, C. Mellot-Draznieks, C. Serre, F. Millange, J. Dutour, S. Surblé and I. Margiolaki, *Science*, 2005, **309**, 2040-2042.
12. J.H. Cavka, S. Jakobsen, U. Olsbye, N. Guillou, C. Lamberti, S. Bordiga and K.P. Lillerud, *Journal of the American Chemical Society*, 2008, **130**, 13850-13851.
13. H. Li, M. Eddaoudi, M. O'Keeffe and O.M. Yaghi, *Nature*, 1999, **402**, 276-279.
14. I. Senkovska, F. Hoffmann, M. Fröba, J. Getzschmann, W. Böhlmann and S. Kaskel, *Microporous and Mesoporous Materials*, 2009, **122**, 93-98.
15. Y.-Y. Liu, S. Couck, M. Vandichel, M. Grzywa, K. Leus, S. Biswas, D. Volkmer, J. Gascon, F. Kapteijn, J.F.M. Denayer, M. Waroquier, V. Van Speybroeck and V.D.V. Pascal, *Inorganic Chemistry*, 2013, **52**, 113-120.
16. S.S.-Y. Chui, S.M.-F. Lo, J.P.H. Charmant, A.G. Orpen and I.D. Williams, *Science*, 1999, **283**, 1148-1150.
17. K.S. Park, Z. Ni, A.P. Côté, J.Y. Choi, R. Huang, F.J. Uribe-Romo, H.K. Chae, M. O'Keeffe and O.M. Yaghi, *Proceedings of the National Academy of Sciences*, 2006, **103**, 10186-10191.
18. N.L. Rosi, J. Kim, M. Eddaoudi, B. Chen, M. O'Keeffe and O.M. Yaghi, *Journal of the American Chemical Society*, 2005, **127**, 1504-1518.

19. H.K. Chae, D.Y. Siberio-Perez, J. Kim, Y. Go, M. Eddaoudi, A.J. Matzger, M. O'Keeffe and O.M. Yaghi, *Nature*, 2004, **427**, 523-527.
20. H. Deng, S. Grunder, K.E. Cordova, C. Valente, H. Furukawa, M. Hmadeh, F. Gándara, A.C. Whalley, Z. Liu, S. Asahina, H. Kazumori, M. O'Keeffe, O. Terasaki, J.F. Stoddart and O.M. Yaghi, *Science*, 2012, **336**, 1018-1023.
21. Y.J. Sun and H.C. Zhou, *Science and Technology of Advanced Materials*, 2015, **16**, 1-11.
22. H. Furukawa, K.E. Cordova, M. O'Keeffe and O.M. Yaghi, *Science*, 2013, **341**, 1-12.
23. N. Stock and S. Biswas, *Chemical Reviews*, 2012, **112**, 933-969.
24. S. Kitagawa, *Chemical Society Reviews*, 2014, **43**, 5415-5418.
25. L.R. MacGillivray, *Metal-organic frameworks: design and application*, John Wiley & Sons, 2010.
26. D. Farrusseng, *Metal-organic frameworks: applications from catalysis to gas storage*, John Wiley & Sons, 2011.
27. S. Kaskel, *The chemistry of metal-organic frameworks: synthesis, characterization, and applications*, John Wiley & Sons, 2016.
28. O.K. Farha, I. Eryazici, N.C. Jeong, B.G. Hauser, C.E. Wilmer, A.A. Sarjeant, R.Q. Snurr, S.T. Nguyen, A.Ö. Yazaydın and J.T. Hupp, *Journal of the American Chemical Society*, 2012, **134**, 15016-15021.
29. W. Xuan, C. Zhu, Y. Liu and Y. Cui, *Chemical Society Reviews*, 2012, **41**, 1677-1695.
30. C.S. Diercks and O.M. Yaghi, *Science*, 2017, **355**, 1-8.
31. J. Rouquerol, D. Avnir, C. Fairbridge, D. Everett, J. Haynes, N. Pernicone, J. Ramsay, K. Sing and K. Unger, *Pure and Applied Chemistry*, 1994, **66**, 1739-1758.
32. K. Sumida and J. Arnold, *Journal of Chemical Education*, 2011, **88**, 92-94.
33. M.G. Goesten, TU Delft, PhD thesis, 2015.
34. T. Loiseau, C. Serre, C. Huguenard, G. Fink, F. Taulelle, M. Henry, T. Bataille and G. Férey, *Chemistry-A European Journal*, 2004, **10**, 1373-1382.
35. P. Van Der Voort, K. Leus, Y.-Y. Liu, M. Vandichel, V. Van Speybroeck, M. Waroquier and S. Biswas, *New Journal of Chemistry*, 2014, **38**, 1853-1867.
36. K. Leus, T. Bogaerts, J. De Decker, H. Depauw, K. Hendrickx, H. Vrielinck, V. Van Speybroeck and P. Van Der Voort, *Microporous and Mesoporous Materials*, 2016, **226**, 110-116.
37. Y. Li and R.T. Yang, *Langmuir*, 2007, **23**, 12937-12944.
38. A.G. Wong-Foy, A.J. Matzger and O.M. Yaghi, *Journal of the American Chemical Society*, 2006, **128**, 3494-3495.
39. A. Phan, C.J. Doonan, F.J. Uribe-Romo, C.B. Knobler, M. O'Keeffe and O.M. Yaghi, *Accounts of Chemical Research*, 2010, **43**, 58-67.

40. S. Maurer, H. Mattenheimer and U. Müller, *Process for the recovery of components forming a metal-organic framework material*, 2015, **WO/2015/040593**.
41. S. Natarajan, S. Manual, P. Mahata, V.K. Rao, P. Ramaswamy, A. Banerjee, A.K. Paul and K.V. Ramya, *Journal of Chemical Sciences*, 2006, **118**, 525-536.
42. C. Gerardin, M. In, L. Allouche, M. Haouas and F. Taulelle, *Chemistry of Materials*, 1999, **11**, 1285-1292.
43. M.P. Attfield and P. Cubillas, *Dalton Transactions*, 2012, **41**, 3869-3878.
44. F. Millange, R. El Osta, M.E. Medina and R.I. Walton, *CrystEngComm*, 2011, **13**, 103-108.
45. J. Klinowski, F.A. Almeida Paz, P. Silva and J. Rocha, *Dalton Transactions*, 2011, **40**, 321-330.
46. R. Luque, J.A. Menendez, A. Arenillas and J. Cot, *Energy & Environmental Science*, 2012, **5**, 5481-5488.
47. U. Mueller, H. Puetter, M. Hesse, M. Schubert, H. Wessel, J. Huff and M. Guzmann, *Method for electrochemical production of a crystalline porous metal organic skeleton material*, 2005, **WO/2005/049892**.
48. A.U. Czaja, N. Trukhan and U. Muller, *Chemical Society Reviews*, 2009, **38**, 1284-1293.
49. A. Pichon, A. Lazuen-Garay and S.L. James, *CrystEngComm*, 2006, **8**, 211-214.
50. J.F. Fernández-Bertran, *Pure and applied chemistry*, 1999, **71**, 581-586.
51. R. Service, *This new solar-powered device can pull water straight from the desert air*, Science, 2017, https://sciencemag.org/news/2017/04/new-solar-powered-device-can-pull-water-straight-desert-air
52. M. Jacoby, *New Sorbents For Greener Cooling*, 2014, https://yaghi.berkeley.edu/research-news/14-mofcooling.pdf
53. C. Pettinari, F. Marchetti, N. Mosca, G. Tosi and A. Drozdov, *Polymer International*, 2017, **66**, 731-744.
54. S.A. Rackley, *Carbon capture and storage*, Butterworth-Heinemann, 2017.
55. J. Schmidt, R. Meade and L. Raymond, *Plating and surface finishing*, 2000, **87**, 53-55.
56. S.R. Caskey and A.J. Matzger, *Mater. Matters*, 2009, **4.4**, 1-8.
57. A. Schoedel, Z. Ji and O.M. Yaghi, 2016, **1**, 1-15.
58. FCTO, *Hydrogen storage*, 2017, https://energy.gov/eere/fuelcells/materials-based-hydrogen-storage
59. DOE, *ARPA-E*, 2017, https://arpa-e.energy.gov/sites/default/files/documents/files/MOVE_ProgramOverview.pdf

60. B. Li, H.-M. Wen, W. Zhou, Jeff Q. Xu and B. Chen, *Chem*, 2016, **1**, 557-580.
61. Y. Peng, V. Krungleviciute, I. Eryazici, J.T. Hupp, O.K. Farha and T. Yildirim, *Journal of the American Chemical Society*, 2013, **135**, 11887-11894.
62. C.M. Simon, J. Kim, D.A. Gomez-Gualdron, J.S. Camp, Y.G. Chung, R.L. Martin, R. Mercado, M.W. Deem, D. Gunter, M. Haranczyk, D.S. Sholl, R.Q. Snurr and B. Smit, *Energy & Environmental Science*, 2015, **8**, 1190-1199.
63. O. Edenhofer, R. Pichs-Madruga, Y. Sokona and J.C. Minx, 2014.
64. P. Tans and R. Keeling, *Trends in atmospheric carbon dioxide*, 2014, https://esrl.noaa.gov/gmd/ccgg/trends/
65. D. Britt, H. Furukawa, B. Wang, T.G. Glover and O.M. Yaghi, *Proceedings of the National Academy of Sciences*, 2009, **106**, 20637-20640.
66. J. Yu, L.-H. Xie, J.-R. Li, Y. Ma, J.M. Seminario and P.B. Balbuena, *Chemical Reviews*, 2017, **117**, 9674-9754.
67. B. Metz, O. Davidson, H. De Coninck, M. Loos and L. Meyer, IPCC special report on carbon dioxide capture and storage, Intergovernmental Panel on Climate Change, Geneva (Switzerland). Working Group III.
68. C. Redondo-Gil, L. Esquibel, A. Alonso Sanchez and P. Zapico. *European strategic energy technology plan*, in *International Conference on Renewable Energy and Power Quality (ICREPQ'09), Valencia, Spain, April*. 2009.
69. S. Bourrelly, P.L. Llewellyn, C. Serre, F. Millange, T. Loiseau and G. Férey, *Journal of the American Chemical Society*, 2005, **127**, 13519-13521.

2 *Dynamic materials in the MOF family*

The second chapter of this dissertation introduces the fundamentals of adsorption and describes the flexibility of MOFs. The physisorption of gases in porous materials is a very strong tool for material characterization and is moreover one of their major applications. Therefore, it is of great importance to understand the parameters that influence the adsorption properties. MOFs can respond to different physical and chemical triggers, acting as smart materials. Among these fascinating properties is the so-called breathing phenomenon. Phase transitions are triggered by guest adsorption/desorption, thermal and mechanical stimuli. Breathing implies that different states are possible, these states are elaborately explained. The MIL-53(Cr) framework is used in this chapter to explain the fundamentals of flexibility. In the last section of this chapter, the reader is introduced to the different types of triggers in relation to varying degrees of freedom for flexibility.

2.1 Introduction to adsorption

Adsorption is defined as the adhesion of layers of atoms or molecules (as gases, liquids or solutes) to a surface. [1] Gas adsorption is an essential tool for the characterization of the structure of porous solids and fine powders. The general recommendation for physisorption of gases is standardized by IUPAC in 1985 in the manual "*Reporting Physisorption Data for Gas/Solid systems*", which was recently updated in 2015. [2] Over the latest 30 years, different porous materials (e.g., mesoporous molecular sieves, carbon nanotubes, periodic mesoporous organosilicas, MOFs and materials with hierarchical pore structures) have been constructed with uniform and tailor-made pores. The isotherm is generally characteristic for the pore structure, making adsorption a very interesting analytical tool to investigate them. The material adsorbing gas is called the adsorbent while the gas/liquid is labelled adsorbate.

Sorption can visually be presented *via* adsorption and desorption isotherms. The sorption isotherm represents at a constant temperature over a range of relative pressure, the quantity of adsorbate on the surface of adsorbent at equilibrium. Prior to

the adsorption, the adsorbent is outgassed to make sure that all physisorbed species are removed from the adsorbent as well as to make sure irreversible change of the solid's surface is avoided. Exposure of the structure to a high vacuum, usually at elevated temperature, achieves this.

A molecule or atom will adsorb when the total interaction energy (∅) is equal to the work (W) needed to bring a gas molecule to the adsorbed state Here is the chemical potential μ and N represents the adsorbing molecules. [3]:

$$\emptyset = W = \int \mu \, dN \tag{2.1}$$

For a reservoir at a fixed pressure P, temperature T and μ:

$$dU = Tds - PdV + \mu \, dN \tag{2.2}$$

Applying the fundamental relation of thermodynamics ($G = U - TS + PV$):

$$dG = -SdT + VdP + \mu \, dN \tag{2.3}$$

At a fixed temperature and pressure this equation becomes:

$$dG = \mu \, dN \tag{2.4}$$

Implemting this in formula 2.1:

$$W = \int \mu \, dN = \Delta G = \mu \Delta N \tag{2.5}$$

Considering an ideal gas, with $\mu_0 =$ chemical potential at P_0 and T:

$$\mu = \mu_0 + RT \ln\left(\frac{P}{P_0}\right) \tag{2.6}$$

If at P_0, $\mu_0 = 0$:

$$\mu = RT \ln\left(\frac{P_0}{P}\right) = \Delta G = W = \emptyset \tag{2.7}$$

In here, ΔG is the Gibbs free energy change, P the equilibrium pressure at which the adsorption takes place, P_0 the saturated vapour pressure and R is the ideal gas constant. The molecules in the gasphase can condense, layering on the sorbent's surface and are in the pores of the MOF mainly present as a liquid.

There are two types reversible condensation of layers of adsorption: physical and chemical adsorption. The general features of physisorption and chemisorption are compared in Table 2.1. The former deals with intermolecular forces (Van der Waals Forces) whereas the latter results from chemical bond formation, a much stronger interaction. [4, 5]

Table 2.1 Comparison between physisorption and chemisorption. (Reproduced from reference [6])

Physisorption	Chemisorption
Low heat of adsorption (less than 2 or 3 times latent heat of evaporation)	High heat of adsorption (more than 2 or 3 times latent heat of evaporation)
Monolayer and multilayer	Monolayer only
No dissociation of adsorbed species. Only significantly happens at relative low temperatures.	May involve dissociation. It is possible over a wide range of temperature.
Rapid, non-activated and reversible. No chemical bonding thus no electron tranfer, although polarization or sorbate might occur.	Activated, possibly slow and irreversible. Involves bonding so electron transfer happens between sorbate and sorbent.

Most of the adsorption processes, in particular those involving MOFs, are based on physisorption. Numerous different adsorbents are known, in fact, particularly four types of artificial sorbents are currently dominating the commercial market of adsorption: activated carbon (86,7 %), zeolites (8,7 %), silica gel (2,3 %) and activated alumina (2,3 %) with a total annual market value of 1.15 billion dollar. [3]

2.1.1 Forces and energy of adsorption

The total potential between adsorbent and adsorbate molecules is the sum of the total adsorbate-adsorbent and adsorbate-adsorbate interaction potentials:

$$\emptyset_{total} = \emptyset_{adsorbate-adsorbent} + \emptyset_{adsorbate-adsorbate} \quad (2.8)$$

From here on, the adsorbate-adsorbent interaction, which is the primary effect, will be referred to as Ø. Three main contributions to Ø are reported: dispersion, electrostatic and chemical bonding. The forces engaged in physisorption contain both Van der Waals forces: dispersion = $\emptyset_D$ and repulsion = $\emptyset_R$ and electrostatic interactions: $\emptyset_{ind}$ = induction energy (interaction between an induced dipole and electrical field), $\emptyset_{F\mu}$ = interaction between electric field (F) and a permanent dipole (μ) and $\emptyset_{FQ}$ = interaction between the field gradient (∇F) and the quadrupole moment (Q). [7] For physisorption, the adsorbate potential is described as follows [3]:

$$\emptyset = \emptyset_D + \emptyset_R + \emptyset_{ind} + \emptyset_{F\mu} + \emptyset_{\nabla FQ} \quad (2.9)$$

The resulting electrostatic forces are most noticeable in the presence of adsorbents such as MOFs with an electrostatic field caused by either (metal) ions in the structure or hydrogen bridges.

2.1.2 Heat of adsorption

The equation below proves that isosteric heat of adsorption (ΔH = J/mol) is equal at ambient temperature and low coverage to the adsorbate-adsorbent interaction potential (Ø):

$$\Delta H = \emptyset - RT + F(T) \tag{2.10}$$

Here, F(T) stands for the vibrational and translational energies of the adsorbate molecule, R is the ideal gasconstant and T is the temperature. Physisorption is an exothermic process implying that all sorbents possess negative enthalpy (ΔH < 0), primarily ranging between -10 and -100 kJ mol^{-1}. Three terms refer to the heat of adsorption:

1. **Isothermal integral heat of adsorption** is the total amount of heat released when the adsorbate is loaded from zero to a final value at isothermal conditions.

2. **Differential heat of adsorption** $\Delta\overline{H}_l$ is defined as the change in integral heat of adsorption with a change of adsorbate loading and obtained *via* the next equation:

$$\Delta\overline{H}_l = \overline{H}_l - \widetilde{H}_g \tag{2.11}$$

where $\widetilde{H}_g$ and $\overline{H}_l$ represent partial molar enthalpy and molar enthalpy of gaseous adsorbate, respectively. The differential heat of adsorption is determined by temperature, pressure and adsorbate coverage between two points on the isotherm.

3. **Isosteric heat of adsorption** on an adsorbent by an adsorbate derives from adsorption isosteres, lines of constant adsorbate loading, and it is obtained *via* the Clausius-Clapeyron equation from the slopes of adsorption isosteres, drawn on the plot of the lnP vs. 1/T.

$$\frac{d\ lnP}{d(\frac{1}{T})} = -\frac{\overline{\Delta H}_l}{R} = \frac{q_{iso}}{R} \tag{2.12}$$

The isosteric heat of adsorption is directly related to the differential heat of adsorption:

$$q_{iso} = -\Delta\bar{H}_l \tag{2.13}$$

Using the isosteric heat of adsorption, it is possible to calculate the integral heat of adsorption. In the typical profile for non-flexible MOFs at adsorbate loadings, the isosteric heat of adsorption progressively drops with increased loading. The energetically most favourable places are filled up first, leaving some adsorption sites to interact stronger with adsorbate molecules than others.

2.1.3 Adsorption measuring techniques

Two types of sorption techniques volumetric and gravimetric are discussed in this dissertation. A comprehensible introduction to the working principles of these instruments is given underneath.

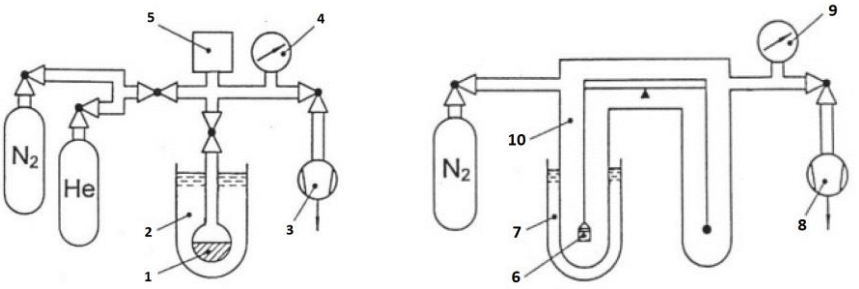

Figure 2.1 (left) Volumetric apparatus; 1 - sample cell, 2 - Dewar vessel, 3 - vacuum aggregate, 4 - manometer, 5 -calibrated volume; (right) Gravimetric apparatus; 6 - sample cell, 7 - Dewar vessel, 8 - vacuum aggregate, 9 - manometer, 10 - balance. [8]

A **volumetric** sorption measuring apparatus (Figure 2.1, left) consist of a sample cell that can be filled with degassed adsorbent (1). The dead volume of the empty cell is calibrated in advance by using He. To measure a N_2 adsorption isotherm, the sample cell is cooled down in a Dewar vessel (2) filled with liquid N_2 and certain quantities of N_2 are loaded stepwise. A calibrated volume (5) is filled with N_2 at a well know temperature and pressure. The connection valve between the calibrated volume and sample cell allows deviation of the gas between the two cells. The equilibrium is reached when constant gas pressure in the sample cell is attained. The gas volume consumed by the adsorption can be calculated.

In **gravimetric** sorption measuring apparatus (Figure 2.1, right) the sample cell (6) is mounted to a balance (10). The sample cell containing the adsorbent is cool down in a Dewar vessel (7). The change in weight of the sample cell at equilibrium is determined at a certain pressure and constant temperature. This method allows direct measurement of the change in mass which is not the case for the volumetric method.

2.2 The breathing behaviour

Since the discovery of MOFs in the late 1990 until today, multiple advances have been made in the field of flexible and functional MOFs. The structural flexibility combines crystalline order of the network with cooperative structural transformation. Although we know the general parameters responsible for this effect and the overall idea behind flexibility, we are not able to completely understand this phenomenon and in order to design new flexible materials. At this moment, the latter is still unrealizable, mainly because different material properties play an essential role in this flexibility such as the size of the crystals, the organic linker and the metal ion. This appears to be similar to reticular design which seems hampered by the unpredictability of coordination chemistry.

An overview of possible flexible modes for MOFs is given in Figure 2.2. Four different types of flexibility can be distinguished: breathing (A), swelling (B), linker rotation (C) and subnetwork displacement (D). The most intriguing flexibility mode is "breathing", referred to as the process of moving air in and out of the lungs to facilitate gas exchange. Around 20000 coordination network structures are classified as "MOFs", yet only about a 100 compounds show substantial breathing or stimuli responsive behaviour. [9]

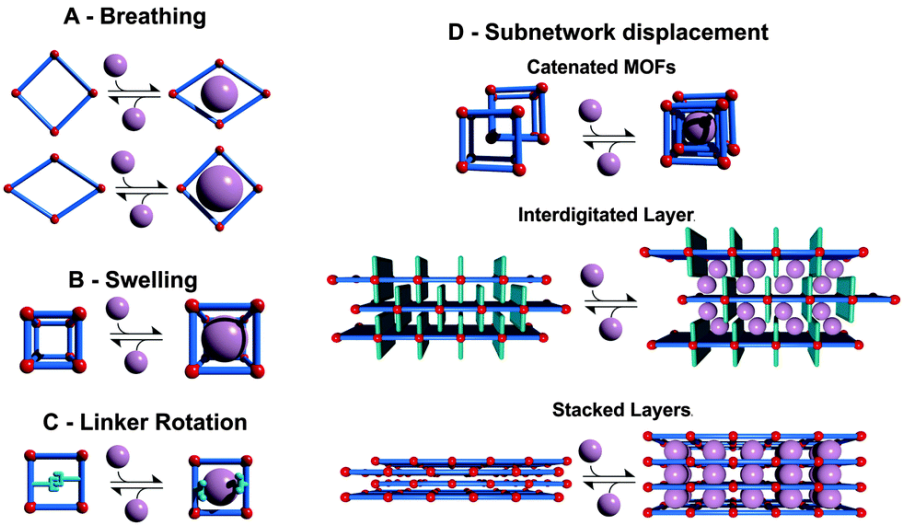

Figure 2.2 Classification of the different flexible modes of MOFs. Class I with volume changes (ΔV≠0; A, B and D) while for the other class II the volume does not change (ΔV=0; C and D). (Reproduced from reference [9])

Breathing is a collaborative effect between the inorganic metal node and the organic moiety, characterized by a change in unit cell volume. Knowledge about this effect is based on experimental results complemented with calculated data. [9] What triggers the effect is diverse (temperature, guest-induced, mechanical pressure) yet both the effect and structural displacement highly depend on it. Although no comprehensive theory is established based on existing experimental results, G. Férey and C. Serre formulated 4 empirical rules that all need to be fulfilled for the structure to possibly breathe [10]:

1. The only secondary building unit (SBU) that allow breathing are those which possess a mirror plane with the carboxylates in symmetrical position towards it;
2. The ratio C/M (C: number of carboxylates surrounding the SBU, M number of metallic atoms within the SBU) must be $\geqslant 2$ to have a flexible structure;
3. Breathing can solely occur with ditopic carboxylates, between two SUBs, the kneecaps provided by the O···O axes ought to be parallel for a possible rotation;
4. The existence of odd cycles in the structure are unfavoured for the dynamic effects of the structure.

A checklist with the empirical rules for the MOFs represented Table 1.1 Chapter 1 is given in Table 2.2.

Table 2.2 Checklist of the empirical rules for different MOF structures

MOF	1.	2.	3.	4.
MIL-47(V)	✓	✓	✓	✓
MIL-53(M)	✓	✓	✓	✓
MIL-101(Cr)	✓	✓	✓	✘
UIO-66(Zr)	✓	✓	✓	✘
MOF-5(Zr)	✘	✓	✓	✓
COMOC-2(V)	✓	✓	✓	✓
DUT-5(Al)	✓	✓	✓	✓
UiO-67(Zr)	✓	✓	✓	✘
HKUST-1(Cu)	✓	✓	✘	✓
ZIF-8(Zn)	✘	✓	✘	✓
MOF-74(M)	✓	✓	✓	✘
MOF-177(Zn)	✘	✓	✘	✘

2.3 Explanation of the characteristic states

The microporous MOFs examined in the experimental part of this manuscript , Chapter 4 and 5 are MIL-53(M) (M = Al, Cr, Ga, V, Fe, Sc), MIL-47(V), DUT-5(Al), COMOC-2(V). A brief introduction to these materials can be found in Chapter 1. The frameworks appear prior to previous treatments in a well-defined state. After the synthesis they are generally in an as-synthesized state labeled **as**, containing organic unreacted leftovers that block the pores. The following discussion focusses on MIL-53(M) and excludes compounds MIL-53(In) [11] and MIL-53(Cu) [12] because for the first no activated state is present and for the second no adsorption measurements have been carried out. The **as** framework is activated by a solvent extraction [13, 14] or calcination [15, 16], creating empty voids, which makes the frameworks surface area completely available. Subsequently after activation, they have change state, this state depends on the type of performed manipulation. These general states are summarized for each framework in Table 2.3. We can distinguish: large pore (**lp**), narrow pore (**np**), intermediate pore (**int**), very narrow pore (**vnp**) and closed pore (**cp**).

Because framework history (contact with solvent/gases) can play an essential role in the adsorption, additional labelling is used in this work. Such labelling is not common in literature, it corresponds to the prehistory or current state of the framework. Direct examples are the dehydrated narrow pore (**np-d**), hydrated narrow pore (**np-h**) and CO_2 exposed dehydrated (**np-d-CO_2**), hydrated (**np-h-CO_2**) narrow pore state and large pore (**lp-CO_2**).

For MIL-53(M), MIL-47(V), COMOC-2(V) and DUT-5(Al) different breathing triggers – guests, temperature and mechanical pressure – have been identified and elaborately described in literature of which a summary is presented in Table 2.4. Breathing is the only flexible mode for these set of frameworks. Besides these four examples, other well-known relevant flexible structures are: MIL-118(Al) [17], MIL-88(M (A, B, C, D)) (with M = Fe, Cr, A = fumaric acid, B = BDC, C = naftaleen-2,6-dicarboxylate (NDC) or D = BPDC) [18, 19], DUT-8(Ni) [20] and different paddle-wheel [21] based MOFs. For more information about breathing, we refer the reader to different topical reviews. [9, 22, 23]

Table 2.3 Representation of the possible states for the structures MIL-53(M), MIL-47(V), COMOC-2(V) and DUT-5(Al).

State		MIL-53(M)						MIL-47(V)	COMOC-2(V)	DUT-5 (Al)
		M=Al	M=Cr	M=Ga	M=V	M=Fe	M=Sc			
large pore (lp)	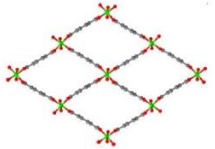	✓	✓	✓	✓	✘	✘	✓	✓	✓
narrow pore (np)	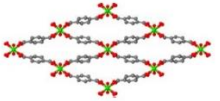	✓	✓	✓	✓	✘	✘	✘	✓	✘
intermediate pore (int)	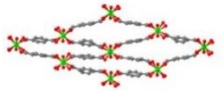	✘	✘	✘	✓	✓	✓	✘	✘	✘
very narrow pore (vnp)	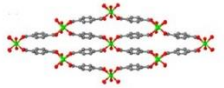	✘	✘	✘	✓	✓	✓	✘	✘	✘
closed pore (cp)	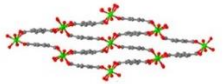	✘	✘	✘	✘	✓	✓	✘	✘	✘

Table 2.4 Non-exhaustive literature overview: triggers that stimulate breathing of MIL-53(M) and MIL-47(V): grey (flexible) and white (unknown or no flexibility observed).

	CO_2	CH_4	Alkanes	Xylene	Xenon	Water	Temp.	Pres.
MIL-53(Al)	[24]	[25]	[26]	[27]	[28]	[16]	[29]	[30]
MIL-53(Cr)	[24, 31, 32]	[33]	[26, 33]			[15]	[15, 34]	[35, 36]
MIL-53(Ga)						[17, 37]	[17, 38]	
MIL-53(V)*	[39]					[39]	[39]	
MIL-53(Fe)	[32, 40]	[33]	[33]			[41]	[41]	
MIL-53(Sc)	[42, 43]							
MIL-47(V)	[24]	[44]	[45]					[35]
COMOC-2(V)	[46, 47]	[46, 47]	[47]				[48]	
DUT-5(Al)	[49]	[49]						

*In literature one speaks about MIL-47(V^{III}) to avoid confusion for the reader, we will always label MIL-47(V^{III}) as MIL-53(V) as this seems for us a more straightforward labeling, work by Leclerc *et al*. [39]

The transition from one state to another results in a great volume change of the unit cell, shown in Figure 2.3 for the MIL-53(M) series. Over the years, it is this series in particular that has served as the primary example of reversible flexibility. It is however, worth noting that a ca. 50% cell volume variation is in fact not considered extreme, MIL-88(Cr) [18] for example exhibits a reversible cell volume change of more than 300 %, corresponding to atomic movements of around 10 Å without any decrease in the material's crystallinity.

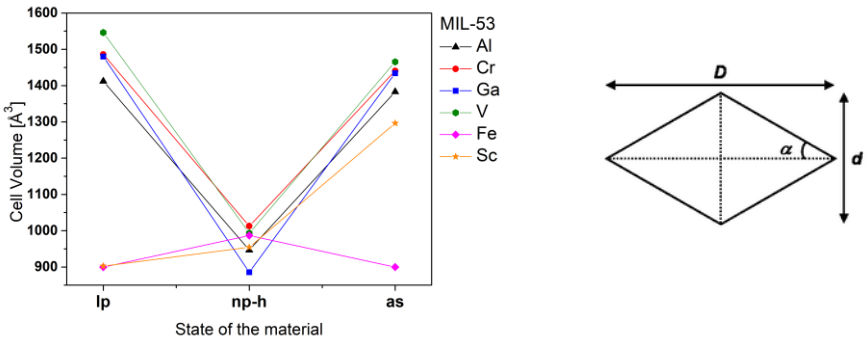

Figure 2.3 (left) Depiction of the cell volume evolution in different forms of MIL-53(M). (right) Lozenge section of a MOF crystal.

The cell volume is calculated by determine the angle α, the short d and D the long diagonal of the lozenge section (Figure 2.3, right). The volume of Al and Cr based MOFs e.g., after hydration approximates 1000 $Å^3$. During dehydration, a sudden drastic increase occurs, up to ca. 1500 $Å^3$ while maintaining their topology. In contrast, in iron based structures, this occurs in a two-step process with a decrease of the anhydrous cell volume to 900 $Å^3$. [50]

The most striking difference between the MIL-53(M) series and MIL-47(V) is the metal's oxidation number. In fact, the **as** structures exhibit M^{III} metal ions. After activation the oxidation state of the metal in the MIL-53(M) series is +III, whereas that of V in MIL-47(V) is +IV. Such remarkable difference in oxidation state, influences the physical properties of these materials significantly. MIL-53(M) is considered a flexible structure, while MIL-47(V) is reported to be a rigid framework. Leclerc *et al.* [39] described an alternative activation method, under high vacuum for MIL-47(V), that results in an activated framework with V^{III} ion centres. Unlike V^{IV} containing MOFs, V^{III} containing materials have a flexible structure with μ_2-OH groups as preferential adsorption sites. In this work to avoid confusion we will use MIL-53(V) in-stead of MIL-47(V^{III}) as is used by Leclerc *et al.*

COMOC-2(V) [46] and DUT-5(Al) [49] are two BPDC frameworks, synthesized in DMF resulting in tetra- and trivalent microporous materials. A remarkable feature of the COMOC-2(V) structure is its flexibility when exposed to certain gases (CO_2, C_2H_4 and other hydrocarbons), whereas DUT-5(Al) is a completely rigid structure.

2.4 Explanation of the breathing phenomenon explained by one typical example MIL-53(Cr)

For the adsorption of N_2 at cryogenic circumstances these materials, e.g., MIL-53(M), MIL-47(V), COMOC-2(V) and DUT-5(Al), follow a typical Type I isotherm with a characteristic Langmuir surface area. [15, 16, 51, 52] More information about the classes of isotherms (I-VI) can be found in the IUPAC protocols. [6, 53]. A Type I isotherm is defined as a reversible isotherm that is observed when the adsorbate is adsorbed on a microporous solid, where the size of the adsorbed gases is smaller than the pore diameter.

However, literature reports certain anomalies for dehydrated MIL-53(Fe) and MIL-53(Sc): they display no uptake of N_2 neither show microporosity. This is attributed to the presence of a **cp** form in these two MIL-53(M) frameworks. [43, 54] In contrast, the N_2 adsorption isotherm of COMOC-2(V) is a two-step adsorption, typically with pore opening around 0.5-0.6 p/p_0. During our experimental work, we observed that the flexibility of COMOC-2(V) is not omnipresent in every sample but it is a rather that it is a batch dependent phenomenon.

However, with gases other than N_2, e.g., CO_2, Xenon, CH_4 or other alkanes, and within a certain pressure and temperature range, two-step adsorption occurs as is elaborately discussed in the next paragraphs. This two-step Figure 2.4, (top) adsorption is a result of the structural flexibility of the material. A flexible MOF is a bi- or multistable crystalline material, with a long range structural order that is able to transform between states. By means of characterization techniques revealing the lattice parameters, e.g., X-ray powder diffraction (XRPD), this behaviour can be studied.

Here, we will briefly explain the basic idea of flexibility, *via* a coupled gas adsorption and XRPD study for MIL-53(Cr). Gas adsorption was found to be the first physical stimulus to trigger breathing transitions, well before temperature and mechanical pressure were identified to induce this **lp** -> **np** -> **lp** transition

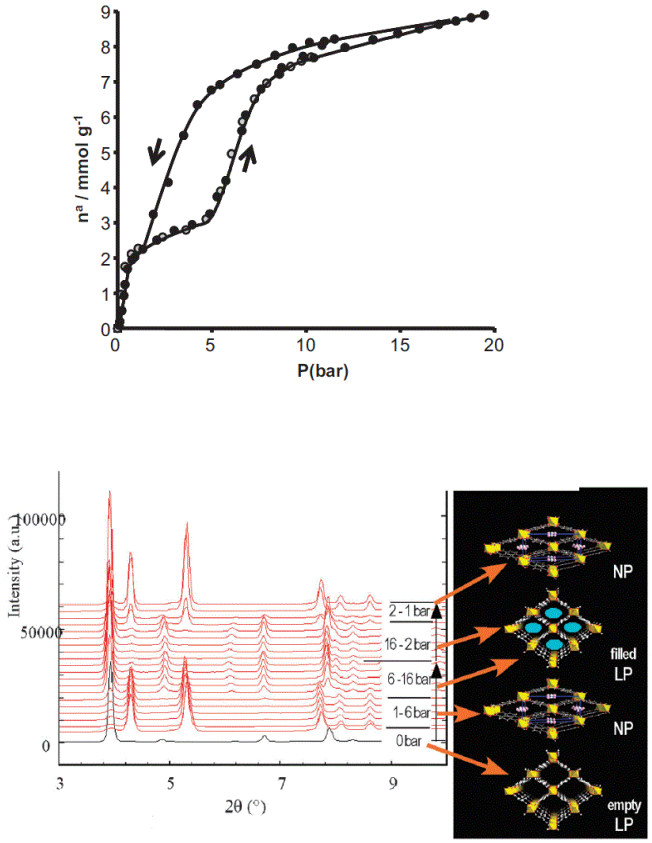

Figure 2.4 (top) CO_2 adsorption and desorption isotherms of MIL-53(Cr) at 304 K (Reproduced from reference [13]); (bottom) structural transformations upon CO_2 adsorption followed by *in situ* XRPD at 293 K of MIL-53(Cr) with large pore (lp) and narrow pore (np-d-CO_2) transition. (Reproduced from reference) [55]

Both the adsorption and desorption isotherm and the evolution in X-ray diffraction patterns are presented in Figure 2.4, (bottom). Prior to the analysis the sample as presented in Figure 2.4, (top) is degassed at elevated temperature, and in the open **lp** state with empty pores. When the framework is exposed to CO_2, the structure shrinks to a **np-d-CO_2** state due to the CO_2-OH interactions, clearly visible in the isotherm around 0.3 bar. This framework persists in this state till the end of the adsorption plateau and corresponds with the insertion of about 2 molecules CO_2 per unit cell. It is worth mentioning that *via* calculated data, at least one molecule per unit cell is necessary to contract the complete framework. [13] Increasing pressure above 6 bar evokes a structural transition from **np-d-CO_2** back to **lp-CO_2** with a characteristic inflection point. At the final pressure of 20 bar, the total amount of CO_2 has increased

up to 10 molecules per unit cell. When decreasing the pressure this **lp-CO_2** form is persistent and stable up to 2 bar, followed by a retransformation to the **np-d-CO_2.** This effect is completely reversible, although it is important to mention that after this cycle, the final state will be **np-d-CO_2** and not the empty **lp** state. The XRPD data revealed that in a narrow range, the two states co-exist as the **np-d-CO_2** and **lp-CO_2** phases are observed simultaneously. [55]

Framework changes [56] or electrostatic interactions [57] between adsorbate molecules influence the presence and/or position of the inflection point in the adsorption isotherm Figure 2.4 (top). The delayed desorption depends on the retransformation of the crystalline structure and is not related with capillary condensation as it is in mesoporous materials.

The main difference to other frameworks described in this work is: they have different states or the states behave different e.g., MIL-53(Fe), has **int**, **vnp** and **cp** states, whereas COMOC-2(V) never exhibits one crystalline phase after degassing but shows a mixture of co-existing **lp** and **np** phases. These differences lead to a slightly altered adsorption behaviour.

2.5 Degrees of freedom for flexibility

The next paragraphs, first introduce the different degrees of freedom, presented in Figure 2.5, that allow flexibility in the structure to appear.

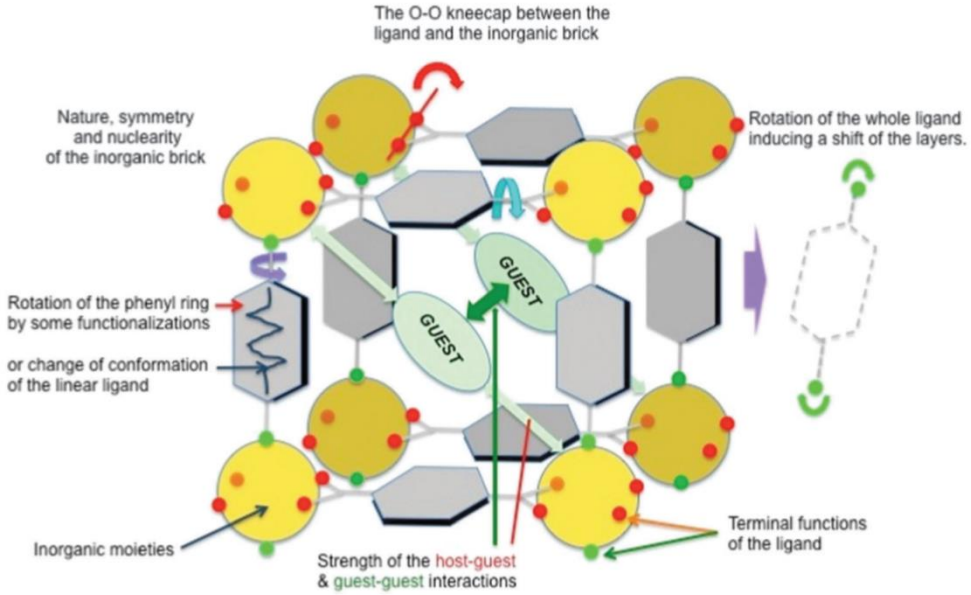

Figure 2.5 Various degrees of freedom in an open structure allowing flexibility. (Reproduced from reference [50])

These degrees of freedom allowing flexibility are of both organic and inorganic nature, where guest molecules can furthermore play a decisive role. We will discuss the degrees of freedom and their influence on the flexibility according to the following interactions which are the topics of the next sections [50]:

- Host-guest and guest-guest interactions;
- Host-host interactions;
- Influence of the ligand functionalisation.

The main focus will be on the first, host-guest interactions.

2.5.1 Host-guest interactions

The next sections describe the influence of multiple guests (moisture, solvent, gas, …) on the lattice of MIL-53(M), MIL-47(V), COMOC-2(V) and DUT-5(Al). These guest interactions show each a different influence on the flexibility of the framework, related to the incorporated metal node. We have tried to present a clear overview of every trigger that stands in correlation with this central metal ion. The next section introduces the reader to different types of adsorbate as well as the adsorbent's behaviour corresponding to the host-guest interactions.

Various polar [13, 25, 46] and apolar [25, 27, 33, 47, 58, 59] guest molecules have been reported to induce structural flexibility in the MIL-53(M) series as well as in COMOC-2(V). Concretely, they result in either a decrease or increase of the pore volume. A select number of reviews appeared in literature to discuss the breathing behaviour of MOFs. [9, 23] Researchers are trying to reveal the rationales behind this remarkable behaviour from a thermodynamic viewpoint. Furthermore, they endeavour to unveil strategies to "tailor" the gas sorption capacity of MOFs.

2.5.1.1 Flexibility induced in MIL-53 (M) by a change in temperature or moisture concentration

Temperature breathing and moisture breathing are often related. Water molecules can hydrate the framework, resulting in a contracted structure (**cp**, **np-h**, **int**). Temperature increase will remove the included water resulting in a change in state. Moreover, it can also transfer energy causing a transition in state e.g., **np-d** to **lp**. With this idea in mind, in this section, we have decided to group these two triggers as one topic. Breathing is a general term to describe the flexibility. Nevertheless, one may notice that the phase transition diagrams are specific for each MOF structure. Moreover, for compounds within series e.g., MIL-53(M), the diagrams differ from one metal to another.

Table 2.5 Overview of the space group, lattice parameters and volume of MIL-53(M) organized *via* the different states. (Adapted from reference [42])

Compound	Space group	*a* / *Å*	*b*/ *Å*	*c*/ *Å*	α / °	β / °	γ / °	Volume ($Å^3$)	Ref.
MIL-53(Cr)-as	Pnma	17.340	6.822	12.178	90.000	90.000	90.000	1440.6	[15]
MIL-53(Cr)-np-h	C 2/c	19.685	7.849	6.782	90.000	104.900	90.000	1012.6	[15]
MIL-53(Cr)-lp	Imma	6.812	16.733	13.038	90.000	90.000	90.000	1486.1	[15]
MIL-53(Al)-as	Pnma	17.129	6.628	12.182	90.000	90.000	90.000	1383.1	[16]
MIL-53(Al)-np-h	Cc	19.513	7.612	6.576	90.000	104.240	90.000	946.8	[16]
MIL-53(Al)-np-d	C 2/c	20.756	7.055	6.609	90.000	113.580	90.000	886.9	[29]
MIL-53(Al)-lp	Imma	6.609	16.675	12.813	90.000	90.000	90.000	1412.1	[16]
MIL-53(Ga)-as	Pnma	17.525	6.722	11.893	90.000	90.000	90.000	1401.0	[60]
MIL-53(Ga)-np-h	P 2_1/c	19.710	15.160	6.680	90.000	103.790	90.000	1938.8	[17]
MIL-53(Ga)-np-d	C 2/c	19.830	6.860	6.710	90.000	103.880	90.000	886.3	[17]
MIL-53(Ga)-lp	Imma	6.720	16.680	13.210	90.000	90.000	90.000	1479.7	[17]
MIL-53(Fe)-np-h	P 2_1/c	19.320	15.036	6.835	90.000	96.305	90.000	1973.6	[41]
MIL-53(Fe)-int	P -1	6.887	10.558	13.466	109.856	88.058	103.967	892.4	[41]
MIL-53(Fe)-vnp	C 2/c	21.269	6.759	6.884	90.000	114.625	90.000	899.6	[41]
MIL-53(Sc)-DMF	P n a 2_1	19.344	9.180	7.301	90.000	90.000	90.000	1296.5	[42]
MIL-53(Sc)-H_2O	P -1	7.267	13.452	20.677	71.570	84.212	87.729	1908.77	[42]
MIL-53(Sc)-cp	P -1	20.300	7.440	11.35	90.000	104.960	90.000	1680.75	[61]
MIL-53(Sc)-vnp	C 2/c	21.505	6.630	7.274	90.00	113.543	90.000	950.83	[61]
MIL-53(In)-as	P 2_1/c	18.228	11.970	34.062	90.000	122.360	90.000	6278.00	[11]
MIL-53(V)-as	Pnma	17.519	6.875	12.168	90.0000	90.000	90.000	1465.5	[52]
MIL-53(V)-np-h	C 2/c	19.808	7.593	6.816	90.000	104.290	90.000	993.5	[39]
MIL-53(V)-int	P-1	6.900	10.700	13.700	111.000	89.000	104.000	914.0	[39]
MIL-53(V)-vnp	C 2/c	21.200	6.900	6.800	90.000	115.000	90.000	908.0	[39]
MIL-53(V)-lp	Pmcn/ Imcm	16.515	13.647	6.860	90.000	90.000	90.000	1546.1	[39]

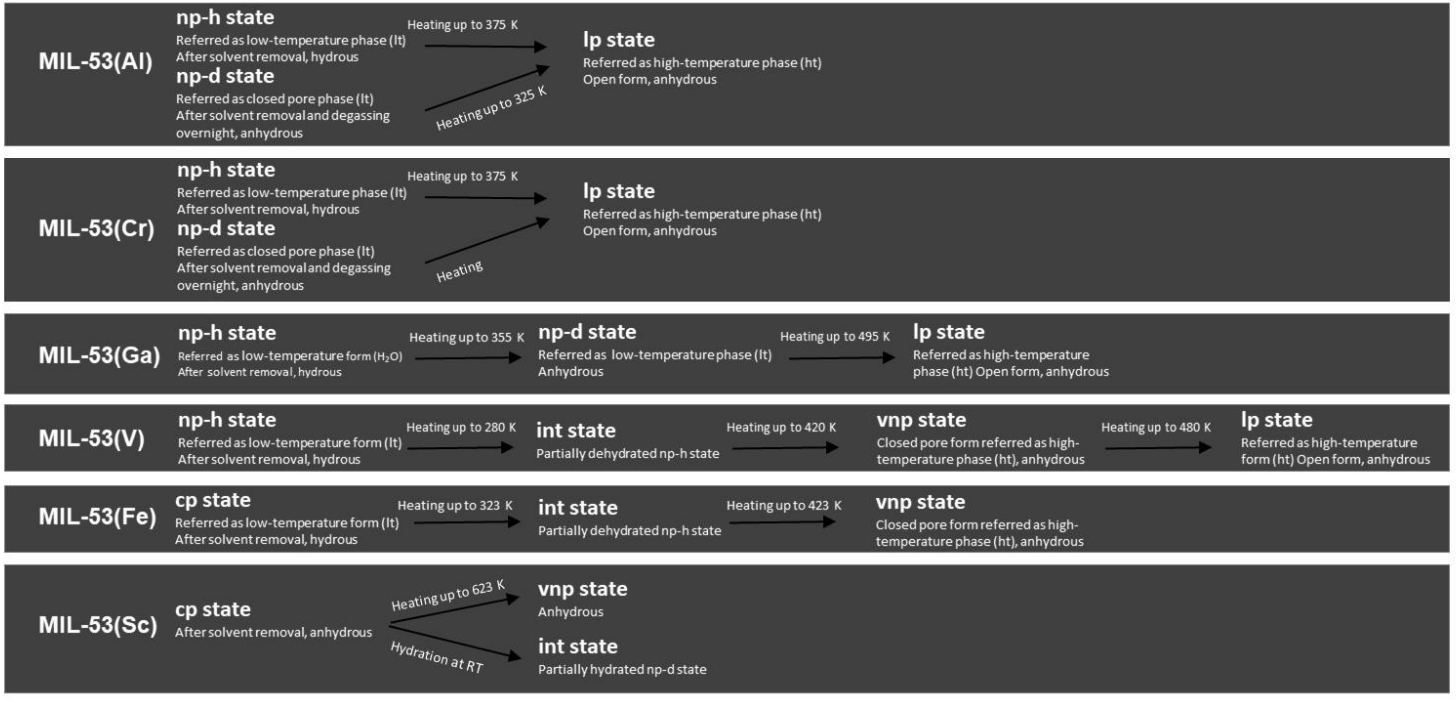

Figure 2.6 Overview of the various de(hydrated) np, lp, int, cp and vnp states for MIL-53(Al) [16, 29, 62], MIL-53(Cr) [15, 63], MIL-53(Ga) [17, 38, 60], MIL-53(V) [39, 52], MIL-53(Fe) [41, 64] and MIL-53(Sc) [42, 43, 61] lattices. (Reproduced from our own work [62])

In Figure 2.7 the breathing effect is presented over a large temperature range for the different metal nodes, arranged with increasing effective radius for M^{III} (Al , 0.535 Å; Cr, 0.615 Å; Ga, 0.620 Å; V, 0.640 Å; Fe, 0.645 Å; Sc, 0.745 Å) of the metal in a high spin state (for iron), all in oxidation state +III and octahedral coordination. The smaller the atomic radius the faster the framework exhibits a large pore state. From vanadium onwards (0.640 Å) two new states, **vnp** and **int** are identified. Moreover, Fe and Sc exhibit the largest radius and have even a completely **cp**. However, also other factors are influencing the flexibility, it is also suggested that the electronic structure of the cation can be important. In the latter case, magnetic dipolar interactions could provoke strengthening interactions between the chains and the cation. Even though hydrogen bonds in the hydrated forms play an important role for the contraction of the framework, they cannot alone explain the breathing phenomenon. The metal ion seems to play a predominant role. [17]

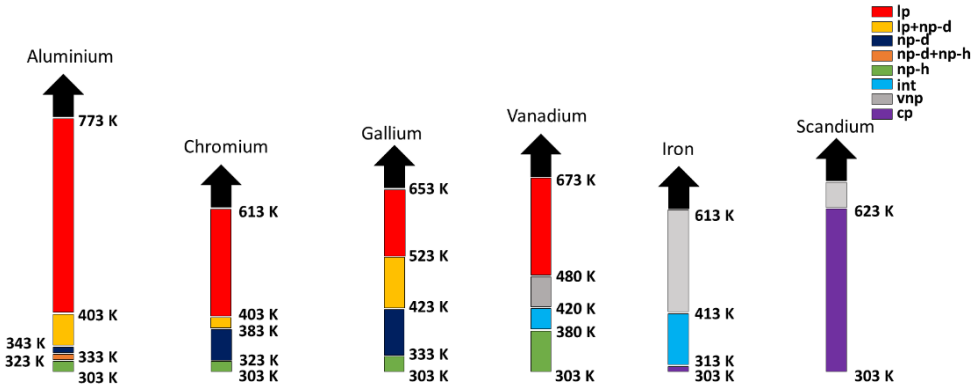

Figure 2.7 Evolution of the states in the different MOFs, MIL-53(M = Al, Cr, Ga, V, Fe, Sc) as a function of temperature (vertical) and as a function of increasing effective radius of the metal (horizontally, from left smallest to right biggest). All structures are initially in the hydrated (H_2O) narrow pore state, except scandium which is in the dehydrated form. (Adapted from reference [17] and own work [34, 62])

Temperature breathing in MIL-53(Al), MIL-53(Cr) or MIL-53(Ga) is most often defined in literature as a reversible process between two states: an orthorhombic **lp** sometimes referred to as high temperature (**ht**), and a monoclinic **np-h** also referred to as low temperature (**lt**) state. The change from one state to another is reversible and exhibits a significant hysteresis in the sorption isotherm. [29] An overview of the evolution between states: **cp**, **lp**, **np-h** and **-d**, **int** and **vnp** due to increasing temperature is

presented in Figure 2.7. Whereas in Figure 2.6, the possible phase transitions of MIL-53(M) are given in a complete overview diagram, additionally the lattice parameters are presented in Table 2.5. In literature one will frequently find the notation **np** for narrow pore state without the **–h** or **–d** suffix. However, both **np-h** and **np-d** have different lattice parameters as observed in our work through XRPD analysis for the compounds MIL-53(Al) and MIL-53(Cr). Although the Al, Cr and Ga structures can occur in one of these three states (**np-h**, **np-d**, **lp**), the transition from one state to another takes place in a different temperature interval. This indicates the thermal energy is related to the metal node, which on its turn influences the framework characteristics. [17] A transition from hydrated to dehydrated is possible by temperature, but also by exposure to a high vacuum or reducing the humidity. For more information, we refer to the article of Nevjestić *et al.* [62] for MIL-53(Al) and to Chapter 5 for MIL-53(Cr).

The work of Leclerc *et al*. [39] revealed that vacuum activation of MIL-47(V)-**as** results in the MIL-47(V^{III}) structure. This structure exhibits a significantly different flexibility from MIL-47(V^{IV}). After activation under ambient conditions and due to the humidity of the air, MIL-47(V^{III}) adopts the **np-h** state. Upon heating, the structure behaves similarly to MIL-53(Fe). Consequently the **np-h** state structurally transforms, closing the pores of the framework to an **int** state. Further temperature increase results in the transformation to a **vnp** state and in a final phase transition, the structure reopens entirely to a **lp** state. This behaviour is unique when compared to the previously mentioned MIL-53(M) structures.

On the other hand, variants MIL-53(Fe) and MIL-53(Sc) show an even greater structural diversity. MIL-53(Fe) for example, is under ambient conditions and after activation in a **cp** form (sometimes denoted as MIL-53(Fe)**lt**). MIL-53(Fe) does not open upon dehydration but rather closes to an **int** state. Further temperature increase induces in a final stage, a slightly reopened structure, the **vnp** state (sometimes denoted as MIL-53(Fe)**ht**). In comparison, starting from a hydrated closed pore form at RT, MIL-53(Sc) transforms at elevated temperature to a structure with a similar state as observed for MIL-53(Fe), the **vnp** state. [43]

2.5.1.2 Flexibility induced by a temperature change for the frameworks COMOC-2(V) and DUT-5(Al)

Only temperature influence is discussed in this section since water has no influence on the state of these compounds. The general composition of these structures are given in Chapter 1. For COMOC-2(V) the flexibility is characterized by a **lp** and **np** form, co-existing at RT and at 233 K. This is plotted in Figure 2.8. Theoretical calculations suggest that the **lp** state of COMOC-2(V) is favoured when temperature rises [46, 48].

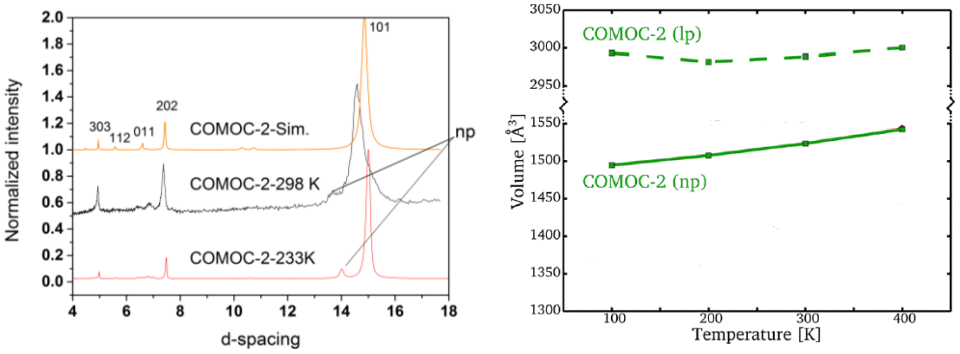

Figure 2.8 (left) Comparison of collected XRPD patterns collected during this dissertation of COMOC-2-Sim. (orange), COMOC-2(V)-298 K (black) and COMOC-2(V)-233 K (red); (right) Influence of temperature on the pore volume. (Reproduced from reference [48])

However, there is no direct indication in our own experimental results that the **lp** is favoured. Since the ratio **np/lp** in both experimental diffractograms are rather identical, we do not observe any preference for **lp** neither **np** in the temperature range from 200 - 300 K. In Figure 2.8, (left) which represents personally collected data, a smaller shift to a higher d-value with lower temperature of the **lp** (101), (202) and (303) intensities is observed. In the temperature range of 200 - 400 K, calculations by Wieme *et al*. predict a positive linear expansion (PLE) of the unit cell for both the **lp** and **np** phase of COMOC-2(V) as is shown in Figure 2.8, (right).

2.5.1.3 Flexibility induced by a solvent

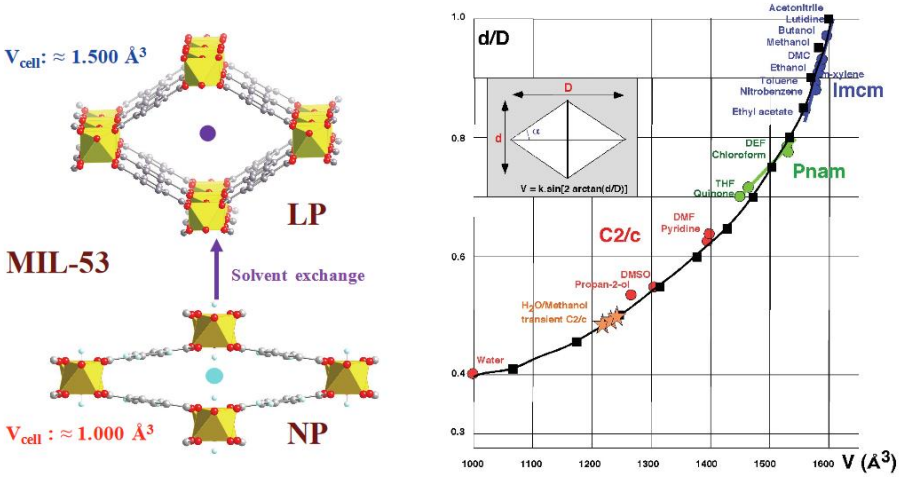

Figure 2.9 (left) The effect of an exchange of solvents on the swelling of the MIL-53(Fe) topology; (right) the evolution of the d/D ratio vs. cell volume for some solvent trapped in the pores. The black line corresponds the theoretical evolution of d/D with the volume of the cell. The change of the space groups is also mentioned. (Reproduced from reference [50])

Solvents influence the state of the framework, correlated with a change in the lattice parameters as well as with the total pore volume. Figure 2.9 describes the volume change of MIL-53(Fe)-H_2O which is ca. 1000 Å^3, according to the different solvents used. When put in a solvent, the exchange between water and the new guest was total and immediate. The experimental results lay between 1000 - 1500 Å^3 and have a d/D value between 0.4 - 1.0. Moreover, the different cell volumes fit with the theoretical curve and the d/D = f(V_{cell}). The length of the first diagonal, with d an indicator for the extent of swelling, is directly related to the relative interaction strength between guest-guest (I_{G-G}) and host-guest (I_{H-G}).

The interactions are strong if $I_{G-G} \sim I_{H-G}$, represented by the first part of the right graph in Figure 2.9, resulting in a shrinkage of the pores. If $I_{G-G} > I_{H-G}$, a strong backbone is preserved but weak host-guest interactions lead to an opening of the pores corresponding to the middle part of the right graph in Figure 2.9. Finally, when $I_{G-G} >>> I_{H-G}$, this effect leads to a disappearance of the ordered guests in the pores and the cell volume maximizes (ca. 1500 Å^3).

Surprisingly, it was reported that very limited contact of renewed solvent immediately induces a change of the cell volume. This is caused by destruction of the initial interactions, with no intermediate displacements of the Bragg peaks. This phenomenon is called 'the forceps effect'. Depending on their nature, solvents can induce different changes of the framework structure, influencing the d and D parameter without influencing the OH-M-OH connection.

2.5.1.4 Flexibility induced by CO_2 and CH_4

CO_2 and CH_4 act as a remarkably different trigger for the flexibility in MIL-53(M). This difference can be explained by a closer look to the adsorbate – adsorbent interaction Ø. CO_2 has no dipole moment but it does have a high quadrupole moment (-1.4 x 10^{-35} C.m^2). Hence, the $\emptyset_{F\mu}$ contribution is zero, while the field gradient interaction $\emptyset_{\nabla FQ}$ is non-zero. The total heat of adsorption for CO_2 will be: $\emptyset = \emptyset_D + \emptyset_R + \emptyset_{ind} + \emptyset_{\nabla FQ}$. CH_4 has no dipole nor quadrupole moment. However methane does have van der Waals interactions that will contribute to the total interaction. The total heat of adsorption for CH_4 will be: $\emptyset = \emptyset_D + \emptyset_R + \emptyset_{ind}$. In contrast to CH_4, CO_2 has a significant quadrupole which is responsible for the largest contribution to the adsorbate-adsorbent interactions (molecular orientation, hydrogen bonding). Besides dehydrating the structure, the CO_2 molecule was reported to be one of the first gas molecules capable of inducing transition in the MIL-53(M) series. [24]

The change of the MOF structure occurs within a certain pressure and temperature range. As a general example plotted in Figure 2.10, (top), CO_2 triggers the breathing in MIL-53(Al) demarcated by pressure and temperature. The reversible transition of MIL-53(Al) between the **np-CO_2** and **lp-CO_2** takes place within a relatively broad temperature (200 K - 343 K) and pressure (0 - 5 bar) range. [25] Generally, one starts with the **lp** form to analyse sorption behaviour on a pre-activated sample between 150 K - 500 K. Upon CO_2 contact, MIL-53(Al) immediately contracts evolving from the orthorombic **lp** to the monoclinic **np-CO_2** state. This is analogue to the ealier explained example MIL-53(Cr) in Chapter 1. [24] During this first step, strong donor-acceptor interactions between μ_2-OH groups and the CO_2 molecules take place at RT. This in

contrast with exposure of the framework to CH_4, at this temperature the compound stays in the **lp** form. [13, 65-67]

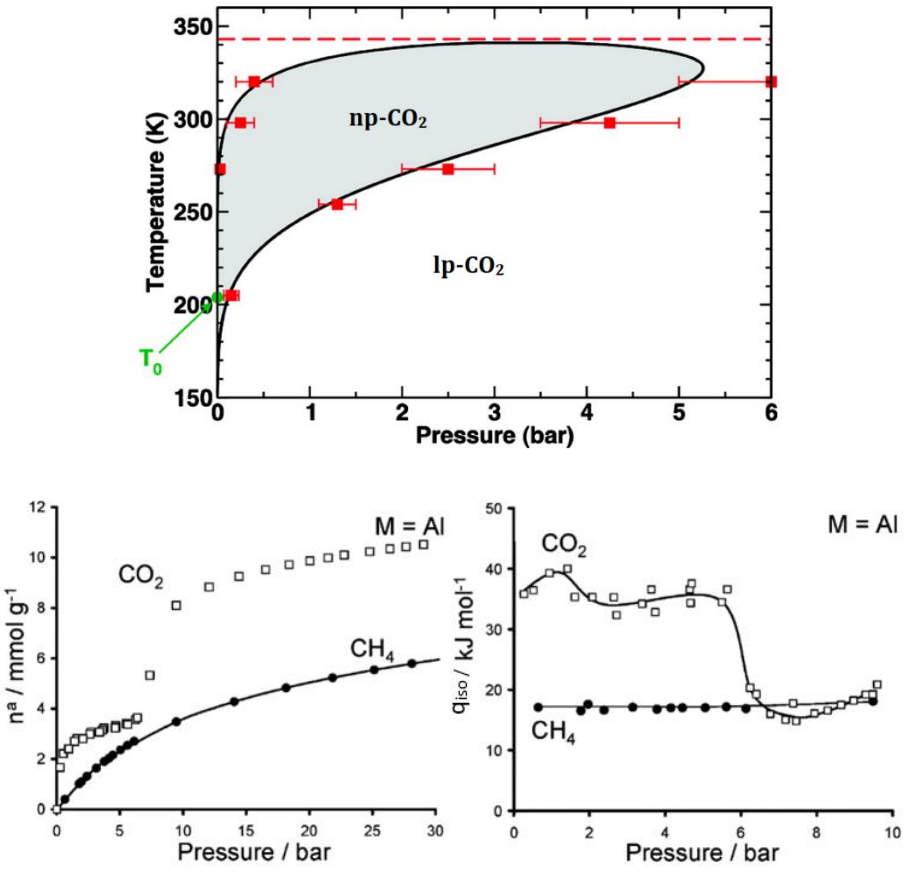

Figure 2.10 (top) Predicted temperature-vapor phase diagram for CO_2 adsorption in MIL-53(Al)(black line) compared with experimental data points (red squares and error bars). Top line represents the isotherm at 343 K for which no transition was observed. (Reproduced from reference [25]) (bottom, left) Isotherm and (bottom, right) isosteric heat of adsorption as a function of pressure; for CO_2 and CH_4 in MIL-53(Al) measured at 304 K. The lines are drawn only to guide the eye. (Reproduced from reference [24, 65])

Information about the strength of host-guest interaction can be retrieved from microcalorimetry or from the adsorption isotherms. CO_2's unusual behaviour during this adsorption measurement was attributed to the framework's "breathing" mechanism. Figure 2.10, (bottom, left) presents the isotherms and (bottom, right) correlated adsorption enthalpy of MIL-53(Al) upon CO_2 and CH_4 adsorption. For CO_2,

there are two constant enthalpy regions, one around -40 kJ mol^{-1} and a second almost constant region around -17 kJ mol^{-1} after a sudden drop at 6 bar.

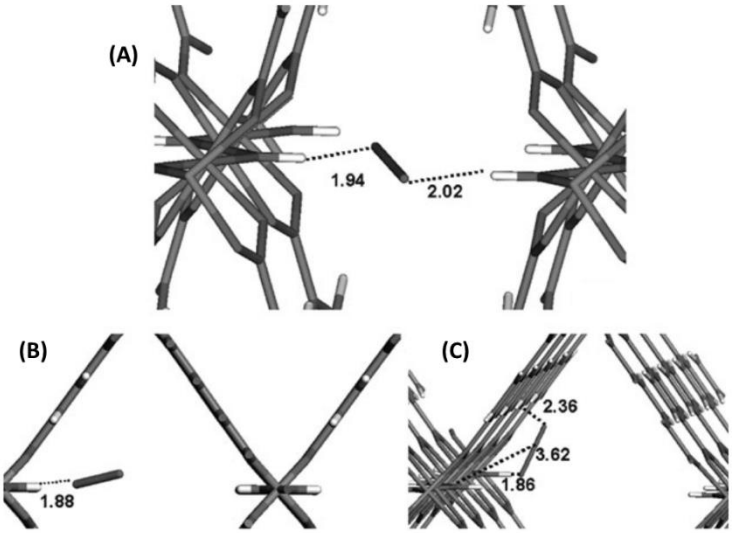

Figure 2.11 Typical arrangements of CO_2 in the MIL-53(Al)-np (A), MIL-53(Al)-lp (B) and (C) at the initial stage of loading. (Reproduced from reference [65])

The transition between **np-CO_2** and **lp-CO_2** of MIL-53(Al) could be responsible for the decrease of enthalpy, to the same level of CH_4. The quadrupolar adsorbate molecule, CO_2 mainly interacts with the μ_2-OH groups. However, when solely considering the **np-CO_2** in Figure 2.11 (A), a double interaction between the CO_2's oxygen atoms and the two protons from the μ_2-OH groups on the opposite pore walls is considered the main adsorption arrangement.

Owing to its **np** width and characteristic short O_CO_2---H_O distances (d=1.94 and 2.02 Å), the **np-CO_2** form is responsible for the high adsorption enthalpy value at low coverage. These interactions are only slightly weaker than hydrogen bonds, which were previously observed for water when interacting with the BDC units. Furthermore, the increase in pore width to 13 Å, due to the **np-CO_2** to **lp-CO_2** transition, rules out this double interaction. The CO_2 molecule now probably either interacts directly to O_CO_2---H_O with a single geometry or between two entities, the hydroxyl and the phenyl group. These interactions are however, in both cases very weak, as presented in Figure

2.11 (B) and (C). [65] In the meantime, the CH_4 adsorption enthalpy remains relatively constant around -17 kJ mol^{-1} indicating no observable flexibility within this temperature range. These findings truly demonstrate the adsorbate's homogeneous nature characterized by a homogeneous pore system. [24]

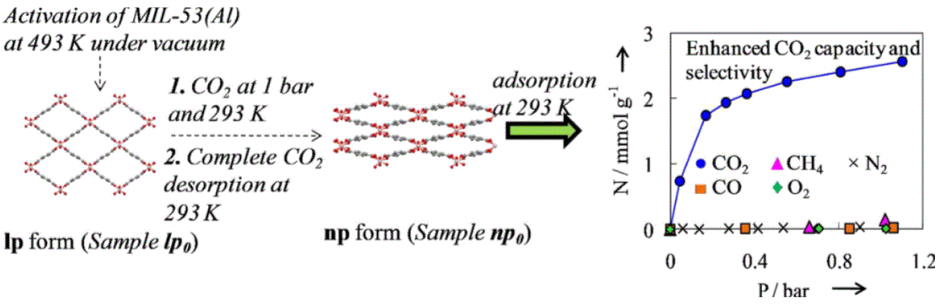

Figure 2.12 Adsorption capacity at 293 K on np structure MIL-53(Al), sample np-d-CO_2. (Reproduced from reference)[68]

Although MIL-53(Al) is a rather stable compound, it has not gained much attention for CO_2 separation due to the low uptake and selectivity when starting from the **lp** state. [31, 69, 70] Hence, it seems important to select the appropriate pre-treating pathway to optimize the uptake capacity and selectivity. Tuning the pores from the **lp** into the **np-d-CO_2**, and using the latter as the adsorbent, quadruples the uptake capacity of CO_2 around 0.17 bar and 293 K. This increased uptake is accompanied with an enhancement of the selectivity over N_2, CH_4, CO and O_2 at subatmospheric pressure. The breathing effect can be used to bring a sorbent in a particular state, were it serves as a molecular sieve to separate CO_2 out of a gas mixture. This **np-d-CO_2** is created by a pre-treatment as shown in Figure 2.12. After activation, the material is exposed to 1 bar CO_2 at 293 K followed by a desorption step. [68] It is interesting to note that our research (Nevjestić *et al.*) has shown other ways to obtain the **np-d** form. [62]

Furthermore, it was reported that the adsorption speed influences the flexible and sorption behaviour of the adsorbent. A fast gravimetric pressurization method immediately fills the pores with CO_2, obstructing the transition from **lp** to **np-CO_2**. This is not the case for normal pressurization where breathing is observed. The final isotherm, *via* a fast pressurization method, results in a normal type I isotherm similar as reported for MIL-47(V). [68]

The group of Férey and co-workers [31] showed that water molecules drastically influence the sorption isotherms of CO_2 and CH_4 at 304 K for MIL-53(Cr), as shown in the adsorption isotherm plotted in Figure 2.13. Comparable isotherms for MIL-53(Cr) are collected, starting form a different initial state, i.e., a first **lp** and a second **np-h** framework. The difference in adsorption behaviour is striking. Mainly for the latter, shown in Figure 2.13 (B) is the CH_4 adsorption uptake negligible. CO_2 shows very little uptake until 10 bar, with a sudden increase between 12 - 18 bar induces a change to the **lp-h-CO_2** state. In contrast to the adsorption experiment starting from the **lp** form as already explained previously in Chapter 1 for MIL-53(Cr), the framework first closes around 0.3 bar followed by a reopening around 5 bar. A disadvantage is the weak long-term stability of MIL-53(M), causing structural decomposition and reducing the adsorption capacity. Especially long term water contact destroys the framework. [71]

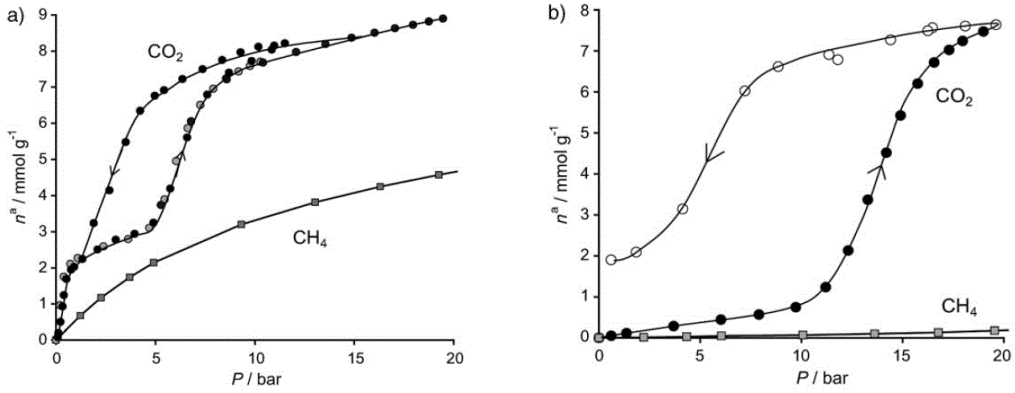

Figure 2.13 Comparison of the adsorption isotherms of CO_2 and CH_4 at 304 K with initial state (A) lp; (B) np-h. (Reproduced from reference [31])

In a second example, the same group examined the influence of the framework history on the behaviour by a breakthrough experiment. Quantitative data of co-adsorption on MIL-53(Cr) is collected *via* breakthrough curves and presented in Table 2.6. Two different mixtures are used, namely one of 25 - 75 mol% and the other of 75 - 25 mol% CO_2-CH_4.

Table 2.6 CH_4 adsorbed quantities (mmol g^{-1}) at 1.0 MPa for 25-75 mol% and 75-25 mol% CO_2-CH_4 gas mixtures for different initial saturations of the column. (Data reproduced from [72])

	25-75 mol%			75-25 mol%		
CO_2-CH_4 fraction in feed	CH_4 adsorbed amount (mmol g^{-1})	Initial state	Final state	CH_4 adsorbed amount (mmol g^{-1})	Initial state	Final state
Saturation by pure CO_2	2.89	lp-CO_2	lp-CO_2/CH_4	1.37	lp-CO_2	lp-CO_2/CH_4
Saturation by feed	0.00	np-CO_2/CH_4	np-CO_2/CH_4	0.33	lp-CO_2/CH_4	lp-CO_2/CH_4 + np-CO_2/CH_4
Without intital saturation	2.92	lp	lp-CO_2/CH_4	0.99	lp	lp-CO_2/CH_4 + np-CO_2/CH_4

In here, pre-saturation of the chromatographic columns plays a decisive role in the final adsorbed amount as can be seen from the table. The three columns are filled with MIL-53(Cr) and prior to the experiment pre-treated: saturated by pure CO_2 (**lp-CO_2**), saturated by 25 - 75 mol% CO_2-CH_4 (**np-CO_2/CH_4**) and without initial saturation (**lp**). Injection of a 25 - 75 mol% CO_2-CH_4 mixture indicates a significant difference between initial states. CH_4 adsorption is almost non-existing in the **np-CO_2/CH_4** form, in agreement with the results obtained for **np-h** as reported in previous paragraph. Meanwhile, both measurements starting off in the **lp** forms, show a rather identical (2.89 - 2.91 mmol g^{-1}) amount of adsorbed CH_4. A rather identical behaviour is recognized for the experiment with 75 - 25 mol% CO_2-CH_4. However, the methane breaks faster when the column is pre-treated with a higher amount of CO_2, here 75 mol%, which indicates a slower adsorption behaviour. [72]

In stark contrast with Al and Cr, Sc and Fe Mil-53's both exhibit a different flexible behaviour. The MIL-53(Fe) transition is plotted in Figure 2.14, and clearly shows a gradual reopening of the structure from a volume of 880 $Å^3$ to 1570 $Å^3$. Both Sc and Fe frameworks are in the **cp** form after dehydration and small amounts of CO_2 initiate an **int-CO_2** state. [13, 32] A next phase transition results in the **np-CO_2** form, presenting a slightly reopened structure, which becomes pronounced at elevated pressure. After an initial period of low uptake, a second clear adsorption step occurs, completely filling the pores and opening the structure to its final **lp-CO_2** state. [61]

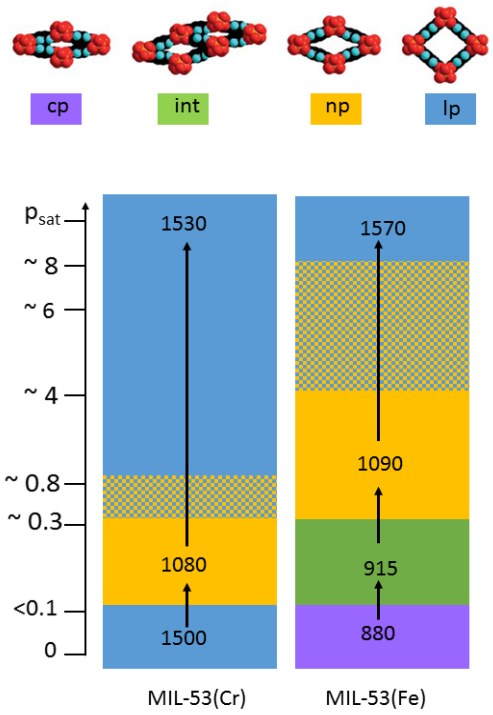

Figure 2.14 Schematic representation of the *in-situ* XRPD results at 230 K for MIL-53(Cr) and MIL-53(Fe). (Reproduced from reference [32])

2.5.1.5 Flexibility induced by mixture of CO_2 and CH_4

The flexibility of the MIL-53(Al) structure when using a mixture of CO_2 and CH_4 highly depends on the ratio of that mixture. The obtained phase diagrams surprisingly show non-monotonic behaviour as presented in Figure 2.15. In this figure, the evolution of (T,P) phase diagrams is represented as different parts of the 3D diagram along constant-composition planes. When comparing CO_2 and CH_4 in a mixture, they create a dissymmetry, together with a very high breathing sensitivity for a low fraction of CO_2 in almost pure CH_4. The sensitivity is particularly highlighted by the difference between the phase diagrams for pure methane and 20 mol% of CO_2, which have very different extensions in terms of pressure (2 bar versus 11 bar) and temperature (245 versus 315 K). These extensions and thus the stability of the **np** state diminish gradually when increasing the CO_2 ratio. [73]

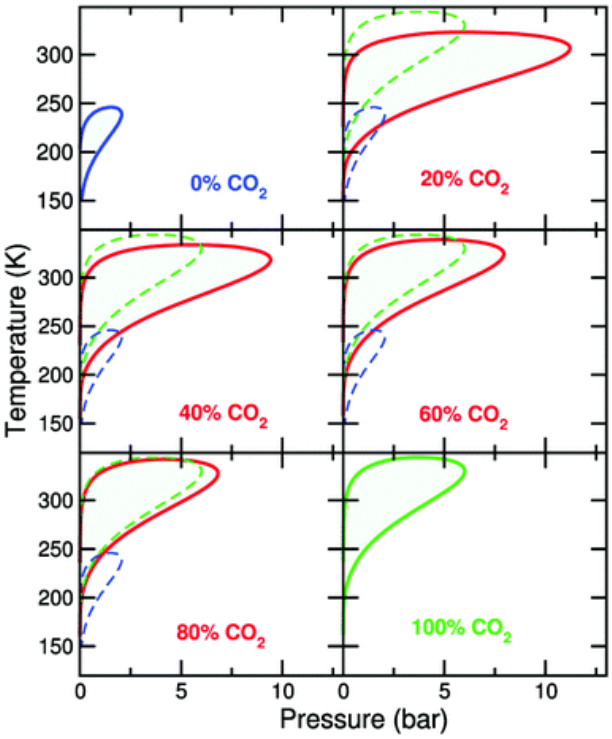

Figure 2.15 Temperature pressure diagram of MIL-53(Al) upon adsorption of CO_2/CH_4 mixture, with increasing CO_2 mole fraction. CH_4 (blue), CO_2 (green), dashed lines correspond to the pure component diagrams. Filled diagram corresponds with the actual component diagram at a certain concentration (mol%) of CO_2. (Reproduced from reference [73])

2.5.1.6 Flexibility induced by xenon

The breathing effect in MIL-53(M) is in fact a general phenomenon observed within a limited temperature range, regardless of the guest molecule. As a result, a new thermodynamic model was developed in combination with Xenon, CH_4 and CO_2 sorption measurements. Based on this model three new phase diagrams were constructed, presented in Figure 2.16, (left). [25, 28] The **np** occurrence area is defined by temperature and pressure and is in comparison with CO_2 (350 K and 5 bar), more restricted for Xe (up to 300 K and 1.5 bar) and CH_4 (up to 250 K and 2 bar). Moreover, both large and narrow pore state were identifiable based on the ^{129}Xe NMR spectrum Figure 2.16, (right). [74]

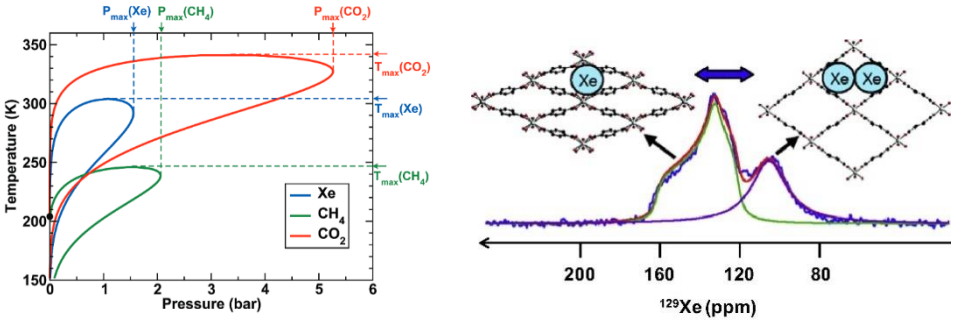

Figure 2.16 (left) Schematic representation of vapour-pressure phase diagram (np and lp) for Xe, CH_4 and CO_2. (Reproduced from reference [25]) (right) Study of the flexibility of porous hybrid MIL-53(Al) by ^{129}Xe NMR at 83.02 MHz; purple corresponds to large-pore, green to narrow-pore form. (Reproduced from reference [74])

2.5.1.7 Flexibility induced by other gases

More complex breathing behaviour is generally observed when the adsorbate has long-chain alkanes, such as propane and butane. The adsorption isotherms of MIL-53(Cr), MIL-53(Al) and MIL-53(Fe) measured at different pressures, are characterized by a multi-step adsorption. Increasing the amount of guest molecules induces different discrete pore changes, four in MIL-53(Fe) and two in MIL-53(Cr) and MIL-53(Al) as shown in the diagram in Figure 2.17. These states are identical to those observed during temperature breathing, a topic previously described in this chapter.

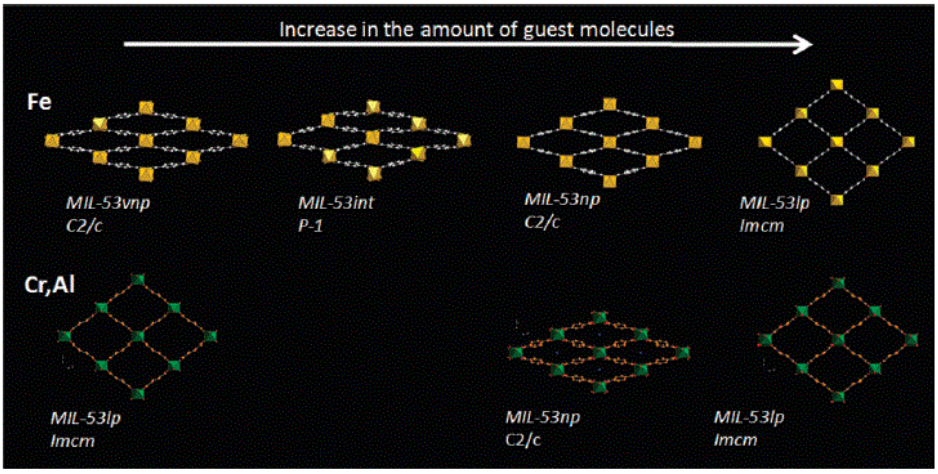

Figure 2.17 Schematic diagram of structural evolutions in MIL-53(M): Cr, Al, Fe upon adsorption of n-alkanes. (Reproduced from reference [33])

Worth mentioning here is that MIL-47 (V) maintains its rigidity with any hydrocarbon adsorbent. [45] MIL-53(Cr) and MIL-53(Al) behave rigid in the temperature range of 303 - 313 K for both methane and ethane. Within this particular temperature interval, the adsorbates cannot overcome the threshold for adsorption enthalpy (-20 kJ mol^{-1}) above which the breathing takes place. This in contrast to the more carbon rich linear alkanes, from propane to nonane, for which stepped adsorption isotherms are observed, as presented in Figure 2.18 (B), (C) and (D). The occurrence of the stepped isotherm shifts towards a higher relative pressure when longer chains are employed. It was speculated that the presence of stepped isotherms is influenced by host - guest interaction as well as entropic and confinement effects.

In contrast, MIL-53(Fe) exhibits stepped isotherms for all tested linear alkanes C_1-C_4 shown in Figure 2.18 (A). [23, 26, 33] Also, other gases such as xylenes and toluene have been reported to trigger breathing in MIL-53 series. [27, 75]

Couck *et al*. [47] investigated the breathing effect of COMOC-2(V) under influence of different hydrocarbons: ethane, ethylene, propane and propylene at different temperatures such as 281.5, 293 and 303 K. Based on their results, they conclude that the breathing pressure decreases with increasing hydrocarbon molecular weight as can be seen in Figure 2.18 (E). The typical two-step isotherms were almost identical for both alkanes and alkenes.

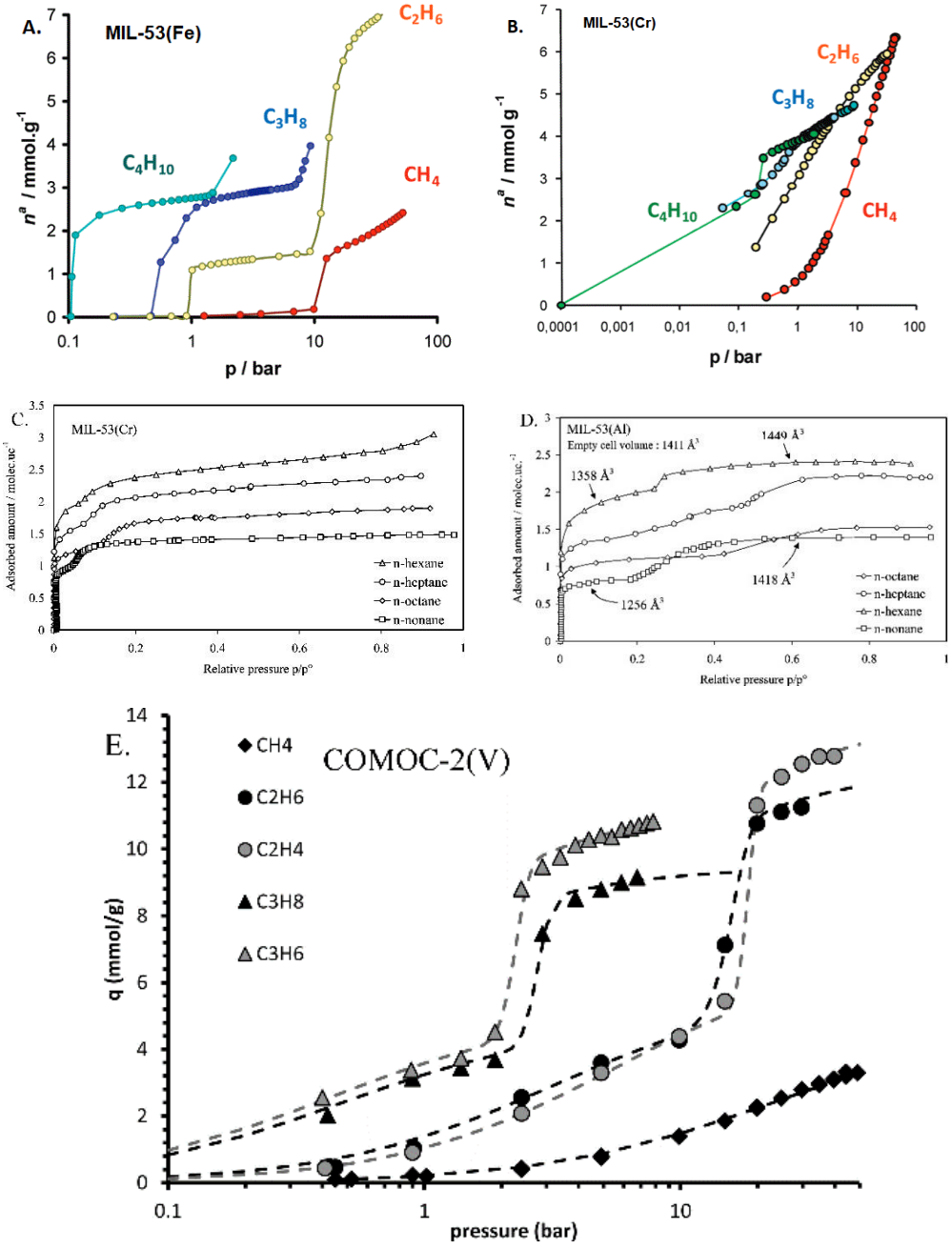

Figure 2.18 Adsorption isotherms (A) MIL-53(Fe) at 303 K; (B) MIL-53(Cr) at 303 K; (C) MIL-53(Cr) at 313 K; (D) MIL-53(Al) at 313 K; (E) COMOC-2(V) at 303 K; symbols represent adsorption points; the lines are drawn only to guide the eye. (Reproduced from references [33, 47])

2.5.2 Flexibility induced by mechanical pressure

The topic "mechanical pressure" is an exception as it deals with mechanical pressure that induces breathing in which no guest molecules are involved. Theoretical and experimental results show that independent of the adsorbate, solely mechanical pressure can induce breathing. Mechanical pressure experiments are considered as extremely interesting for theoretical calculations as the flexibility is not influenced by "guests". In this work we have not investigated mechanical pressure as a breathing trigger. Nevertheless, it is important to include mechanical induced pressure in this overview as it sheds new light on the breathing behaviour. High pressure Hg porosimetry has been used to investigate the structural behaviour upon mechanical pressure of MIL-53(Al) and MIL-53(Cr) compared to the rigid MIL-47(V). [30] The applied pressure lies mostly within the MPa range and can cause pressure-induced transition between a **lp** and **np** or **cp**. Because of the high adsorption energy, these materials are particularly interesting candidates for further use as shock absorber. [48]

In Figure 2.19, the cumulative volume of intruded mercury (mL g^{-1}) is plotted in function of the applied mercury pressure. Both MIL-53 structures in Figure 2.19, MIL-53(Cr) (middle) and MIL-53(Al) (top) show flexibility but surprisingly, so does MIL-47(V) (top). [35] This is in stark contrast to guest induced flexibility where MIL-47(V) does not behave flexible. In these figures, two regions can be distinguished: the first (A) below 2 MPa, where mercury intrusion corresponds to the powder compaction and filling of the interparticular porosity, and (B) a second occurs depending on the metal node in different pressure ranges: (13 - 18 MPa) for Al, (55- ~85 MPa) for Cr and (85 - 125 MPa) for V. The latter is assigned to the compound contraction and the compressibility follows the order Al > Cr > V. The mechanical energy from one compression-decompression cycle (with $W = P \times \Delta V$) is 6,7 J g^{-1}, 12 J g^{-1} and 33 J g^{-1} for MIL-53(Al), MIL-53(Cr) and MIL-47(V), respectively. This makes these structures extremely interesting as shock absorbers. Mesoporous hydrophobic materials for example alter between 4 - 10 J g^{-1}. Upon mechanical pressure, the flexibility highly depends on the nature of the metal centre. Interestingly, MIL-53(Al) shows an irreversible structural transition and stays in the **cp** form, whereas MIL-53(Cr) and MIL-47(V) undergo fully reversible transitions. The authors contribute this effect to the

stronger $\pi - \pi$ packing interaction that stabilizes the Al structure. [36] The material becomes amorphous when higher pressures, between 5 GPa and 16 GPa, are applied using pressurizing media such as ethanol and mineral oil. [76]

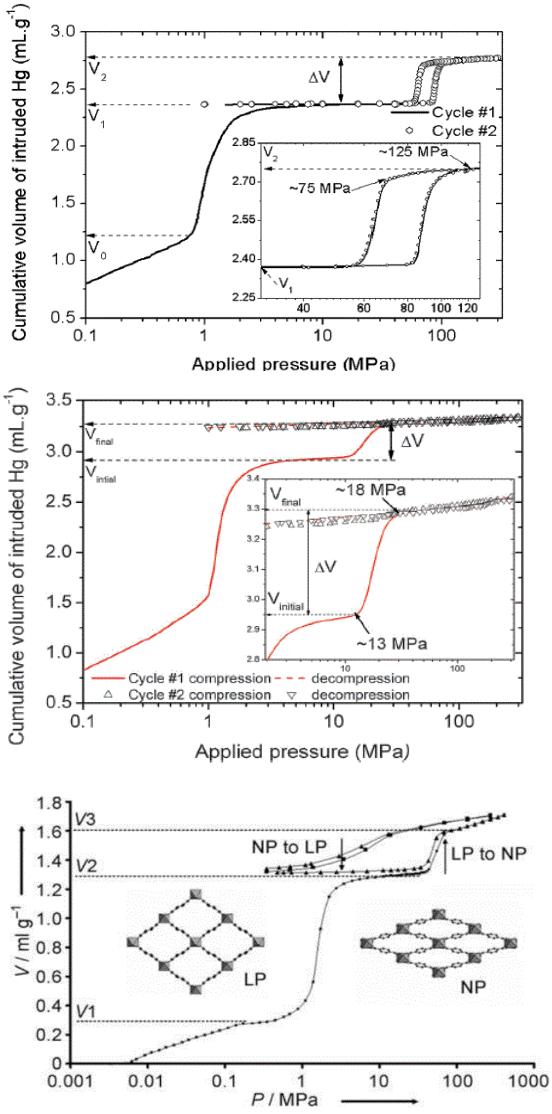

Figure 2.19 Cumulative volume of intruded mercury in a two cycles intrusion-extrusion as a function of the applied pressure (MPa) obtained for (top) MIL-47(V) [35]; (middle) MIL-53(Al) [36]; (bottom) MIL-53(Cr) [30]. (Reproduced from references [30, 35, 36])

2.5.3 Host-host interactions

The host-host interaction of MIL-47(V) was aforementioned when ascribing the framework stiffening, changing the hydroxyl bridges between the metal nodes by oxides as this excludes the formation of hydrogen bonds. A second example is the MIL-53(Al) related structure MIL-69(Al). [77] In the latter, NDC serves as the organic linker. This structure exhibits $\pi - \pi$ intermolecular interactions between two adjacent organic linkers together with strong hydrogen bond interactions. Both interactions have a major influence on the framework flexibility and inhibit transition to a novel state. As a result the MIL-69(Al) is permanently in the **np** form.

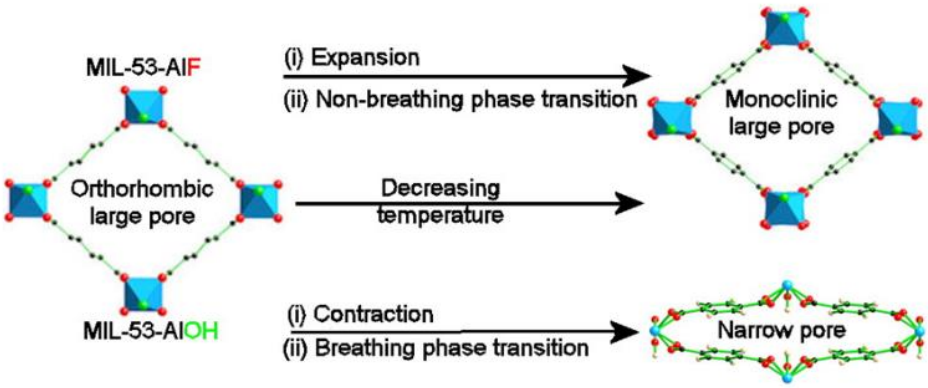

Figure 2.20 Contradistinct thermoresponsive behaviour between two isostructural MIL-53 structures: MIL-53(Al) (green) and MIL-53(Al)F (red). (Reproduced from reference [78])

The thermoresponsive behaviour of two isoreticular MIL-53 materials, the original MIL-53(Al) (labelled as MIL-53-AlOH) and MIL-53AlF, are plotted in Figure 2.20. The bridging group –OH or -F plays a decisive role in the flexibility and thermal response. In the temperature range of 150 K – 500 K, MIL-53(Al) behaves flexible, going from a monoclinic np to an orthorhombic lp structure. The orthorhombic MIL-53(Al) **lp** form exhibits a positive linear thermal volume expansion. Meanwhile the MIL-53AlF, solely different by a replacement of the OH by F, is a non-breathing framework. In addition, the framework exhibits a monoclinic instead of an orthorhombic **lp** structure, and shows a negative linear thermal expansion. [78]

2.5.3.1 Mechanism behind flexibility

In this part the structural mechanism behind the thermal flexibility of MIL-53(Al) **lp** and from **lp** to **np-d** as heretofore known, will be explained. Temperature is the physical parameter that triggers this effect, inducing structural changes of the MIL-53(Al) lattice. The framework flexibility of MIL-53(M) series was already the subject of different studies, both experimental and computational. This structure, is considered as one of the key examples of breathing in the MIL-53(M) series.

The framework MIL-53(Al) **lp** opens and closes under influence of temperature in a similar way as a wine rack. The front plane of this wine-rack, MIL-53(Al) **lp** is shown in Figure 2.21 (A). The structure has nonbonding Al···Al, with distance d(Al···Al), forming the sides of the rhombus with an internal rhombus angle α shown in Figure 2.21 (A) and (C). Generally this flexibility follows a positive thermal expansion. A linear decrease in a (-6.27×10^{-6} Å K^{-1}) and b (-2.43×10^{-4} Å K^{-1}) and linear increase in c (3×10^{-4} Å K^{-1}) is observed over the entire temperature range from 150 K to 500 K. Overall, the positive expansion in the [001] direction outweighs the overall changes in the [100] and [010] directions (planes are presented in Figure 2.21 (D)), with an overall linear volume expansion of 1.25×10^{-6} $Å^3$ K^{-1}. [78] Temperature contracts the chain (Figure 2.21 (B)) of the corner-sharing $AlO_4(OH)_2$ that are lying along the a-axis. Two phenomena will increase with elevated temperature and can explain this contraction along the a-axis. A first one is the rocking of the carboxylate (black arrows) along the major axis of the BDC linker, a second is the twisting motion (blue arrows) along the Al-OH-Al linkage of the relatively rigid $AlO_4(OH)_2$, which have been deduced previously from single crystal studies. [42, 79, 80]

The pores are formed by the connection of four bounded BDC ligands with Al atoms at the vertices of the rhombus. Moreover, the BDC ligands rotate, with a change in α, around the Al-OH-Al with the $AlO_4(OH)_2$ octahedra as a central "anchor point", presented in Figure 2.21 (C) (burgundy arrows).

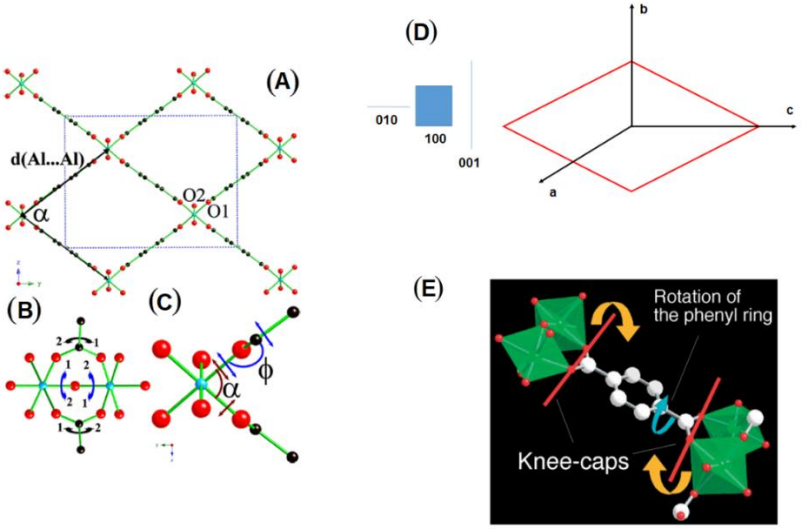

Figure 2.21 (A) Structure of [Al(OH)(BDC)] in the lp state, view along the a-axis. The rhombus shaped channels are constructed by the BDC ligands and connected to aluminium atoms at each vertex. Characteristic nonbonding distance d(Al---Al) and internal rhombus angle α are defined in the figure. (B) Representation of the connection along the a-axis and correlated motions of rocking of the carboxylate (black) and twisting of Al-OH-Al (blue) linkage around the $AlO_4(OH)_2$. (C) Schematic representation of the rotation of the BDC linkers around Al-OH-Al chain, indicated by α (burgundy) arrows and the knee-cap bending ϕ (blue arrows). (D) Different orientations (a, b, c) and explanation of the lattice parameters (100, 010, 001). (E) Geometrical rearrangement occurring in MIL-53(M) at the origin of giant breathing.
(Reproduced from reference [13, 78])

The sides of the rhombus d(Al···Al) stay fairly constant during this process, decreasing from 10.5432 Å at 150 K to 10.5415 Å at 500 K. Another flexible unit is the O-O axis of each carboxylate, which acts as a knee-cap during the reversible shrinkage indicated by ϕ (blue arrows). Moreover, the free C-C bond rotation in Figure 2.21 (E) (white arrow) releases the tension during the shrinkage, leading to a stable lattice energy at the end of the process.

In the transition **lp** to the **np-d** form for MIL-53(Al), several collective vibrations may play a role as described by the work of Hoffman *et al*. Strong π-π interactions result in a pore contraction. The transition mechanism from **lp** to **np-d** by the thermoresponsive behaviour of the framework seems to be the result of multiple host-host interactions. [78, 81]

2.5.4 Influence of the ligand functionalisation

The rotation of the central part of the organic linker is influenced by the functionalization, so steric hindrance is possible. Additional functionalization generally lowers the micropore volume, shown by Devic *et al*. [32] for MIL-53(Fe)-X and *Biswas et al.* [82] for MIL-53(Al)-X, with X representing the functionalization on the organic carboxylate group. The example of the MIL-53(Fe) framework illustrates the importance of such rotations in Figure 2.22. The state at 230 K of MIL-53(Fe)-X adsorbing CO_2, is influenced by functionalization X, undoubtedly as is shown in Figure 2.22. Transitions starting from a **cp** state can be slowed down or even become non-existing by the choice of X. For example, as shown in the summarizing Figure 2.22, (top) for methyl groups. Here, a slightly higher pressure is necessary to reopen the pores to the **np-d-CO_2** state, meanwhile a double carboxyl $(COOH)_2$ or amine (NH_2) functionalization completely hinders the structure to reopen. Indeed, these two structures are only observed in the **cp** form. Furthermore, CO_2 measurements in Figure 2.22, (bottom) indicate that the functionalization X has a major influence on the CO_2-framework interaction. The capacity of the **np-d-CO_2** form is affected by steric hindrance, either due to direct pore blocking or by inducing rotation of the phenyl cores reducing space available for guest molecules. [32]

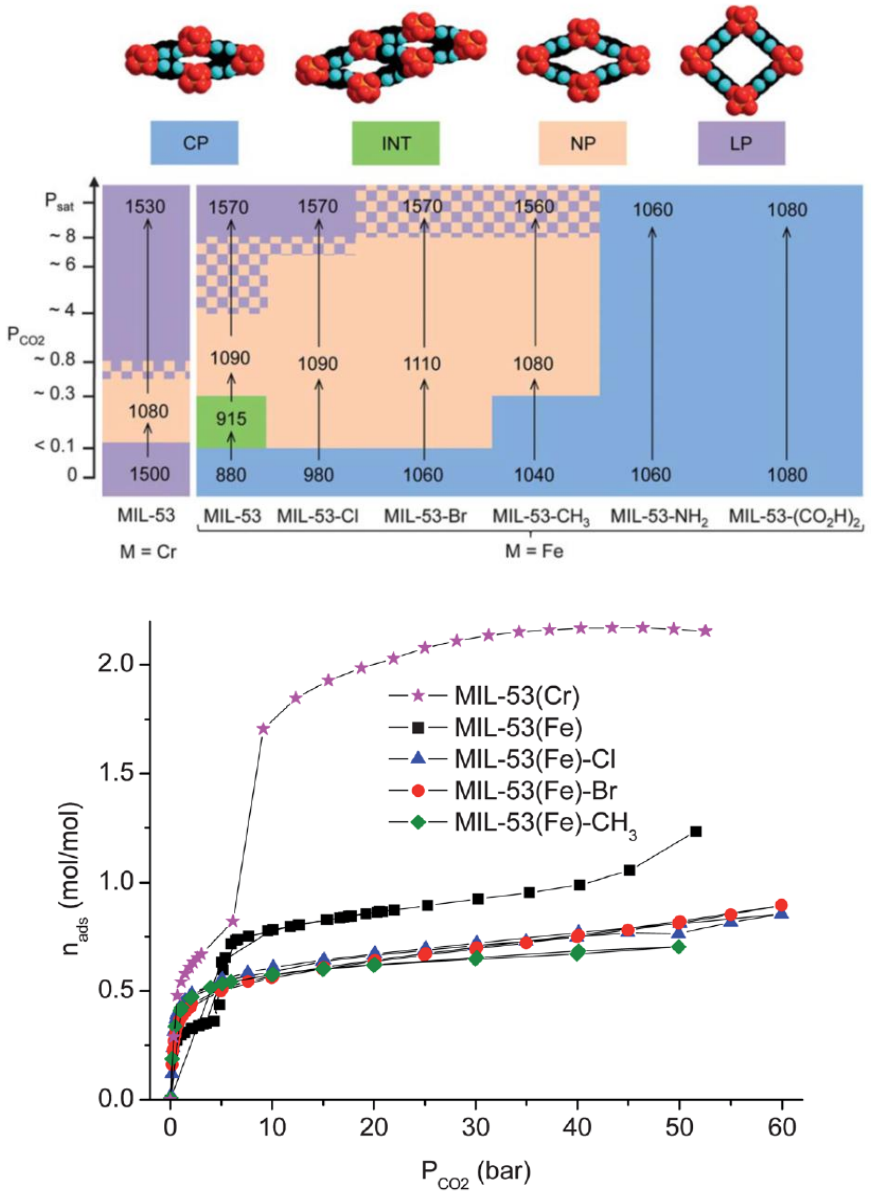

Figure 2.22 (top) Schematic representation of the results of *in-situ* XRPD experiments; pore openings in the MIL-53 system (cp: closed pore, int: intermediate, np: narrow pore, lp: large pore) and the evolution of the pore opening and unit cell volume with the CO_2 pressure at 230 K for the MIL-53(Cr) and MIL-53(Fe)-X solids. (bottom) Adsorption isotherms of CO_2 on MIL-53(Cr) and MIL-53(Fe)-X (X = -, Cl, Br, CH_3) at 303 K. (Reproduced from reference [32])

2.6 Conclusion

To summarize, this chapter gives a general introduction to the fundamentals of adsorption. Flexible MOFs combine the order and stability in a crystalline matrix with cooperative structural transformability. The triggers for this flexible behaviour are chemical or physical stimuli of various kinds, which is a very unique property that is non-existing for other known solid-state materials. After a brief introduction to flexibility, the adsorption isotherm of a flexible MIL-53(Cr) material is explained.

The discussion about breathing is organized by three parameters, namely influence of the ligand, host-host and host-guest/guest-guest interactions. Different structural states are briefly explained: **np**, **lp**, **int**, **vnp** and **cp**.

Functionalization of the ligand of the MOF can induce steric hindrance. A case study of MIL-53-Fe(X) (X=-, -Cl, -Br, -CH_3) is described. This functionalization has a major impact on the final framework transition and gas uptake.

Host-host interactions are used to describe the phenomenon of breathing *via* a well-known example MIL-53(Al). The metal node is an essential parameter that influences the breathing, as is clearly demonstrated *via* the examples of MIL-53(M). A second parameter is the connection between the metal centres. Here, the octahedral metal nodes can be linked *via* a M^{III}-OH-M^{III}, M^{III}-F-M^{III} or M^{IV}=O-M^{IV} connections, and this bridge is a determining factor whether the structure acts as a rigid entity or behaves flexible. In contrast to the flexible BDC homologues MIL-53(M), the NDC MIL-69(Al) framework is influenced by predominance of the $\pi - \pi$ intermolecular interactions and stays in the **np** form.

The final stimuli are host-guest and guest-guest interactions which initiate phase transitions. They are divided in different types of stimuli: guests, thermal and mechanical stimuli. The body of the discussion focuses on four materials: MIL-53(M), MIL-47(V), COMOC-2(V) and DUT-5(Al), which are the frameworks used in the experimental part of this work. This overview shows that the flexibility depends on the temperature range and guest (pressure, concentration). The MIL-53(Al) structure is considered as flexible under certain circumstances while MIL-47(V) is rigid. However,

mechanical stimuli can also create flexibility in the latter structure. In contrast for COMOC-2(V) mainly guests as CO_2 and alkanes are reported to initiate flexibility. It is rather remarkable that here the vanadium framework is flexible, while the isotopologic aluminium compound DUT-5(Al) is completely rigid.

Although a plethora of papers describe and try to tackle the theory behind flexible MOFs, a comprehensive theory that combines all theoretical and experimental knowledge is still at its emerging stage. The theory behind this unique property should be further developed. Not only to be able to explain this effect, but also to predict whether or not the framework is flexible. This model would support experimental chemists in their unaccomplished desire to design new flexible frameworks guided by theoretical insights (through molecular modelling). In the field of characterization, *in-situ* methods should be further developed to identify and characterize the relevant interactions that play a key role, focused on host-host, host-guest and guest-guest interactions.

2.7 References

1. Merriam-Webster, 2017, https://merriam-webster.com
2. M. Thommes, K. Kaneko, A.V. Neimark, J.P. Olivier, F. Rodriguez-Reinoso, J. Rouquerol and K.S. Sing, *Pure and Applied Chemistry*, 2015, **87**, 1051-1069.
3. R.T. Yang, *Adsorbents: fundamentals and applications*, John Wiley & Sons, 2003.
4. J.G. Calvert, *Pure and applied chemistry*, 1990, **62**, 2167-2219.
5. D. Everett, *Pure and Applied Chemistry*, 1972, **31**, 577-638.
6. D.M. Ruthven, *Principles of adsorption and adsorption processes*, John Wiley & Sons, 1984.
7. W.J. Thomas and B.D. Crittenden, *Adsorption technology and design*, Butterworth-Heinemann, 1998.
8. J. Keller and E. Robens, *Journal of thermal analysis and calorimetry*, 2003, **71**, 37-45.
9. A. Schneemann, V. Bon, I. Schwedler, I. Senkovska, S. Kaskel and R.A. Fischer, *Chemical Society Reviews*, 2014, **43**, 6062-6096.
10. G. Ferey and C. Serre, *Chemical Society Reviews*, 2009, **38**, 1380-1399.
11. E.V. Anokhina, M. Vougo-Zanda, X. Wang and A.J. Jacobson, *Journal of the American Chemical Society*, 2005, **127**, 15000-15001.
12. M. Anbia and S. Sheykhi, *Journal of Natural Gas Chemistry*, 2012, **21**, 680-684.
13. C. Serre, S. Bourrelly, A. Vimont, N.A. Ramsahye, G. Maurin, P.L. Llewellyn, M. Daturi, Y. Filinchuk, O. Leynaud, P. Barnes and G. Férey, *Advanced Materials*, 2007, **19**, 2246-2251.
14. E. Haque, N.A. Khan, J.E. Lee and S.H. Jhung, *Chemistry – A European Journal*, 2009, **15**, 11730-11736.
15. C. Serre, F. Millange, C. Thouvenot, M. Noguès, G. Marsolier, D. Louër and G. Férey, *Journal of the American Chemical Society*, 2002, **124**, 13519-13526.
16. T. Loiseau, C. Serre, C. Huguenard, G. Fink, F. Taulelle, M. Henry, T. Bataille and G. Férey, *Chemistry-A European Journal*, 2004, **10**, 1373-1382.
17. C. Volkringer, T. Loiseau, N. Guillou, G. Ferey, E. Elkaim and A. Vimont, *Dalton Transactions*, 2009, **12**, 2241-2249.
18. C. Serre, C. Mellot-Draznieks, S. Surblé, N. Audebrand, Y. Filinchuk and G. Férey, *Science*, 2007, **315**, 1828-1831.
19. C. Mellot-Draznieks, C. Serre, S. Surblé, N. Audebrand and G. Férey, *Journal of the American Chemical Society*, 2005, **127**, 16273-16278.
20. H.C. Hoffmann, B. Assfour, F. Epperlein, N. Klein, S. Paasch, I. Senkovska, S. Kaskel, G. Seifert and E. Brunner, *Journal of the American Chemical Society*, 2011, **133**, 8681-8690.

21. D.N. Dybtsev, H. Chun and K. Kim, *Angewandte Chemie*, 2004, **116**, 5143-5146.
22. G. Ferey, *Chemical Society Reviews*, 2008, **37**, 191-214.
23. M. Alhamami, H. Doan and C.-H. Cheng, *Materials*, 2014, **7**, 3198-3250.
24. S. Bourrelly, P.L. Llewellyn, C. Serre, F. Millange, T. Loiseau and G. Férey, *Journal of the American Chemical Society*, 2005, **127**, 13519-13521.
25. A. Boutin, F.-X. Coudert, M.-A. Springuel-Huet, A.V. Neimark, G. Férey and A.H. Fuchs, *The Journal of Physical Chemistry C*, 2010, **114**, 22237-22244.
26. T.K. Trung, P. Trens, N. Tanchoux, S. Bourrelly, P.L. Llewellyn, S. Loera-Serna, C. Serre, T. Loiseau, F. Fajula and G. Férey, *Journal of the American Chemical Society*, 2008, **130**, 16926-16932.
27. V. Finsy, C.E. Kirschhock, G. Vedts, M. Maes, L. Alaerts, D.E. De Vos, G.V. Baron and J.F. Denayer, *Chemistry-A European Journal*, 2009, **15**, 7724-7731.
28. A. Boutin, M.A. Springuel-Huet, A. Nossov, A. Gedeon, T. Loiseau, C. Volkringer, G. Férey, F.X. Coudert and A.H. Fuchs, *Angewandte Chemie International Edition*, 2009, **48**, 8314-8317.
29. Y. Liu, J.-H. Her, A. Dailly, A.J. Ramirez-Cuesta, D.A. Neumann and C.M. Brown, *Journal of the American Chemical Society*, 2008, **130**, 11813-11818.
30. A. Ghoufi, A. Subercaze, Q. Ma, P.G. Yot, Y. Ke, I. Puente-Orench, T. Devic, V. Guillerm, C. Zhong, C. Serre, G. Férey and G. Maurin, *The Journal of Physical Chemistry C*, 2012, **116**, 13289-13295.
31. P.L. Llewellyn, S. Bourrelly, C. Serre, Y. Filinchuk and G. Férey, *Angewandte Chemie International Edition*, 2006, **45**, 7751-7754.
32. T. Devic, F. Salles, S. Bourrelly, B. Moulin, G. Maurin, P. Horcajada, C. Serre, A. Vimont, J.-C. Lavalley, H. Leclerc, G. Clet, M. Daturi, P.L. Llewellyn, Y. Filinchuk and G. Ferey, *Journal of Materials Chemistry*, 2012, **22**, 10266-10273.
33. P.L. Llewellyn, P. Horcajada, G. Maurin, T. Devic, N. Rosenbach, S. Bourrelly, C. Serre, D. Vincent, S. Loera-Serna, Y. Filinchuk and G. Férey, *Journal of the American Chemical Society*, 2009, **131**, 13002-13008.
34. H. Depauw, I. Nevjestić, J. De Winne, G. Wang, K. Haustraete, K. Leus, A. Verberckmoes, C. Detavernier, F. Callens, E. De Canck, H. Vrielinck and P. Van Der Voort, *Chemical Communications*, 2017, **53**, 8478-8481.
35. P.G. Yot, Q. Ma, J. Haines, Q. Yang, A. Ghoufi, T. Devic, C. Serre, V. Dmitriev, G. Ferey, C. Zhong and G. Maurin, *Chemical Science*, 2012, **3**, 1100-1104.

36. P.G. Yot, Z. Boudene, J. Macia, D. Granier, L. Vanduyfhuys, T. Verstraelen, V. Van Speybroeck, T. Devic, C. Serre, G. Ferey, N. Stock and G. Maurin, *Chemical Communications*, 2014, **50**, 9462-9464.
37. F.-X. Coudert, A.U. Ortiz, V. Haigis, D. Bousquet, A.H. Fuchs, A. Ballandras, G. Weber, I. Bezverkhyy, N. Geoffroy, J.-P. Bellat, G. Ortiz, G. Chaplais, J. Patarin and A. Boutin, *The Journal of Physical Chemistry C*, 2014, **118**, 5397-5405.
38. A. Boutin, D. Bousquet, A.U. Ortiz, F.-X. Coudert, A.H. Fuchs, A. Ballandras, G. Weber, I. Bezverkhyy, J.-P. Bellat, G. Ortiz, G. Chaplais, J.-L. Paillaud, C. Marichal, H. Nouali and J. Patarin, *The Journal of Physical Chemistry C*, 2013, **117**, 8180-8188.
39. H. Leclerc, T. Devic, S. Devautour-Vinot, P. Bazin, N. Audebrand, G. Férey, M. Daturi, A. Vimont and G. Clet, *The Journal of Physical Chemistry C*, 2011, **115**, 19828-19840.
40. F. Nouar, T. Devic, H. Chevreau, N. Guillou, E. Gibson, G. Clet, M. Daturi, A. Vimont, J.M. Greneche, M.I. Breeze, R.I. Walton, P.L. Llewellyn and C. Serre, *Chemical Communications*, 2012, **48**, 10237-10239.
41. F. Millange, N. Guillou, R.I. Walton, J.-M. Greneche, I. Margiolaki and G. Ferey, *Chemical Communications*, 2008, 4732-4734.
42. J.P.S. Mowat, S.R. Miller, A.M.Z. Slawin, V.R. Seymour, S.E. Ashbrook and P.A. Wright, *Microporous and Mesoporous Materials*, 2011, **142**, 322-333.
43. J.P.S. Mowat, V.R. Seymour, J.M. Griffin, S.P. Thompson, A.M.Z. Slawin, D. Fairen-Jimenez, T. Duren, S.E. Ashbrook and P.A. Wright, *Dalton Transactions*, 2012, **41**, 3937-3941.
44. S. Biswas, D.E.P. Vanpoucke, T. Verstraelen, M. Vandichel, S. Couck, K. Leus, Y.-Y. Liu, M. Waroquier, V. Van Speybroeck, J.F.M. Denayer and P. Van Der Voort, *The Journal of Physical Chemistry C*, 2013, **117**, 22784-22796.
45. T.K. Trung, I. Déroche, A. Rivera, Q. Yang, P. Yot, N. Ramsahye, S.D. Vinot, T. Devic, P. Horcajada, C. Serre, G. Maurin and P. Trens, *Microporous and Mesoporous Materials*, 2011, **140**, 114-119.
46. Y.-Y. Liu, S. Couck, M. Vandichel, M. Grzywa, K. Leus, S. Biswas, D. Volkmer, J. Gascon, F. Kapteijn, J.F.M. Denayer, M. Waroquier, V. Van Speybroeck and V.D.V. Pascal, *Inorganic Chemistry*, 2013, **52**, 113-120.
47. S. Couck, T.R.C. Van Assche, Y.-Y. Liu, G.V. Baron, P. Van Der Voort and J.F.M. Denayer, *Langmuir*, 2015, **31**, 5063-5070.
48. J. Wieme, L. Vanduyfhuys, S.M.J. Rogge, M. Waroquier and V. Van Speybroeck, *The Journal of Physical Chemistry C*, 2016, **120**, 14934-14947.
49. I. Senkovska, F. Hoffmann, M. Fröba, J. Getzschmann, W. Böhlmann and S. Kaskel, *Microporous and Mesoporous Materials*, 2009, **122**, 93-98.
50. G. Ferey, *New Journal of Chemistry*, 2016, **40**, 3950-3967.

51. P. Rallapalli, K.P. Prasanth, D. Patil, R.S. Somani, R.V. Jasra and H.C. Bajaj, *Journal of Porous Materials*, 2011, **18**, 205-210.
52. K. Barthelet, J. Marrot, D. Riou and G. Férey, *Angewandte Chemie*, 2002, **114**, 291-294.
53. S. Brunauer, L.S. Deming, W.E. Deming and E. Teller, *Journal of the American Chemical Society*, 1940, **62**, 1723-1732.
54. N.A. Ramsahye, T.K. Trung, S. Bourrelly, Q. Yang, T. Devic, G. Maurin, P. Horcajada, P.L. Llewellyn, P. Yot, C. Serre, Y. Filinchuk, F. Fajula, G. Férey and P. Trens, *The Journal of Physical Chemistry C*, 2011, **115**, 18683-18695.
55. G. Ferey, C. Serre, T. Devic, G. Maurin, H. Jobic, P.L. Llewellyn, G. De Weireld, A. Vimont, M. Daturi and J.-S. Chang, *Chemical Society Reviews*, 2011, **40**, 550-562.
56. A.J. Fletcher, E.J. Cussen, T.J. Prior, M.J. Rosseinsky, C.J. Kepert and K.M. Thomas, *Journal of the American Chemical Society*, 2001, **123**, 10001-10011.
57. K.S. Walton, A.R. Millward, D. Dubbeldam, H. Frost, J.J. Low, O.M. Yaghi and R.Q. Snurr, *Journal of the American Chemical Society*, 2008, **130**, 406-407.
58. L. Alaerts, M. Maes, L. Giebeler, P.A. Jacobs, J.A. Martens, J.F.M. Denayer, C.E.A. Kirschhock and D.E. De Vos, *Journal of the American Chemical Society*, 2008, **130**, 14170-14178.
59. P.L. Llewellyn, G. Maurin, T. Devic, S. Loera-Serna, N. Rosenbach, C. Serre, S. Bourrelly, P. Horcajada, Y. Filinchuk and G. Férey, *Journal of the American Chemical Society*, 2008, **130**, 12808-12814.
60. M. Vougo-Zanda, J. Huang, E. Anokhina, X. Wang and A.J. Jacobson, *Inorganic Chemistry*, 2008, **47**, 11535-11542.
61. L. Chen, J.P.S. Mowat, D. Fairen-Jimenez, C.A. Morrison, S.P. Thompson, P.A. Wright and T. Düren, *Journal of the American Chemical Society*, 2013, **135**, 15763-15773.
62. I. Nevjestić, H. Depauw, P. Gast, P. Tack, D. Deduytsche, K. Leus, M. Van Landeghem, E. Goovaerts, L. Vincze, C. Detavernier, P. Van Der Voort, F. Callens and H. Vrielinck, *Physical Chemistry Chemical Physics*, 2017, **19**, 24545-24554.
63. F. Millange, C. Serre and G. Ferey, *Chemical Communications*, 2002, **0**, 822-823.
64. T.R. Whitfield, X. Wang, L. Liu and A.J. Jacobson, *Solid State Sciences*, 2005, **7**, 1096-1103.
65. N.A. Ramsahye, G. Maurin, S. Bourrelly, P. Llewellyn, T. Loiseau and G. Ferey, *Physical Chemistry Chemical Physics*, 2007, **9**, 1059-1063.
66. N.A. Ramsahye, G. Maurin, S. Bourrelly, P.L. Llewellyn, C. Serre, T. Loiseau, T. Devic and G. Férey, *The Journal of Physical Chemistry C*, 2008, **112**, 514-520.

67. A. Vimont, A. Travert, P. Bazin, J.-C. Lavalley, M. Daturi, C. Serre, G. Férey, S. Bourrelly and P.L. Llewellyn, *Chemical Communications*, 2007, 3291-3293.
68. P. Mishra, S. Edubilli, H.P. Uppara, B. Mandal and S. Gumma, *Langmuir*, 2013, **29**, 12162-12167.
69. P. Mishra, H.P. Uppara, B. Mandal and S. Gumma, *Industrial & Engineering Chemistry Research*, 2014, **53**, 19747-19753.
70. S. Couck, J.F.M. Denayer, G.V. Baron, T. Rémy, J. Gascon and F. Kapteijn, *Journal of the American Chemical Society*, 2009, **131**, 6326-6327.
71. K. Leus, T. Bogaerts, J. De Decker, H. Depauw, K. Hendrickx, H. Vrielinck, V. Van Speybroeck and P. Van Der Voort, *Microporous and Mesoporous Materials*, 2016, **226**, 110-116.
72. L. Hamon, P.L. Llewellyn, T. Devic, A. Ghoufi, G. Clet, V. Guillerm, G.D. Pirngruber, G. Maurin, C. Serre, G. Driver, W. van Beek, E. Jolimaître, A. Vimont, M. Daturi and G. Férey, *Journal of the American Chemical Society*, 2009, **131**, 17490-17499.
73. A.U. Ortiz, M.-A. Springuel-Huet, F.-X. Coudert, A.H. Fuchs and A. Boutin, *Langmuir*, 2012, **28**, 494-498.
74. M.-A. Springuel-Huet, A. Nossov, Z. Adem, F. Guenneau, C. Volkringer, T. Loiseau, G. Férey and A. Gédéon, *Journal of the American Chemical Society*, 2010, **132**, 11599-11607.
75. B. Seoane, S. Sorribas, Á. Mayoral, C. Téllez and J. Coronas, *Microporous and Mesoporous Materials*, 2015, **203**, 17-23.
76. P. Serra-Crespo, A. Dikhtiarenko, E. Stavitski, J. Juan-Alcaniz, F. Kapteijn, F.-X. Coudert and J. Gascon, *CrystEngComm*, 2015, **17**, 276-280.
77. T. Loiseau, C. Mellot-Draznieks, H. Muguerra, G. Férey, M. Haouas and F. Taulelle, *Comptes Rendus Chimie*, 2005, **8**, 765-772.
78. C. Nanthamathee, S. Ling, B. Slater and M.P. Attfield, *Chemistry of Materials*, 2015, **27**, 85-95.
79. Y. Wu, A. Kobayashi, G.J. Halder, V.K. Peterson, K.W. Chapman, N. Lock, P.D. Southon and C.J. Kepert, *Angewandte Chemie*, 2008, **120**, 9061-9064.
80. N. Lock, Y. Wu, M. Christensen, L.J. Cameron, V.K. Peterson, A.J. Bridgeman, C.J. Kepert and B.B. Iversen, *The Journal of Physical Chemistry C*, 2010, **114**, 16181-16186.
81. A.E.J. Hoffman, L. Vanduyfhuys, I. Nevjestić, J. Wieme, S.M.J. Rogge, H. Depauw, P. Van Der Voort, H. Vrielinck and V. Van Speybroeck, *The Journal of Physical Chemistry C*, 2018, **122**, 2734-2746.
82. S. Biswas, T. Ahnfeldt and N. Stock, *Inorganic Chemistry*, 2011, **50**, 9518-9526.

3 *Bimetallic MOFs*

Bimetallic MOFs create the advantage of including more than one ion in a single crystal. In first place, this chapter describes the synthesis strategies to obtain bimetallic MOFs. The second part summarizes the state-of-the-art research concerning CO_2 adsorption in bimetallic MOFs.

Introducing different functional groups is more straightforward in MOFs than in other inorganic structures due to the presence of organic moieties, suitable to anchor any type of chemical group. This functional group anchoring is realized by pre-functionalization or executed *via* a post-synthetic modification. [1] Also the metal node plays an important role and can act as a proper functionality. The diversity and flexibility in MOF design and synthesis gives the unique opportunity to create frameworks with more than one metal in the framework.

The incorporation of two or more metal nodes in close neighbourhood in the same framework can create a synergistic effect which may enhance the MOFs intrinsic properties. Using this approach an extra degree of freedom is created which allows to tailor the structure towards a desired application. An example is the optimization of a sorbent by tuning the pore size, *via* the incorporation of smaller or larger metal ions. Bi- or even multimetallic catalyst in cascade or tandem reactions can result in a process intensification. Meanwhile, the doping of secondary metals ions into a crystalline matrix of metal oxides may have a beneficial effect on the optical, electronic and magnetic properties. [2]

The field of mixed-metal MOFs is innovative and a very hot topic, however, the research field is rather unorganized and a complete overview is non-existing. Nevertheless, there are a few highly recommended reviews which focus on three main topics: catalysis [3], adsorption [2] and transmetallation. [4] Furthermore, bimetallic frameworks have already been described in patent literature by the chemical company BASF. [5] Table A1 in the addendum of this dissertation supplies the reader with an overview of existing bimetallic and multimetallic frameworks. The table is organized *via* the well-known

MOF families (MIL, UiO, MOF, ZIF, HKUST), supplemented with frameworks that do not belong to these categories.

The complexity of synthesizing bimetallic MOFs and the limitation of current characterization techniques at present still leaves different important issues unanswered. Especially the possibility of preferential arrangement at the core or on the external surface of the crystal due to different crystallization rates is barely mentioned and in literature not yet properly investigated. To prove homogeneous incorporation of both metal ions is, without any doubt, challenging. Researchers use multiple techniques to convince that in their work the created framework is completely homogeneous. Few articles state the possibility of clustering or inhomogeneous zones. Most of the described characterization techniques used merely give an indication of homogeneous dispersion but are mostly not reliable enough to completely answer this question. Electron paramagnetic resonance (EPR), electron nuclear double resonance (ENDOR), Mössbauer spectroscopy and bright-field scanning transmission electron microscopy-energy dispersive X-ray spectroscopy (BF-STEM EDX) are the most reliable techniques. However, application of only one of these techniques may still leave ambiguity, whereas a combination of these techniques delivers the most powerful proof

3.1 Synthetic strategies for the preparation of bimetallic MOFs

A first synthesis method is schematically shown in Figure 3.1 (top): the "**one-pot**" also called "**one step**" reaction. This method has been widely used for preparing bimetallic MOFs. The direct synthesis of bimetallic frameworks is still a "black box" compared to the monometallic synthesis design where a lot of parameters are known that influence the structural design. Using metals with the same ionic charge and radius is expected to increase the chance of obtaining homogeneous and equally possible co-incorporation of both metals. Critical information like crystal nucleation and growth speed is not available, yet indispensable for further progress in this field. Detailed information about different synthesis methods can be found in Chapter 1, merely MW and SOL methods have been used to obtain bimetallic MOFs. The concept of a one-pot reaction seems simple, however, there are considerable challenges. The incorporation of a new, secondary metal node often yields fragile frameworks, this route is synthetically not possible or it creates unexpected topologies and functionalities. [2, 6]

A second method is the "**post-synthetic modification (PSM)**" (Figure 3.1, bottom).The major advantage is a reliable synthesis method of the single MOF *via* a known recipe, resulting in a framework with high crystallinity. In a second step, a complete or partial replacement of a metal ion in the framework takes place. Different routes and variable parameters are reported, from room to elevated temperature, *via* SOL or MW incubation. Multiple solvents are applied as a mother liquid to perform this metal exchange e.g., DMF, H_2O, methanol and DMSO. It is illustrated that the solvent influences the cation exchange speed and mechanism, so it is a crucial factor that determines the final ratio of exchange. [7]

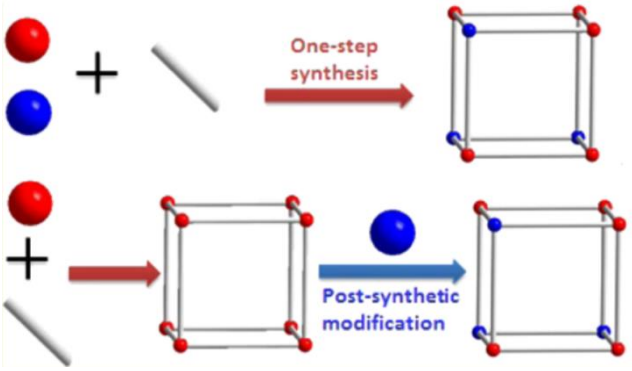

Figure 3.1 Overview of the synthesis methods to create bimetallic metal-organic frameworks: (top) one-step direct synthesis, (bottom) post-synthetic modification. (Reproduced from reference [2])

Recently the PSM has been exploited to create MOFs which are impossible to synthesize or have an extremely low yield by one-pot synthesis. [8-14] Important challenges for a successful exchange are large kinetic barriers, diffusion problems due to ultrafine pores, steric hindrance as well as confinement in unusual topologies. This method results frequently in semi-exchanged MOFs. Nevertheless a limited exchange already creates potential for gas storage, separation and catalysis. [2, 6]

A third pathway is "**the mixing of synthesized MOFs**". This was reported for MIL-53(Al)-Br and MIL-53(Fe)-Br. [15] These two monometallic MOF structures incubated in water at 85 °C result in the bimetallic MIL-53(Al/Fe)-Br compound mixed with leftovers of non-exchanged MIL-53(Al)-Br and MIL-53(Fe)-Br. Reports about this method are very scarce at present.

3.2 CO_2 and temperature flexibility in bimetallic MOFs

Reviews about the adsorption capacity of mono-metallic frameworks are widely known [16-19] and state-of-the-art frameworks are described in Chapter1. Nevertheless, for bimetallic frameworks a general overview of adsorption uptake for different materials is still missing. An attempt to compare different materials can be found in a paper of Spanopoulos *et al*. [20] Comparing the adsorption capacity is important to gain knowledge about these frameworks and may guide further material optimization. The different apparatus to determine the adsorption capacity are summarized in Chapter 2, paragraph 2.1.3.

Figure 3.2 summarizes the top class frameworks for CO_2 adsorption for both mono- and bimetallic frameworks at 273 K and 298 K. This graphical representation is divided in three parts: part one (normal labeling) are the top-class mono-metallic frameworks. A second part (with bold labels) are the bimetallic frameworks with the highest reported adsorption capacity of CO_2; and a third part (with green labels) are the mono-metallic representatives of the bimetallic frameworks used in this dissertation. In the next paragraph, we will discuss the most remarkable bimetallic frameworks in carbon dioxide adsorption. The frameworks will be classified according to their MOF family, and each of these frameworks can also be found back in the overview Table A1 of the addendum.

In the next paragraphs several interesting bimetallic MOFs will be discussed that are relevant in relation with this work. As relevant application only MOFs with the topic "temperature flexibility" or CO_2 are discussed:

MIL-53(Al/V), **MIL-53 (Cr/Fe)** and **MIL-53 (Fe/V)**: The MIL-53 series, as described in Chapter 1 and 2 , is known for their breathing behaviour. One of the most investigated structures in this series is the aluminium variant MIL-53(Al). Since the development of MIL-53(Al) in 2004, more than 250 papers have been published about this structure and its functionalized variants.

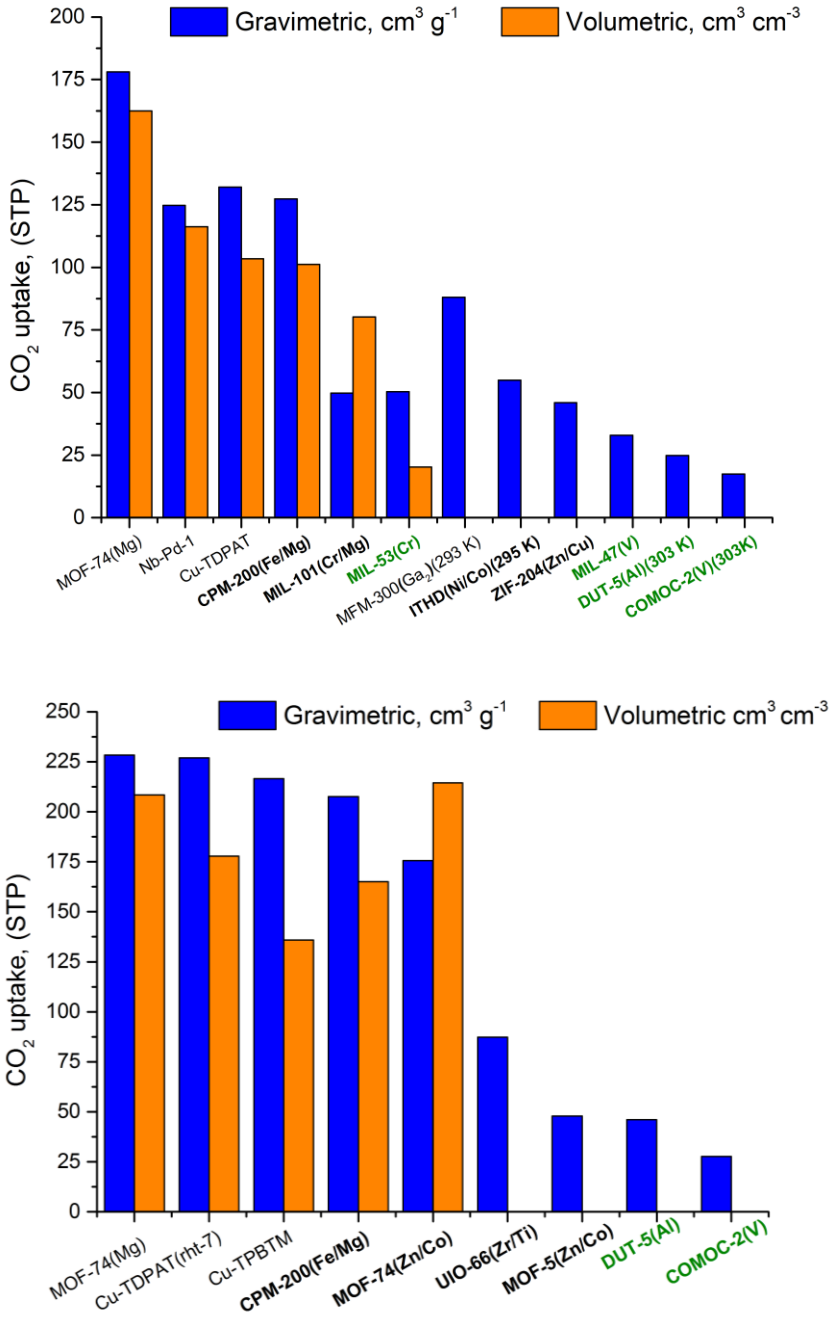

Figure 3.2 Comparison of the gravimetric (blue) and volumetric (orange) CO_2 uptake at (top) 298 K and (bottom) 273 K between 0 to 1 bar for the bimetallic MOFs (bold) and monometallic frameworks (green) used in this work. (Based on reference [20])

Kozachuk *et al*. [21] developed a series of bimetallic **MIL-53(Al/V)** = $[Al(OH)_{1-x}(VO)_xBDC]_n$. The gradual transformation from the complete flexible structure MIL-53(Al) to a stiff MIL-47(V^{IV}) framework was evaluated v*ia* CO_2 sorption measurements, and the result is shown in Figure 3.3, top. The dark green isotherm of MIL-53(Al) follows a step-wise adsorption, characteristic for a flexible material, whereas the rigid MIL-47(V) (black line) is marked by a type I Langmuir isotherm. The step-wise adsorption diminishes gradually by replacing $(Al(OH))^{2+}$ by $(VO)^{2+}$. The borderline for flexibility, characterized by the transformation from a stepped to a complete type I isotherm, is localized between x = 68-87 mol% of vanadium. This example demonstrates that incorporation of $(VO)^{2+}$ metal nodes in the MIL-53(Al) structure can be used to fine tune the breathing properties of the resulting material. [21]

Nouar *et al.* [22]reported the replacement of 40% of $Cr^{III}(OH)$ by $Fe^{III}(OH)$ in the MIL-53(Cr) structure, resulting in a **MIL-53(Cr/Fe)** framework. This substitution of the central metal ion has a major influence on the breathing behaviour, illustrated in Figure 3.3, (bottom) and is significantly different from the mono-metallic Cr or Fe frameworks which are discussed in Chapter 1 and 2. The adsorption steps of **MIL-53(Cr/Fe)** do not match those for the single cation phase neither for the theoretical mixture. The dehydrated bimetallic solid **MIL-53(Cr/Fe)** is at the start of the analysis in the **cp** form and a two-step transformation takes place, associated with the adsorption of CO_2, from the **cp** over the **np-CO_2** to a final **lp-CO_2** state. The reopening of the framework, related with the transition from **np-CO_2** to **lp-CO_2**, is shifted from ±3 bar for pure Cr to ± 10 bar for the Cr-Fe framework. This shift indicates that the bimetallic structure is slightly more rigid than the MIL-53(Cr) framework but the lattice is more flexible in comparison with MIL-53(Fe), see Chapter 2, section 2.5.1.4. This mixed-metal approach changes significantly the breathing pattern of the original framework and the MOF behaves as an intermediate between the Cr and Fe based compounds. Extensive research on the use of different metal loadings would provide a better understanding on this remarkable evolution: how the structure evolves from a pure Fe containing framework, over the bimetallic MOF towards the pure Cr variant. [22]

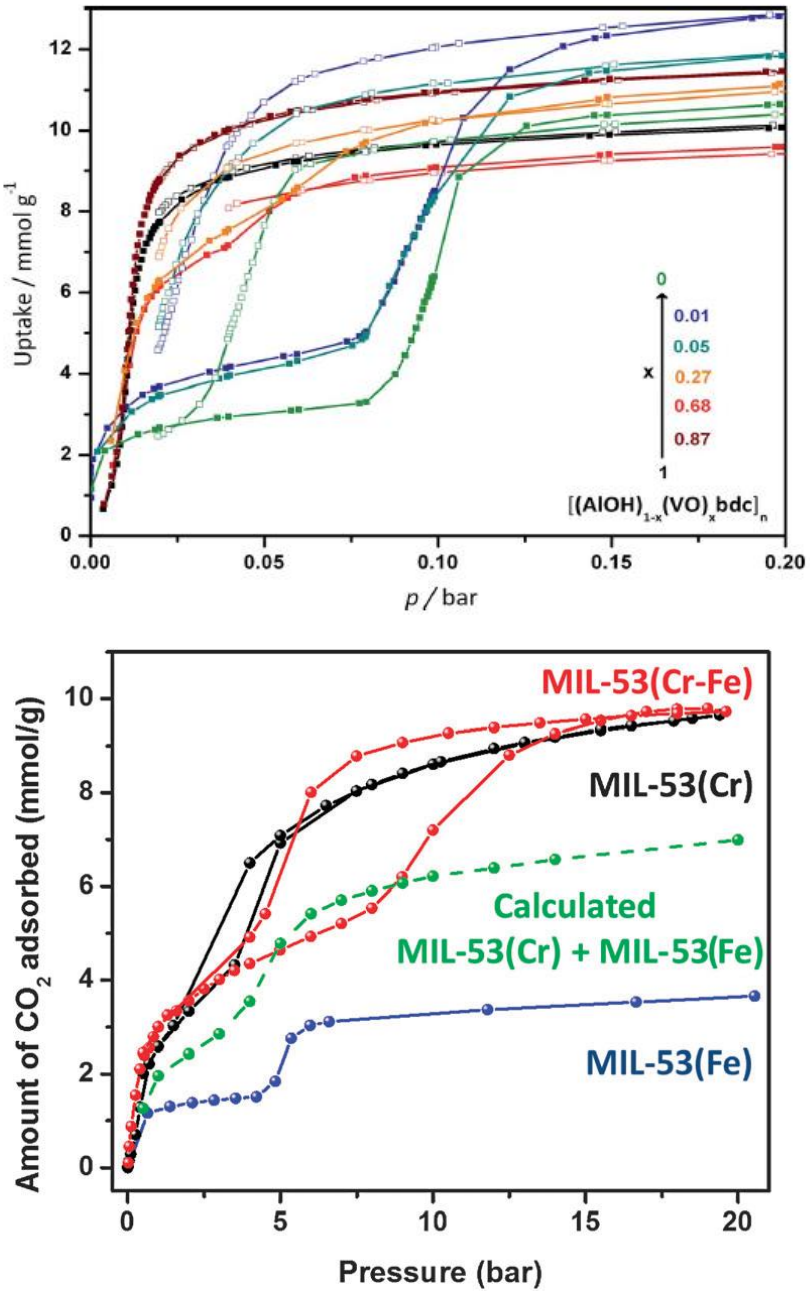

Figure 3.3 (top) Representation of CO_2 sorption isotherms (195 K) of $[(AlOH)_{1-x}(VO)_xBDC]_n$ and the parent monometallic MOFs in the 0-0.2 bar region. Open and closed symbols represent adsorption and desorption, respectively. (bottom) CO_2 sorption isotherms at 283 K for the MIL-53 materials with M-Fe (blue); M-Cr (black); M-Cr/Fe (60%/40%) (red) and calculated M-Cr/Fe (60%/40%) (green). (Reproduced from references [21] and [22])

Temperature dependent XRPD measurements reveal critical information about the breathing pattern of bimetallic frameworks. Besides the CO_2 adsorption, Serre's group also investigated the flexibility by temperature dependent XRPD for Fe/Cr cation containing structures. This bimetallic framework is after hydration the **np-h** form, in a similar way as the monometallic Cr solid. The temperature induced transition of **MIL-53(Cr/Fe)**, upon increased temperature, occurs in a two-step process. A first step around 343 K leads to a **cp**, followed by a final thermal reopening at 463 K to a **lp** state. The XRPD pattern showing this transition is presented in Figure 3.4. This behaviour is rather identical to MIL-53(Ga) with the exception that the Ga compound transforms to a **np-d** state instead of a **cp** form. [23] A description of this thermal behaviour can be found in Chapter 2, Figure 2.6 and 2.7. [22]

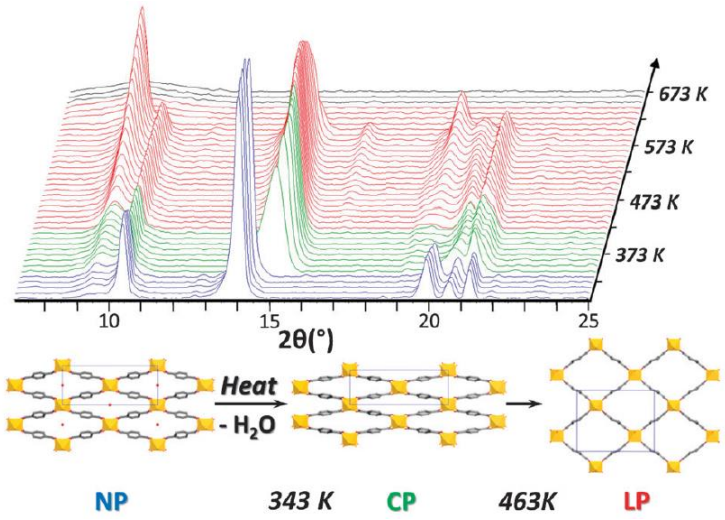

Figure 3.4 (top) Temperature dependent X-ray diffraction patterns and (bottom) schematic representation of the states of MIL-53(Cr/Fe) upon heating. (Reproduced from reference [22])

Breeze *et al*. observed that the thermal response behaviour of **MIL-53(Fe/V)** [24] is different depending on the Fe/V ratio. The Fe-rich structure MIL-53($Fe^{II}_{0.74}V^{III}_{0.26}$) transforms during activation from the **as** to a **lp** form. Subsequent cooling to RT under ambient conditions leads to a **np-h**, with identical lattice parameters as the hydrated MIL-53(Fe) [25] (Figure 3.5). Important here is that the flexible behaviour is similar as previously examined for MIL-53(Cr) [26] or MIL-53(Al) [27] but differs from that of MIL-53(Fe). However, when the ratio of Fe/V is decreased to 1, the structure MIL-

53($Fe^{II}_{0.49}V^{III}_{0.51}$) acts like an analogue of MIL-47(V^{IV}) [6] and stays in a rigid **lp** form after activation and subsequent cooling to RT under ambient conditions. Although X-ray absorption near edge structure (XANES) measurements indicate that the oxidation state is close to +III, the authors suggest that sufficient tetravalent vanadium (V^{IV}=O) groups should be present to force and maintain the structure in this fully open **lp** form.

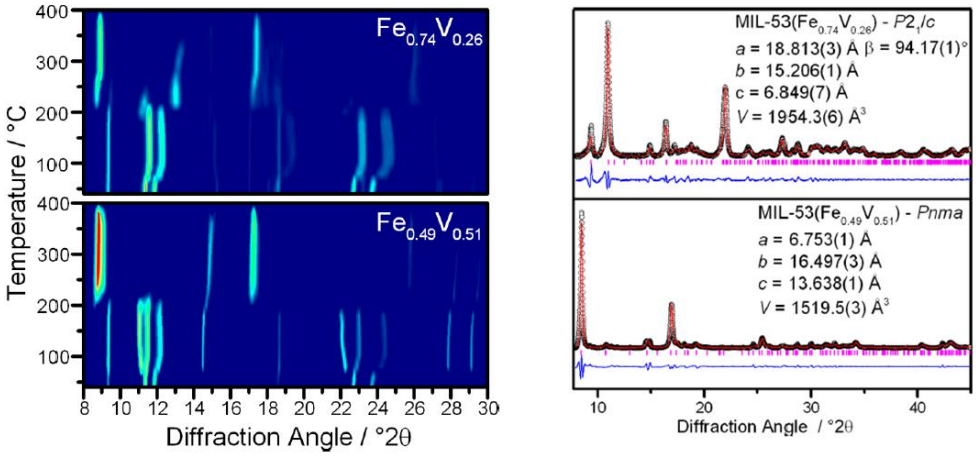

Figure 3.5 (left) Temperature variation of XRPD patterns of MIL-53 (Fe^{II}/V^{III}) upon heating; (right) room temperature XRPD patterns of MIL-53 (Fe^{II}/V^{III}) calcined at 573 K. (Reproduced from reference [24])

MIL-101(Cr/Mg): MIL-101(Cr) has drawn much attention due to its high chemical and moisture stability in comparison with other MOFs. [28] A novel bimetallic structure MIL-101(Cr/Mg) [29] was successfully obtained *via* a one pot synthesis adding dopant magnesium to the synthesis of MIL-101(Cr). Upon magnesium incorporation, the exceptional moisture stability is sustained. The bimetallic MOF has the advantage of having unsaturated magnesium sites, and already at a very low Mg concentration (0.023 to 0.052 at% Mg), a higher adsorption capacity is observed along with stronger adsorptive sites for CO_2. Temperature dependent desorption (TPD) of CO_2 shows that MIL-101(Cr) has only one desorption peak at 315 K, originating from the coordination of CO_2 at unsaturated Cr-sites. Meanwhile when Mg is incorporated, a second more stable desorption occurs at 340 K at the Mg unsaturated sites. Moreover, the increase in isosteric heat, employed to express the interaction between adsorbate and adsorbent, is a second direct indication that the incorporation of Mg increases the interaction of the framework with the adsorbent CO_2. The incorporation of Mg^{2+} results in a 44 % enhancement of CO_2 adsorption up to a capacity of 3.28 mmol g^{-1} at 298 K and 1 bar.

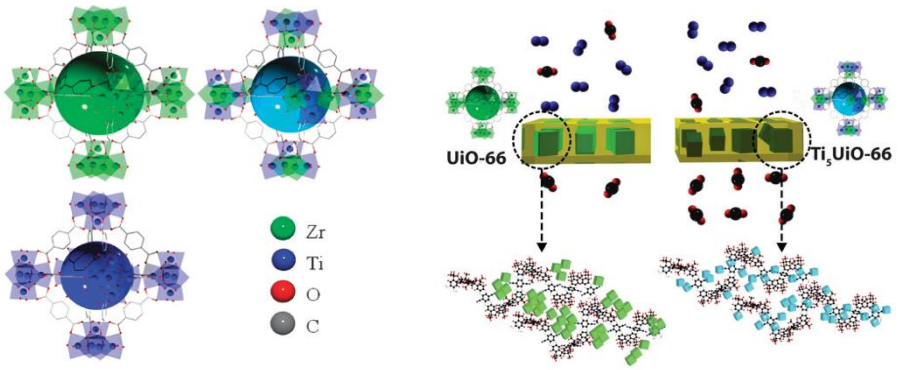

Figure 3.6 (left) The Zr(IV)-based metal-organic framework UiO-66 can undergo post-synthetic exchange with Ti(IV) to deliver heterometallic MOFs, with a decreased size of the octahedral cages. (right) Ti-exchange of UiO-66 MOF increases the interaction with PIM-1 polymer, leading to a drastic increase in CO_2 permeability in comparison to a UiO-66-PIM-1 membrane. (Reproduced from reference [30])

UiO-66 (Zr/Ti): Hon Lau *et al*. observed that the CO_2 uptake on the zirconium MOF UiO-66, modified *via* a post-synthetic exchange with Ti(IV) was significantly enhanced. This capacity increases with 82 % from 2.2 mmol g^{-1} to 4 mmol g^{-1} at a loading of 56 at% Ti. [31] A general picture of the bimetallic framework is presented in Figure 3.6, (left). The BET surface area and the pore volume is in general higher for the Ti-exchanged UiO-66 compared to the parent UiO-66(Zr). Replacing heavy (e.g., Zr) by lighter (e.g., Ti) ions, can explain an increase in specific surface area as this is calculated per gram of material. The additional enhancement in pore volume might originate from a contribution of the interstitial spaces. At the other hand the shorter Ti-O compared to Zr-O bonds, diminishes the pore size of the octahedral cages resulting in a stronger binding environment for CO_2. Besides the smaller cages, two other main factors explain this vast increase in S_{BET}: (1) the inherent stronger adsorption characteristics of Ti(IV) and (2) the charge transfer towards the ligand by replacing Zr(IV) by Ti(IV). The combination of these factors explain the enhanced uptake and enthalpy increase of ~10 kJ mol^{-1}.

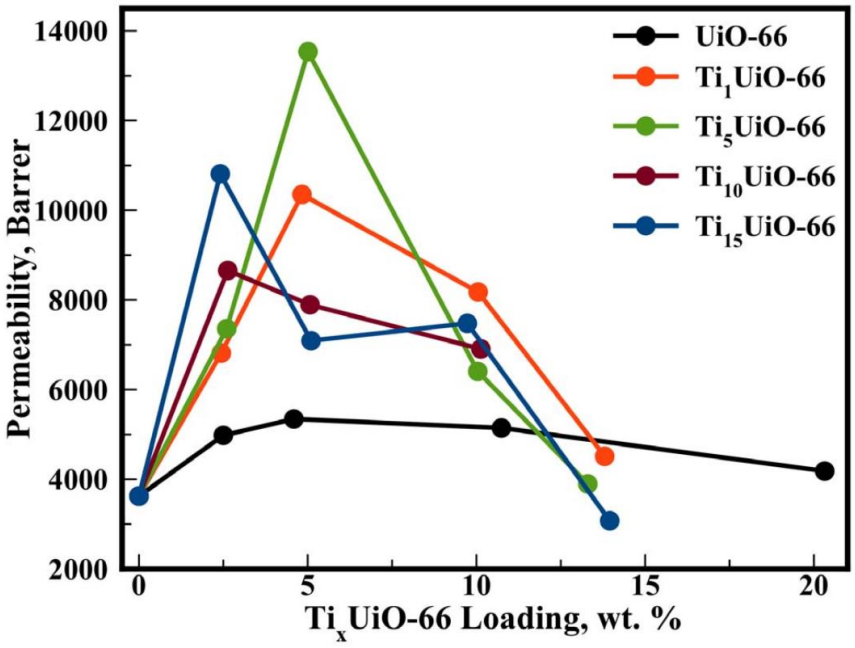

Figure 3.7 CO_2 permeability of PIM-1 Ti_xUiO-66 mixed matrix membranes. (Reproduced from reference [30])

Smith *et al.* [30] proposed transmetallation of MOFs as a route to improve the CO_2 permeability and selectivity of a mixed matrix membrane. An overview picture of this approach can be seen in Figure 3.6, (right). The incorporation of a post-synthetic Ti-exchanged UiO-66 framework in a polymeric membrane PIM-1 (PIM = polymer of intrinsic microporosity) was performed. As can be seen from Figure 3.7, different wt% of Ti_xUiO-66 are incorporated in the PIM-1 membrane, with X = 1, 2, 5, 15 representing the days that the UiO-66(Zr) MOF was incubated with a Ti-precursor. *Via* this approach the gas permeability tripled without loss in selectivity. The doped membrane shows in comparison with the pure polymeric PIM-1 an outstanding performance. It only contains 5 wt% Ti-MOF, but nevertheless the doped membrane generates a 153% increase of CO_2 permeability compared to PIM-1 with 5 wt% UiO-66 and a 274% increase towards the pure polymeric PIM-1 membrane. The significant increase of permeability at an optimal loading of 5 wt% MOF. This was according to the authors, related to the stronger interaction between the Ti_xUiO-66's exposed metal centres and the polymer PIM-1. This approach creates an interfacial free volume resulting in a decrease in density.

MOF-74(Zn/Co): The MOF-74(M) (M = Mg, Zn, Co, Ni) [32], also known as M-CPO-27 (CPO = coordination polymer of Oslo) or M_2(DOBDC) is a very promising material for CO_2 collection due to the high density of the coordinated unsaturated sites (CUS). In this prospect a simultaneous incorporation of Zn and Co ions into MOF-74 was developed to raise the adsorption capacity. [33] Using a static gravimetric analyser up to 10 bar at 298 K, the CO_2 adsorption capacity upsurges with 10 % when performing a transmetallation of 14 wt% of zinc by cobalt in the MOF-74(Zn). The incorporation of Co brings along a decrease in temperature stability from 352 °C to 230 °C.

MOF-5(Zr/Co): The zirconium MOF-5 was one of the first MOFs reported to be stable after activation and solvent removal. [34] In the adsorption range of 0-1 bar and doping MOF-5(Zr) with 21 wt% Co, the doping appears to have no significant influence on the adsorption capacity, which is in sharp contrast with the enhanced uptake of Co-doped MOF-74(Zn). A remarkable sudden contribution to the adsorption capacity in Co-MOF-5 is observed at 4 bar. The authors assign this slope change to a certain framework flexibility of the bimetallic MOF-5 structure, produced by Co incorporation which

breaks the highly-ordered distribution of metal clusters in the non-doped MOF-5 material. [33]

ZIF-204(Zn/Cu): A series of three bimetallic Zn/Cu ZIF frameworks, termed ZIF-202, ZIF-203 and ZIF-204, are constructed. The zeolite-like frameworks ZIF-203 and ZIF-204 arise from combining square planar CuN_4 with tetrahedral ZnN_4 units, while ZIF-202 is a combination of the tetrahedral ZnN_4 and linear CuN_2. Only ZIF-204 was examined as adsorbent, where this framework has a final composition of [Zn_2Cu_3(imidazolate)$_{10}$], and has proven to be chemically (pH 4-12) and water stable. The structure demonstrates a final volumetric adsorption capacity of 0.083 g g^{-1} (1.88 mmol g^{-1}, 7.7 wt%) at 298 K and 1 bar. The highly porous structures demonstrate enhanced selectivity of CO_2 over CH_4. Analysing the isotherms of CO_2 and CH_4, and applying Henry's law, a selectivity of 4.6 CO_2/CH_4 can be derived. [35]

Table 3.1 CO_2 uptake of different mono- and bimetallic MOFs

CPM-200(Fe/Mg)	
273K	207.6 cm^3/g
298 K	127.3 cm^3/g
NbO-Pd-1	
273 K	201.8 cm^3/g
298 K	124.8 cm^3/g
Ni-ITHD(Ni/Co)	
295 K	54.94 cm^3/g
MOF-74(Mg)	
273 K	228.3 cm^3/g
298 K	178.1 cm^3/g

Despite the possible applications and their structural diversity, mixed-metal frameworks have unexplored opportunities, moreover the research lags far behind their monometallic counterparts. Especially the CO_2 uptake performance is barely investigated. The uptake of different mono- and bimetallic frameworks are listed in Figure 3.2. In this table four bimetallic structures show an impressive CO_2 uptake: CMP-200 (CPM = crystalline porous material) [36], NbO-Pd-1 [20], Ni-ITHD (ITHD net topology) [37]. These uptake values are amongst the highest reported for bimetallic

MOFs as CO_2 adsorbent and can even compete with one of the highest uptakes ever reported for MOFs: the monometallic MOF-74(Mg) [20]. In the next paragraph the top record for CO_2 uptake by a bimetallic MOF, CPM-200(M_1/M_2) will be discussed.

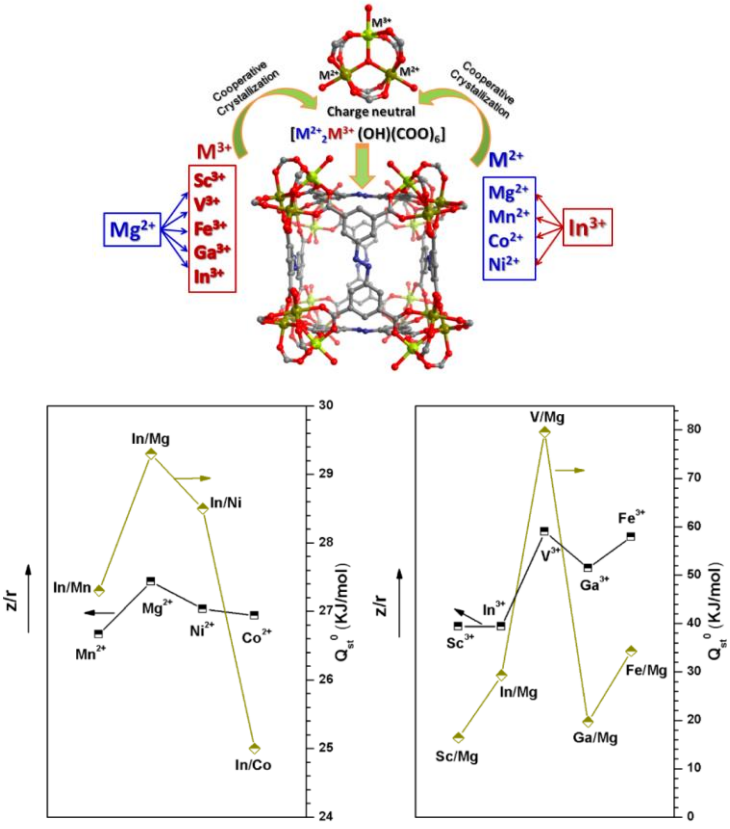

Figure 3.8 (top) M^{2+} and M^{3+} combinations for CPM-200, (bottom) Correlation between isosteric heat at zero loading of CO_2 (Qst^0) and charge-to-radius (Z/r) of metal ions for CPM-200s. (Reproduced from reference [36])

CPM-200(M_1/M_2): The group of Zhai synthesized a large series of CMPs (all reported in Figure 3.8, top). [36] They discovered that the bimetallic CMP-200(Fe/Mg) performed excellently and shows the highest CO_2 uptake out of a series of 9 heterometallic CMP-200 [$M^{II}_2M^{III}(\mu_3\text{-OH})(CO_2)_6$] frameworks, namely Fe/Mg; In/Mg; Sc/Mg; Ga/Mg; V/Mg; In/Co; In/Mn; In/Ni and In/Mg. These measurements were performed at 273 K up to 1 bar, and CPM-200(Fe/Mg) showed a superior carbon dioxide uptake of 0.41 g g^{-1} (9.27 mmol g^{-1}, 29.1 wt%). This is one of the highest uptakes

for MOFs with lewis acid sites ever reported and this approximates the uptake of MOF-74(Mg) 0.45 g g^{-1} (10.22 mmol g^{-1}, 31.0 wt%) at identical temperature and pressure.

A remarkable observation was made when the metal ion In^{3+} remained constant. In this case the CO_2 uptake of CPM-200-In/M^{2+} followed the order $Mg^{2+} > Co^{2+} > Mn^{2+} > Ni^{2+}$. At the other hand if Mg^{2+} was kept constant, uptakes of CPM-200-M^{3+} followed the order $Fe^{3+} > In^{3+} > V^{3+} > Ga^{3+} > Sc^{3+}$. By combination of different metals in "one" MOF platform, a correlation between the charge-to-radius ratios and the isosteric heat for CO_2 was established. An increase in the strength of adsorption of CO_2 is related to higher charge-to-radius values as can be seen in Figure 3.8, (bottom). The synergetic effect in the CPM-200 frameworks is responsible for the high CO_2 uptake with values close to the all-time record.

3.3 Conclusion

This chapter introduces the reader to the topic "bimetallic metal-organic frameworks". The integration of different building blocks, here metal ions which possess a similar coordination geometry and connectivity, can lead to the construction of bimetallic frameworks. In these mixed-metal solids, at least two types of different metals are combined in a single phase material. These metals can be homogenously or inhomogenously incorporated. Mixed-metal frameworks can lead to frameworks with specific adapted properties and more complex functionalities. Also the framework itself can be constructed *via* various synthetic pathways: *via* a direct route or transmetallation, using incubation, electrical or microwave heating. Conceptually it is possible to control the composition and the resulting pore dimensions, offering an extremely powerful tool to tune and adjust the physicochemical properties of a desired porous material. This already has led to reports of new materials with extremely high CO_2 adsorption capacity, and flexible structures in which the breathing behaviour differs completely from the parent monometallic structures.

With the aid of literature examples we described that it is possible to tune the flexibility of the MIL-53 materials and create a new bimetallic framework with a unique flexible behaviour.

Vanadium doping can be used to shut down the original flexibility, this was proven by two different experimental reports for MIL-53(Al/V) and MIL-53(Fe/V). Additionally, Ti(IV) incorporation in UiO-66(Zr) almost doubles the adsorption uptake.

New multimetallic structures as CPM-200(M_1/M_2), with an uptake capacity close to the track record of monometallic MOFs, show that mixed-metal MOFs can compete with their monometallic counterparts.

3.4 References

1. S.M. Cohen, *Chemical Reviews*, 2012, **112**, 970-1000.
2. X. Yang and Q. Xu, *Crystal Growth & Design*, 2017, **17**, 1450-1455.
3. A. Dhakshinamoorthy, A.M. Asiri and H. Garcia, *Catalysis Science & Technology*, 2016, **6**, 5238-5261.
4. M. Lalonde, W. Bury, O. Karagiaridi, Z. Brown, J.T. Hupp and O.K. Farha, *Journal of Materials Chemistry A*, 2013, **1**, 5453-5468.
5. Markus Schubert, Ulrich Mueller, Roger Ruetz and S. Hatscher, *Dotierte metallorganische Gerüstmaterialien*, **DE 102005053430 A1**.
6. K. Barthelet, J. Marrot, D. Riou and G. Férey, *Angewandte Chemie*, 2002, **114**, 291-294.
7. C.K. Brozek, L. Bellarosa, T. Soejima, T.V. Clark, N. López and M. Dincă, *Chemistry – A European Journal*, 2014, **20**, 6871-6874.
8. J.-H. Liao, W.-T. Chen, C.-S. Tsai and C.-C. Wang, *CrystEngComm*, 2013, **15**, 3377-3384.
9. T.K. Pal, D. De, S. Senthilkumar, S. Neogi and P.K. Bharadwaj, *Inorganic Chemistry*, 2016, **55**, 7835-7842.
10. X.-S. Wang, M. Chrzanowski, L. Wojtas, Y.-S. Chen and S. Ma, *Chemistry – A European Journal*, 2013, **19**, 3297-3301.
11. S. Das, H. Kim and K. Kim, *Journal of the American Chemical Society*, 2009, **131**, 3814-3815.
12. T.K. Pal, D. De, S. Neogi, P. Pachfule, S. Senthilkumar, Q. Xu and P.K. Bharadwaj, *Chemistry – A European Journal*, 2015, **21**, 19064-19070.
13. T.-F. Liu, L. Zou, D. Feng, Y.-P. Chen, S. Fordham, X. Wang, Y. Liu and H.-C. Zhou, *Journal of the American Chemical Society*, 2014, **136**, 7813-7816.
14. J. Park, D. Feng and H.-C. Zhou, *Journal of the American Chemical Society*, 2015, **137**, 11801-11809.
15. M. Kim, J.F. Cahill, H. Fei, K.A. Prather and S.M. Cohen, *Journal of the American Chemical Society*, 2012, **134**, 18082-18088.
16. J. Yu, L.-H. Xie, J.-R. Li, Y. Ma, J.M. Seminario and P.B. Balbuena, *Chemical Reviews*, 2017, **117**, 9674-9754.
17. A. Alonso, J. Moral-Vico, A. Abo Markeb, M. Busquets-Fité, D. Komilis, V. Puntes, A. Sánchez and X. Font, *Science of The Total Environment*, 2017, **595**, 51-62.
18. J.-R. Li, Y. Ma, M.C. McCarthy, J. Sculley, J. Yu, H.-K. Jeong, P.B. Balbuena and H.-C. Zhou, *Coordination Chemistry Reviews*, 2011, **255**, 1791-1823.
19. Y. Lin, C. Kong, Q. Zhang and L. Chen, *Advanced Energy Materials*, 2017, **7**, 1-29.

20. I. Spanopoulos, I. Bratsos, C. Tampaxis, D. Vourloumis, E. Klontzas, G.E. Froudakis, G. Charalambopoulou, T.A. Steriotis and P.N. Trikalitis, *Chemical Communications*, 2016, **52**, 10559-10562.
21. O. Kozachuk, M. Meilikhov, K. Yusenko, A. Schneemann, B. Jee, A.V. Kuttatheyil, M. Bertmer, C. Sternemann, A. Pöppl and R.A. Fischer, *European Journal of Inorganic Chemistry*, 2013, **2013**, 4546-4557.
22. F. Nouar, T. Devic, H. Chevreau, N. Guillou, E. Gibson, G. Clet, M. Daturi, A. Vimont, J.M. Greneche, M.I. Breeze, R.I. Walton, P.L. Llewellyn and C. Serre, *Chemical Communications*, 2012, **48**, 10237-10239.
23. C. Volkringer, T. Loiseau, N. Guillou, G. Ferey, E. Elkaim and A. Vimont, *Dalton Transactions*, 2009, **12**, 2241-2249.
24. M.I. Breeze, G. Clet, B.C. Campo, A. Vimont, M. Daturi, J.-M. Grenèche, A.J. Dent, F. Millange and R.I. Walton, *Inorganic Chemistry*, 2013, **52**, 8171-8182.
25. F. Millange, N. Guillou, R.I. Walton, J.-M. Greneche, I. Margiolaki and G. Ferey, *Chemical Communications*, 2008, 4732-4734.
26. C. Serre, F. Millange, C. Thouvenot, M. Noguès, G. Marsolier, D. Louër and G. Férey, *Journal of the American Chemical Society*, 2002, **124**, 13519-13526.
27. T. Loiseau, C. Serre, C. Huguenard, G. Fink, F. Taulelle, M. Henry, T. Bataille and G. Férey, *Chemistry-A European Journal*, 2004, **10**, 1373-1382.
28. S. Bhattacharjee, C. Chen and W.-S. Ahn, *RSC Advances*, 2014, **4**, 52500-52525.
29. Z. Zhou, L. Mei, C. Ma, F. Xu, J. Xiao, Q. Xia and Z. Li, *Chemical Engineering Science*, 2016, **147**, 109-117.
30. S.J. Smith, B.P. Ladewig, A.J. Hill, C.H. Lau and M.R. Hill, *Scientific reports*, 2015, **5**, 1-6.
31. C. Hon Lau, R. Babarao and M.R. Hill, *Chemical Communications*, 2013, **49**, 3634-3636.
32. J. Xu, R. Sinelnikov and Y. Huang, *Langmuir*, 2016, **32**, 5468-5479.
33. J.A. Botas, G. Calleja, M. Sánchez-Sánchez and M.G. Orcajo, *International Journal of Hydrogen Energy*, 2011, **36**, 10834-10844.
34. H. Li, M. Eddaoudi, M. O'Keeffe and O.M. Yaghi, *Nature*, 1999, **402**, 276-279.
35. N.T.T. Nguyen, T.N.H. Lo, J. Kim, H.T.D. Nguyen, T.B. Le, K.E. Cordova and H. Furukawa, *Inorganic Chemistry*, 2016, **55**, 6201-6207.
36. Q.-G. Zhai, X. Bu, C. Mao, X. Zhao and P. Feng, *Journal of the American Chemical Society*, 2016, **138**, 2524-2527.
37. X. Song, M. Oh and M.S. Lah, *Inorganic Chemistry*, 2013, **52**, 10869-10876.

4 *Discovery of a second large pore phase in a bimetallic Al/V MOF*

A new series of bimetallic COMOC-2(V)/DUT-5(Al) frameworks are developed and fully characterized. Electron paramagnetic resonance and transmission electron microscopy confirm the homogeneous dispersion of Al/V in the entire framework. The study of their flexibility by means of CO_2 pressure dependent X-ray powder diffraction and high pressure sorption reveals the co-existence of two different large and a narrow pore phase.

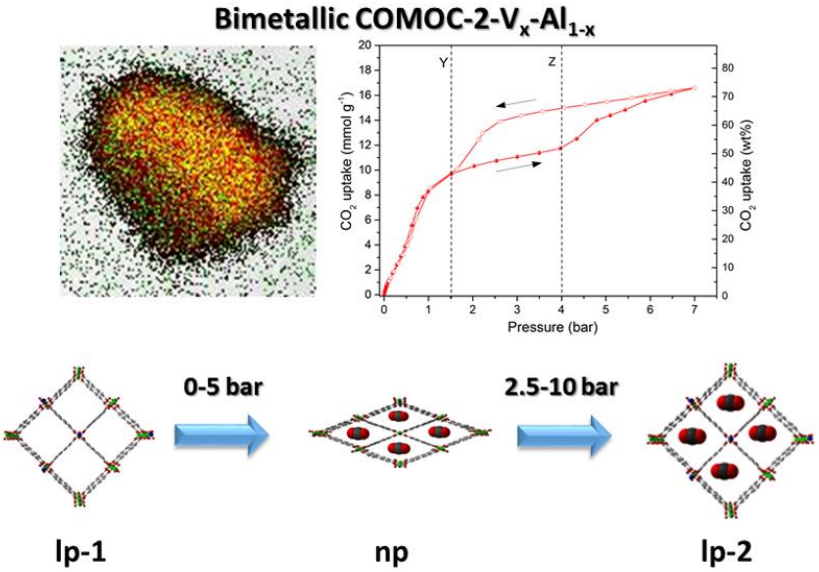

This work was published as:

Discovery of a novel, large pore phase in a bimetallic Al/V metal-organic framework. H. Depauw, I. Nevjestić, G.B. Wang, K. Leus, F. Callens, E. De Canck, K. De Buysser, H. Vrielinck, P. Van Der Voort, Journal of Materials Chemistry A, 2017, **5**, 24580-24584.

4.1 Introduction

The goal of this research is the development of a bimetallic Al/V MOF. In this study, we present for the first time, the bimetallic variant of the **COMOC-2(V)** structure, which will be denoted as **COMOC-2-V_x-Al_{1-x}**. By the gradual introduction of the dopant ion aluminium into the **COMOC-2(V)** structure, we can easily tune the breathing behaviour of the resulting materials. The state of the V ions is characterized by advanced spectroscopy and the flexible behaviour is thoroughly investigated by high-pressure synchrotron X-ray powder diffraction (XRPD) and adsorption-desorption experiments.

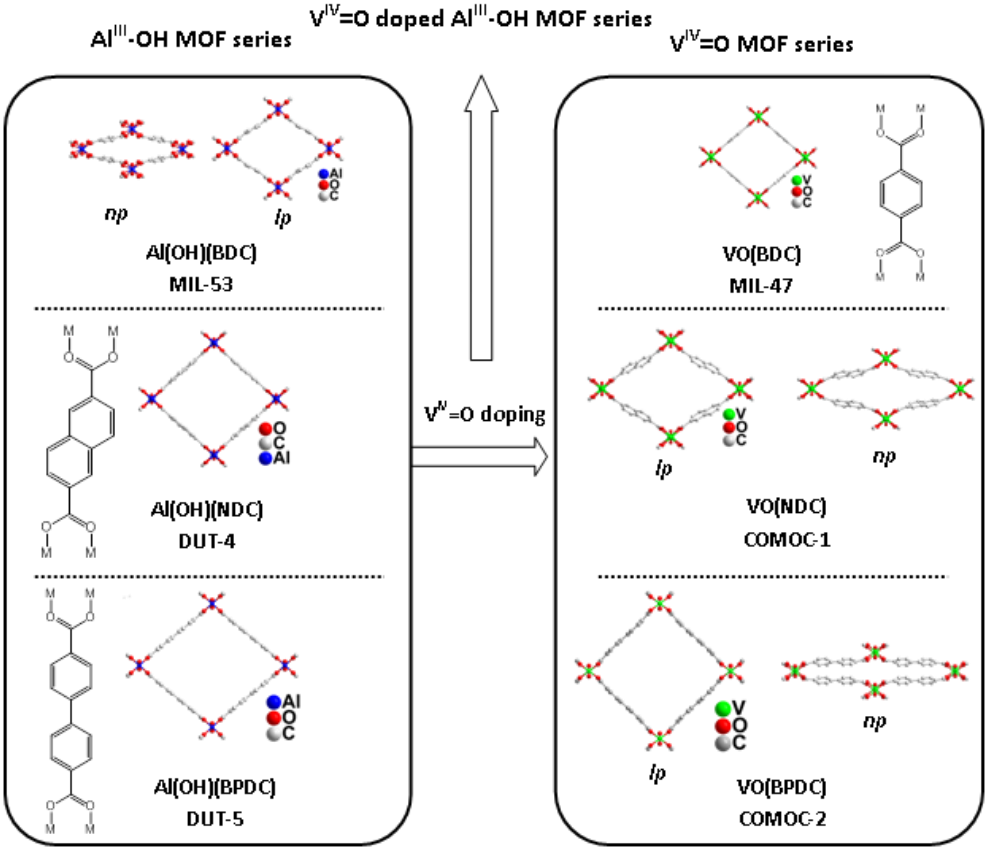

Figure 4.1 Schematic representation of doping Al^{III}-OH-MOFs with V^{IV}=O. The organic linkers used in this research along with the coordination mode (M = Al^{3+}, V^{4+}) are shown, from top to bottom: MIL-53(Al)/MIL-47(V), DUT-4(Al)/COMOC-1(V), DUT-5(Al)/COMOC-2(V).

Introducing different metal ions into one single framework offers the ability to incorporate multiple active sites to tune the framework towards a desired application. An introduction about bimetallic frameworks, we advise the reader to consult the 3th Chapter "*Bimetallic MOFs*".

The goal of the first part of this research is the synthesis optimization of a series of new bimetallic frameworks and to gain *via* metal doping insight in the flexibility of the structures. A set of six frameworks, presented in Figure 4.1, were selected to study this flexibility: MIL-53(Al)/MIL-47(V), DUT-4(Al)/COMOC-1(V) and **DUT-5(Al)/COMOC-2(V)**.

For elaborated research results on the first combination, MIL-53(Al)/MIL-47(V), we refer to the work of Pöppl and co-workers [1] and Nevjestić *et al*. [2-4] The synthesis and activation procedures of these latter materials are also documented in the dissertation of Nevjestić. [5] The second combination, DUT-4(Al)/COMOC-1(V) is not tackled in this work but would be very interesting for future research.

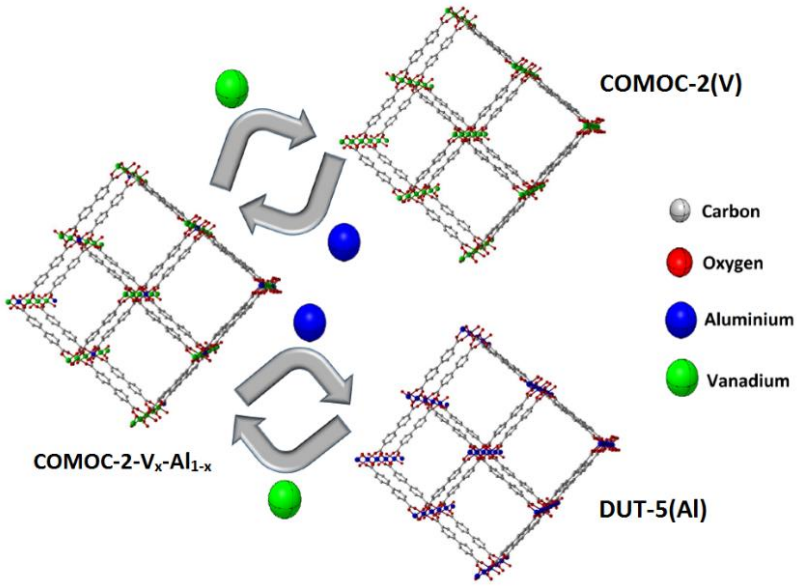

Figure 4.2 Schematic representation of COMOC-2(V) (top), mixed-metal COMOC-2-V_x-Al_{1-x} (left) and DUT-5(Al) (bottom).

The final combination **DUT-5(Al)** and **COMOC-2(V)** is elaborately discussed in this 4th Chapter. More information about these two MOFs can be found in Chapter 1, section 1.5. Figure 4.2 shows the synthesis concept behind the $[(V(O)BPDC)_x(Al(OH)BPDC)_{1-x}]$ mixed-metal series with **COMOC-2(V)** and **DUT-5(Al)** as monometallic representants.

Table 4.1 Possible state of the structure in a certain pressure range at 232 K.

		State		
Structure	**Pressure**	**lp-1**	**lp-2**	**np**
COMOC-2(V)	0-2.5 bar	✓	✗	✓
	2.5-10 bar	✓	✓	✓
COMOC-2-V_x-Al_{1-x}	0-2.5 bar	✓	✗	✓
	2.5-10 bar	✓	✓	✓

In previous studies, by Liu [6], Couck [7] and Wieme [8], two structures, a large pore (**lp**) and a narrow pore (**np**) were experimentally reported. We report here that two large pore structures (**lp-1** and **lp-2**) and a narrow pore (**np**) form, exist for the **COMOC-2(V)** framework. At 232K in vacuum, the **COMOC-2(V)** structure contains a mixture of **lp-1** and **np**. The **np** phase was found to possess a monoclinic symmetry, whereas both large pore phases exhibit an orthorhombic lattice. For the aluminium structure **DUT-5(Al)** is perpetually in the open **lp** form and possesses an orthorhombic crystal structure. [9] A summary of the possible states of the frameworks: **COMOC-2(V)**, **COMOC-2-V_x-Al_{1-x}** in the different pressure ranges: 0 - 2.5 bar and 2.5 - 10 bar is presented in Table 4.1.

4.2 Experimental section

All chemicals (presented in Table 4.2) were bought from Sigma-Aldrich or TCI Europe and used as received without further purification.

Diffuse reflectance infrared Fourier transform spectroscopy (DRIFTS) measurements were recorded in the range 4000 - 750 cm^{-1} on a Thermo Nicolet 6700 spectrometer, equipped with a N_2-cooled MCTA detector and a KBr beam splitter at 393 K under vacuum, using a Graseby Specac diffuse reflectance cell. Raman spectra were obtained on an RXN1 Raman spectrometer (Kaiser Optical Systems) equipped with a 532 nm laser operating at 40 mW using an optical probe. XRPD patterns were collected on a Thermo Scientific ARL X'Tra diffractometer, operated at 40 keV and 40 mA using a Cu anode (Cu-Kα, λ = 1.5406 Å).

Thermogravimetric analyses (TGA) were performed on a Netzsch STA 449 F3 Jupiter-simultaneous TG-DSC (thermogravimetric - differential scanning calorimetry) analyser in the temperature range 25 - 800 °C under air and with a heating rate of 2 °C min^{-1}. N_2 sorption measurements were done on a Belsorp Mini (Bel Japan, Inc.) apparatus. Before the sorption measurements, the temperature activated samples (activation see section 4.3) were degassed at 353 K for 2 hours.

The vanadium content was determined by using an ICP-MS (inductively coupled plasma mass spectroscopy) Perkin Elmer Elan DRC 6000, whereas the Al content was obtained on an ICP-OES (ICP optical emission spectroscopy) Varian Vista MPX setup. For both elements, argon was used to create the plasma. Before the analysis, the MOF powders were completely dissolved in an acidic medium.

Equilibrium isotherms of CO_2 and C_2H_4 were measured by means of the static volumetric method using an Isorb-HP1 device from Quantachrome. The measurements were performed in a temperature range from 228 K - 303 K. Approximately 150 mg of sample was loaded in the stainless-steel sample holder. Before each measurement, the powder was degassed at a heating rate of 2 K min^{-1} to 363 K and kept at this temperature for 2 hours.

Bright-field scanning transmission electron microscopy (BF-STEM) and energy dispersive X-ray spectroscopy (EDX) was performed on a JEOL JEM-2200FS high resolution scanning transmission electron microscope equipped with an EDX spectrometer with a spatial resolution of 0.13 nm, image lens spherical aberration corrector, electron energy loss spectrometer (filter) and an field emission gun (FEG) operating at 200 KeV.

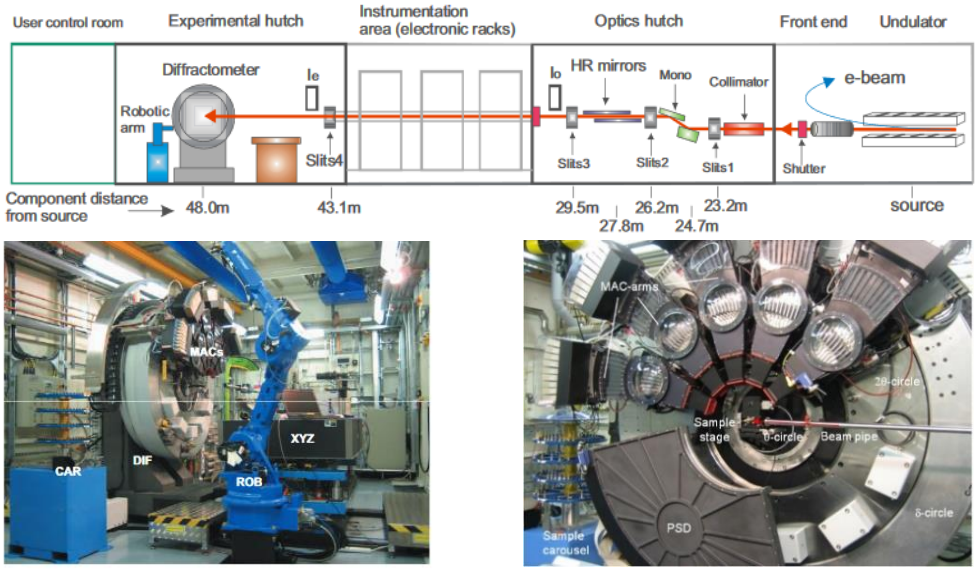

Figure 4.3 (top) Schematic representation of Beamline I11 at the Diamond Light source synchrotron showing the main components and their approximate distances from the IVU (X-ray source). (bottom, left) A photograph of I11 experimental hutch showing the heavy-duty diffractometer (DIF), 5 arms for MAC detectors (MACs), robotic arm (ROB), carousel with 200 specimen positions (CAR), and heavy-duty table (XYZ). (bottom, right) MAC arms on 2θ circle; each with S(111) analysing crystals (x 9) mounted on α and detectors (x 9) on 2α rotary table. Position sensitive detector (PSD) mounted on the δ-circle, using Mythen-2 modules as its detection elements. (Reproduced from [10])

The X-band EPR (electron paramagnetic resonance) setup was a Bruker ESP300E spectrometer equipped with an ER 4102ST standard resonator, a HP5350 B frequency counter and a Bruker ER 035M Gaussmeter. The magnetic fields were calibrated using the spectrum of diphenyl picrylhydrazyl (DPPH; g=2.0036). The EPR spectra were recorded at room temperature at 5 mW microwave power (avoiding saturation) and 100 kHz modulation with an amplitude of 0.2 mT.

High-resolution *in-situ* synchrotron XRPD data were collected at Beamline I11 at the Diamond Light source synchrotron facilities (UK, Oxfordshire) using a monochromatic X-ray beam (λ = 0.82696 Å) and a Mythen position sensitive detector, with a total scan time of 5 s. A schematic representation of Beamline I11 is presented in Figure 4.3, (top) the experimental setup is shown in Figure 4.3, (bottom). The samples were packed into a 0.5 mm quartz glass capillary and held in place by a quartz wool plug. The capillary was sealed, mounted onto a motorized goniometer head and connected to the high-pressure system. To ensure the complete removal of entrapped gas molecules, the sample was evacuated under a dynamic vacuum with a turbo pump to 10^{-6} bar and heated for 30 min at 353 K with a heating rate of 2 K min^{-1} which was controlled by a N_2-cryostream and a hot gas blower. Prior to the analysis, the sample was cooled down to 233 K and a gas dosing system was used to increase the CO_2 pressure from vacuum to 17.5 bar. [10] Rietveld refinement for powder pattern fitting was performed for all samples by using Topas Academic 3 on the CO_2-XRPD data (Figure 4.13) . The refined parameters were the measurement specific or global zero error and cosine Chebyshev function of 12 polynomial terms and the phase specific scale factors and the unit cell parameters.

4.3 Synthesis

An overview of the general synthesis method for monometallic and bimetallic MOF materials is presented in Figure 4.4. The reagent concentrations are summarized in Table 4.2.

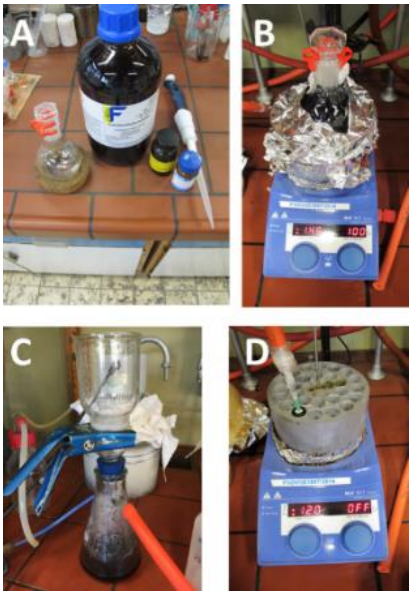

Figure 4.4 Schematic representation of the synthesis steps: (A) starting reagents; (B) synthesis setup: reaction mixture is added in a sealed glass flask and heated under constant stirring in oil bath; (C) filtration of the crystalline compound; (D) activation under vacuum.

4.3.1 Monometallic frameworks

The synthesis and activation of both **COMOC-2(V)** [11] and **DUT-5(Al)** [9] were performed according to previously reported procedures. An identical synthesis procedure was used for both compounds. After addition of all reagents, the reaction vessel was sealed and slowly heated while stirring to 421 K. The reaction mixture was kept for 16 h at this temperature. The obtained crystalline powder was filtered and washed with DMF, methanol and acetone. All solvents were removed by a drying step at 393 K under vacuum for 2 h.

The synthesis of **COMOC-2(V)** was performed as previously reported. [6] In brief , an amount of 0.5 g vanadyl(IV)sulfate hydrate ($VOSO_4.H_2O$), 1.02 g H_2BPDC and 70 mL

DMF were transferred into a 100 mL round-bottom flask equipped with a magnetic stirrer.

DUT-5(Al) was synthesized and activated according to a reported procedure. [9] In a typical synthesis, 0.52 g aluminium(III)nitrate nonahydrate ($Al(NO_3)_3.9H_2O$), 0.26 g H_2BPDC and 30 mL of DMF were mixed in a 50 mL round-bottom flask equipped with a magnetic stirrer.

4.3.2 Bimetallic frameworks

The mixed-metal MOFs were all synthesized *via* a direct one-pot synthesis and labeled from **1 (V=81%)** to **8 (V=1%)**, where the mol% vanadium of compound **1** is 81% while compound **8** contains 1%. These mol% were experimentally determined *via* ICP analysis. Throughout the result discussion, in the labeling, only the experimental metal concentrations will be used. The different concentrations of the starting reagents are listed up in Table 4.2, whereas the sample characteristics and Al/V ratios are presented in Table 4.3. Identical synthesis and activation conditions were used as previously described in section 4.3.1

Table 4.2 Solvent, linker and metal ratio of reported samples.

Sample name	Dimethyl-formamide [DMF]		4,4'-biphenyl-dicarboxylic acid [H_2bpdc]		Vanadyl(IV)sulfate hydrate [$VO(SO_4).H_2O$]		Aluminium (III)nitrate nonahydrate [$Al(NO_3)_3.9H_2O$]	
	mL	mmol	g	mmol	g	mmol	g	mmol
COMOC-2(V)*	70	908	1.0200	4.21	0.5000	2.76	0	0
COMOC-V_xAl_{1-x}-1 1 (V=81%)	25	324	0.2572	1.06	0.1800	0.99	0.0200	0.05
COMOC-V_xAl_{1-x}-2 2 (V=66%)	25	324	0.2572	1.06	0.1700	0.94	0.0400	0.11
COMOC-V_xAl_{1-x}-3 3 (V=46%)	30	389	0.3500	1.44	0.2850	1.57	0.1520	0.41
COMOC-V_xAl_{1-x}-4 4 (V=23%)	30	389	0.3500	1.44	0.2167	1.20	0.2972	0.79
COMOC-V_xAl_{1-x}-5 5 (V=9%)	30	389	0.3500	1.44	0.1430	0.79	0.4464	1.19
COMOC-V_xAl_{1-x}-6 6 (V=7%)	30	389	0.3500	1.44	0.0716	0.40	0.5936	1.58
COMOC-V_xAl_{1-x}-7 7 (V=3%)	30	389	0.3500	1.44	0.0180	0.10	0.7049	1.88
COMOC-V_xAl_{1-x}-8 8 (V=1%)	30	389	0.3500	1.44	0.0070	0.04	0.7272	1.94
DUT-5(Al)*	30	389	0.2600	1.07	0	0	0.52	1.39

Table 4.3 Theoretical and experimental vanadium and aluminium composition, Langmuir Surface Area and isosteric heat of adsorption of the synthesized samples.

Sample	Theoretical[a]		Experimental[b]		$S_{Langmuir}$	[c]CO_2-q_{st}^0	[c]C_2H_4-q_{st}^0
	V(x)	Al(1-x)	V(x)	Al(1-x)	($m^2 g^{-1}$)	(kJ mol^{-1})	(kJ mol^{-1})
COMOC-2(V)	1	0	1	0	958	-24.2	-20.4
1 (V=81%)	0.95	0.05	0.81	0.19	1280	-23.7	-21.9
2 (V=66%)	0.90	0.10	0.66	0.34	1264	-23.3	-21.7
3 (V=46%)	0.80	0.20	0.46	0.54	1238	-22.9	-23.6
4 (V=23%)	0.60	0.40	0.23	0.77	1339	-	-
5 (V=9%)	0.40	0.60	0.09	0.91	1648	-	-
6 (V=7%)	0.20	0.80	0.07	0.93	1965	-	-
7 (V=3%)	0.05	0.95	0.03	0.97	2203	-	-
8 (V=1%)	0.02	0.98	0.01	0.99	2147	-	-
DUT-5(Al)	0	1	0	1	1958	-22.1	-22.5

[a] Theoretical molar ratio of vanadium and aluminium added in the synthesis of the samples.

[b] The experimental molar ratio of vanadium and aluminium in all samples are determined with ICP analysis. Prior to the analysis, the samples are destructed under acid conditions and diluted to fit the detection range of the equipment.

[c] Isosteric heat of adsorption obtained by fitting adsorption data collected at 228 K and 303 K.

4.4 Characterization of the frameworks

In Figure 4.5 the successful synthesis and structural integrity of the bimetallic compounds is ensured by XRPD and compared with the experimental and simulated patterns of both monometallic MOFs, **COMOC-2(V)** and **DUT-5(Al)**. The diffraction pattern of the mixed-metal MOFs corresponds well with the XRPD pattern of **DUT-5(Al)** and **COMOC-2(V)**, proving the structural analogy and phase purity, conform with earlier reported data. [6, 9] In these patterns, no pronounced diffraction peaks of free H_2BPDC linker are observed. Replacing aluminium by a vanadium atom should result in a slight shift of the diffractions in the XRPD with increasing vanadium concentration. The diffraction patterns indeed show a shift to lower 2Θ values with increasing vanadium concentration. A similar shift was also observed in the work of Kozachuk *et al.* [1] on the mixed-metal MIL-47(V)/MIL-53(Al) frameworks.

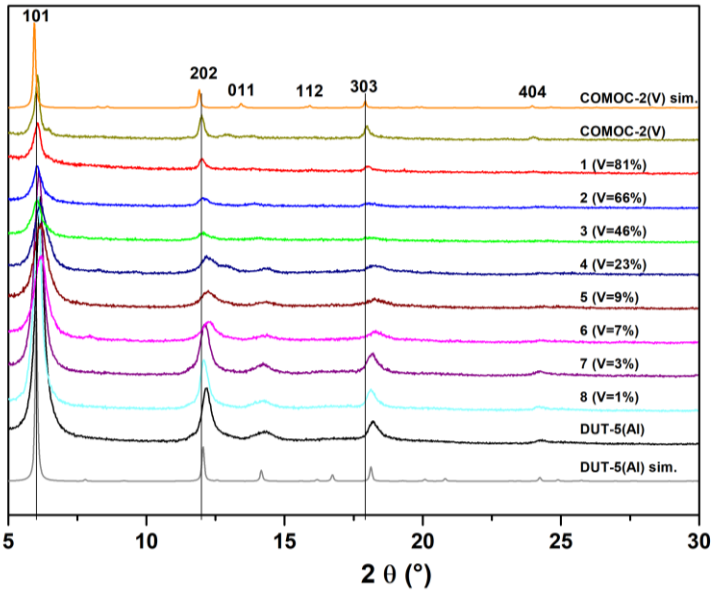

Figure 4.5 XRPD of the pristine COMOC-2(V), pristine DUT-5(Al) and the mixed-metal COMOC-2(V)$_x$-Al$_{1-x}$ series. Simulated diffractograms of the pristine materials are also represented and indicated with "sim.".

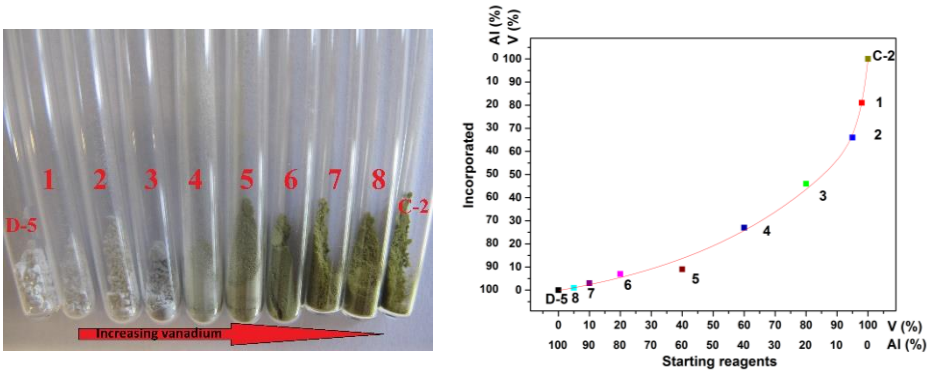

Figure 4.6 (left) Visual representation of the powder samples in a quartz tube. The two extremes are D-5 for DUT-5(Al), a completely white crystalline powder and C-2 for COMOC-2(V) a yellow-green powder. From (1-8): 1 (V=81%) to 8 (V=1%) with increasing number, the aluminium content increases. (right) ICP analysis of the Al/V ratio in the monometallic COMOC-2(V) (C-2), DUT-5(Al) (D-5) and mixed-metal COMOC-2(V)$_x$-Al$_{1-x}$ series. The plotted line is a guide for the eye.

A first indication of the successful synthesis and inclusion of both metal ions aluminium and vanadium in the **COMOC-2-V$_x$-Al$_{1-x}$** series, was seen from the colour of the different samples. Overall, the colour changed from white to yellow-green with increasing the V content as presented in Figure 4.6, (left). In Figure 4.6, (right), a graphical representation of the incorporated Al/V ratios (%) determined by ICP as a function of the starting reagents (%) is given. Starting from the **DUT-5(Al)** (black) structure at the complete left side, and moving on from compound **8 (V=1%)** towards **3 (V=46%)**. The fraction of vanadium is consistently lower than the initial V over the total metal salt fraction in the starting mixture.

A major factor for the final metal ratio in the bimetallic frameworks is the lability of the cations which influences the rate of nucleation and crystal growth. Haque *et al*. [12] determined the relative nucleation rate for the isoreticular frameworks MIL-53(Al) and MIL-47(V) and they show that the relative solvothermal rates of nucleation and crystal growth for MIL-53(Al)/MIL-47(V) are 1/2.34 and 1/2.76 respectively. This observation indicates that Al^{3+} cations are kinetically more inert in this system than V^{3+}. The work of Kozachuk *et al*. [1] supports this observation for mixed-metal MIL-47(V)/MIL-53(Al) frameworks, where metal analysis reveals that V^{3+} atomic fractions in the MOFs are systematically higher than in the solutions. However, we have used $VO(SO_4)$. The vanadyl cation $(VO)^{2+}$ seems to be kinetically more inert, resulting in a favourable

incorporation of the Al^{3+} ion in the MOF. From earlier reports, it is known that **DUT-5(Al)** crystals are thermodynamically nucleating and growing in a broader temperature range in comparison with **COMOC-2(V)**. This seems to support this explanation.

The Raman spectra of several representative compounds, **COMOC-2(V)**, **1 (V=81%)**, **2 (V=66%)**, **3 (V=46%)** and **DUT-5(Al)**, are presented in Figure 4.7, (left) and the DRIFT spectra in Figure 4.7, (right). Based on earlier investigations of Liu *et al.* [6] , Salazar *et al.* [13] and Senkovska *et al.* [9], we can assign the most prominent vibrational bands. Greek letters are used to label the different types of vibrational motion, ν is used for stretches, δ indicate bending, ω is the designation for out-of-plane wagging mode.

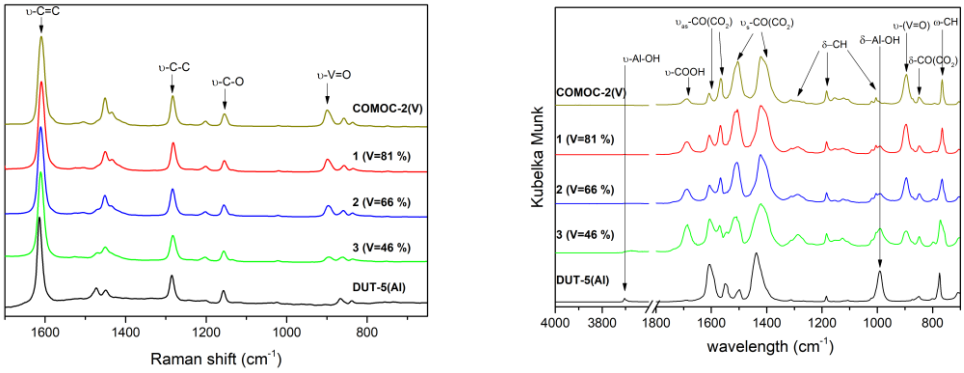

Figure 4.7 (left) Raman spectra in the range 1700-750 cm^{-1}. (right) DRIFT spectra in the range 4000-3600 cm^{-1} and 1800-750 cm^{-1} both of compounds COMOC-2(V), 1 (V=81%), 2 (V=66%), 3 (V=46%) and DUT-5(Al).

A first interesting observation in the Raman spectrum is the signal located at 898 cm^{-1} related to ν-V=O mode of the asymmetric (V=O)-(V=O) bond. The intensity of this band decreases from the pristine **COMOC-2(V)** material towards **3 (V=46%)**. This decrease in intensity indicates the replacement of the vanadium by aluminium in the framework. Furthermore, different characteristic vibrations of the carbon matrix are visible. A first characteristic signal appears at 1285 cm^{-1} from the biphenyl connection, corresponding to the ν-C-C stretch. Another peak around 1614 cm^{-1} (ν-C=C) indicates the presence of the benzene ring. The signal at 1157 cm^{-1} originates from the dicarboxylate species of the framework.

Infrared spectroscopy measurements were performed in the mid-infrared range 4000 - 750 cm^{-1}. Also in IR, the ν-V=O band at 896 cm^{-1} is visible, and follows an identical behaviour as observed in the Raman measurements. Moreover, proof of the Al-OH interconnection is seen in the IR spectrum by the -OH stretch and in-plane bending vibrations. The δ-Al-OH is located at 991 cm^{-1}, the dilution with vanadium from compound **3 (V=46%)** towards **1 (V=81%)** gradually decreases the signal intensity of this bending mode. Additionally, another characteristic vibration ν-Al-OH at 3704 cm^{-1} is only visible in the two most aluminium rich structures, **DUT-5(Al)** and **3 (V=46%)**.

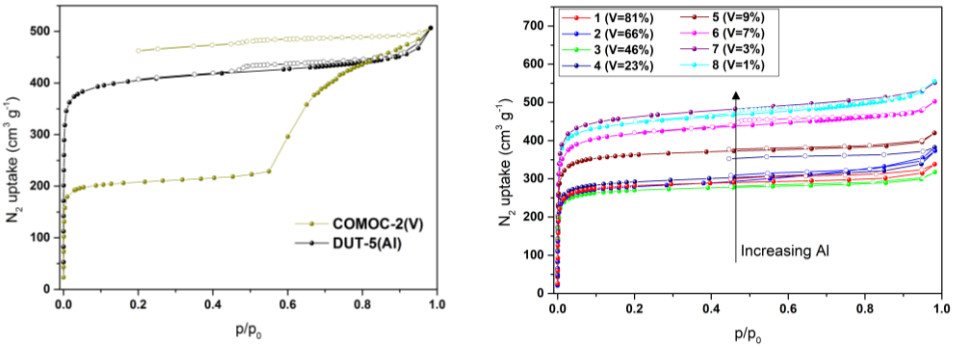

Figure 4.8 N_2 sorption isotherms of (left) DUT-5(Al) and COMOC-2(V), (right) mixed-metal COMOC-2-V_x-Al_{1-x} structures from 1 (V=81%) to 8 (V=1%).

The experimental spectra show various spectral features related to the organic entities. At 770 cm^{-1} the ω-CH vibration and different δ-CH bendings between 1100 - 1350 cm^{-1} are identified. Furthermore, numerous vibrational modes are indicated: ν_s-CO(CO_2) at 1436 cm^{-1}/1506 cm^{-1} and ν_{as}-CO(CO_2) at 1564 cm^{-1}/1606 cm^{-1}, these observed vibrational modes are similar as in MIL-53(Al). In addition, a trace amount of free linker is still present in the MOF materials, indicated by the presence of the ν-COOH stretch vibration at 1688 cm^{-1} in the spectra, originating from the H_2BPDC-linker inside the framework.

The Langmuir specific surface areas of all the materials shown in Table 4.3. The isotherms can be found in Figure 4.8. The results for the monometallic **COMOC-2(V)** and **DUT-5(Al)** materials is presented in Figure 4.8, (left), with final N_2 uptake of 500 cm^3 g^{-1} and 450 cm^3 g^{-1}, respectively. **DUT-5(Al)** shows a typical type I adsorption isotherm whereas **COMOC-2(V)** exhibits a pronounced flexibility starting at p/p_0 value

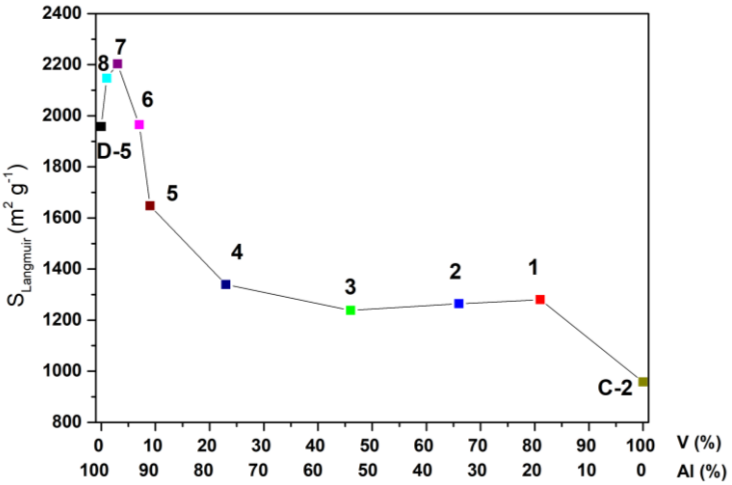

Figure 4.9 N_2 sorption isotherms of (left) DUT-5(Al) and COMOC-2(V), (right) mixed-metal COMOC-2-V_x-Al_{1-x} structures from 1 (V=81%) to 8 (V=1%).

of 0.6. These observations are shown in Table 4.3. For all mixed-metal compounds, type I adsorption isotherms were obtained. None of the compounds in the mixed-metal series shows significant flexibility in N_2 adsorption. Higher aluminium concentration in the MOFs increases the adsorption uptake of the framework as can be extracted from Figure 4.9 and Table 4.3. Figure 4.9 shows that small quantities of dopant ions increase the surface area of the material. Small defects created by adding aluminium to the starting mixture could be responsible for this increased uptake. [14]

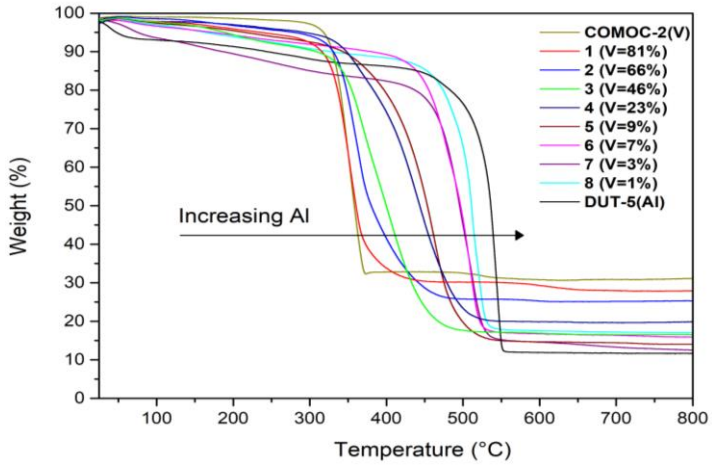

Figure 4.10 Thermogravimetric analysis data of the monometallic frameworks COMOC-2(V), DUT-5(Al) and the mixed-metal COMOC-2-V_x-Al_{1-x} series.

Thermogravimetric analyses (TGA) were performed to compare the thermal stability of the monometallic **DUT-5(Al)**, **COMOC-2(V)** and the series of mixed-metal frameworks in Figure 4.10. **DUT-5(Al)** and **COMOC-2(V)** are thermally stable up to 500 °C and 325 °C, respectively, which corresponds to earlier observed values. For **DUT-5(Al)** and sample **7 (V=3%)**, an initial mass loss of approximately 8% is observed in the temperature range 25 - 100 °C which corresponds to the loss of the entrapped solvent molecules. For all frameworks, the decomposition occurs in one step at one temperature, this is a direct indication that no traceable amounts of free linker molecules are left inside the framework. However, infrared measurements presented in Figure 4.7, (right), show the presence of linker leftovers. An enhanced thermal stability is observed with increasing aluminium concentration in the series **COMOC-2-V_x-Al_{1-x}.** This can be related to the strength of the metal-oxygen bonds as suggested by Low *et al*. [15] and described by Jhung *et al.* [16] who described a relation between the thermal stability of oxides and MOF frameworks.

4.4.1 STEM and EPR

BF-STEM-EDX mapping of aluminium and vanadium atoms in the crystalline framework of **3 (V=46%)** is presented in Figure 4.11. The EDX-measurements clearly show that both metal ions are uniformly distributed in the entire framework.

The RT X-band EPR spectra of the MOF series were recorded under vacuum conditions ($p \approx 1$ mbar) and are presented in Figure 4.12. The spectrum of the fully V-concentrated **COMOC-2(V)** exhibits one very broad EPR line at $g \approx 1.964$ (V^{4+}, $3d^1$ electron configuration). This is consistent with the situation for other concentrated V-MOFs like MIL-47(V) [1, 17], NH_2-MIL-47(V) [11, 17], NH_2-MIL-47(V)Ti [18], and COMOC-3(V) [19], where strong interactions occur between the V^{4+} ions in the infinite (V=O)-(V=O) chains in the framework. In the mixed Al/V samples, a component with resolved hyperfine structure gradually grows in as the Al concentration increases. This narrow-lines component is barely visible in the spectrum of sample **1 (V=81%)**, but quite pronounced in the spectra of **2 (V=66%)** and **3 (V=46%)** (dashed lines). The identification of this component as disperse V^{4+} ions incorporated as metal nodes in framework follows from a comparison between EPR spectra of V-doped (a few %) **DUT-5(Al)** and MIL-53(Al) in the **lp** state, in Figure 4.12 (B). The spectra of these two V-doped Al-MOFs are very similar and coincide with the narrow-line features in the spectrum of **3 (V=46%)**. Both the EPR and the BF-STEM EDX measurements strongly indicate a homogeneous dispersion of the metal ions.

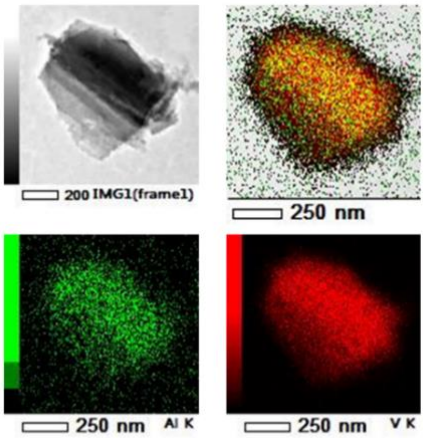

Figure 4.11 Bright-field scanning transmission electron microscopy BF-STEM-EDX mapping of aluminium (green) and vanadium (red) on a mixed-metal particle of 3 (V=46%).

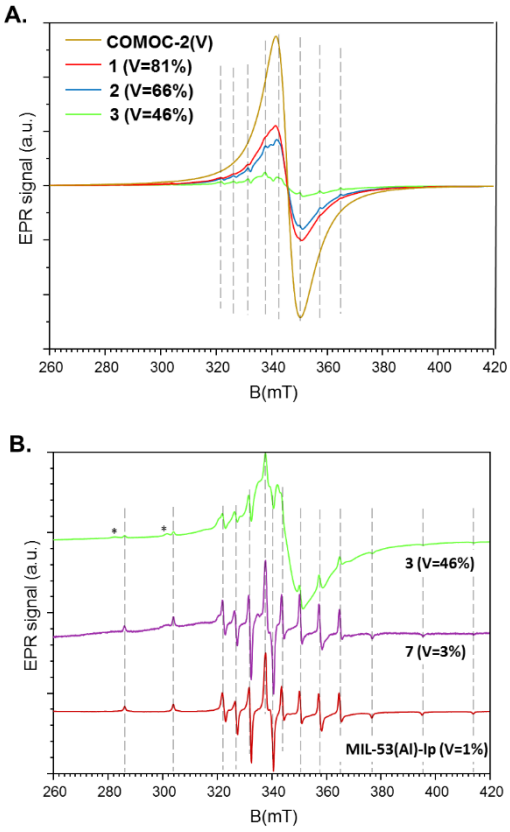

Figure 4.12 Powder EPR spectra of: (A) COMOC-2(V) and the mixed-metal compounds 1 (V=81%), 2 (V=66%), 3 (V=46%); (B) 3 (V=46%), 7 (V=3%), MIL-53(Al)-lp V=1%,. The EPR spectra of 7 (V=3%) and 3 (V=46%) contain extra V^{4+} related features, indicated with *.

4.4.2 High pressure CO_2 XRPD

To study the breathing, high pressure CO_2 measurements were performed at the Diamond Light Source synchrotron facility. Four different samples were analyzed: **COMOC-2(V)**, **1 (V=81%)**, **2 (V=66%)** and **3 (V=46%)**. Prior to the measurements, the samples were degassed at 353 K for 30 min. The XRPD data were collected at 228 K in the CO_2 pressure range 0 - 17.5 bar and presented in Figure 4.13 (B), (D), (F), (H). Additional analysis was executed on these data *via* Rietveld refinements in the lower 2θ range from 2.75 - 3.75 ° presented in Figure 4.13 (A), (C), (E), (G).

Rietveld refinements revealed a surprising coexistence of three communicating fractions: two large pore phases, i.e., **lp-1**, the novel **lp-2**, and a narrow pore **np**. These results are shown in Figure 4.13 (A), (C), (E), (G), where the estimated values of each fraction obtained *via* the refinements are plotted. The detailed numerical data can be found in addendum Table A2. Only two fractions, **lp-1** (97% - 70%) (red, dot) and **np** (3% - 30%) (black, square) are identified in the 0-2.5 bar range. The **np** fraction has the smallest cell volume (2766.2 $Å^3$) for **COMOC-2(V)** at 0 bar, with a long b-axis and a smaller c-axis. For the first open pore phase **lp-1**, the volume increases to 3226.0 $Å^3$ for the same compound under identical conditions. This volume increase is accompanied with a shrinkage along the b-axis, while an increase along the a- and c-axis is observed. Exposing the framework to CO_2 induces the transition from the **lp-1** state to a **np** form. This a general trend observed in the high-pressure CO_2-XRPD measurements in the range 0 and 5 bar. A second novel state appears at elevated CO_2 pressure, which induces more stress on the framework. This second phase is labeled as **lp-2** (blue, triangle). In contrast with the **lp-1** state, this structure has opened due to the pressure of the CO_2 molecules, resulting in a slightly increased volume of 3368.0 $Å^3$ at 10 bar for **COMOC-2(V)**. For structures with a higher Al concentration **2 (V=66%)** and **3 (V=46%),** the **lp-2** shows the highest volume as can be seen in Figure A1, while the opposite behavior is observed for compounds with low Al concentration. These lattice parameters change under influence of CO_2 pressure. The evolution of the parameters under elevated pressure can be found in Table A3 - A6 and Figure A1 (A) to (D) of the addendum.

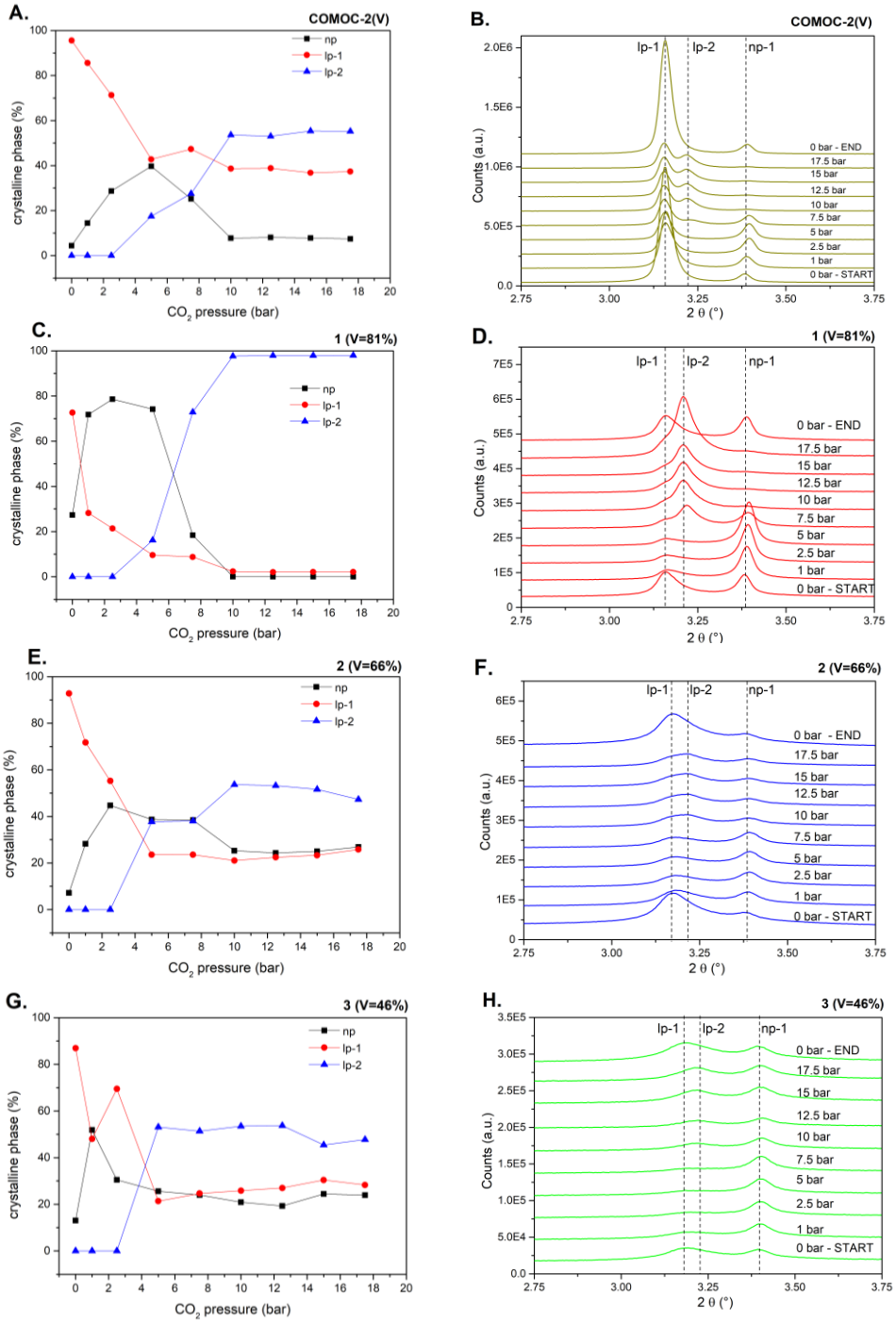

Figure 4.13 High pressure CO_2-XRPD analysis between 0-17.5 bar at 233 K and Rietveld refinements of: (COMOC-2(V) (A, B); 1 (V=81%) (C, D); 2 (V=66%) (E, F), 3 (V=46%) (G, H). Three fractions are identified as np (■), lp-1 (●) and lp-2 (▲).

As stated before, under vacuum conditions, according to the reported data, and up to 2.5 bar solely the first most prominent state **lp-1** (70% - 97%) coexists with the **np** (30% - 3%) state (Figure 4.13 (A), (C), (E), (G)). The **lp-1** state decreases in general between 0 and 5 bar and transforms to **np** fraction which shows a steady increase between 0 - 2.5 bar. Once passed the threshold pressure, the **np** fraction reopens to a **lp-2** fraction. These transformations result in a more or less constant **np** concentration as observed between 2.5 - 5 bar. Once the **lp-1** to **np** transformation has stopped, only the **np** to **lp-2** transition still proceeds, resulting in a decrease of the former and an increase of the latter fraction. Clearly a certain part of the **lp-1** fraction is still maintained, most probably as a result of physical blocking of the pores. Infrared measurements show a higher amount of linker, which may also explain the lower adsorption capacity (Figure 4.7, right). Once the pressure reaches 10 bar, at the measurement temperature, CO_2 liquefies and as a result the **lp-1, lp-2** and **np** fractions no longer significantly change. After reducing the CO_2 pressure back to 0 bar, the structure transforms back to the original composition.

A divergent behaviour is observed for compound **3 (V=46%)** (Figure 4.13 (G) and (H)). Here, the transition **np** to **lp-2** is already completed at 5 bar. The higher Al concentration seems to accelerate this transition.

4.4.3 Volumetric high pressure CO_2 adsorption analysis

Complementary CO_2 sorption measurements at 233 K between 0 - 7 bar were executed on an in house volumetric high pressure setup. Earlier reports indicate that CO_2 and C_2H_4 trigger the breathing behaviour of the flexible **COMOC-2(V)** while **DUT-5(Al)** stays completely rigid. The adsorption of CO_2 in the **COMOC-2(V)**, **DUT-5(Al)** and compounds **1 (V=81%)**, **2 (V=66%)**, **3 (V=46%)** at 228 K are depicted in Figure 4.14 (A) to (C).

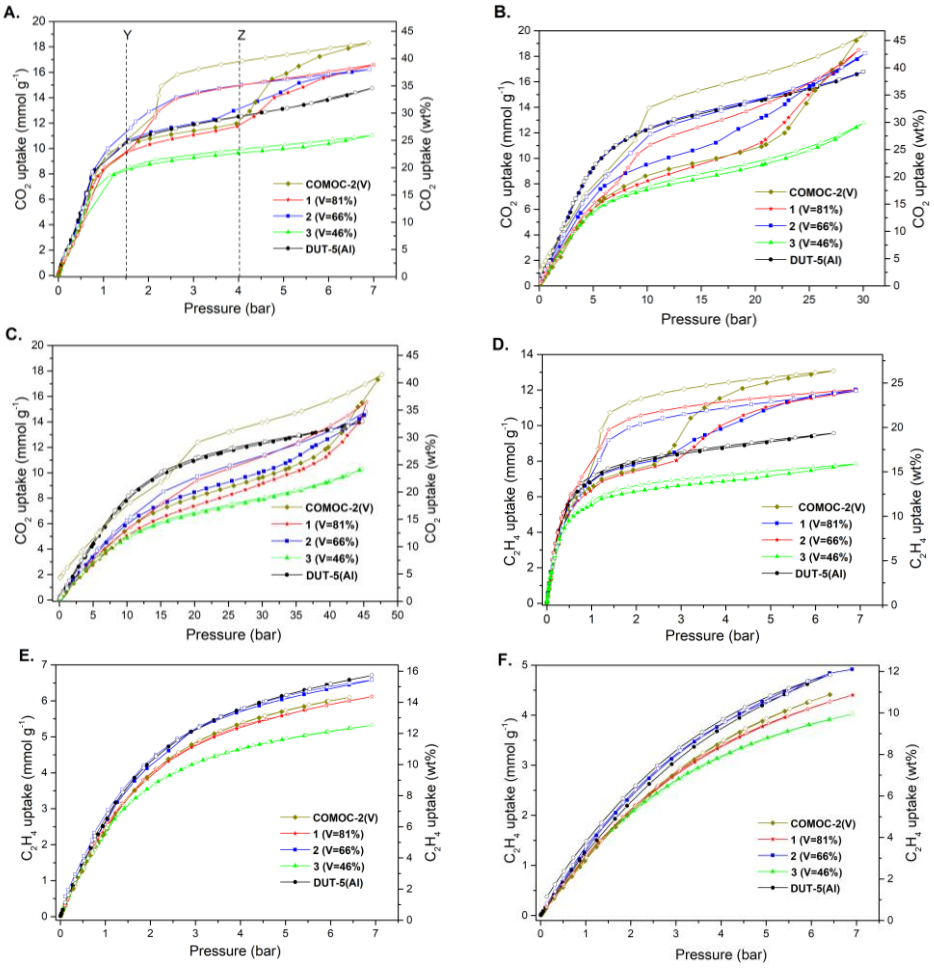

Figure 4.14 High-pressure CO_2 sorption measurement at (A) 228 K from 0 - 7 bar; (B) 273 K from 0 - 35 bar; (C) 303 K from 0 - 45 bar; high-pressure ethylene sorption measurements between 0 - 7 bar measured at (D) 228 K; (E) 273 K; (F) 303 K; for the compounds COMOC-2(V), DUT-5(Al), 1 (V=81%), 2 (V=66%), 3 (V=46%).

DUT-5(Al) and **3 (V=46%)** show a typical type I isotherm without distinct breathing behaviour. The flexible compounds **1 (V=81%)**, **2 (V=66%)** and **COMOC-2(V)** are characterized by a multi-step adsorption Figure 4.14 (A) to (C). Correlated to the XRPD data in Figure 4.13, we will explain the adsorption isotherm in Figure 4.14 (A). In a first step, a fraction of crystals in the **lp-1** state transforms to the **np** phase, followed by a saturation part around 1.5 bar, indicated by a dashed line labeled as Y. This multistep adsorption behaviour progresses with a partial reopening of the crystals from **np** to **lp-2** state around 4 bar, marked by the line Z.

Increasing the amount of vanadium, increases the flexibility and this creates an enhanced CO_2 uptake with a final capacity of 16 mmol g^{-1} for both **1 (V=81%)**, **2 (V=66%)** and 18 mmol g^{-1} for **COMOC-2(V)**. It is clear that metal doping changes the height of the hysteresis loop. Hence, metal doping is a pathway to tailor the breathing behaviour. The enhanced flexibility and adsorption capacity for vanadium rich structures, is observed at different temperatures. Moreover, C_2H_4 adsorption-desorption isotherms at 273 K and 303 K are plotted in Figure 4.14 (D) to (F). A general trend for these adsorbents is the decrease in total gas uptake when raising the temperature. Adsorption-desorption isotherms at three different temperatures 228 K, 273 K, 303 K clearly show this trend for CO_2 (Figure 4.14 (A) to (C)). An identical effect is observed for C_2H_4 (Figure 4.14 (D) to (F)). To compare the adsorption properties, the heat of adsorption (q_{st}^0) for CO_2 was determined by fitted data collected at 228 K and 303 K and is summarized in Table 4.3.

4.4.4 Temperature induced flexibility

In an attempt to better understand this flexibility, we also evaluated the behaviour of a set of bimetallic frameworks under elevated temperature. Heating the **COMOC-2(V)** doped framework induces no direct flexibility. T-XRPD measurements presented in Figure 4.15 between 7 and 23 ° show that its main intensities are preserved and do not increase upon elevated temperature. In the studied interval (233 K – 450 K), for none of the pure and mixed **COMOC-2(V)/DUT-5(Al)** frameworks, any indication of transition between **np** and **lp** structures has been detected.

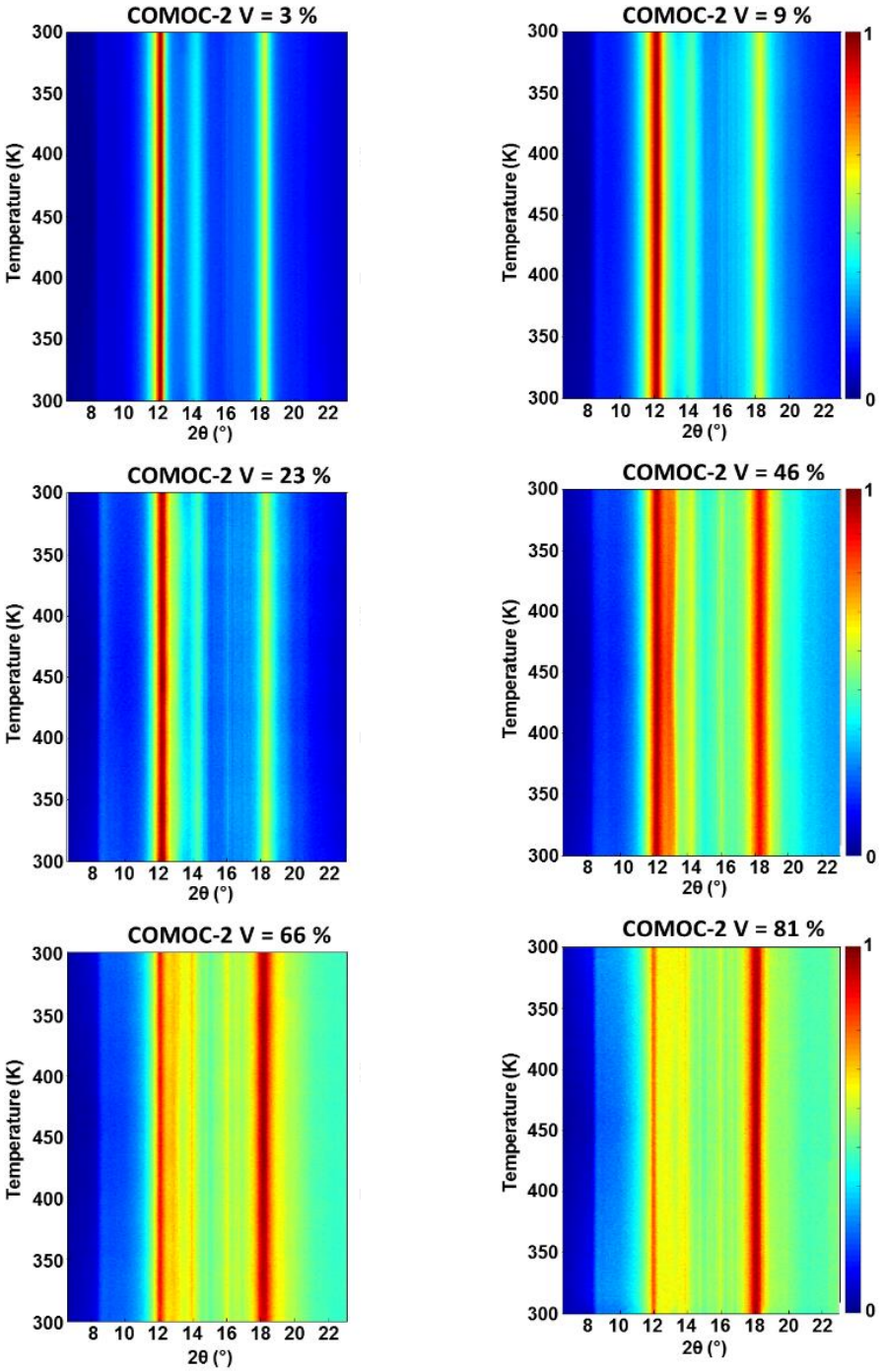

Figure 4.15 T-XRPD measurements collected during this work in air between 300 - 450 K in the 2 Θ range 7 - 23 °, for six bimetallic Al/V structures.

4.5 Conclusion

In conclusion, a series of novel Al/V BPDC-based mixed-metal MOFs are reported *via* a straightforward solvothermal synthesis in which aluminium incorporation is favoured. An increasing concentration of Al significantly enhances the thermal stability and the surface area. EPR and BF-STEM EDX analysis techniques give clear evidence for a homogeneous dispersion of the metal ions in the framework. All compounds from 100% to 46% V always exhibit a mixture of **lp** and **np** phases. A particular fraction of the **lp-1** closes during adsorption to a **np** state. In a final pressurizing step, a second not earlier recognized **lp-2** fraction appears. The CO_2-XRPD analysis reveals that the more aluminium is incorporated in the framework, the faster (at lower pressure) the transition from **np** to **lp-2** takes place. In the high pressure-adsorption-desorption measurements, with increasing aluminium the height of the hysteresis loop decreases. This shows that it is possible to tailor the breathing of the vanadyl structure **COMOC-2(V)** *via* metal doping.

4.6 References

1. O. Kozachuk, M. Meilikhov, K. Yusenko, A. Schneemann, B. Jee, A.V. Kuttatheyil, M. Bertmer, C. Sternemann, A. Pöppl and R.A. Fischer, *European Journal of Inorganic Chemistry*, 2013, **2013**, 4546-4557.
2. I. Nevjestić, H. Depauw, P. Gast, P. Tack, D. Deduytsche, K. Leus, M. Van Landeghem, E. Goovaerts, L. Vincze, C. Detavernier, P. Van Der Voort, F. Callens and H. Vrielinck, *Physical Chemistry Chemical Physics*, 2017, **19**, 24545-24554.
3. I. Nevjestić, H. Depauw, K. Leus, G. Rampelberg, C.A. Murray, C. Detavernier, P. Van Der Voort, F. Callens and H. Vrielinck, *The Journal of Physical Chemistry C*, 2016, **120**, 17400-17407.
4. I. Nevjestić, H. Depauw, K. Leus, V. Kalendra, I. Caretti, G. Jeschke, S. Van Doorslaer, F. Callens, P. Van Der Voort and H. Vrielinck, *ChemPhysChem*, 2015, **16**, 2968-2973.
5. I. Nevjestić, Ghent University, PhD thesis, 2018.
6. Y.-Y. Liu, S. Couck, M. Vandichel, M. Grzywa, K. Leus, S. Biswas, D. Volkmer, J. Gascon, F. Kapteijn, J.F.M. Denayer, M. Waroquier, V. Van Speybroeck and V.D.V. Pascal, *Inorganic Chemistry*, 2013, **52**, 113-120.
7. S. Couck, T.R.C. Van Assche, Y.-Y. Liu, G.V. Baron, P. Van Der Voort and J.F.M. Denayer, *Langmuir*, 2015, **31**, 5063-5070.
8. J. Wieme, L. Vanduyfhuys, S.M.J. Rogge, M. Waroquier and V. Van Speybroeck, *The Journal of Physical Chemistry C*, 2016, **120**, 14934-14947.
9. I. Senkovska, F. Hoffmann, M. Fröba, J. Getzschmann, W. Böhlmann and S. Kaskel, *Microporous and Mesoporous Materials*, 2009, **122**, 93-98.
10. S.P. Thompson, J.E. Parker, J. Potter, T.P. Hill, A. Birt, T.M. Cobb, F. Yuan and C.C. Tang, *Review of Scientific Instruments*, 2009, **80**, 075107.
11. K. Leus, S. Couck, M. Vandichel, G. Vanhaelewyn, Y.-Y. Liu, G.B. Marin, I.V. Driessche, D. Depla, M. Waroquier, V.V. Speybroeck, J.F.M. Denayer and P. Van Der Voort, *Physical Chemistry Chemical Physics*, 2012, **14**, 15562-15570.
12. E. Haque, J.H. Jeong and S.H. Jhung, *CrystEngComm*, 2010, **12**, 2749-2754.
13. J.M. Salazar, G. Weber, J.M. Simon, I. Bezverkhyy and J.P. Bellat, *The Journal of Chemical Physics*, 2015, **142**,
14. X. Zhang, B. Shen, X. Zhang, F. Wang, G. Chi and M. Si, *RSC Advances*, 2017, **7**, 5928-5936.
15. J.J. Low, A.I. Benin, P. Jakubczak, J.F. Abrahamian, S.A. Faheem and R.R. Willis, *Journal of the American Chemical Society*, 2009, **131**, 15834-15842.
16. S.H. Jhung, N.A. Khan and Z. Hasan, *CrystEngComm*, 2012, **14**, 7099-7109.

17. K. Leus, M. Vandichel, Y.-Y. Liu, I. Muylaert, J. Musschoot, S. Pyl, H. Vrielinck, F. Callens, G.B. Marin, C. Detavernier, P.V. Wiper, Y.Z. Khimyak, M. Waroquier, V. Van Speybroeck and P. Van Der Voort, *Journal of Catalysis*, 2012, **285**, 196-207.
18. K. Leus, G. Vanhaelewyn, T. Bogaerts, Y.-Y. Liu, D. Esquivel, F. Callens, G.B. Marin, V. Van Speybroeck, H. Vrielinck and P. Van Der Voort, *Catalysis Today*, 2013, **208**, 97-105.
19. Y.-Y. Liu, K. Leus, M. Grzywa, D. Weinberger, K. Strubbe, H. Vrielinck, R. Van Deun, D. Volkmer, V. Van Speybroeck and P. Van Der Voort, *European Journal of Inorganic Chemistry*, 2012, **2012**, 2819-2827.

5 *Microwave induced "egg yolk" structure in MIL-53(Cr/V)*

This chapter is dedicated to the synthesis of a second microporous bimetallic framework MIL-53(Cr/V). Using a one pot microwave procedure, mixed-metal "egg yolk" MOFs are created, with a core of MIL-53(Cr/V) and a shell of MIL-53(Cr). On the contrary, the solvothermal method yields homogeneous mixed-metal MOFs. This difference in dispersion is mapped by bright-field scanning transmission electron microscopy energy dispersive electron X-ray measurements. The influence of Cr and V on the flexibility and breathing was studied by temperature dependent X-ray powder diffraction and CO_2 adsorption measurements.

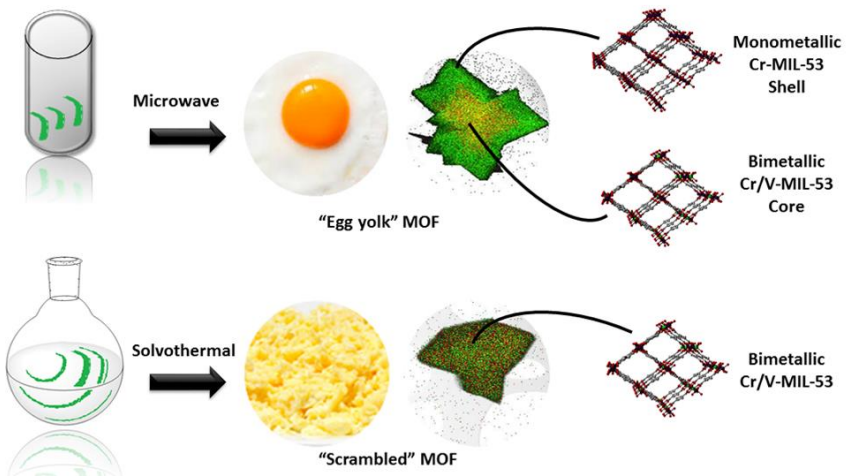

This work was published as:

Microwave induced "egg yolk" structure in Cr/V-MIL-53

H. Depauw, I. Nevjestić, J. De Winne, G.B. Wang, K. Haustraete, K. Leus, A. Verberckmoes, C. Detavernier, F. Callens, E. De Canck, H. Vrielinck, P. Van Der Voort, *Chemical Communications*, 2017, **53**, 5478-5481.

5.1 Introduction

A recent trend in the MIL-53 series is the development of mixed-metal frameworks to investigate the influence of metal incorporation and induced variations on the structural flexibility. Different bimetallic analogues of MIL-53 have been described such as Al/V [1-3], Cr/Al [4, 5], Fe/V [6] and Cr/Fe [7], see Chapter 3, section 3.3 for more information. All reports state that these materials prepared *via* a one pot solvothermal synthesis, show a homogeneous dispersion of both cations in the framework. This implies that metal cations concomitantly nucleate and grow, avoiding the formation of two monometallic phases. However, when synthesizing MOFs in the kinetic regime, different results are a priori possible. So far, the existence of clustered phases *via* a direct synthesis for MIL-53 like structures has already been suggested, but to the best of our knowledge never unambiguously proven [6], although some papers mention "core-shell" MOFs synthesized under very different circumstances. [8-10] In this work, we have used a MW [11, 12] technique to synthesize "egg yolk" type mixed-metal MOFs and compared these materials to the SOL grown counterparts. [13, 14] Both recipes are adapted methods from earlier reports. Both synthesis methods are executed with the same V^{3+} and Cr^{3+} salts, which are together with the organic linker dissolved in demineralized water. The crystals are formed in a MW in 3 h, while the SOL method was carried out over a time span of 96 h.

5.2 Thermodynamic and synthesis factors for MIL-47(V) and MIL-53(Cr)

In the present work, bimetallic **MIL-53(Cr/V)** compounds have been synthesized based on the synthesis of monometallic frameworks **MIL-47(V)** and **MIL-53(Cr)**. It is first of all important to understand the influence of the parameters time, temperature, solvent and acidity (pH) on the phase purity of monometallic materials. This is a first step in the process to synthesize bimetallic frameworks.

The MW and SOL synthesis, with the reagents vanadium chloride and terephthalic acid above 200 °C in water, result exclusively in one thermodynamically stable compound **MIL-47(V)**. Product synthesis schemes are shown in Figure 5.1. Whereas MIL-101(V) is the kinetic isomer (high pH/ethanol concentration, low temperature) of **MIL-47(V)** and is formed in the first time period of the synthesis**,** MIL-88(V) can be considered as the thermodynamic isomer (low pH/ethanol concentration, higher temperature). When the synthesis temperature is above 200 °C, both frameworks transform to **MIL-47(V)**. This transformation is reported for an ethanol/HCl solvent mixture, as aqueous conditions solely result to the best of our knowledge in one phase **MIL-47(V)**. [15, 16]

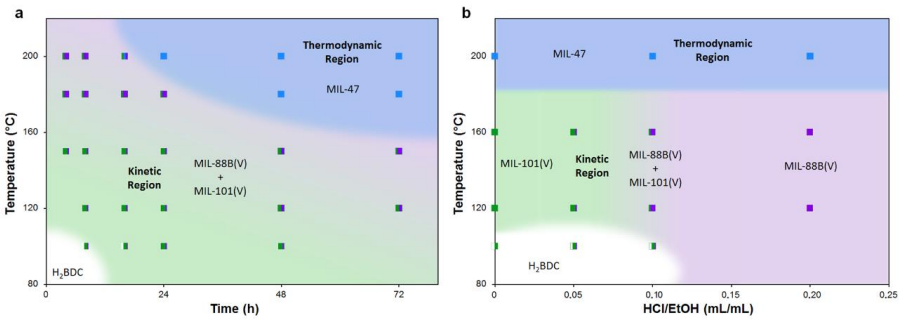

Figure 5.1 Product synthesis scheme for MIL-88(V), MIL-101(V), and MIL-47(V); (left) time influence (right) HCl/ethanol influence. (Reproduced from [15])

From synthesis perspective **MIL-47(V)** follows a very straightforward SOL and MW synthesis procedure, while for **MIL-53(Cr)** this is not the case. Here the MIL-101(Cr), a transient phase, can be formed under certain conditions (pH, H_2O concentration, time) and after initial formation, reconstruct to **MIL-53(Cr)**. Because both MIL-101(Cr) and **MIL-53(Cr)** can be produced from nearly the same reaction composition, we will first

discuss the influence of the parameters such as solvent concentration, reaction time, acidity (pH) in correlation with the yield.

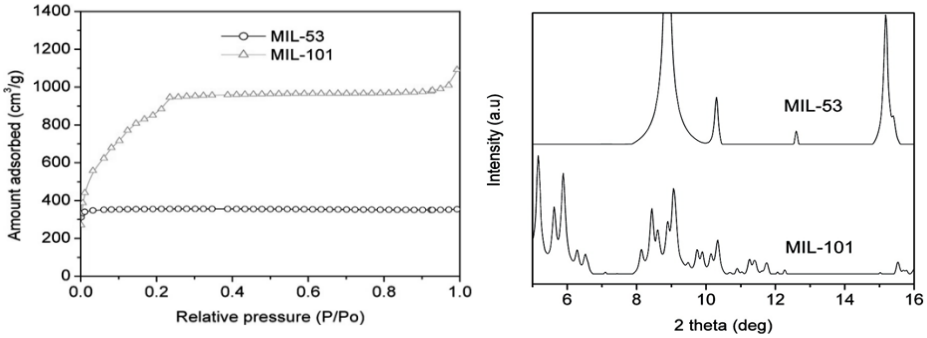

Figure 5.2 (left) N_2 adsorption isotherms of the activated MIL-53(Cr) and MIL-101(Cr) obtained in 12 h at 210 °C *via* SOL synthesis with reaction composition MIL-101(Cr) = 1 $CrCl_3.6H_2O$/ 1 H_2BDC/400 H_2O (1/1/400 = equivalents in mol) and MIL-53(Cr) = 1 $CrCl_3.6H_2O$/1 H_2BDC/100 H_2O. (right) Calculated XRPD patterns of the as-synthesized Cr-BDCs MIL-53 and MIL-101. (Reproduced from [17])

This research field is mainly explored by the group of Jhung and co-workers [12, 17], summarizing the major reaction conditions yielding MIL-101(Cr) or **MIL-53(Cr)**. Both Cr-BDCs, MIL-53 and MIL-101 possess a very high surface area, and are synthesized in water under autogenous pressure with reagents terephthalic acid and chromium chloride. While **MIL-53(Cr)** is an orthorhombic microporous structure with a Langmuir surface area of 1436 $m^2\ g^{-1}$ and low total pore volume of 0.55 $cm^3\ g^{-1}$, MIL-101(Cr) is a cubic micro- and mesoporous structure, containing a large surface area of 3310 $m^2\ g^{-1}$ and total pore volume of 1.56 $cm^3\ g^{-1}$. The pore sizes are 0.85 nm for **MIL-53(Cr)** and for the cage MOF, MIL-101(Cr) this varies between 2.9-3.4 nm. Each compound has its own characteristic isotherm. Both sorption isotherms are presented in Figure 5.2, (left). The XRPD fingerprint diffractograms, a second characteristic of **MIL-53(Cr)** and MIL-101(Cr) are presented in Figure 5.2, (right).

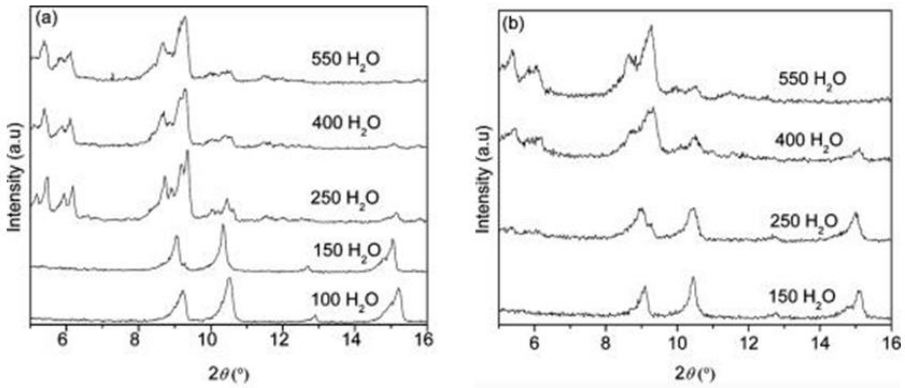

Figure 5.3 XRPD patterns of the as-synthesized Cr-BDCs depending on the water concentration. The reactant composition was 1 $CrCl_3.6H_2O$/ 1 H_2BDC/x H_2O (with x =100 – 550), and the reaction was carried out at 210 °C with (left) SOL for 12 h (right) MW for 3 h.
(Reproduced from [12])

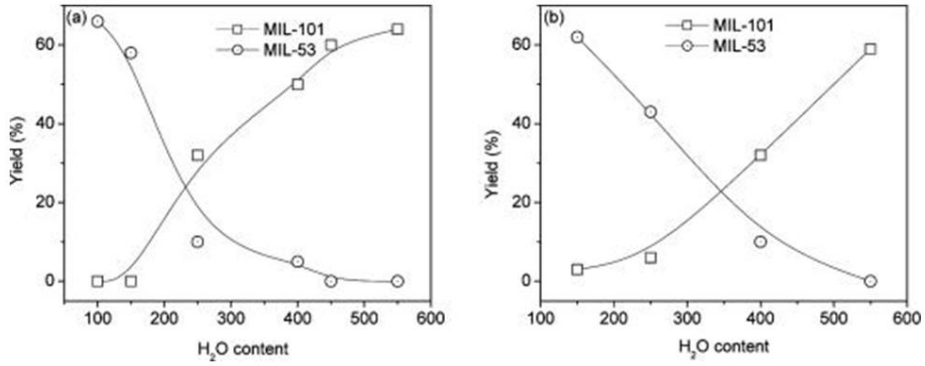

Figure 5.4 Changes of yields of Cr-BDCs depending on the concentration of water. The reaction composition was 1 $CrCl_3.6H_2O$/ 1 H_2BDC/x H_2O (with x = 100 - 550), and the reaction was carried out at 210 °C with (left) SOL for 12 h, (right) MW for 3 h.
(Reproduced from [12])

A first parameter that was investigated is the influence of the solvent quantity. **MIL-53(Cr)** and MIL-101(Cr) were obtained *via* an experimental setup with the same amounts of starting reagents but with different quantities of solvent. The XPRD patterns of the crystals obtained *via* two different synthesis pathways are plotted in Figure 5.3, SOL (left) and MW (right). By comparing them with the theoretical XRPD pattern in Figure 5.2, (right), it was found that **MIL-53(Cr)** formation is clearly preferred when the reagent concentrations are high, MIL-101(Cr) is preferentially produced at low reagent concentrations (higher dilution). **MIL-53(Cr)** is selectively obtained when the H_2O/Cr ratio for SOL remains underneath 150 and for MW underneath 250. The authors

demonstrate in Figure 5.4 clearly that the yield of **MIL-53(Cr)** decreases with increasing water content. However, increasing yield of MIL-101(Cr) is observed at higher water content and this is representative for both synthesis methods.

Time is a second key parameter to take into account. The calculated yields in the SOL and MW synthesis at variable time for **MIL-53(Cr)** and MIL-101(Cr) are described in Figure 5.5, SOL (left), MW (right). The data is extracted from XRPD analysis of the as-synthesized compounds.

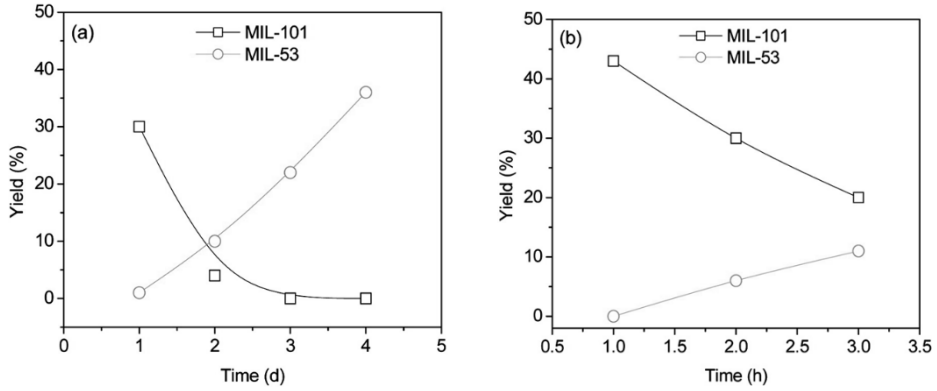

Figure 5.5 Yields of Cr-BDCs depending on the reaction time and methods with reaction composition 1 $CrCl_3.6H_2O$/1 H_2BDC/400 H_2O at 210 °C: (left) SOL; (right) MW. (Reproduced from [17])

Particularly, the longer the crystals are left to age in the reaction mixture, the more they transform to **MIL-53(Cr)**, as can be seen from both figures. The study established that MIL-101(Cr) can be converted in **MIL-53(Cr)**. Since this transition is based on the relative stabilities of the two materials, they conclude that **MIL-53(Cr)** is more stable than MIL-101(Cr) under the used reaction conditions.

A last and very important factor is acidity. As shown in Figure 5.6, the yield of **MIL-53(Cr)** increases with lower pH values. This pH variation was realized by addition of NaOH or HCl. However, too low pH values are also not recommended as the experiments indicate that the yield strongly drops when the pH is lower than 1.5, and in this case the synthesis becomes very inefficient. This effect is rather complex, from literature reports it is known that prior to the construction of MIL-101(Cr) framework chromium trimers, also called super tetrahedron (ST), are necessary to build up. It has

been previously reported [18] that this ST concentration increases with decreasing monomer concentration and increasing pH. This can explain the increase in yield of MIL-101(Cr) crystals at increasing pH.

Formation of Cr-BDCs MIL-101 and MIL-53 can be controlled by changing the synthesis and thermodynamic parameters. Diluted conditions (thus low reagent concentration), short contact time and high pH yield MIL-101(Cr) while opposite reaction conditions, high reagent concentrations, long contact time and low pH-results in **MIL-53(Cr)**.

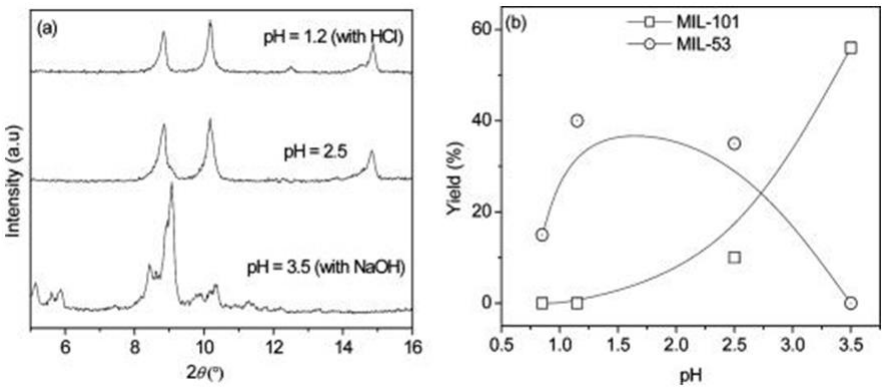

Figure 5.6 (left) XRPD patterns of as-synthesized Cr-BDCs depending on the pH of the reaction mixture. (right) Yields of Cr-BDCs depending on the pH of the reaction mixture. For both cases, the reaction was carried out for 10 min at 210 °C by MW heating. The composition of the reaction mixture was 1 $CrCl_3 \cdot 6H_2O$/1 H_2BDC /100 H_2O, and aqueous NaOH or HCl solution was used to control the pH. (Reproduced from [12])

5.3 Kinetic factors for MIL-47(V) and MIL-53(Cr)

Besides the thermodynamic factors, also the kinetic factors are of major importance. Understanding the kinetics of the monometallic frameworks in different synthesis methods US, MW and SOL for **MIL-47(V)** and **MIL-53(Cr)** is summarized underneath. This data can be useful to explain the nucleation and growth of a crystalline material and so the final dispersion of metal ions in the mixed-metal crystal.

The advantage of the MW synthesis of porous materials is the speed-up of the reaction resulting in a fast synthesis of MOFs. Different studies were executed regarding the synthesis of BDC based MOFs and all reported rates of nucleation and crystal growth follow the sequence: US > MW > SOL, for more information about these methods can be found in Chapter 1. Jhung and co-workers [19] explained the MW assisted acceleration in terms of kinetic parameters: activation energy (E_a), pre-exponential factor (A) and nucleation and crystal growth rates. These factors are determined from the crystallization curves presented for MIL-53(Al), **MIL-53(Cr)** and **MIL-47(V)** in Figure 5.7, with MW (A, C, E) and SOL (B, D, F). A crystallization curve plots the relative crystallinity as a function of the crystallization time. The phases of the products are identified *via* XRPD, mostly comparing one or more relative intensities of a diffraction peak of the as-synthesized MOFs, with a fully crystallized sample prepared under certain reaction conditions.

The relative rates of nucleation and crystal growth were estimated from the crystallization curve, induction period and slope of the curve. The first factor, the nucleation rate, is calculated from the value 1/(nucleation time). The induction period or nucleation time is the time required to observe any crystallinity (XRPD intensity of 0-5 % to the fully crystallized samples). The second factor, crystal growth rate is determined *via* the slope of the crystallization curve with a crystallinity between 20 % and 80 %.

The pre-exponential factor (A) and activation energies (E_a) are calculated *via* the Arrhenius equation (1) :

$$k = Ae^{-E_a/RT} \quad (1)$$

$$\ln k = \ln A - \frac{E_a}{R}\frac{1}{T} \quad (2)$$

E_a and A are derived from the slope and intercept of the logarithm of the Arrhenius equation (2), respectively. The final relative rate (r_{MW}/ r_{SOL}) is calculated with the Arrhenius equation at medium temperature.

Table 5.1 Relative reaction rates at 150 °C for the SOL synthesis of MIL-47(V) and MIL-53(Al) compared to MIL-53(Cr).[20, 21]

Porous material (SOL)	Nucleation rate	Crystal growth rate
MIL-53(Cr)	1	1
MIL-53(Al)	31.4	18.3
MIL-47(V)	73.6	50.6

Table 5.2 Relative reaction rates calculated from experimental data at 150 °C for the MW synthesis of MIL-47(V) and MIL-53(Al) compared to MIL-53(Cr).[21]

Porous material (MW)	Nucleation rate	Crystal growth rate
MIL-53(Cr)	1	1
MIL-53(Al)	238.6	44.6
MIL-47(V)	487.5	201.0

Table 5.3 Relative reaction rates calculated from experimental data comparing the MW versus the SOL method for MIL-47(V) and MIL-53(Cr).[21]

MW vs SOL	Nucleation rate	Crystal growth rate
MIL-47(V)	15.5	5.0
MIL-53(Cr)	2.2	2.8

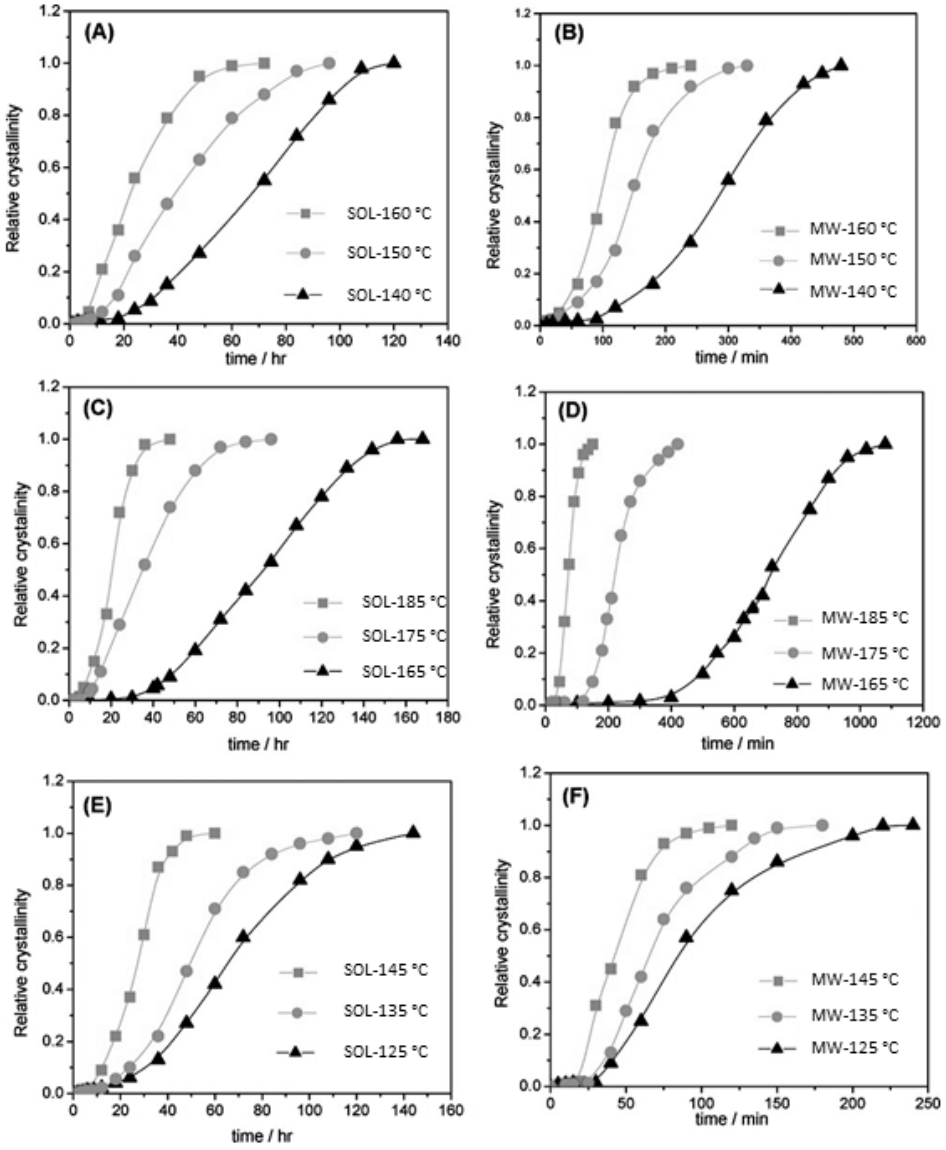

Figure 5.7 Crystallization curves of MOFs synthesized at various reaction temperatures: (A) MIL-53(Al) SOL synthesized; (B) MIL-53(Al) MW synthesized; (C) MIL-53(Cr) SOL synthesized; (D) MIL-53(Cr) MW synthesized; (E) MIL-47(V) SOL synthesized; (F) MIL-47(V) MW synthesized. (Reproduced from [21])

Table 5.1 and 5.2 presents the relative nucleation and crystal growth rates for the SOL and MW methods. The data shows that the rates follows the sequence: **MIL-47(V)** > MIL-53(Al) > **MIL-53(Cr)**. Table 5.3 is obtained by dividing the rate constants (k) calculated *via* the Arrhenius equation for the MW methods by the rate constant of compound **MIL-47(V)** *via* the SOL method. The relative nucleation rate of **MIL-47(V)** is 15.5 versus 2.2 for **MIL-53(Cr)**. This difference in nucleation rate could explain the formation of the egg-yolk structure. During the synthesis, first mainly the V nucleates, mixed with small quantities of Cr. Once most V is used, the only metal leftover Cr, creates a shell around the bimetallic core.

5.4 Experimental section

All chemicals (Table 5.4 and 5.5) were bought from Sigma-Aldrich or TCI Europe and used without further purification.

DRIFTS measurements were recorded in the region of 3700-850 cm^{-1} on a Thermo Nicolet 6700 spectrometer, equipped with a N_2-cooled MCT-A detector and a KBr beam splitter at 393 K under vacuum. Raman spectra were obtained on an RXN1 Raman spectrometer (Kaiser Optical Systems) equipped with a 532 nm laser operating at 40mW using an optical probe at RT in air. X-ray fluorescence (XRF) spectroscopy measurements were performed using an energy-dispersive Rigaku NexCG spectrometer equipped with a silicon drift detector. Prior to the analysis, compounds were mounted in a plastic cup containing a Prolene film. XRPD were collected on a Thermo Scientific ARL X'Tra diffractometer. *In situ* T-XRPD in air was carried out on a Bruker D8 Discover XRPD system equipped with a Cu-X-ray source (λ= 1.5406 Å) and a linear X-ray detector. The powder samples were mounted on a silicon wafer and placed on the heating stage. Measurements were carried out in air under atmospheric pressure. The sample was heated from RT to 450 K and finally cooled down to RT at a heating/cooling rate of 5 K min^{-1}. The temperature was measured with a K-type thermocouple. Data were collected in a time frame of 10 s per total scan. TGA were performed on a Netzsch STA 449 F3 Jupiter-simultaneous thermogravimetric - differential scanning calorimetry (TG-DSC) analyzer in the temperature range of 25 - 800 °C under air and with a heating rate of 2 °C min^{-1}. N_2 sorption measurements were done on a Belsorp Mini (Bel Japan, Inc.) apparatus at 77 K. Prior to the measurements, the activated samples (activation see section 5.5) were degassed at 353 K for 2 hours.

BF-STEM EDX was performed on a JEOL JEM-2200FS high resolution scanning transmission electron microscope equipped with an EDX spectrometer with a spatial resolution of 0.13 nm, image lens spherical aberration corrector, electron energy loss spectrometer (filter) and an field emission gun operating at 200 KeV.

Equilibrium isotherms of CO_2 were measured using the static volumetric method using an Isorb-HP1 device from Quantachrome. The measurements were performed at RT, the cell temperature was stabilized *via* an external heating bath and on board

monitored. Approximately 150 mg of sample was loaded in the stainless steel sample holder. Before each measurement, the activated powder was degassed with a heating stage of 2 K min^{-1} to 363 K and kept at this temperature for 2 hours (activation procedure see section 5.5).

Table 5.4 Overview of the amount of solvent, linker and metal ratio of the different samples synthesized *via* the MW procedure.

*Sample name	BDC (mmol)	Vanadium (mmol)	Chromium (mmol)	Theoretical Cr concentration (mol%)	Experimental Cr concentration (mol%)
MIL-47(V)	1.66	1.66	0.00	0	0
1	1.66	1.41	0.25	15	5
2	1.66	1.16	0.5	30	10
3	1.66	0.83	0.83	50	23
4	1.66	0.50	1.16	70	50
5	1.66	0.25	1.41	85	75
MIL-53(Cr)	1.66	0.00	1.66	100	100

* For all syntheses 167 mmol of demineralized water is used.

Table 5.5 Overview of the amount of solvent, linker and metal ratio of the different samples synthesized *via* the SOL procedure.

*Sample name	BDC (mmol)	Vanadium (mmol)	Chromium (mmol)	Theoretical Cr concentration (mol%)	Experimental Cr concentration (mol%)
MIL-47(V)	2.21	8.73	0.00	0	0
1	2.21	7.42	1.31	15	7
2	2.21	6.11	2.62	30	13
3	2.21	4.37	4.37	50	17
4	2.21	2.62	6.11	70	37
5	2.21	1.31	7.42	85	58
MIL-53(Cr)	2.21	0.00	8.73	100	100

* For all syntheses 899 mmol of demineralized water is used.

5.5 Synthesis

An overview of the synthesis method for these MOF materials is presented in Figure 5.8. The reagent concentrations are summarized in Table 5.4 and 5.5.

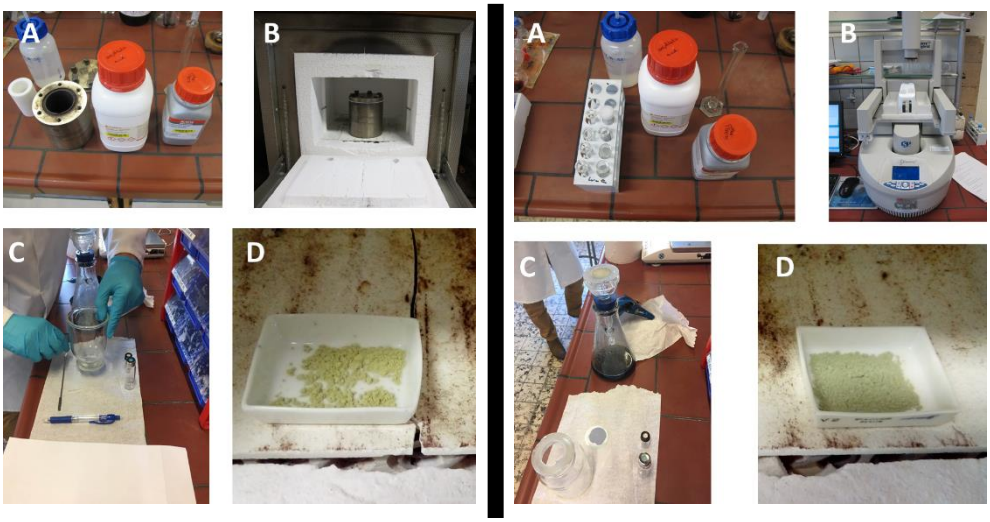

Figure 5.8 Visualization of the synthesis steps:
(A) starting reagents; (B) synthesis setup, the reaction mixture is added to a sealed autoclave equipped with an internal Teflon liner, heating takes place in a muffle furnace; (C) filtration of the crystalline compound; (D) calcination (left) SOL; (right) MW.

5.5.1 Microwave procedure

All MW synthesis are performed in a CEM Discover SP microwave using Pyrex pressure reaction tubes of 10 mL (Chapter 1, section 1.6.2 explains the MW synthesis method). The tubes are equipped with a magnetic stirring bar and sealed with a silicon cap. Before the start of the synthesis, the reagents are stirred for 2 minutes to obtain a homogeneous distribution. In a next step the mixture is heated under mild stirring to 473 K at 200 W and held under these conditions for 3 h with a pressure platform set at 23 bar. Afterwards all crystals are filtered and washed three times with distilled water and twice with acetone.

(MIL-53(Cr)): The synthesis of **MIL-53(Cr)** is based on the work of Kahn *et al*. [12] In this synthesis, the parameters are slightly adapted to an equimolar ratio of $CrCl_3.6H_2O$ and terephthalic acid of 1.66 mmol. Both components are mixed in a MW tube, 167

mmol of deionized water (0.05 µS/cm) is added and the general MW procedure is followed as described above. Finally a grey crystalline material is obtained.

(MIL-47(V)): The synthesis of MIL-47(V) is based on an adapted recipe reported by Centrone *et al.* [11] Equimolar ratios, both 1.66 mmol, of anhydrous VCl_3 and terephthalic acid are combined in a microwave tube together with 167 mmol of deionized water. Afterwards a yellow solid is collected.

($MW_{Cr(x)-V(1-x)}$): An amount of 167 mmol deionized water and 1.66 mmol terephthalic acid are added to the microwave tube. The total sum of metal salts is held fixed at 1.66 mmol and contains a mixture of anhydrous VCl_3 and $CrCl_3.6H_2O$. The experimental concentrations are listed in Table 5.4.

5.5.2 Solvothermal procedure

All solvothermal syntheses (SOL) are performed in a Nabertherm muffle furnace with an operation temperature between 293 K - 1673 K (Chapter 1, section 1.6.1 discusses the solvothermal synthesis). All reagents are added to a Teflon holder and placed in an ultrasonic bath for 5 min at RT. Afterwards the holder is inserted in a stainless steel autoclave and sealed. The reaction mixtures are heated 2 K min^{-1} to 473 K, kept under these conditions for 96 h. In a final step the crystals are collected *via* filtration and washed three times with distilled water and twice with acetone.

(MIL-53(Cr)): The synthesis of **MIL-53(Cr)** is based on earlier work of Serre. [13, 22] In this synthesis, the parameters are slightly adapted, a molar ratio of 8.73 mmol $CrCl_3.6H_2O$ and 2.21 mmol terephthalic acid are added to the Teflon liner. Afterwards 899 mmol deionized water (0.05 µS/cm) is added, finally a grey solid is obtained.

(MIL-47(V)): The synthesis of **MIL-47(V)** is based on the recipe of Leus and Barthelet. [14, 23] The Teflon liner is filled with 8.73 mmol anhydrous VCl_3 and 2.21 mmol terephthalic acid. In a next step both reagents are immersed in 899 mmol deionized water, afterwards the yellow solid is collected.

(SOL$_{Cr(x)-V(1-x)}$): An amount of 899 mmol deionized water and 2.21 mmol terephthalic acid are loaded in a Teflon holder. The total sum of metal salts is 8.72 mmol and contains of a mixture of VCl_3 and $CrCl_3.6H_2O$. The experimental concentrations are listed in Table 5.5.

5.6 Results and discussion

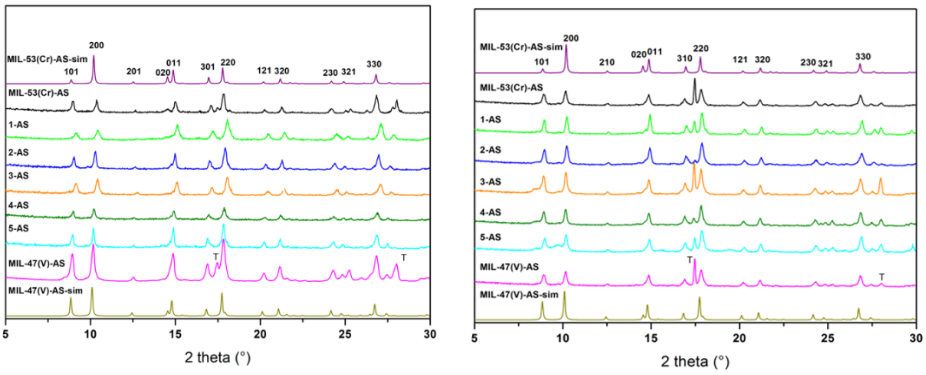

Figure 5.9 XRPD data between 0 - 30° of (left) SOL synthesized mixed-metal series 1-5 and monometallic MIL-53(Cr) and MIL-47(V); (right) MW synthesized mixed-metal series 1-5, monometallic MIL-53(Cr) and MIL-47(V). In both graphs, simulated (sim) diffraction patterns of MIL-53(Cr) and MIL-47(V) are presented. T in the spectra indicates the diffractions of terephthalic acid.

For both synthetic routes, two sets of seven samples have been prepared. The complete monometallic frameworks **MIL-47(V)** and **MIL-53(Cr)** are start and end points of the sequence. In between, *via* both MW and SOL, five bimetallic Cr/V structures labeled from 1-5 were synthesized. The structural integrity of the compounds was confirmed by XRPD (Figure 5.9, left SOL, right MW). The absolute Cr/V concentration of the compounds is determined *via* XRF analysis as shown in Figure 5.10.

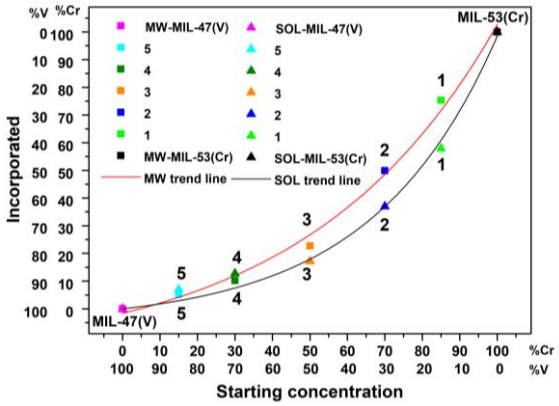

Figure 5.10 XRF analysis of mixed compounds 1-5, MIL-53(Cr), MIL-47(V) synthesized *via* MW (squares, red curve) and SOL (triangles, black curve) method.

The results indicate that vanadium is the most abundant cation in the framework and is preferentially incorporated in the structure, regardless of the synthesis method. This observation is in line with an earlier report, in which the authors prove that the nucleation and growth rates of **MIL-47(V)** are 73.6 and respectively 50.6 times faster than for **MIL-53(Cr)** during solvothermal synthesis when using V^{3+} and Cr^{3+} salts. [20, 21] A literature overview of nucleation and growth rates of MIL-53 metal analogues can be found in Table 5.1 and 5.2. The as-frameworks contain free terephthalic linker, this organic moiety is removed by a thermal treatment at 573 K for 21h45 in air. The activated bimetallic frameworks are labeled with the Cr_xV_{1-x} ratios in subscript, with experimental values (Table 5.4 and 5.5) as determined *via* XRF on the bulk phase. TGA analysis of the activated frameworks reveals that the structures are stable up to 400 °C under oxygen atmosphere (Figure 5.11).

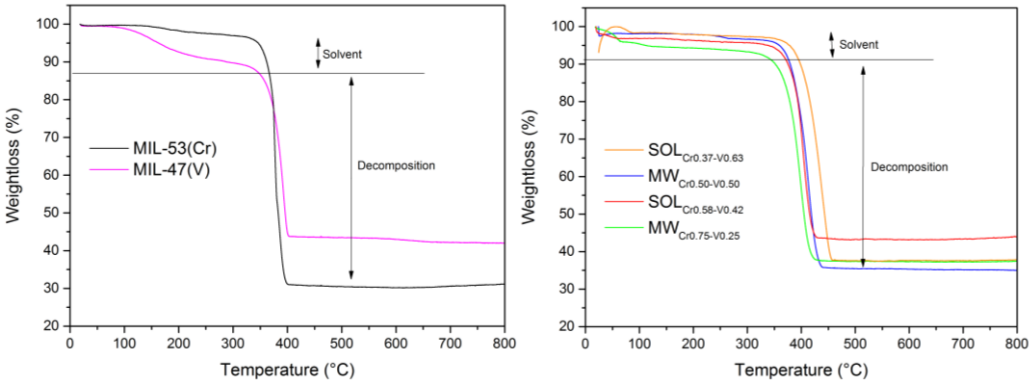

Figure 5.11 TGA analysis between 25-800°C in air; (left) compounds MIL-47(V), MIL-53(Cr); (right) mixed-metal frameworks $SOLCr_{0.37}$-$V_{0.63}$, $MWCr_{0.50}$-$V_{0.50}$, $SOLCr_{0.58}$-$V_{0.42}$ and $MWCr_{0.75}$-$V_{0.25}$.

The Langmuir surface area (Table 5.6) of the compounds varies between 1345 $m^2\ g^{-1}$ and 1550 $m^2\ g^{-1}$, completely in agreement with earlier literature reports. [13, 23] DRIFTS and Raman measurements are presented in Figure 5.12. The spectra give clear evidence for the presence of both vanadyl and chromium hydroxide moieties. The N_2 adsorption isotherms of all activated frameworks follow a type I isotherm, characteristic for microporous materials shown in Figure 5.13.

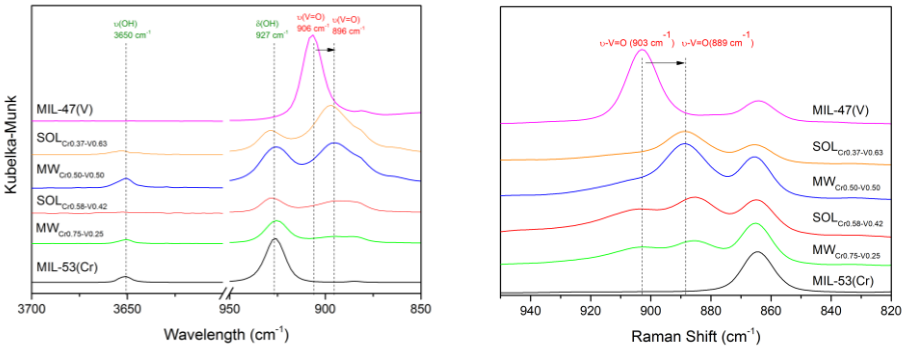

Figure 5.12 (left) DRIFTS spectra in the region between 3700-3600 and 950-850 cm^{-1}; (right) Raman spectra in the region between 950-820 cm^{-1} of both compounds MIL-47(V), $SOL_{Cr0.37\text{-}V0.63}$, $MW_{Cr0.50\text{-}V0.50}$, $SOL_{Cr0.58\text{-}V0.42}$, $MW_{Cr0.75\text{-}V0.25}$ and MIL-53(Cr).

The position of Cr- and V-ions in the crystals is investigated by BF-STEM EDX, the results are presented in Figure 5.14 (A to D). The figure shows that not all synthesis methods result in a homogeneous dispersion of metal ions. During TEM analysis, line EDX measurements were recorded at the edge and in the center of the crystal, giving an indication of the variation in metal concentration. The analysis has been performed on four compounds, two bimetallic frameworks obtained *via* MW method: **$MWCr_{0.75\text{-}V0.25}$**, **$MWCr_{0.50\text{-}V0.50}$** and two *via* SOL method: **$SOL_{Cr0.37\text{-}V0.63}$**, **$SOLCr_{0.58\text{-}V0.42}$**. It shows clearly that the MW treatment results in "egg yolk" type materials with a core of mixed-metal **MIL-53(Cr/V)** surrounded by a crust or shell of almost pure **MIL-53(Cr)**. The much slower SOL method results in one homogeneous phase.

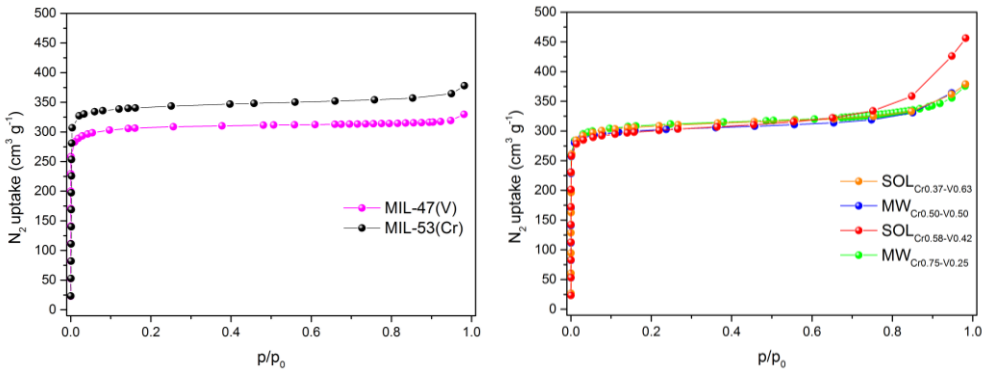

Figure 5.13 N_2 adsorption isotherms from 0-1 bar at 77 K; (left) compounds MIL-47(V), MIL-53(Cr); (right) mixed-metal frameworks $SOL_{Cr0.37\text{-}V0.63}$, $MW_{Cr0.50\text{-}V0.50}$, $SOL_{Cr0.58\text{-}V0.42}$ and $MW_{Cr0.75\text{-}V0.25}$.

These results are summarized in Table 5.6. The SOL crystals clearly show a uniform dispersion of metal ions in the lattice (Figure 5.14 (A and B)) with no variation of the metal ratio. The MW method (Figures 5.14 (C and D)) provides core-shell compounds with a mixed core and a monometallic chromium shell. EDX analysis indicates a decrease of 25 % Cr for **MW$_{Cr0.50\text{-}V0.50}$** and 5% Cr for **MW$_{Cr0.75\text{-}V0.25}$** moving from the edge to the crystal center.

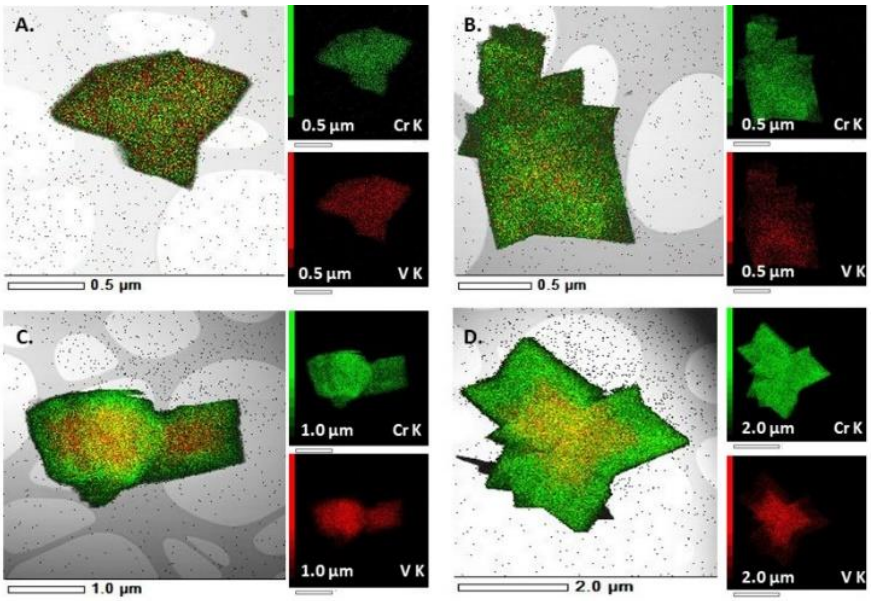

Figure 5.14 BF-STEM EDX mapping of chromium (green) and vanadium (red) on a mixed-metal particle: (A) SOL$_{Cr0.37\text{-}V0.63}$; (B) SOL$_{Cr0.58\text{-}V0.42}$; (C) MW$_{Cr0.50\text{-}V0.50}$ and (D) MW$_{Cr0.75\text{-}V0.25}$.

The way the core-shell structure is formed stays still unclear, although we speculate that the determining factor for the metal distribution is the synthesis time. One factor that confirms this speculation is the solvothermal method which results in a better dispersion and avoids the formation of a core-shell structure. To investigate the framework flexibility, T-XRPD between 300 K - 450 K and CO_2 sorption measurements at 298 K have been performed on the activated MW and SOL compounds. The T-XRPD results are summarized in Figure 5.15 (A to F).

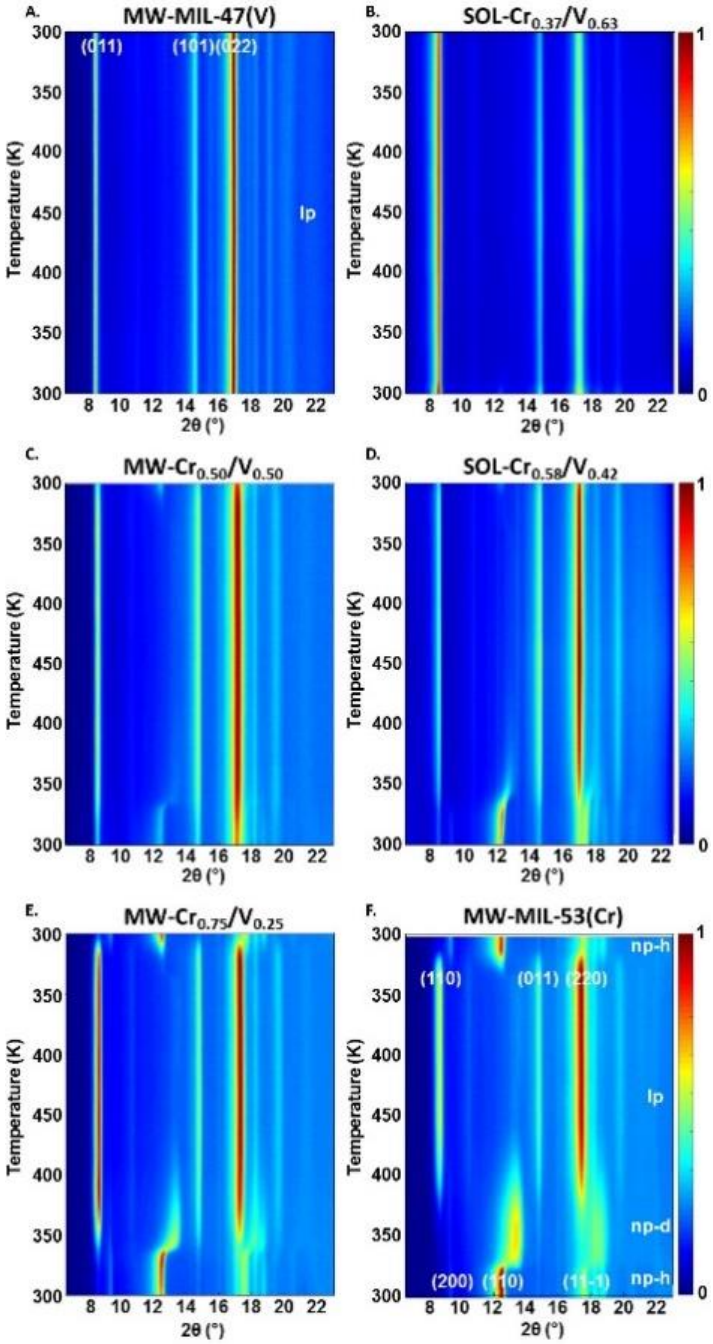

Figure 5.15 T-XRPD measurements in air between 300 K - 450 K in the 2theta range 6 - 23°. (A) MW-MIL-47(V); (B). $SOL_{Cr0.37\text{-}V0.63}$; (C) $MW_{Cr0.50\text{-}V0.50}$; (D) $SOL_{Cr0.58\text{-}V0.42}$; (E). $MW_{Cr0.75\text{-}V0,25}$; (F) MW-MIL-53(Cr); with the Miller indices for all high intensity peaks for np-h (bottom) and the lp (top).

Table 5.6 Overview of the EDX data *via* line analysis of Cr and V at the edge and in center of the crystal. In the final right column the surface area of the compounds after activation is presented.

Sample name	Chromium edge (mol%)	Vanadium edge (mol%)	Chromium center (mol%)	Vanadium center (mol%)	Langmuir surface area (m^2g^{-1})
MIL-47(V)	n.a*	n.a*	n.a*	n.a*	1368
$SOL_{Cr0.37-V0.63}$	50	50	50	50	1415
$MW_{Cr0.50-V0.50}$	85	15	60	40	1418
$SOL_{Cr0.58-V0.42}$	82	18	82	18	1405
$MW_{Cr0.75-V0.25}$	93	7	88	12	1345
MIL-53(Cr)	n.a*	n.a*	n.a*	n.a*	1550

* n.a.: not analyzed, theoretical values of single metal compounds are expected.

The pure vanadium **MW-MIL-47(V)** stays in the **lp** phase throughout the complete investigated temperature range (300 K - 450 K, Figure 5.15 (A)). On the contrary, the **MW-MIL-53(Cr)** (Figure 5.15 (F)), similar as its aluminum variant MIL-53(Al) [2, 24] has a flexible framework, that can adopt a hydrated narrow pore (**np-h**), a dehydrated narrow pore (**np-d**) and a large pore (**lp**) state. [25] At the start of the experiment, **MW-MIL-53(Cr)** is at RT and has been exposed to (humid) air for considerable time. As a result the framework is in the **np-h** state. Upon heating two transformations occur. At 325 K, all XRPD peaks shift towards larger 2Θ values (smaller spacing's between lattice planes) and broaden. We assign this rather abrupt change to the dehydration (**np-d**) of the framework. Between 375 and 425 K the XRPD pattern undergoes a second, more drastic change, as an increasing fraction of the sample transforms into the **lp** state, and above 425 K this state is practically exclusively present.

Cooling down in air, near RT a retransformation to the **np-h** structure occurs. Substituting 25 mol% of the Cr by V increases the stability of the **lp** state, which now already appears at 350 K (Figure 5.15 E). The complete disappearance of **np-d** fraction occurs at only slightly lower temperature (420 K) in comparison with pure **MW-MIL-53(Cr)**. The desorption of water, on the other hand, is significantly delayed: it occurs between 325 and 350 K. By introducing V in the framework, not only the **lp** state gets more stable, also the binding strength between water and framework increases.

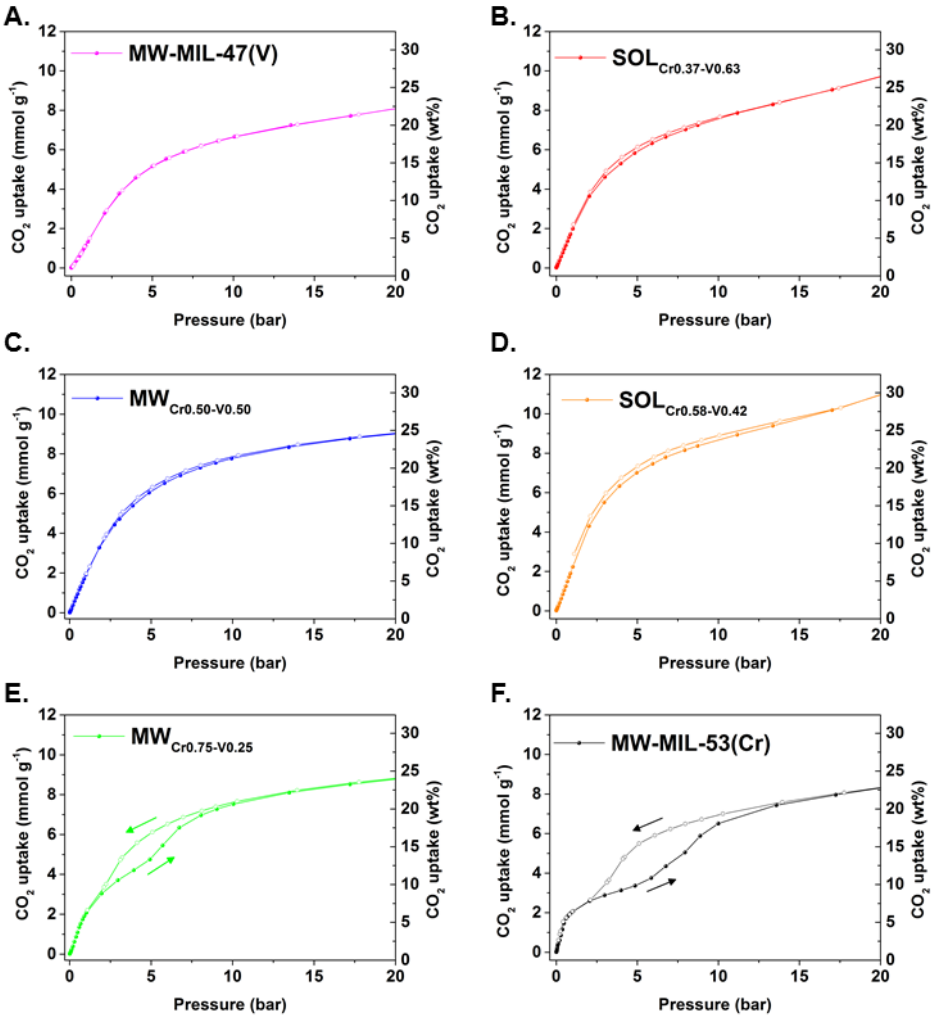

Figure 5.16 CO_2 adsorption-desorption isotherms at 298 K of (A) MW-MIL-47(V); (B) $SOL_{Cr0.37\text{-}V0.63}$; (C) $MW_{Cr0.50\text{-}V0.50}$; (D) $SOL_{Cr0.58\text{-}V0.42}$; (E) $MW_{Cr0.75\text{-}V0.25}$; (F) MW-MIL-53(Cr).

These findings are confirmed by the results on the other bimetallic MOFs (Figure 5.15 (B to E)). The onset of transition from **np-d** to **lp** drops steadily from 420 K for 75 mol% Cr to 340 K for 58 mol% Cr, and for the samples with 50 and 37 mol% Cr a considerable fraction of the sample remains in the **lp** state throughout the whole temperature range. At the same time, the temperature range in which the **np-d** form **MW-MIL-53(Cr)** occurs shirks.

We have performed high pressure CO_2 sorption on these samples as well, results are shown in Figure 5.16 (A to F). The compounds are originally in their **lp** state after onboard activation, water is removed after activation, **np-h** is not under discussion in this paragraph. The CO_2 adsorption and desorption isotherms of the bimetallic frameworks are compared to the monometallic **MW-MIL-53(Cr)** and **MW-MIL-47(V)**. Exposing the frameworks to CO_2, the **MW-MIL-53(Cr)** structure (Figure 5.16 (F)) exhibits a stepped adsorption isotherm. [26] On the contrary, the **MW-MIL-47(V)** structure (Figure 5.16 (A)) is known to be structurally rigid in the V^{4+} state. [27] The sorption isotherms of the **MW-MIL-47(V)**, the **MWCr$_{0.50\text{-}V0.50}$**, **SOLCr$_{0.37\text{-}V0.63}$** and **SOL$_{Cr0.58\text{-}V0.42}$** compounds follow a type I adsorption isotherm with no distinct breathing behaviour (Figure 5.16 (A to D)). Increasing the chromium concentration increases the flexibility, as seen in sample **MW$_{Cr0.75\text{-}V0.25}$** which shows a stepped isotherm (Figure 5.16 (E)). This latter compound is in an intermediate phase between the pure Cr (flexible) and V (rigid) solids with a reduced flexible behaviour in CO_2 adsorption. The final **MW-MIL-53(Cr)** (Figure 5.16 (F)) compound has a structure which is the easiest to open up and exhibits the largest hysteresis effect. All structures have a total uptake between 8-10 mmol g^{-1} of CO_2 at 20 bar, corresponding with literature reports. [26, 27] The boundary for flexibility is located between 25 - 50 mol% of vanadium.

5.7 Conclusion

In summary, we discovered that the synthesis method determines the organization of the metal ions in the bimetallic **MIL-53(Cr/V)** frameworks. BF-STEM EDX mapping clearly shows that the MW method results in "egg yolk" MOFs with a central Cr/V core surrounded by a chromium shell. This was the first time that a MW method was used to create MIL-53 bimetallic frameworks. Meanwhile the solvothermal synthesis gives homogeneous bimetallic Cr/V MOFs. The synthesis time and method have a crucial influence on the metal dispersion in the crystals. To understand the growth of the mixed-metal crystals, from reagents towards the final framework for both MW and SOL, further research is still necessary. Higher chromium concentration results in a more flexible structure with decreased **lp** and stabilization of the **np-d** fraction. Already from 37 mol% Cr a small part of the crystals behaves flexible in T-XRPD, while for CO_2 sorption at 298 K the flexibility appears at 75 mol% Cr.

5.8 References

1. O. Kozachuk, M. Meilikhov, K. Yusenko, A. Schneemann, B. Jee, A.V. Kuttatheyil, M. Bertmer, C. Sternemann, A. Pöppl and R.A. Fischer, *European Journal of Inorganic Chemistry*, 2013, **2013**, 4546-4557.
2. I. Nevjestić, H. Depauw, K. Leus, G. Rampelberg, C.A. Murray, C. Detavernier, P. Van Der Voort, F. Callens and H. Vrielinck, *The Journal of Physical Chemistry C*, 2016, **120**, 17400-17407.
3. I. Nevjestić, H. Depauw, K. Leus, V. Kalendra, I. Caretti, G. Jeschke, S. Van Doorslaer, F. Callens, P. Van Der Voort and H. Vrielinck, *ChemPhysChem*, 2015, **16**, 2968-2973.
4. M. Mendt, B. Jee, D. Himsl, L. Moschkowitz, T. Ahnfeldt, N. Stock, M. Hartmann and A. Pöppl, *Applied Magnetic Resonance*, 2014, **45**, 269-285.
5. M. Mendt, B. Jee, N. Stock, T. Ahnfeldt, M. Hartmann, D. Himsl and A. Pöppl, *The Journal of Physical Chemistry C*, 2010, **114**, 19443-19451.
6. M.I. Breeze, G. Clet, B.C. Campo, A. Vimont, M. Daturi, J.-M. Grenèche, A.J. Dent, F. Millange and R.I. Walton, *Inorganic Chemistry*, 2013, **52**, 8171-8182.
7. F. Nouar, T. Devic, H. Chevreau, N. Guillou, E. Gibson, G. Clet, M. Daturi, A. Vimont, J.M. Greneche, M.I. Breeze, R.I. Walton, P.L. Llewellyn and C. Serre, *Chemical Communications*, 2012, **48**, 10237-10239.
8. X. Song, M. Oh and M.S. Lah, *Inorganic Chemistry*, 2013, **52**, 10869-10876.
9. X. Song, T.K. Kim, H. Kim, D. Kim, S. Jeong, H.R. Moon and M.S. Lah, *Chemistry of Materials*, 2012, **24**, 3065-3073.
10. L.J. Wang, H. Deng, H. Furukawa, F. Gándara, K.E. Cordova, D. Peri and O.M. Yaghi, *Inorganic Chemistry*, 2014, **53**, 5881-5883.
11. A. Centrone, T. Harada, S. Speakman and T.A. Hatton, *Small*, 2010, **6**, 1598-1602.
12. N.A. Khan, J.W. Jun and S.H. Jhung, *European Journal of Inorganic Chemistry*, 2010, **2010**, 1043-1048.
13. F. Millange, C. Serre and G. Ferey, *Chemical Communications*, 2002, **0**, 822-823.
14. K. Leus, M. Vandichel, Y.-Y. Liu, I. Muylaert, J. Musschoot, S. Pyl, H. Vrielinck, F. Callens, G.B. Marin, C. Detavernier, P.V. Wiper, Y.Z. Khimyak, M. Waroquier, V. Van Speybroeck and P. Van Der Voort, *Journal of Catalysis*, 2012, **285**, 196-207.
15. F. Carson, J. Su, A.E. Platero-Prats, W. Wan, Y. Yun, L. Samain and X. Zou, *Crystal Growth & Design*, 2013, **13**, 5036-5044.
16. N. Stock and S. Biswas, *Chemical Reviews*, 2012, **112**, 933-969.
17. N.A. Khan and S.H. Jhung, *Crystal Growth & Design*, 2010, **10**, 1860-1865.

18. S.H. Jhung, N.A. Khan and Z. Hasan, *CrystEngComm*, 2012, **14**, 7099-7109.
19. X. Zhang, B. Shen, X. Zhang, F. Wang, G. Chi and M. Si, *RSC Advances*, 2017, **7**, 5928-5936.
20. E. Haque, J.H. Jeong and S.H. Jhung, *CrystEngComm*, 2010, **12**, 2749-2754.
21. E. Haque, N.A. Khan, C.M. Kim and S.H. Jhung, *Crystal Growth & Design*, 2011, **11**, 4413-4421.
22. C. Serre, F. Millange, C. Thouvenot, M. Noguès, G. Marsolier, D. Louër and G. Férey, *Journal of the American Chemical Society*, 2002, **124**, 13519-13526.
23. K. Barthelet, J. Marrot, D. Riou and G. Férey, *Angewandte Chemie*, 2002, **114**, 291-294.
24. T. Loiseau, C. Serre, C. Huguenard, G. Fink, F. Taulelle, M. Henry, T. Bataille and G. Férey, *Chemistry-A European Journal*, 2004, **10**, 1373-1382.
25. Y. Liu, J.-H. Her, A. Dailly, A.J. Ramirez-Cuesta, D.A. Neumann and C.M. Brown, *Journal of the American Chemical Society*, 2008, **130**, 11813-11818.
26. C. Serre, S. Bourrelly, A. Vimont, N.A. Ramsahye, G. Maurin, P.L. Llewellyn, M. Daturi, Y. Filinchuk, O. Leynaud, P. Barnes and G. Férey, *Advanced Materials*, 2007, **19**, 2246-2251.
27. S. Bourrelly, P.L. Llewellyn, C. Serre, F. Millange, T. Loiseau and G. Férey, *Journal of the American Chemical Society*, 2005, **127**, 13519-13521.

6 *English summary and future prospects*

Metal-organic frameworks (MOFs) make up an interesting novel class of hybrid materials containing organic linkers that connect metal ions to form a three dimensional framework. This material category furthermore gains great attention owing to its potential as an emerging class of adsorbents for CO_2 storage and separation.

In this dissertation, two novel series of bimetallic smart MOF materials are developed. The effect of two parameters, temperature and gas adsorption, as triggers for their flexible behaviour is investigated. Chapter 4 and 5 elaborately describe the synthesis of the two bimetallic frameworks. An overview of the different systems that are scrutinized in this work is presented in Figure 6.1.

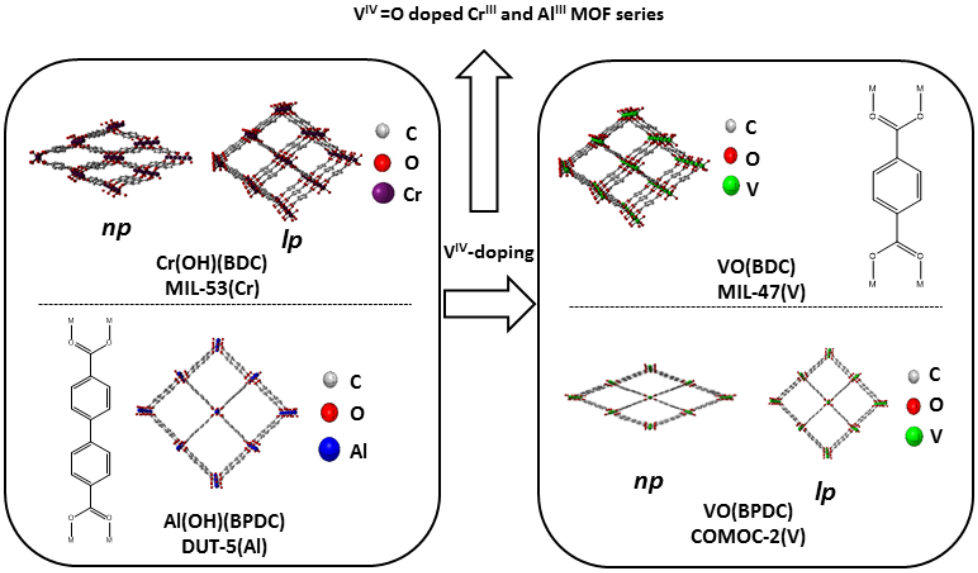

Figure 6.1 : Schematic representation of the doping of Cr and Al MOFs with V^{IV}=O.

The first project in Chapter 4 aimed at developing bimetallic Al/V MOFs based on a straightforward solvothermal synthesis method via conductional heating. Exactly 10 compounds, denoted as **COMOC-2-V_x-Al_{1-x}**, with a variable Al/V ratio were synthesized. After their successful synthesis, the materials were thoroughly characterized using a

variety of techniques. Temperature stability analysis indicated that increasing amounts of Al in the structure strongly enhance the stability of the framework. Moreover, quantitative metal analysis demonstrates that incorporating aluminium is in fact preferable. Analysis of the metal dispersion was subsequently performed via EPR and BF-STEM EDX. The combination of these techniques unambiguously showed a homogenous distribution over the crystal lattice.

This work also reports our observations regarding the adsorption of CO_2 by two large pore (**lp-1** and **lp-2**) and one narrow pore (**np**) structure in the **COMOC-2(V)** framework. At 232K in vacuum, the **COMOC-2(V)** structure contains a mixture of **lp-1** and **np**. The **np** phase was found to possess a monoclinic symmetry, whereas **lp-1** and **lp-2** exhibit an orthorhombic lattice. **DUT-5(Al)** remains rigid due to its structure's open **lp** form and is furthermore characterized by an orthorhombic crystal structure.

The compounds moreover show clear unique breathing behaviour. Such flexibility was thoroughly investigated by a combination of HP CO_2 synchrotron XRPD and adsorption-desorption experiments. A particular fraction of the **lp-1** closes during adsorption to a **np** state. In a final pressurizing step, a second and most importantly previously unrecognized **lp-2** fraction appears. The CO_2-XRPD analysis reveals that the incorporation of more aluminium in the framework leads to a faster (thus at lower pressure) transition from **np** to **lp-2**. Meanwhile, the height of the hysteresis loop decreases for the high pressure-adsorption-desorption measurements with increasing amount of aluminium. These observations prove that it is indeed possible to tailor the "breathing" behaviour of the vanadyl structure **COMOC-2(V)** via metal doping.

The 5th Chapter focuses on the second type of microporous bimetallic frameworks synthesized in this work. As a result of this research, these novel bimetallic combinations of **MIL-53(Cr)** and **MIL-47(V)** are now reported for the first time. Both synthesis methods were executed using identical V^{3+} and Cr^{3+} chloride salts dissolved in demineralized water. In one method the crystals are formed in a batch process via a very fast microwave procedure within 3 h, while in the solvothermal method resistive heating was applied over a time span of 96 h.

We discovered that the synthesis method has a strong impact on the organization of metal ions within the bimetallic **MIL-53(Cr_x/V_{1-x})** frameworks. BF-STEM EDX mapping shows "egg yolk" MOFs with a central Cr/V core surrounded by a chromium shell as a result of the MW method. It was the first time a MW method was used to create bimetallic MIL-53 frameworks as well as the first time that unmistakable proof was given for the heterogeneous distribution of two metals in one same MOF. In contrast, the SOL method yielded completely homogeneous mixed-metal MOFs. Our results indicate that the synthesis time and method are of crucial influence on the metal dispersion within the crystals.

To understand the growth of these mixed-metal crystals, from reagents towards the final framework for both MW and SOL, further research is without any doubt still necessary. The influence of Cr and V on the flexibility and breathing behaviour was examined by T-XRPD and CO_2 adsorption measurements. The **np-d** to **lp** transition temperature is observed to be higher when increasing Cr^{3+} concentration. Increasing the chromium concentration enhances the flexibility of the framework. Already from 37 mol% Cr, a small part of the crystals behaves flexible in T-XRPD, while in the CO_2 sorption experiments at 298 K the flexibility only appears at 75 mol% Cr.

The research performed in this dissertation and the literature overview presented in Chapter 1, 2 and 3, show that great opportunities still lie within the field of hybrid porous materials. However, many challenges remain to improve their overall properties.

It is clear from our work and the literature study that MOFs have real potential as gas adsorption and separation materials. These crystalline, sponge-like materials are applicable in multiple industrial applications because of their two key attributes: the easy tunability of the structure and extremely large surface areas.
It is important to harness the power of MOFs for large scale applications to solve present industrial limitations. Recent MOF materials came into the picture as promising adsorbents to separate, capture and store gasses, especially for atmospheric carbon containing molecules. Developing MOF based CO_2 capture technologies will allow CO_2 to be stored, preventing release into the atmosphere.

Innovative bimetallic MOFs offer possibilities to bridge the gap and solve problems of limited uptake, separation capacity and stability of the monometallic frameworks. Combining different metals into one single framework greatly increases the range of opportunities they have to offer. Moreover, such element synergetic behaviour strengthens both their qualities and could thus possibly create new materials with undiscovered capacities that can outperform other MOF materials in their field of application. Designing a multimetalic framework could offer a unique method to tailor the framework towards better adsorption uptake and/or separation capacity. However, research limitations such as the quantification of metal dispersion and organization in the lattice of the compounds need to be overcome first.

Key here is not only to enhance the adsorption capacity but also to understand the influence of different material characteristics (e.g., history, flexibility, and temperature) on the final separation capacity and adsorption uptake. Elaborated experimental research efforts are necessary to collect a broad data set of fundamental information to make predicting "smart MOF materials" feasible and realistic. Implementation of (flexible) MOFs at an industrial scale is still in its research stage yet.

7 *Nederlandstalige samenvatting en toekomstperspectieven*

Metaal organische roosters (MOFs) zijn een klasse van hybride, vaak poreuze materialen waar de afgelopen twee decennia intensief onderzoek naar is gevoerd. Een MOF is opgebouwd uit organische moleculen, de linkers, die via coördinatiechemie anorganische 'nodes' verbinden. Het resultaat is een driedimensionele kristallijne en poreuze netwerkstructuur. Een veel belovende toepassing van MOFs is de scheiding en adsorptie van CO_2. Dit vormt nog steeds een industriële uitdagingen, bovendien is CO_2 ongetwijfeld het belangrijkste broeikasgas.

Adsorptie en scheiding van gassen met monometallische MOFs zijn reeds intensief onderzocht. Diverse MOF structuren en een waaier aan gassen werden getest. Verschillende MOFs hebben de unieke eigenschappen dat hun rooster onder invloed van externe factoren (druk, temperatuur, solvent,…) gaat transformeren. Bij deze transformatie wijzigen de roosterparameters al dan niet omkeerbaar. Deze MOFs worden in de literatuur geklasseerd als flexible en ademende structuren, die een bewegingspatroon vertonen dat lijkt op dat van longen.

Tot op heden bleven MOFs met verschillende metalen in de nodes, de zogenaamde "multimetallische" MOFs uit het gezichtsveld van onderzoekers. Een extra metaal creëert echter een bijkomende vrijheid. Metaalnodes kunnen een synergetische werking vertonen, hetgeen nieuwe mogelijkheden biedt voor verscheidene toepassingen.

De synthese van nieuwe multimetallische MOFs is uitdagend gezien een extra metaal de synthesecondities sterk beïnvloedt. Twee nieuwe reeksen van bimetallische MOFs werden in deze thesis gemaakt. De invloed van temperatuur en de gasmolecule CO_2 op de flexibiliteit van de MOFs werden in beide reeksen grondig geanalyseerd.

De belangrijkste vraag bij het gebruik van meerdere metaalprecursoren is de finale dispersie in het kristalrooster. Deze dispersie kan homogeen of heterogeen zijn. Verscheidene analysetechnieken helpen deze vraag te beantwoorden en vaak is een combinatie van technieken noodzakelijk om tot een sluitend antwoord te komen. In deze scriptie wordt daarom beroep gedaan op twee analysetechnieken, een eerste is helderveld raster transmissie elektronen microscopie (BF-STEM) gekoppeld aan energie dispersieve X-straal spectroscopie (EDX), een tweede techniek is elektronen paramagnetische resonantie (EPR).

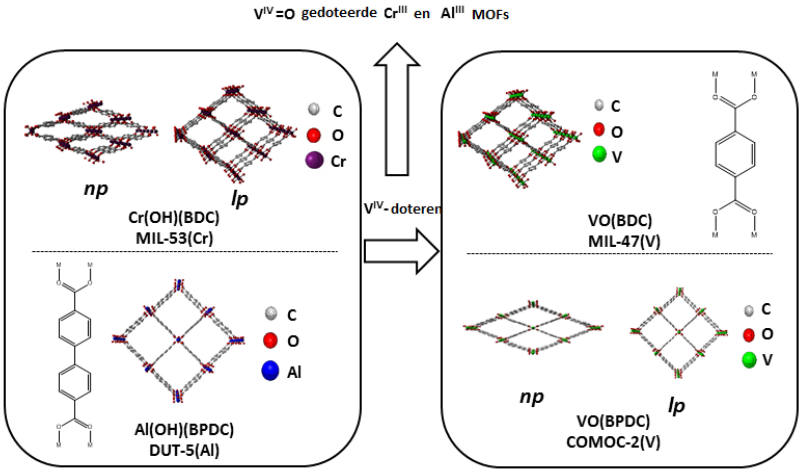

Figuur 7.1 : Schematische voorstelling van het doteren van Cr en Al MOFs met V^{IV}=O.

De eerste combinatie in deze scriptie wordt besproken in Hoofdstuk 4. Hier wordt de bimetallische MOF **COMOC-2-V_x-Al_{1-x}** gesynthetiseerd. De naam COMOC is de afkorting van onze onderzoeksgroep (Center for ordered materials organometallics and catalysis). **COMOC-2(V)** [V(O)(BPDC)] is de unieke vanadiumstructuur voor het eerst gesynthetiseerd door onze groep. Bij totale vervanging van vanadium door aluminium in de **COMOC-2(V)** structuur wordt **DUT-5(Al)** gevormd. DUT komt van *Dresden University of Technology*, de universiteit die deze structuur voor het eerst rapporteerde. Een schematisch overzicht van de uitwisseling wordt in figuur 7.1 geschetst. Uit onze analyse blijkt dat aluminium preferentieel incorporeert in de gedoteerde variant. Stapsgewijze introductie van aluminium in de vanadiumstructuur **COMOC-2(V)** maakt

het mogelijk de roosterflexibiliteit te verminderen. De toename van de aluminiumconcentratie in het rooster zorgt voor een verhoogd intern oppervlak en verhoogde thermische stabiliteit. Daarnaast bevestigen BF-STEM EDX en EPR de homogene distributie van Al en V in het rooster.

De coördinatie- en valentietoestand van vanadium en aluminium in het rooster werden geanalyseerd via geavanceerde spectroscopische technieken. De roosterflexibiliteit werd onderzocht via hogedruk synchrotron X-straal poeder diffractie (XRPD) en adsorptie-desorptie experimenten. Allereerst zijn tijdens dit onderzoek twee grote poriestructuren waargenomen voor **COMOC-2(V)** en voor de bimetallische **COMOC-2-V_x-Al_{1-x}** structuren. Deze grote poriefasen worden benoemd als **lp-1** en **lp-2** (**lp** = grote porievorm), daarnaast wordt een derde, gesloten porievorm **np** gerapporteerd. Twee vormen, de **lp-1** en de **np**, zijn stabiel onder vacuum bij 232 K. De gesloten **np** bezit een monoklinische symmetrie, terwijl de **lp-1** en **lp-2** beschreven worden als een orthorombische kristalstructuur. De aluminium variant **DUT-5(Al)** is een rigide, orthorombische **lp** stuctuur. Uit de bekomen resultaten kunnen we concluderen dat de flexibiliteit van **COMOC-2-V_x-Al_{1-x}** behouden blijft tot een Al/V ratio van 54/46.

De CO_2-XRPD analyse toont aan dat het inbouwen van grotere hoeveelheden aluminium de druk waarbij de transitie van **np** naar **lp-2** plaatsvindt verlaagt. Uit de hogedruk adsorptie-desorptie metingen, volgt dat bij toenemende concentratie van aluminium, de hoogte van de hysteresis afneemt. Dit toont aan dat metaaldotering in de vanadylstructuur **COMOC-2(V)** kan gebruikt worden om de flexibiliteit van het "ademen" te beïnvloeden.

In Hoofdstuk 5 wordt de bimetallische structuur **MIL-53-Cr_x-V_{1-x}** gesynthetiseerd (figuur 7.1). Verschillende tweemetalige MIL-53 structuren werden reeds beschreven : Al/V, Cr/Al, Fe/V en Cr/Fe, deze literatuur resultaten worden beschreven in Hoofdstuk 3. Andere combinaties waaronder Al/Fe en acht verschillende structuren met Ga en Sc werden tot op heden nog niet gerapporteerd. Alle publicaties van tweemetalige MIL-53 structuren maken gebruik van een éénpotsynthese, waaruit volgens de auteurs telkens homogene structuren worden bekomen. Dit toont aan dat metallische kationen op een gelijkaardige snelheid groeikernen vormen en verder aangroeien. De vorming van

inhomogene fasen wordt blijkbaar vermeden, hoewel tijdens het synthetiseren van MOFs, onder een welbepaald kinetisch regime, verschillende resultaten worden verwacht.

In dit onderzoek wordt voor het eerst vermeld dat de synthesemethode een beslissende factor is voor de finale metaaldispersie, en dit voor de **MIL-53(Cr/V)** structuur. De toegepaste microgolfsynthese resulteert in de vorming van "*egg-yolk MOFs*" met een kern van **MIL-53(Cr/V)** omringd door een schil van **MIL-53(Cr)**. De solvothermale synthese geeft homogeen gemengde structuren. Voor het in kaart brengen van deze dispersie werd de analysetechniek BF-STEM EDX gebruikt.

De twee gerapporteerde synthesemethodes komen voort uit literatuursrecepten. Hiervoor worden de metaalchloridezouten VCl_3 en $CrCl_3$ samen met de organische linker vóór de synthese opgelost in gedemineraliseerd water. De kristallen worden gevormd in een batchproces, gedurende 3 uur in de microgolf, terwijl dit voor de solvothermale synthese gebeurt in 96 uur.

Zowel de synthesetijd als de synthesemethode hebben een kritische invloed op de metaaldispersie in de kristallen. Om invloeden op de metaalverdeling en de vorming van de gemengde MOF's beter te begrijpen, zowel via de microgolfsynthese als solvothermale synthese, is bijkomend onderzoek echter noodzakelijk.

De invloed van Cr en V op de flexibiliteit en het ademend effect werd onderzocht via temperatuurafhankelijke XRPD en CO_2 adsorptiemetingen. Hoe hoger de Cr concentratie hoe meer dit kan resulteren in een flexibele structuur met verminderde stabiliteit van de **lp** fase. Dit resulteert eveneens in een stabilisatie van de **np-d** (gedehydrateerde **np**) toestand. Reeds vanaf 37 mol% Cr vertonen een welbepaald deel van de kristallen flexibiliteit in T-XRPD, terwijl in CO_2 adsorptie bij 298 K de flexibiliteit wordt waargenomen vanaf 75 mol% Cr.

MOFs zijn veelbelovende materialen voor gasadsorptie en gasscheiding. Door hun eenvoudige structurele aanpasbaarheid en extreem hoge oppervlakte zijn mogelijke toepassingen van deze materialen dan ook zeer ruim. MOFs worden vaak aangezien als veel belovende materialen voor verschillende toepassingen die momenteel economisch

of chemisch gezien nog niet realiseerbaar zijn. Deze poreuze materialen zijn als adsorbents uitermate geschikt voor het scheiden, opslaan en opvangen van atmosferische koolstofhoudende gassen. Bovendien maakt het ontwikkelen van MOF gebaseerde scheidingstechnologieën de opslag van CO_2 mogelijk en voorkomt het de uitstoot hiervan in de atmosfeer.

Innovatieve tweemetalige MOFs zijn in staat door de extra vrijheden gecreëerd door een additioneel metaal, de capaciteit, de scheidingsgraad en de stabiliteit te verhogen in vergelijking met de monometallische structuren. Door een doordachte keuze van de metaalnodes kan een synergetisch effect tussen de twee nodes gevormd worden. Hieruit kan een nieuw materiaal voortvloeien dat superieur is in zijn applicatiegebied. Bovendien is het mogelijk om door inbouw van een bijkomend metaal in de nodes de structuur toepassingsgericht te gaan modificeren. Een voorbeeld is het aanpassen van de poriëgrootte, affiniteit, enz… voor het optimaliseren van de adsorptie- en scheidingscapaciteit. Voor fundamenteel onderzoek is het belangrijk een correcte karakterisatie uit te voeren. De metaalverdeling in het rooster bepalen, blijft een uitdaging, hoewel dit een zeer belangrijke parameter is voor de finale eigenschappen en voor het verklaren van de resulterende materiaaleigenschappen.

Naast het verbeteren van de adsorptiecapaciteit, is ook het begrijpen van de materiaaleigenschappen (bv. flexibiliteit, voorgeschiedenis van het materiaal, invloed van de temperatuur,…) op de scheiding- en adsorptiecapaciteit een belangrijk aandachtspunt. Het verzamelen van fundamentele informatie zorgt voor een brede data set. Het doordacht synthesiseren van "*smart MOF materials*" komt hierdoor een stap dichterbij. Tot op heden bevindt het onderzoek naar twee- en multimetalige MOFs en hun applicaties zich nog in de onderzoeksfase. De vele industriële onderzoeksprojecten in verschillende onderzoeksdomeinen zijn een veelbelovende stap.

Addendum

Table A.1: Literature overview of reported mixed-metal MOFs, organized according to their family. In light blue articles published during this dissertation.

MIL	Metal*	Synthesis approach	Subject	Reference
MIL-53	Al^{3+}/Cr^{3+}	Direct Synthesis	Incorporation, Breathing	Mendt *et al*. [1, 2]
		Direct Synthesis	Incorporation, Breathing, Gas adsorption	Kozachuk *et al.* [3]
			Incorporation	Nevjestić *et al.* [4]
			Breathing	Nevjestić *et al.* [5]
			Breathing, Influence of oxygen	Nevjestić *et al.*[6]
			Catalysis	Timofeeva *et al.* [7]
	Cr^{3+}/Fe^{3+}	Direct Synthesis	Incorporation, Gas adsorption	Nouar *et al.* [8]
	Fe^{3+}/V^{3+}	Direct Synthesis	Incorporation	Breeze *et al.* [9]
	Cr^{3+}/V^{3+}	Direct Synthesis	Incorporation, Breathing	Depauw *et al.* [10]
MIL-53-Br	Al^{3+}/Fe^{3+}	Post-Synthetic exchange in H_2O	Incorporation	Min Kim *et al.* [11]
MIL-88B	Fe^{3+}/Ni^{2+}	Direct Synthesis	Incorporation	Wongs-akulphasatch *et al.* [12]
MIL-100	$Sc^{3+}/Cr^{3+}/Fe^{3+}/Al^{3+}$	Direct Synthesis	Incorporation, Catalysis	Mitchell *et al.* [13]

	Fe^{3+}/Ni^{2+}	Direct Synthesis	Incorporation	Wongsakulphasatch *et al.* [12]
MIL-101	$Cr^{3+}/Fe^{3+}/Al^{3+}$	Post-synthetic exchange in H_2O	Incorporation, Adsorption	Szilágyi *et al.* [11]
	Cr^{3+}/Fe^{3+}	Direct synthesis	Incorporation, Catalysis	Vu *et al.* [14]
		Post-synthetic exchange in Ethanol	Incorporation, Catalysis	Leng *et al.* [15]
	Cr^{3+}/Mg^{2+}	Direct synthesis	Adsorption	Zhou *et al.* [16]
MIL-127	Fe^{3+}/Ni^{2+}	Direct synthesis	Adsorption Incorporation	Wongsakulphasatch *et al.* [12]
	Fe^{3+}/Co^{2+}	Direct synthesis	Incorporation	Wongsakulphasatch *et al.* [12]
	Fe^{3+}/Mg^{2+}	Direct synthesis	Incorporation	Wongsakulphasatch *et al.* [12]
MIL-808	Zr^{4+}/Ce^{4+}	Direct synthesis	Incorporation	Lammert *et al.* [17]

MIL = Materials Institute Lavoisier; * = including oxidation state of the metal salts used during synthesis.

COMOC	**Metal***	**Synthesis approach**	**Subject**	**Reference**
COMOC-2	Al^{3+}/V^{4+}	Direct synthesis	Incorporation, Breathing	Depauw *et al*. [18]

COMOC = Center for Ordered Materials, Organosillica and Catalysis; * = including oxidation state of the metal salts used during synthesis.

UiO	Metal*	Synthesis approach	Subject	Reference
UiO-66	Zr^{4+}/Ti^{4+}	Post-synthetic exchange in DMF	Incorporation	Kim *et al.* [11]
	Zr^{4+}/Hf^{4+}			
	Zr^{4+}/Ti^{4+}	Post-synthetic exchange in DMF	Adsorption	Lau *et al.* [19]
	Zr^{4+}/Ce^{4+}	Direct synthesis	Incorporation	Lammert *et al.* [17]; Nouar *et al.* [20]
	Zr^{4+}/Ce^{3+}	Direct synthesis	Adsorption	Ebrahim *et al.* [21]
	Zr^{4+}/Ti^{4+}	Post-synthetic exchange in DMF	Separation	Smith *et al.* [22]
			Catalysis	Tu *et al.* [23]
UiO-66 $(NH_2)_x$	Zr^{4+}/Ti^{4+}	Post-synthetic exchange in DMF	Catalysis	Sun *et al.* [24]; Lee *et al.* [25]
UiO-67	Zr^{4+}/Ti^{4+}	Post-synthetic exchange in DMF	Photo-degradation	Amador *et al.* [26]
	Zr^{4+}/Ce^{3+}	Direct synthesis	Adsorption	Ebrahim *et al.* [21]
UiO-67-Ru	$Zr^{4+}/Ti^{4+}/Ru^{3+}$	Post-synthetic exchange in DMF	Photo-degradation	Amador *et al.* [26]

* = including oxidation state of the metal salts used during synthesis.

MOF	Metal*	Synthesis approach	Subject	Reference
MOF-5	Zn^{2+}/Co^{2+}	Post-synthetic exchange in DMF/MeCN	Thermo - dynamic study	Brozek *et al.* [27]
	Zn^{2+}/Ni^{2+}	Post-synthetic exchange in DMF		
	Zn^{2+}/Co^{2+}	Direct synthesis	Adsorption	Botas *et al.* [28]
	$Zn^{2+}/TiCl^{2+}$	Post-synthetic exchange in DMF	Incorporation, redox chemistry	Brozek *et al.* [29]
	Zn^{2+}/V^{2+}			
	Zn^{2+}/VCl^{2+}			
	Zn^{2+}/Cr^{2+}			
	$Zn^{2+}/CrCl^{2+}$			
	Zn^{2+}/Mn^{2+}			
	Zn^{2+}/Fe^{2+}			
MOF-14	Zn^{2+}/Co^{2+}	Post-synthetic exchange in DMF	Incorporation	Yao *et al.* [30]
	Zn^{2+}/Ni^{2+}			
	Zn^{2+}/Cu^{2+}			
MOF-74	Mg^{2+}/Co^{2+}	Direct synthesis	Incorporation	Wang *et al.* [31]
	$Mg^{2+}/Co^{2+}/Ni^{2+}/Zn^{2+}$			
	$Mg^{2+}/Co^{2+}/Ni^{2+}/Zn^{2+}/Sr^{2+}/Mn^{2+}$			
	$Mg^{2+}/Co^{2+}/Ni^{2+}/Zn^{2+}/Sr^{+2}/Mn^{2+}/Cd^{2+}/Ba^{2+}/Fe^{2+}/Ca^{2+}$			
	Zn^{2+}/Co^{2+}	Direct synthesis	Adsorption, Band gap energy	Botas *et al.* [32]
	Co^{2+}/Ni^{2+}	Direct synthesis	Adsorption	Villajos *et al.* [33]
	Mg^{2+}/Ni^{2+}	Direct synthesis	Incorporation, Adsorption	Howe *et al.* [34]
	Mg^{2+}/Cd^{2+}			
	Co^{2+}/Ni^{2+}	Post-synthetic exchange in DMF	Catalysis	Sun *et al.* [35]

	Mg^{2+}/Ni^{2+}	Direct synthesis	Incorporation Adsorption	Jiao *et al.* [36]
	Mg^{2+}/Co^{2+}			
	Cu^{2+}/Co^{2+}	Direct synthesis	Catalysis	Fu *et al.* [37]

MeCN = Acetronitril; * = including oxidation state of the metal salts used during synthesis.

HKUST	Metal*	Synthesis approach	Subject	Reference
HKUST-1	Cu^{2+}/Zn^{2+}	Direct synthesis	Incorporation, Adsorption	Jee *et al.* [38]
			Structural changes	Frieländer *et al.* [39]
			Spin lattice relaxation of Co and CO_2	Gul-E-Noor *et al.* [40]
			Adsorption of small molecules by solid-state NMR	Gul-E-Noor *et al.* [41]
			Three-pulse ESEEM on adsorption and desorption of deuterated H_2	Šimenas *et al.*[42]
		Post-synthetic exchange in methanol	Incorporation	Song *et al.* [43]
		Direct synthesis	Adsorption	Wang *et al.* [44]
	Cu^{2+}/Ru^{3+}	Direct synthesis	Incorporation	Gotthardt *et al.* [45]
	Cu^{2+}/Li^{+}	Direct synthesis	Adsorption	Cao *et al.* [46]
	Cu^{2+}/Na^{+}			
	Cu^{2+}/K^{+}			

* = including oxidation state of the metal salts used during synthesis.

ZIF	Metal*	Synthesis approach	Subject	Reference
ZIF-8	Zn^{2+}/Cu^{2+}	Direct synthesis	Catalysis	Schejn et al. [47]
	Zn^{2+}/Co^{2+}	Direct synthesis	Adsorption	Kaur et al.[48]
BM ZIF-20	Zn^{2+}/Co^{2+}	Direct synthesis	Catalysis	Chen et al. [49]
ZIF-71	Mn^{2+}/Zn^{2+}	Post-synthetic exchange	Incorporation	Fei et al. [50]

* = including oxidation state of the metal salts used during synthesis.

Compound	Metal*	Synthesis approach	Subject	Reference
$Al(OH)_{1-x}V(O)_x$ (1,4-NDC)	Al^{3+}/V^{3+}	Direct synthesis	Incorporation	Kozachuk *et al.* [3]
$[CoNi(\mu_3\text{-tp})_2(\mu_2\text{-pyz})_2]$	Co^{2+}/Ni^{2+}	Direct synthesis	Dye removal	Abbasi *et al.* [51]
CPM-4-M	In^{3+}/Co^{2+}	Direct synthesis	Incorporation	Zheng *et al.* [52]
CPM-15-M	$In^{3+}/Mg^{2+}/Mn^{2+}/Co^{2+}/Ni^{2+}/Cd^{2+}$		Incorporation, Adsorption	Zheng *et al.* [53]
CPM-16-M	$In^{3+}/Mn^{2+}/Co^{2+}/Ni^{2+}$		Incorporation	Zheng *et al.* [54]
CPM-17-M	$In^{3+}/Co^{2+}/Zn^{2+}$		Incorporation	Zheng *et al.* [54]
CPM-18-M	$In^{3+}/Nd^{3+}/Sm^{3+}$		Incorporation	Zheng *et al.* [55]
CPM-19-M	$In^{3+}/Nd^{3+}/Pr^{3+}$		Incorporation	Zheng *et al.* [55]
CPM-20-M	In^{3+}/Co^{2+}		Incorporation, Adsorption	Zheng *et al.* [55]
CPM-21-M	$In^{3+}/Mn^{3}/Co^{3+}/Cu^{3+}$		Incorporation	Zheng *et al.* [55]
CPM-23-M	In^{3+}/Mg^{2+}		Incorporation	Zheng *et al.* [55]
CPM-26-M	$In^{3+}/Co^{2+}/Zn^{2+}$		Incorporation	Zheng *et al.* [54]
CPM-31	In^{3+}/Zn^{2+}		Incorporation	Zheng *et al.* [52]
CPM-32	In^{3+}/Co^{2+}		Incorporation	Zheng *et al.* [52]
CPM-200	V^{3+}/Mg^{2+}		Adsorption	Zhai *et al.* [56]
	Fe^{3+}/Mg^{2+}			
	In^{3+}/Mg^{2+}			
	In^{2+}/Ni^{2+}			

	In^{2+}/Mn^{3+} In^{3+}/Co^{2+} Ga^{3+}/Mg^{2+} Sc^{3+}/Mg^{2+}			
CTOF-1	Ti^{4+}/Co^{2+}	Direct synthesis	Adsorption	Hong *et al.* [57]
CTOF-2	Ti^{4+}/Co^{2+}	Direct-synthesis	Adsorption	Hong *et al.* [57]
Cu(II)–MOF*	Cu^{2+}/Zn^{2+}	Direct synthesis	Adsorption	Pal *et al.* [58]
$CuMg(pdc)_2(H_2O)_4]\cdot 2H_2O\}_n$ (1), $[CuCa(pdc)_2]n$ (2),$[CuSr(pdc)_2(H_2O)_3]_n$ (3), and $\{[CuBa(pdc)_2(H_2O)_5]\cdot H2O\}n$ (4)	$Cu^{2+}/Mg^{2+}/Ca^{2+}/Sr^{2+}/Ba^{2+}$	Direct synthesis	Catalysis	Saha *et al.* [59]
$Eu_{0.0069}Tb_{0.9931}$-DMBDC	Eu^{3+}/Tb^{3+}	Direct synthesis	Lanthanide thermometer	Cui *et al.* [60]
iso1	Cu^{2+}/Mn^{2+}	Direct synthesis	Adsorption	Soria *et al.* [61]
$In_xGa_{1-x}(O_2C_2H_4)_{0.5}$(hfipbb)	$Ga^{3+}/In^{3+}/Al^{3+}$	Direct synthesis	Multi-component reaction Strecker	Díaz *et al.* [62]
MFM-300	Ga^{3+}/Fe^{3+}	Direct synthesis	Adsorption, Catalysis	Krap *et al.* [63]
$[M_xM'_{2-x}(ca)_2(1,4\text{-dimb})]_n$	Ni^{2+}/Co^{2+}	Direct synthesis	Magnetism	Zeng *et al.* [64]
M'MOF-1, M'MOF-2	Fe^{3+}/ Ag^{3+}	Direct synthesis	Incorporation	Zhang *et al.* [65]
M'MOF-4, -5,-6,-7	$Cd^{2+}/ Zn^{2+}/Cu^{2+}$	Direct synthesis	Separation	Das *et al.* [66]
PVDC-1	Yb^{3+}/Er^{3+}	Direct synthesis	Lanthanide MOF barcode	White *et al.* [67]
$Tb_{0.9}Eu_{0.1}$PIA	Tb^{3+}/Eu^{3+}	Direct synthesis	Luminescent Thermometer	Rao *et al*. [68]
$Zn_3(BDC)_3$ [Cu(Pyen)] (M'MOF 1)	Zn^{2+}/Cu^{2+}	Direct synthesis	Molecular sieving	Chen *et al.* [69]
ZTOF-1	Zn^{2+}/Ti^{4+}	Direct synthesis	Adsorption	Hong *et al.* [70]

Zn/Cu-BTC	Cu^{2+}/Zn^{2+}	Direct synthesis	Incorporation, Desulfurization	Wang *et al.* [44]

pyz = pyrazine; CPM = crystalline porous material; CTOF = cobalt-titanium organic framework; pdc = pyridine-2,5-dicarboxylic acid; DMBDC = 2,5-dimethoxy-1,4-benzenedicarboxylate; iso = isoreticular; H_2hfibb = 4,4'-hexafluoroisopropylidene-bis-(benzoic acid); MFM = Manchester framework material; 1,4-dimb = 1,4-di-(1-imidzolyl-methyl)-benzene; H_2PVDC = 4,4'-(1E,1'E)-2,2'-(2,5-dimethoxy-1,4-phenylene)bis(ethane-2,1-diyl)dibenzoic acid; M'MOF = mixed-metal-organic framework; H_2PIA = 5-(pyridin-4yl)isophthalic acid; H_2pyen = 5-mthyl-4-oxo-1,4-dihydro-pyridine-3-carbaldehyde; ZTOF = zinc-titanium-organic framework; H_2BTC = benzene-1,3,5-tricarboxylic acid ; * = including oxidation state of the metal salts used during synthesis.

Compound	Metal	Synthesis approach	Subject	Reference
$Cd_3[(Cd_4Cl)_3(BTT)_8(H_2O)_{12}]_2$	$Co^{2+}/Ni^{2+}/Cd^{2+}$	Post-synthetic exchange in methanol	Adsorption	Liao *et al.* [71]
MFU-4l	Zn^{2+}/Co^{2+}	Post-synthetic exchange in DMF	Thermo-dynamic study	Brozek *et al.* [27]
MFU-4l	Zn^{2+}/Co^{2+}	Post-synthetic exchange in DMF	Catalysis	Denysenko *et al.* [72]
MMPF-5	Cd^{2+}/Co^{2+}	Post-synthetic exchange in DMSO	Catalysis	Wang *et al.* [73]
$Mn_3[(Mn_4Cl)_3(BTT)_8(CH3OH)_{10}]_2$	$Li^{+}/Cu^{+}/Fe^{2+}/Co^{2+}/Ni^{2+}/Cu^{2+}/Zn^{2+}/Mn^{2+}$	Post-synthetic exchange in methanol	Adsorption	Dincă *et al.* [74]
MOF 1, $Cd1.5(H_3O)_3[(Cd_4O)_3(hett)_8]\cdot 6H_2O$	Pb^{2+}/Cd^{2+}	Post-synthetic exchange in water	Incorporation	Das *et al.* [75]
Ni-ITHD	$Zn^{2+}/Ni^{2+}/Co^{2+}/Cu^{2+}$	Direct synthesis and Post-synthetic exchange in DMF	Incorporation Adsorption	Song *et al.* [76, 77]
PCN-333	Cr^{3+}/Fe^{3+}	Post-synthetic exchange in DMF	Incorporation	Park *et al.* [78]
PCN-426	$Mg^{2+}/Fe^{3+}/Cr^{3+}$	Post-synthetic exchange in DMF	Incorporation	Liu *et al.* [79]
PCN-922-PCN921	Cu^{2+}/Zn^{2+}	Post-synthetic exchange in DMF	Incorporation	Wei *et al.* [80]
Porph@MOM-10-M	$Cd^{2+}/Mn^{2+}/Cu^{2+}$	Post-synthetic exchange in methanol	Catalysis	Zhang *et al.* [81]

Post 65	Mn^{2+}/Fe^{2+}/ Co^{2+}/Ni^{2+}/ Cu^{2+}	Post-Synthetic exchange in DMF	Incorporation	Kim *et al.* [82]
$Zn_{1.6}Cu_{6.4}L_{16}$	Zn^{2+}/Cu^{2+}	Post-synthetic exchange in water	Incorporation	Zhao *et al.* [83]
$Co_{1.2}Cu_{6.8}L_{16}$	Cu^{2+}/Co^{2+}	Post-synthetic exchange in water	Incorporation	Zhao *et al.* [83]
Zr(Ti)-NDC	Zr^{4+}/Ti^{4+}	Post-synthetic exchange in DMF	Catalysis	Almansa *et al.* [84]
PMOF-2	Zn^{2+}/Cu^{2+}	Post-synthetic exchange in Methanol	Kinetics	Song *et al.* [43]
SURMOF-1	Cu^{2+}/Zn^{2+}/ Ni^{2+}/Co^{2+}	Post-synthetic exchange in DMF	Incorporation	Yao *et al.* [30]
$\{[M(L)_2(H_2O)_2].2(anion).guest.(2H_2O)\}_n$	Zn^{2+}/Cu^{2+}/ Cd^{2+}	Post-synthetic exchange in water	Incorporation	Mukherjee *et al.* [85]

H_3BTT.2HCl = 1,3,5-Tris(2H-tetrazol-5-yl)benzene hydrochloride; MMPF = metal-metalloporphyrin framework; H_2ett = 5,5',10,10',15,15'-Hexaethayltruxene-2,7,12-tricarboxylic acid; ITHD = ith-d net topology; PCN = porous coordination network; MOM = metal-organic materials; DMSO = dimethylsulfoxide; SURMOF = Surface anchored metal-organic framework; POST = Pohang university of science and technology * = including oxidation state of the metal salts used during synthesis;

Table A.2 Fractions (%) of the np, lp-1 and lp-2 obtained via high-pressure XRPD measurements in the range 0-17.5 bar CO2 at 228 K for compounds COMOC-2(V), 1 (V=81%), 2 (V=66%), 3 (V=46%).

COMOC-2(V)			
Pressure (bar)	np (%)	lp-1 (%)	lp-2 (%)
0-Start	4.40	95.60	0
1	14.43	85.57	0
2.5	28.67	71.33	0
5	39.71	42.81	17.48
7.5	25.2	47.32	27.50
10	7.73	38.66	53.60
12.5	8.10	38.85	53.06
15	7.82	36.81	55.36
17.5	7.45	37.34	55.21
0-End	5.12	94.89	0

1 (V=81%)			
Pressure (bar)	np (%)	lp-1 (%)	lp-2 (%)
0-Start	27.32	72.68	0
1	71.79	28.20	0
2.5	78.62	21.39	0
5	74.16	9.61	16.22
7.5	18.35	8.78	72.88
10	0	2.35	97.65
12.5	0	2.06	97.94
15	0	2.09	97.91
17.5	0	2.11	97.98
0-End	26.91	73.09	0

2 (V=66%)			
Pressure (bar)	np (%)	lp-1 (%)	lp-2 (%)
0-Start	7.20	92.80	0
1	28.23	71.77	0
2.5	44.74	55.26	0
5	38.69	23.59	37.75
7.5	38.44	23.54	38.02
10	25.25	21.07	53.69
12.5	24.30	22.44	53.25
15	25.04	23.33	51.63
17.5	26.87	25.80	47.33
0-End	7.98	92.02	0

3 (V=46%)			
Pressure (bar)	np (%)	lp-1 (%)	lp-2 (%)
0-Start	27.32	72.68	0
1	71.79	28.20	0
2.5	78.62	21.39	0
5	74.16	9.61	16.22
7.5	18.35	8.78	72.88
10	0	2.35	97.65
12.5	0	2.06	97.94
15	0	2.09	97.91
17.5	0	2.11	97.98
0-End	26.91	73.09	0

Table A.3 Empirically determined lattice parameters for COMOC-2(V) at variable pressure for the three states (np, lp-1 and lp-2).

np	**COMOC-2(V)**			
Pressure (bar)	a(Å)	b(Å)	c(Å)	Volume (Å^3)
0	21.26076	6.94049	18.7464	2766.2188
1	21.31003	7.20581	18.77984	2811.72213
2.5	21.51677	6.81396	18.92336	2774.43526
5	21.39871	7.32613	18.84329	2954.05672
7.5	21.40149	7.2396	18.8452	2919.84307
10	21.15791	7.11148	18.65899	2807.50955
12.5	21.16035	6.77265	18.6473	2672.37543
15	21.14909	6.85673	18.64139	2703.25432
17.5	21.13104	6.73041	18.63156	2649.7914
0	21.45219	6.98295	18.87741	2827.82582

lp-1	**COMOC-2(V)**			
Pressure (bar)	a(Å)	b(Å)	c(Å)	Volume (Å^3)
0	24.81274	6.85609	18.96316	3225.98309
1	24.92118	6.27611	18.98926	2970.07226
2.5	25.36087	6.52118	19.21855	3178.41864
5	25.23822	6.48038	19.16507	3134.50822
7.5	25.23969	6.60439	19.16683	3194.88172
10	24.892	6.941	19.01602	3285.50092
12.5	24.89255	7.19671	19.01626	3406.65788
15	24.89541	6.85651	19.01753	3246.20848
17.5	24.8952	7.15383	19.01744	3386.93053
0	25.1972	6.51932	19.15056	3145.8356

lp-2	**COMOC-2(V)**			
Pressure (bar)	a(Å)	b(Å)	c(Å)	Volume ($Å^3$)
0	-	-	-	-
1	-	-	-	-
2.5	-	-	-	-
5	25.03082	6.68856	18.99256	3179.73839
7.5	24.72185	6.85618	18.80828	3187.95555
10	24.32859	7.45649	18.56974	3368.65989
12.5	24.235	7.15328	18.62305	3228.48792
15	24.1958	7.326	18.64658	3305.61829
17.5	24.19832	7.49979	18.64974	3384.5981
0	-	-	-	-

Table A.4 Empirically determined lattice parameters for compound 1 (V=81%) at variable pressure for the three states (np, lp-1 and lp-2).

np	**1 (V=81%)**			
Pressure bBar)	a(Å)	b(Å)	c(Å)	Volume (Å^3)
0	24.36559	7.23967	18.85828	3326.58065
1	24.09406	7.02418	18.73145	3170.13085
2.5	24.08016	6.68667	18.72494	3015.01532
5	24.08018	6.85448	18.72497	3090.68719
7.5	24.09787	6.81234	18.73329	3075.31224
10	24.14143	6.5196	18.75493	2951.88622
12.5	24.13205	6.72776	18.75053	3044.23506
15	24.11402	6.72797	18.74205	3040.67823
17.5	24.08003	6.81213	18.72492	3071.56635
0	24.20635	6.4329	18.62095	2994.09542

lp-1	**1 (V=81%)**			
Pressure (bar)	a(Å)	b(Å)	c(Å)	Volume (Å^3)
0	24.40585	7.18915	19.28844	3384.29579
1	24.73239	7.27758	18.84977	3392.8092
2.5	24.84442	7.49507	18.91306	3521.8144
5	24.83104	6.81069	18.94865	3204.5285
7.5	24.84032	6.81079	18.94972	3205.95548
10	24.8489	6.81068	18.95353	3207.65871
12.5	24.85663	6.6847	18.95696	3149.87389
15	24.8723	6.76813	18.96391	3192.3644
17.5	24.90486	6.80995	18.94745	3213.50095
0	24.78835	7.1942	19.0547	3398.06993

lp-2	**1 (V=81%)**			
Pressure (bar)	a(Å)	b(Å)	c(Å)	Volume ($Å^3$)
0	-	-	-	-
1	-	-	-	-
2.5	-	-	-	-
5	24.4933	7.36473	18.70872	3374.80053
7.5	24.37484	7.71365	18.63387	3503.52091
10	24.59738	7.8021	18.53873	3557.79312
12.5	24.59982	7.98057	18.53977	3639.73686
15	24.66804	7.89078	18.52633	3606.15083
17.5	24.66091	7.89067	18.52324	3604.45658
0	-	-	-	-

Table A.5 Empirically determined lattice parameters for compound 2 (V=66%) at variable pressure for the three states (np, lp-1 and lp-2).

np	**2 (V=66%)**			
Pressure (bar)	a(Å)	b(Å)	c(Å)	Volume (Å^3)
0	21.24984	6.98274	18.66214	2769.12827
1	21.21767	6.89761	18.68024	2733.87524
2.5	21.17478	6.64604	18.66931	2627.30346
5	21.16352	6.7714	18.66157	2674.32879
7.5	21.1617	6.81333	18.66032	2690.47442
10	21.14769	6.60401	18.65079	2604.75878
12.5	21.15202	6.64572	18.65381	2622.17404
15	21.1548	6.68744	18.65603	2639.29555
17.5	21.1693	6.72937	18.66553	2659.01793
0	21.42646	6.51996	18.63665	2603.53221

lp-1	**2 (V=66%)**			
Pressure (bar)	a(Å)	b(Å)	c(Å)	Volume (Å^3)
0	24.6778	6.72915	18.86866	3128.2576
1	24.51629	6.98186	18.80235	3218.38701
2.5	24.56766	6.89748	18.82551	3190.07546
5	24.59724	6.85545	18.87203	3182.30163
7.5	24.63164	6.93983	18.88757	3228.63081
10	24.68159	7.10911	18.9101	3318.04365
12.5	24.63737	6.93919	18.89018	3229.53057
15	24.64438	6.85492	18.89334	3191.75319
17.5	24.59614	6.85524	18.87157	3181.97955
0	24.62285	7.02271	18.99525	3284.64171

lp-2	**2 (V=66%)**			
Pressure (bar)	a(Å)	b(Å)	c(Å)	Volume ($Å^3$)
0	-	-	-	-
1	-	-	-	-
2.5	-	-	-	-
5	24.08018	6.85448	18.72497	3090.68719
7.5	24.09787	6.81234	18.73329	3075.31224
10	24.14143	6.5196	18.75493	2951.88622
12.5	24.13205	6.72776	18.75053	3044.23506
15	24.11402	6.72797	18.74205	3040.67823
17.5	24.08003	6.81213	18.72492	3071.56635
0	-	-	-	-

Table A.6 Empirically determined lattice parameters for compound 3 (V=46%) at variable pressure for the three states (np, lp-1 and lp-2).

np	**3 (V=46%)**			
Pressure (bar)	a(Å)	b(Å)	c(Å)	Volume (Å^3)
0	21.20742	6.64416	18.71067	2636.43729
1	21.04715	6.89759	18.56368	2694.97665
2.5	21.2187	6.64553	18.69943	2636.79766
5	21.20633	6.81314	18.69093	2700.49629
7.5	21.20514	6.77121	18.69011	2683.60884
10	21.19527	6.77121	18.68334	2681.38916
12.5	21.17781	6.77121	18.67137	2677.46259
15	21.12342	6.72949	18.63403	2648.82242
17.5	21.12837	6.60464	18.63743	2600.76311
0	21.20642	6.68598	18.7101	2652.82731

lp-1	**3 (V=46%)**			
Pressure (bar)	a(Å)	b(Å)	c(Å)	Volume (Å^3)
0	24.36544	7.23697	18.8127	3317.28109
1	24.26094	7.45472	18.82313	3404.32259
2.5	24.29706	6.79616	18.71967	3078.83696
5	25.80337	6.81216	19.8038	3481.04856
7.5	25.50821	6.89654	19.61647	3450.89914
10	25.42682	6.77045	19.57973	3370.66843
12.5	25.42015	6.77055	19.57648	3369.27381
15	25.18666	6.68711	19.40302	3267.97137
17.5	25.21635	6.77086	19.41817	3315.38926
0	24.37585	7.32359	18.81695	3359.17936

lp-2	**3 (V=46%)**			
Pressure (bar)	a(Å)	b(Å)	c(Å)	Volume ($Å^3$)
0	-	-	-	-
1	-	-	-	-
2.5	-	-	-	-
5	24.39725	6.76937	18.79152	3103.49368
7.5	24.27785	6.85374	18.73669	3117.67446
10	24.21992	6.76989	18.75443	3075.09055
12.5	24.21733	6.68635	18.75316	3036.61664
15	24.30298	6.81213	18.82503	3116.57946
17.5	24.28733	6.89672	18.81799	3152.06553
0	-	-	-	-

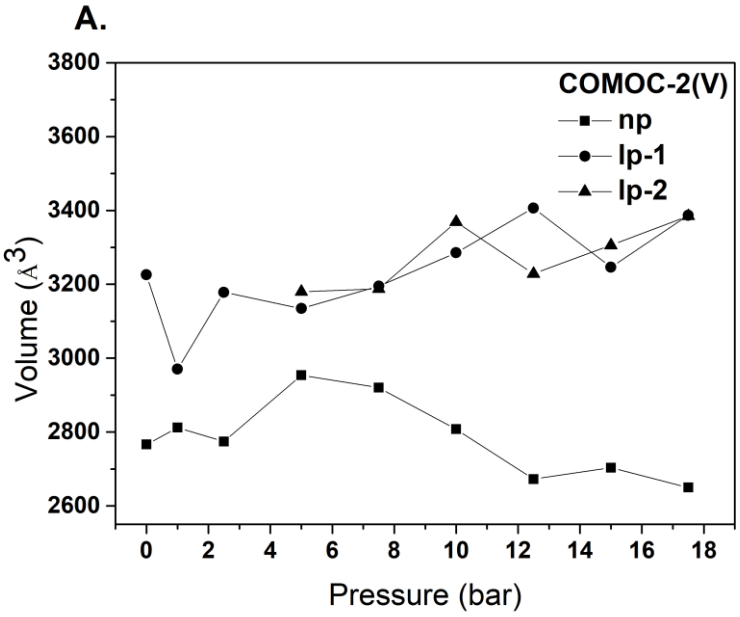
A.
COMOC-2(V)
np
lp-1
lp-2
Volume (Å3)
Pressure (bar)
3800
3600
3400
3200
3000
2800
2600
0
2
4
6
8
10
12
14
16
18

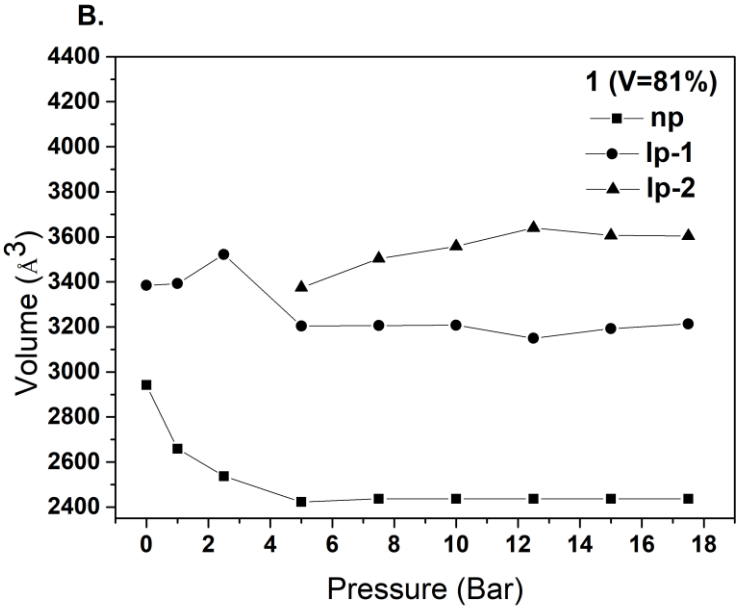
B.
1 (V=81%)
np
lp-1
lp-2
Volume (Å3)
Pressure (Bar)
4400
4200
4000
3800
3600
3400
3200
3000
2800
2600
2400
0
2
4
6
8
10
12
14
16
18

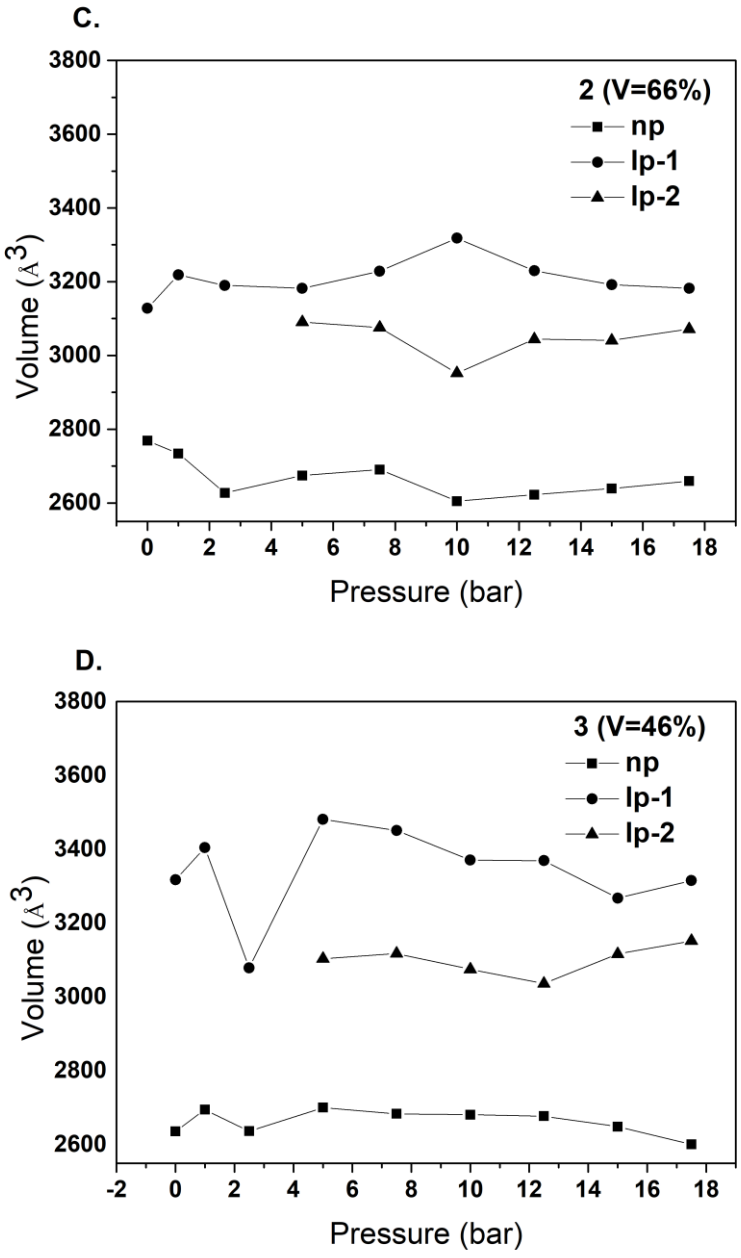

Figure A.1 Evolution of the volume upon induced pressure for COMOC-2(V) in the three states: np, lp-1 and lp-2 for compounds (A) COMOC(2)-V, (B) 1 (V=81%), (C) 2 (V=66%), (D) 3 (V=46%).

References

1. M. Mendt, B. Jee, N. Stock, T. Ahnfeldt, M. Hartmann, D. Himsl and A. Pöppl, *The Journal of Physical Chemistry C*, 2010, **114**, 19443-19451.
2. M. Mendt, B. Jee, D. Himsl, L. Moschkowitz, T. Ahnfeldt, N. Stock, M. Hartmann and A. Pöppl, *Applied Magnetic Resonance*, 2014, **45**, 269-285.
3. O. Kozachuk, M. Meilikhov, K. Yusenko, A. Schneemann, B. Jee, A.V. Kuttatheyil, M. Bertmer, C. Sternemann, A. Pöppl and R.A. Fischer, *European Journal of Inorganic Chemistry*, 2013, **2013**, 4546-4557.
4. I. Nevjestić, H. Depauw, K. Leus, V. Kalendra, I. Caretti, G. Jeschke, S. Van Doorslaer, F. Callens, P. Van Der Voort and H. Vrielinck, *ChemPhysChem*, 2015, **16**, 2968-2973.
5. I. Nevjestić, H. Depauw, K. Leus, G. Rampelberg, C.A. Murray, C. Detavernier, P. Van Der Voort, F. Callens and H. Vrielinck, *The Journal of Physical Chemistry C*, 2016, **120**, 17400-17407.
6. I. Nevjestić, H. Depauw, P. Gast, P. Tack, D. Deduytsche, K. Leus, M. Van Landeghem, E. Goovaerts, L. Vincze, C. Detavernier, P. Van Der Voort, F. Callens and H. Vrielinck, *Physical Chemistry Chemical Physics*, 2017, **19**, 24545-24554.
7. M.N. Timofeeva, V.N. Panchenko, N.A. Khan, Z. Hasan, I.P. Prosvirin, S.V. Tsybulya and S.H. Jhung, *Applied Catalysis A: General*, 2017, **529**, 167-174.
8. F. Nouar, T. Devic, H. Chevreau, N. Guillou, E. Gibson, G. Clet, M. Daturi, A. Vimont, J.M. Greneche, M.I. Breeze, R.I. Walton, P.L. Llewellyn and C. Serre, *Chemical Communications*, 2012, **48**, 10237-10239.
9. M.I. Breeze, G. Clet, B.C. Campo, A. Vimont, M. Daturi, J.-M. Grenèche, A.J. Dent, F. Millange and R.I. Walton, *Inorganic Chemistry*, 2013, **52**, 8171-8182.
10. H. Depauw, I. Nevjestić, J. De Winne, G. Wang, K. Haustraete, K. Leus, A. Verberckmoes, C. Detavernier, F. Callens, E. De Canck, H. Vrielinck and P. Van Der Voort, *Chemical Communications*, 2017, **53**, 8478-8481.
11. M. Kim, J.F. Cahill, H. Fei, K.A. Prather and S.M. Cohen, *Journal of the American Chemical Society*, 2012, **134**, 18082-18088.
12. S. Wongsakulphasatch, F. Nouar, J. Rodriguez, L. Scott, C. Le Guillouzer, T. Devic, P. Horcajada, J.M. Greneche, P.L. Llewellyn, A.

Vimont, G. Clet, M. Daturi and C. Serre, *Chemical Communications*, 2015, **51**, 10194-10197.
13. L. Mitchell, P. Williamson, B. Ehrlichová, A.E. Anderson, V.R. Seymour, S.E. Ashbrook, N. Acerbi, L.M. Daniels, R.I. Walton, M.L. Clarke and P.A. Wright, *Chemistry - A European Journal*, 2014, **20**, 17185-17197.
14. T.A. Vu, G.H. Le, C.D. Dao, L.Q. Dang, K.T. Nguyen, P.T. Dang, H.T.K. Tran, Q.T. Duong, T.V. Nguyen and G.D. Lee, *RSC Advances*, 2014, **4**, 41185-41194.
15. K. Leng, C. Zhang, X. Li, C. Hou and Y. Sun, *Reaction Kinetics, Mechanisms and Catalysis*, 2017, **120**, 345-357.
16. Z. Zhou, L. Mei, C. Ma, F. Xu, J. Xiao, Q. Xia and Z. Li, *Chemical Engineering Science*, 2016, **147**, 109-117.
17. M. Lammert, Gli and N. Stock, *Dalton Transactions*, 2017, **46**, 2425-2429.
18. H. Depauw, I. Nevjestić, G. Wang, K. Leus, F. Callens, E. De Canck, K. De Buysser, H. Vrielinck and P. Van Der Voort, *Journal of Materials Chemistry A*, 2017, **5**, 24580-24584.
19. C. Hon Lau, R. Babarao and M.R. Hill, *Chemical Communications*, 2013, **49**, 3634-3636.
20. F. Nouar, M.I. Breeze, B.C. Campo, A. Vimont, G. Clet, M. Daturi, T. Devic, R.I. Walton and C. Serre, *Chemical Communications*, 2015, **51**, 14458-14461.
21. A.M. Ebrahim and T.J. Bandosz, *ACS Applied Materials & Interfaces*, 2013, **5**, 10565-10573.
22. S.J.D. Smith, B.P. Ladewig, A.J. Hill, C.H. Lau and M.R. Hill, 2015, **5**, 1-6.
23. J. Tu, X. Zeng, F. Xu, X. Wu, Y. Tian, X. Hou and Z. Long, *Chemical Communications*, 2017, **53**, 3361-3364.
24. D. Sun, W. Liu, M. Qiu, Y. Zhang and Z. Li, *Chemical Communications*, 2015, **51**, 2056-2059.
25. Y. Lee, S. Kim, J.K. Kang and S.M. Cohen, *Chemical Communications*, 2015, **51**, 5735-5738.
26. R.N. Amador, M. Carboni and D. Meyer, *RSC Advances*, 2017, **7**, 195-200.
27. C.K. Brozek and M. Dinca, *Chemical Communications*, 2015, **51**, 11780-11782.
28. J.A. Botas, G. Calleja, M. Sánchez-Sánchez and M.G. Orcajo, *Langmuir*, 2010, **26**, 5300-5303.

29. C.K. Brozek and M. Dincă, *Journal of the American Chemical Society*, 2013, **135**, 12886-12891.
30. Q. Yao, J. Sun, K. Li, J. Su, M.V. Peskov and X. Zou, *Dalton Transactions*, 2012, **41**, 3953-3955.
31. L.J. Wang, H. Deng, H. Furukawa, F. Gándara, K.E. Cordova, D. Peri and O.M. Yaghi, *Inorganic Chemistry*, 2014, **53**, 5881-5883.
32. J.A. Botas, G. Calleja, M. Sánchez-Sánchez and M.G. Orcajo, *International Journal of Hydrogen Energy*, 2011, **36**, 10834-10844.
33. J.A. Villajos, G. Orcajo, C. Martos, J.Á. Botas, J. Villacañas and G. Calleja, *International Journal of Hydrogen Energy*, 2015, **40**, 5346-5352.
34. J.D. Howe, C.R. Morelock, Y. Jiao, K.W. Chapman, K.S. Walton and D.S. Sholl, *The Journal of Physical Chemistry C*, 2017, **121**, 627-635.
35. D. Sun, F. Sun, X. Deng and Z. Li, *Inorganic Chemistry*, 2015, **54**, 8639-8643.
36. Y. Jiao, C.R. Morelock, N.C. Burtch, W.P. Mounfield, J.T. Hungerford and K.S. Walton, *Industrial & Engineering Chemistry Research*, 2015, **54**, 12408-12414.
37. Y. Fu, L. Xu, H. Shen, H. Yang, F. Zhang, W. Zhu and M. Fan, *Chemical Engineering Journal*, 2016, **299**, 135-141.
38. B. Jee, K. Eisinger, F. Gul-E-Noor, M. Bertmer, M. Hartmann, D. Himsl and A. Pöppl, *The Journal of Physical Chemistry C*, 2010, **114**, 16630-16639.
39. S. Friedländer, P.S. Petkov, F. Bolling, A. Kultaeva, W. Böhlmann, O. Ovchar, A.G. Belous, T. Heine and A. Pöppl, *The Journal of Physical Chemistry C*, 2016, **120**, 27399-27411.
40. F. Gul-E-Noor, D. Michel, H. Krautscheid, J. Haase and M. Bertmer, *The Journal of Chemical Physics*, 2013, **139**,
41. F. Gul-E-Noor, M. Mendt, D. Michel, A. Pöppl, H. Krautscheid, J. Haase and M. Bertmer, *The Journal of Physical Chemistry C*, 2013, **117**, 7703-7712.
42. M. Šimėnas, B. Jee, M. Hartmann, J. Banys and A. Pöppl, *The Journal of Physical Chemistry C*, 2015, **119**, 28530-28535.
43. X. Song, S. Jeong, D. Kim and M.S. Lah, *CrystEngComm*, 2012, **14**, 5753-5756.
44. T. Wang, X. Li, W. Dai, Y. Fang and H. Huang, *Journal of Materials Chemistry A*, 2015, **3**, 21044-21050.
45. M.A. Gotthardt, R. Schoch, S. Wolf, M. Bauer and W. Kleist, *Dalton Transactions*, 2015, **44**, 2052-2056.

46. Y. Cao, Y. Zhao, F. Song and Q. Zhong, *Journal of Energy Chemistry*, 2014, **23**, 468-474.
47. A. Schejn, A. Aboulaich, L. Balan, V. Falk, J. Lalevee, G. Medjahdi, L. Aranda, K. Mozet and R. Schneider, *Catalysis Science & Technology*, 2015, **5**, 1829-1839.
48. G. Kaur, R.K. Rai, D. Tyagi, X. Yao, P.-Z. Li, X.-C. Yang, Y. Zhao, Q. Xu and S.K. Singh, *Journal of Materials Chemistry A*, 2016, **4**, 14932-14938.
49. Y.Z. Chen, C. Wang, Z.Y. Wu, Y. Xiong, Q. Xu, S.H. Yu and H.L. Jiang, *Advanced Materials*, 2015, **27**, 5010-5016.
50. H. Fei, J.F. Cahill, K.A. Prather and S.M. Cohen, *Inorganic Chemistry*, 2013, **52**, 4011-4016.
51. A. Abbasi, M. Soleimani, M. Najafi and S. Geranmayeh, *Inorganica Chimica Acta*, 2016, **439**, 18-23.
52. S.-T. Zheng, X. Zhao, S. Lau, A. Fuhr, P. Feng and X. Bu, *Journal of the American Chemical Society*, 2013, **135**, 10270-10273.
53. S.-T. Zheng, T. Wu, F. Zuo, C. Chou, P. Feng and X. Bu, *Journal of the American Chemical Society*, 2012, **134**, 1934-1937.
54. S.-T. Zheng, C. Mao, T. Wu, S. Lee, P. Feng and X. Bu, *Journal of the American Chemical Society*, 2012, **134**, 11936-11939.
55. S.-T. Zheng, T. Wu, C. Chou, A. Fuhr, P. Feng and X. Bu, *Journal of the American Chemical Society*, 2012, **134**, 4517-4520.
56. Q.-G. Zhai, X. Bu, C. Mao, X. Zhao and P. Feng, *Journal of the American Chemical Society*, 2016, **138**, 2524-2527.
57. K. Hong, W. Bak, D. Moon and H. Chun, *Crystal Growth & Design*, 2013, **13**, 4066-4070.
58. T.K. Pal, D. De, S. Neogi, P. Pachfule, S. Senthilkumar, Q. Xu and P.K. Bharadwaj, *Chemistry – A European Journal*, 2015, **21**, 19064-19070.
59. D. Saha, D.K. Hazra, T. Maity and S. Koner, *Inorganic Chemistry*, 2016, **55**, 5729-5731.
60. Y. Cui, H. Xu, Y. Yue, Z. Guo, J. Yu, Z. Chen, J. Gao, Y. Yang, G. Qian and B. Chen, *Journal of the American Chemical Society*, 2012, **134**, 3979-3982.
61. J. Ferrando-Soria, P. Serra-Crespo, M. de Lange, J. Gascon, F. Kapteijn, M. Julve, J. Cano, F. Lloret, J. Pasán, C. Ruiz-Pérez, Y. Journaux and E. Pardo, *Journal of the American Chemical Society*, 2012, **134**, 15301-15304.

62. L.M. Aguirre-Díaz, F. Gándara, M. Iglesias, N. Snejko, E. Gutiérrez-Puebla and M.Á. Monge, *Journal of the American Chemical Society*, 2015, **137**, 6132-6135.
63. C.P. Krap, R. Newby, A. Dhakshinamoorthy, H. García, I. Cebula, T.L. Easun, M. Savage, J.E. Eyley, S. Gao, A.J. Blake, W. Lewis, P.H. Beton, M.R. Warren, D.R. Allan, M.D. Frogley, C.C. Tang, G. Cinque, S. Yang, and M. Schröder, *Inorganic Chemistry*, 2016, **55**, 1076-1088.
64. M.-H. Zeng, B. Wang, X.-Y. Wang, W.-X. Zhang, X.-M. Chen and S. Gao, *Inorganic Chemistry*, 2006, **45**, 7069-7076.
65. Y. Zhang, B. Chen, F.R. Fronczek and A.W. Maverick, *Inorganic Chemistry*, 2008, **47**, 4433-4435.
66. M.C. Das, Q. Guo, Y. He, J. Kim, C.-G. Zhao, K. Hong, S. Xiang, Z. Zhang, K.M. Thomas, R. Krishna and B. Chen, *Journal of the American Chemical Society*, 2012, **134**, 8703-8710.
67. K.A. White, D.A. Chengelis, K.A. Gogick, J. Stehman, N.L. Rosi and S. Petoud, *Journal of the American Chemical Society*, 2009, **131**, 18069-18071.
68. X. Rao, T. Song, J. Gao, Y. Cui, Y. Yang, C. Wu, B. Chen and G. Qian, *Journal of the American Chemical Society*, 2013, **135**, 15559-15564.
69. B. Chen, X. Zhao, A. Putkham, K. Hong, E.B. Lobkovsky, E.J. Hurtado, A.J. Fletcher and K.M. Thomas, *Journal of the American Chemical Society*, 2008, **130**, 6411-6423.
70. K. Hong, W. Bak and H. Chun, *Inorganic Chemistry*, 2013, **52**, 5645-5647.
71. J.-H. Liao, W.-T. Chen, C.-S. Tsai and C.-C. Wang, *CrystEngComm*, 2013, **15**, 3377-3384.
72. D. Denysenko, T. Werner, M. Grzywa, A. Puls, V. Hagen, G. Eickerling, J. Jelic, K. Reuter and D. Volkmer, *Chemical Communications*, 2012, **48**, 1236-1238.
73. X.-S. Wang, M. Chrzanowski, L. Wojtas, Y.-S. Chen and S. Ma, *Chemistry – A European Journal*, 2013, **19**, 3297-3301.
74. M. Dincă and J.R. Long, *Journal of the American Chemical Society*, 2007, **129**, 11172-11176.
75. S. Das, H. Kim and K. Kim, *Journal of the American Chemical Society*, 2009, **131**, 3814-3815.
76. X. Song, M. Oh and M.S. Lah, *Inorganic Chemistry*, 2013, **52**, 10869-10876.
77. X. Song, T.K. Kim, H. Kim, D. Kim, S. Jeong, H.R. Moon and M.S. Lah, *Chemistry of Materials*, 2012, **24**, 3065-3073.

78. J. Park, D. Feng and H.-C. Zhou, *Journal of the American Chemical Society*, 2015, **137**, 11801-11809.
79. T.-F. Liu, L. Zou, D. Feng, Y.-P. Chen, S. Fordham, X. Wang, Y. Liu and H.-C. Zhou, *Journal of the American Chemical Society*, 2014, **136**, 7813-7816.
80. Z. Wei, W. Lu, H.-L. Jiang and H.-C. Zhou, *Inorganic Chemistry*, 2013, **52**, 1164-1166.
81. Z. Zhang, L. Zhang, L. Wojtas, P. Nugent, M. Eddaoudi and M.J. Zaworotko, *Journal of the American Chemical Society*, 2012, **134**, 924-927.
82. Y. Kim, S. Das, S. Bhattacharya, S. Hong, M.G. Kim, M. Yoon, S. Natarajan and K. Kim, *Chemistry – A European Journal*, 2012, **18**, 16642-16648.
83. J.a. Zhao, L. Mi, J. Hu, H. Hou and Y. Fan, *Journal of the American Chemical Society*, 2008, **130**, 15222-15223.
84. A.M. Rasero-Almansa, M. Iglesias and F. Sanchez, *RSC Advances*, 2016, **6**, 106790-106797.
85. G. Mukherjee and K. Biradha, *Chemical Communications*, 2012, **48**, 4293-4295.